Systems-level Analysis of the Mitotic Checkpoint



Lukas Hermann Hutter

Lincoln College

University of Oxford

A thesis submitted for the degree of

DPhil

September 2016

Abstract

The mitotic checkpoint regulates a critical transition in the eukaryotic cell cycle. It delays exit from mitosis until all chromosomes have become bi-oriented. In spite of an impressive body of work uncovering mechanistic aspects of the mitotic checkpoint, a detailed understanding of how the mitotic checkpoint operates as a control system continues to evade us. Here, I present three systems-biological studies aimed at elucidating distinct aspects of the mitotic checkpoint control system.

Using a combination of dedicated experiments and mathematical modelling, we[1] investigate the fragile response of the mitotic checkpoint to precocious separation of sister chromatids in *Drosophila neuroblasts*. We show that the lack of a robust response to precocious loss of sister chromatid cohesion results from systems-level crosstalk between error correction and the checkpoint effector module.

Applying dynamical systems theory in the analysis of a live-cell imaging dataset following the degradation of APC/C:Cdc20-susbtrates in RPE1 and HeLa cells that are arrested in prometaphase and treated with different doses of CDK1 inhibitor, we[2] present a simple mathematical model of the mitotic checkpoint as parsimonious explanation for the observed response to CDK1 inhibition. The model gives rise to a bistable switch, which is discussed as a useful tool to conceptualise the transition from prometaphase to metaphase and from metaphase to anaphase in terms of disengagement and inactivation of the mitotic checkpoint.

Employing a simple mathematical model of phosphatase regulation at mitotic exit as a tool in the analysis of a phosphoproteomics dataset, we[3] examine how the decision to silence the checkpoint is dispatched to initiate diverse processes underpinning mitotic exit. We identify new substrates of the phosphatase PP2A:B55, and describe a mechanism whereby substrates are recognised by PP2A:B55 and their rate of dephosphorylation is encoded electrostatically.

[1] Collaboration with RA and M Mirkovic.

[2] Collaboration with DW Gerlich and AE Dick.

[3] Collaboration with FA Barr, MJ Cundell, R Nunes Bastos, S Mohammed, E Poser and J Holder.

Acknowledgements

I would like to thank my supervisor Prof. **Bela Novak** for making his group my scientific home for the last three years, and providing me with the best supervision imaginable.

Likewise, I would like to thank my former and current group members **Vinod PK**, **Tongli Zhang**, **Stefan Heldt**, **Scott Rata**, and **Michael Hopkins** for fruitful scientific discussion, advice, guidance and coffee. In the context of this thesis, I am particularly thankful to Scott and Michael, who provided valuable feedback on this text, and whose keen eyes helped to eliminate numerous typos and loose ends.

The studies presented in this thesis are highly collaborative in nature. Therefore, I would like to acknowledge the indispensable contribution of my collaborators, **Raquel Oliveira**, **Mihailo Mirkovic**, **Daniel Gerlich**, **Amalie Dick**, Prof. **Francis Barr**, **Michael Cundell**, and **Ricardo Nunes Bastos**, and thank them for many interesting and insightful discussions, and for their collaborative spirit.

I would not have been able to conduct this work without the financial support of the **Böhringer Ingelheim Fonds** and **iv Kärnten**, who provided me with generous funding for my living expenses, and the **Systems Biology DTC** who granted me a scholarship covering my tuition fees, and provided a great learning environment.

To my parents, **Anita** and **Herbert**, my siblings, **Julia** and **Elias**, my wider family and my friends, I am eternally thankful for supporting me and for connecting me with the world beyond academia. Finally, I want to thank **Anna**, who was the spark that brought me to Oxford, and continues to be my catalyst.

Preface

This thesis consists of seven chapters. In chapters 1 and 2, I discuss the cell biology of mitosis and provide a broader context for the work presented in the following chapter. In chapter 3, I motivate the work presented in the results-chapters 4, 5 and 6. In chapter 7, I present a concluding discussion.

To provide additional structure to the text, I make use of three types of text-boxes:

> All of the projects presented herein are collaborative. In orange boxes at the beginning of each results chapter, I will detail which aspects of the projects are my own work, and who else contributed to them.

> This type of box will be used extensively throughout this thesis. It will highlight sections that serve a primarily narrative purpose, provide broader context and provide what I hope to be smooth transitions between more disparate sections of text.

Computational modelling of regulatory networks relies heavily on code. To prevent this thesis from becoming bloated with pages over pages of printed code, each chapter is supplemented with a set of interactive notebooks, which contain fully executable code.

> This type of box highlights links to interactive notebooks and other interactive material that supplement particular sections.

All software packages used in my analyses are freely available. To make the handling of dependencies as easy as possible, I set up a docker container. It is a fully self-contained, yet lightweight virtual machine, that allows you to reproduce my work, without having to worry about installing dependencies on your computer. At `https://github.com/el-uhu/thesis-notebooks`, you'll find detailed instructions on how to set it up on your computer. Make sure to start the docker container as detailed on the website, then you will be able to open the notebooks simple by clicking the provided links. Alternatively, the link denoted "(static version)", will point to a non-interactive version of the notebook. In table 7.1, you will find a list of full URLs to the supplementary material.

Contents

List of Figures xii

List of Tables xiv

1 The Cell Cycle 1

1.0.1 Principles of Control . . . 2
1.0.2 Oscillator . . . 2
1.0.3 Bistability . . . 4
1.0.4 Checkpoints . . . 6

2 Mitosis 7

2.1 The Mitotic Spindle . . . 9
2.1.1 Parts . . . 9
2.1.1.1 Microtubules . . . 9
2.1.1.2 Centrosomes . . . 11
2.1.1.3 Kinetochores . . . 12
2.1.1.4 Cohesin . . . 13
2.1.2 Organisation . . . 14
2.2 Molecular Control of Mitosis . . . 16
2.3 Error Correction . . . 18
2.3.1 Quality . . . 18
2.3.2 The Conductor . . . 18
2.3.3 Correction . . . 21
2.3.4 Detection . . . 21
2.3.5 Focus . . . 22
2.4 The Mitotic Checkpoint Enforcement Mechanism . . . 23
2.4.1 Target . . . 23
2.4.2 Assembly . . . 25

2.4.3 Initiation . . . 27
2.4.4 Structure . . . 27
2.4.5 Identity . . . 28
2.4.6 Turnover . . . 29
2.4.7 Termination . . . 29
2.5 Anaphase and Beyond . . . 30
2.5.1 Departure . . . 30
2.5.2 Relay . . . 31

3 Systems-Level Perspective 32
3.1 Models . . . 32
3.2 Boundaries . . . 33
3.3 Signal . . . 35
3.4 Sensitivity . . . 36
3.5 Irreversibility . . . 37
3.6 Finality . . . 39

4 Costly Crosstalk 40
4.1 Data . . . 41
4.1.1 Experimental System . . . 41
4.1.2 Timing of Mitosis . . . 41
4.1.3 Aurora B Localisation . . . 43
4.1.4 Stabilisation of Attachments . . . 45
4.1.5 Aurora B Inhibition . . . 45
4.1.6 Types of Attachments Upon Loss of Cohesin . . . 47
4.1.7 Chromatin Positioning . . . 49
4.1.8 Localisation of Mad2 and BubR1 . . . 49
4.1.9 Degradation of Cyclin B . . . 51
4.2 Model . . . 52
4.2.1 Construction . . . 53
4.2.1.1 Aurora B Localisation . . . 54
4.2.1.2 Attachments . . . 55
4.2.1.3 Aurora B activity . . . 55
4.2.1.4 APC/C . . . 56
4.2.1.5 MCC . . . 56
4.2.1.6 Cyclin B and CDK1 . . . 57
4.2.2 Implementation . . . 58

4.2.3 Simulations . . . 59
4.2.3.1 Core Model . . . 59
4.2.3.2 Single-Feedback Model . . . 61
4.2.3.3 Dual-Feedback Model . . . 62
4.2.4 Model Analysis . . . 62
4.2.4.1 The Effect of Stretch . . . 62
4.2.4.2 Cyclin B Degradation Pattern . . . 63
4.2.5 Prediction . . . 65
4.2.6 Validation . . . 67
4.3 Discussion . . . 67
4.3.1 Findings . . . 67
4.3.2 Interpretation . . . 68
4.3.3 Limitations . . . 68
4.3.4 Contextualisation . . . 69

5 Disengagement and Inactivation 70
5.1 Data . . . 71
5.1.1 Experimental System . . . 72
5.1.2 High Doses of CDK1 Inhibitor . . . 73
5.1.3 Intermediate Doses of CDK1 Inhibitor . . . 74
5.1.4 Long-term imaging of cells treated with nocodazole . . . 76
5.2 Model . . . 79
5.2.1 Construction . . . 80
5.2.1.1 Cyclin B Synthesis and Degradation . . . 81
5.2.1.2 CDK1 activity . . . 81
5.2.1.3 Securin . . . 81
5.2.1.4 Kinetochore Signalling . . . 82
5.2.1.5 MCC and APC/C . . . 82
5.2.2 Implementation . . . 84
5.2.3 Simulations . . . 85
5.2.3.1 Unperturbed Mitosis . . . 85
5.2.3.2 Nocodazole Treatment - Mitotic Slippage . . . 86
5.2.3.3 Titration of CDK1 activity . . . 87
5.2.4 Bifurcation Analysis . . . 91
5.2.4.1 Evolution in Time . . . 91
5.2.4.2 Sensitivity . . . 92
5.2.4.3 CDK1 Dependence . . . 93

5.2.5 Prediction . . . 95
5.2.6 Validation . . . 95
5.3 Discussion . . . 97

6 Dispatch **99**
6.1 Data . . . 100
6.1.1 Theoretical Premise . . . 100
6.1.2 Experimental Setup . . . 101
6.1.2.1 Preparation of Cell Extracts and de-phosphorylation Assay . . . 101
6.1.2.2 Phosphoproteomics Labelling Strategy . . . 103
6.1.2.3 Proteomics Pipeline . . . 104
6.2 Model-Driven Data-Analysis . . . 104
6.2.1 Preparation of the Dataset . . . 105
6.2.1.1 Pre-processing . . . 105
6.2.1.2 Extracting Data from the MaxQuant-Table . . . 106
6.2.1.3 Summarisation and Cleaning of the Dataset . . . 106
6.2.1.4 Curation of the Dataset . . . 107
6.2.2 The Model . . . 108
6.2.2.1 System of ODEs . . . 108
6.2.2.2 Algebraic Equations . . . 109
6.2.2.3 Model States . . . 109
6.2.2.4 Parameters . . . 109
6.2.2.5 Initial conditions . . . 110
6.2.3 Parametrisation Strategy for the Model Core . . . 110
6.2.4 Global Parametrisation Strategy . . . 112
6.2.5 Substrate Identification . . . 114
6.3 Results . . . 115
6.3.1 Categorisation of peptides . . . 115
6.3.2 Recognition Motif . . . 120
6.3.3 Electrostatic Control of Dephosphorylation Kinetics . . . 121
6.3.3.1 Mathematical Model . . . 123
6.3.4 Validation In Vivo . . . 124
6.3.5 Recognition Determinant . . . 125
6.3.6 Amino Acid Preference . . . 125
6.3.7 ENSA Revisited . . . 125
6.4 Discussion . . . 126

6.4.1 Heuristic 126
6.4.2 Generalisable Design Implications 127
6.4.2.1 Model Constraints 127
6.4.2.2 Experimental Design 128
6.4.3 Summary 128

7 Conclusions **130**
7.1 Boundaries & Signal 130
7.2 Irreversibility & Finality 131
7.3 Sensitivity 131
7.4 Beyond the Mitotic Checkpoint 132

References **133**

List of Figures

1.1 The metazoan cell cycle . . . 3
1.2 Cell Cycle Oscillator Control Network . . . 4
1.3 Bistability and Limit Cycle Oscillators . . . 5

2.1 Constituents of a mitotic spindle . . . 10
2.2 Organising Principles Driving Spindle Assembly . . . 14
2.3 Error Correction . . . 19
2.4 The Mitotc Checkpoint Effector Mechanism . . . 24

3.1 A bistable switch and basic terminology of control systems . . . 35

4.1 Mitotic Timing . . . 42
4.2 Aurora B Localisation Upon Cohesin Cleavage . . . 44
4.3 Characterisation of Chromatin Movement . . . 46
4.4 Characterisation of Attachment-Types . . . 48
4.5 Timecourse-Imaging of Mad2, BubR1 and Cyclin B . . . 50
4.6 Wiring Diagram of the Model . . . 53
4.7 Model Simulations . . . 60
4.8 Model Analysis . . . 64
4.9 Model Predictions . . . 65
4.10 Validation of Predictions . . . 66

5.1 Conceptual Framework: Classification of qualitative states of checkpoint signalling . . . 72
5.2 Addition of high doses of RO-3306 to nocodazole-treated cells . . . 73
5.3 Addition of medium doses of RO-3306 to nocodazole-treated cells . . . 75
5.4 Treatment with nocodazole alone . . . 77
5.5 Wiring Diagram . . . 80
5.6 Simulation of Unperturbed Mitosis and Mitotic Slippage . . . 85
5.7 Simulation cyclin B degradation with partial Cdk1 inhbition . . . 89

5.8 Simulation securin degradation with partial Cdk1 inhbition 90
5.9 Transient Bistability 92
5.10 Bifurcation Diagrams: uKT vs. cyclin B 93
5.11 Bifurcation Diagram: maximal CDK1 activity vs. cyclin B 94
5.12 Minimal CDK1 Inhibition Accelerates Mitotic Slippage 96
5.13 Bifurcation diagram and contextual framework 97

6.1 Theoretical Premise 100
6.2 In Vitro de-phosphorylation Assay and Sample Preparation 102
6.3 SILAC-Labelling Strategy 103
6.4 Proteomics Pipeline and Preliminary Data Processing 104
6.5 Wiring Diagram of the de-phosphorylation Model 109
6.6 Parametrisation of the model core 111
6.7 Phospho-proteome-wide fitting of the simplified model to timecourse data 113
6.8 Substrate Identification 114
6.9 Known B55 Substrates 115
6.10 High-Confidence B55 Substrates 116
6.11 High-Confidence B55-independent Substrates 116
6.12 Novel B55 Substrates: Spindle proteins 117
6.13 Novel B55 Substrates: Nuclear pores 118
6.14 Novel B55-independent Substrates: 119
6.15 Bipartite poly-basic recognition motif 120
6.16 Dephosphorylation rate is encoded by the bipartite poly-basic recognition motif 122

List of Tables

4.1 Comparison of duration of mitosis in different treatments depicted in figure 4.1 E 43
4.2 Kinetic parameters used in the three model instances 57

5.1 Kinetic parameters used in the model 83
5.2 Parameters: CDK1 Inhibition 87
5.3 Bifurcation Diagram Snapshots: k_{scycb} and corresponding times 92

6.1 Patterns of missing data 107
6.2 Summary of filtering steps 107
6.3 Parameters for the model core 112
6.4 Phospho-amino acid frequencies 121
6.5 Parameters for the electrostatic model 124

7.1 Interactive Supplementary Material 143

1

The Cell Cycle

From a single ancestral cell at the origin of life 3 to 4 billion years ago to the unfathomable diversity of life on earth today; from a fertilised egg to the 30 trillion human cells that make up an adult human being [1]. - cells grow, replicate their genetic material and divide over and over again. Faithful completion of these processes is fundamental to the perpetuation of life on this planet. The biological process that drives the conversion of a mother cell into two daughter cells is called the cell cycle.

The discussion of the cell cycle is complicated by the diverse spectrum of forms in which we encounter it in biology: Embryos - equipped with large cytoplasm and a rich reservoir of proteins inherited from their mother - can divide without having to grow. Many plant cells, muscle cells and neurons grow to gigantic size, without ever dividing. Some cell types perform endoreduplication, duplicating their genomes multiple times without ever passing these copies on to daughter cells.

In spite of the many forms the cell cycle takes in different cell types and organisms, the molecular mechanism that drives and controls it is remarkably conserved across eukaryotes. In this chapter, I will begin by discussing a model of the cell cycle that emphasises general features at the expense of specificity. The order of the phases of the cell cycle laid out in this discussion will reflect the pattern found in the cell cycle of metazoans, which are most relevant for this work. However, many model organisms that were fundamental to our understanding of the cell cycle, such as yeasts deviate substantially from this pattern. The interested reader is advised to consult David Morgan's excellent book for a more general discussion of the cell cycle [2].

The introductory discussion of the cell cycle will conclude with the introduction of checkpoints - as a useful concept for understanding how transitions that entail irreversible commitment to the next phase in the cycle are regulated - and lead on to a more in-depth discussion of mitosis and its regulation. The final part of the introduction will focus on a transition in the cell cycle that is arguably its most dramatic: The regulation of sister chromatid disjunction by the

mitotic checkpoint and the coordination of consecutive events that underlie mitotic exit. I will discuss fundamental systems-level properties of these control systems and motivate questions that underpin the work discussed in later chapters of this thesis.

1.0.1 Principles of Control

Growth, replication of DNA and division are the fundamental elements of the cell cycle. Phases of DNA-synthesis (S-Phase) and nuclear division (M-Phase) alternate and are generally separated by so-called Gap-phases: G1 precedes S-Phase and G2 precedes M-phase [2]. Additionally, a phase of quiescence (G0), in which cells have not committed to the cell cycle may precede G1.

In its simplest form (such as in some early embryonic cells), the cell cycle is driven by a control system that behaves like a free-running oscillator and is independent of downstream events [3]:

Two classes of highly conserved proteins, cyclins and cyclin-dependent kinases (CDKs), sit at the heart of this regulatory machinery [4]. The ability of CDKs to phosphorylate protein targets and direct downstream events in the cell cycle depends on their binding to regulatory cyclins [5, 6]. These activate CDKs and imbue them with a certain degree of substrate specificity. Whereas the concentration of CDKs remains relatively constant throughout the cell cycle [7], levels of cyclins vary in a periodic, phase-specific manner [8], such that specific heterodimers of cyclins and CDKs are present at distinct stages of the cell cycle. The basis for the periodic activation of specific cyclin:CDK complexes is a peculiar pattern of interactions: at each stage, a cyclin:CDK-heterodimer stabilises its own activity by activating a pathway that protects it from inactivation (positive feedback). However, it also activates the cell cycle regulator that drives the next phase, and initiates its own eventual inactivation (negative feedback).

1.0.2 Oscillator

Early embryo cell cycles are not limited by cell-size. Here, it is the role of the cell-cycle control system to warrant the alternation between S-phase and M-phase. M-phase is driven by high activity of the cyclin B:CDK1-heterodimer (often called M-phase promoting factor - MPF), S-Phase is characterised by low, but increasing activity of cyclin B:CDK1 (figure 1.1). The transition from M-phase to S-phase is regulated by the anaphase promoting complex/cyclosome (APC/C). This E3-ubiquitin

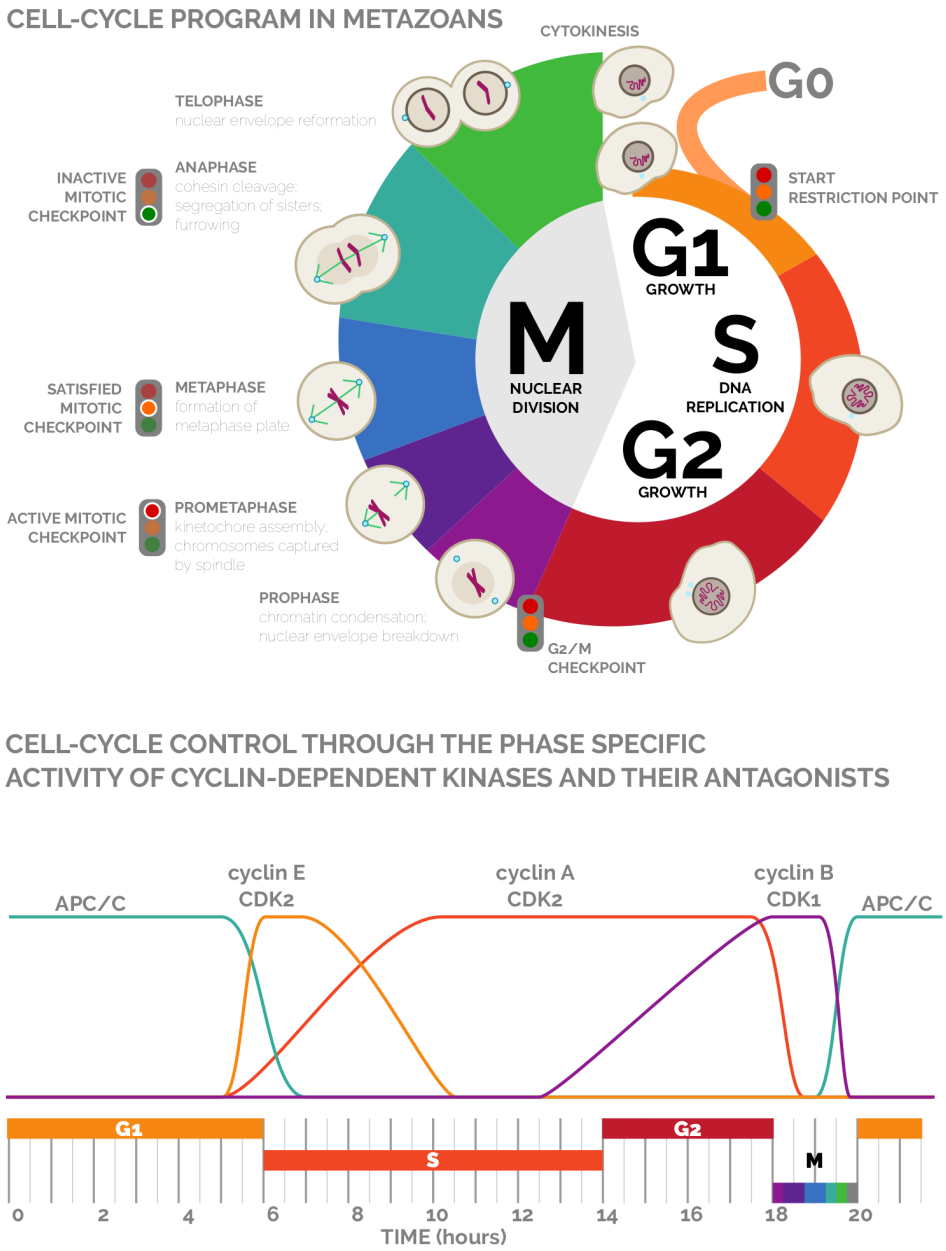


Figure 1.1: The metazoan cell cycle - A schematic overview of the cell cycle program and its regulation

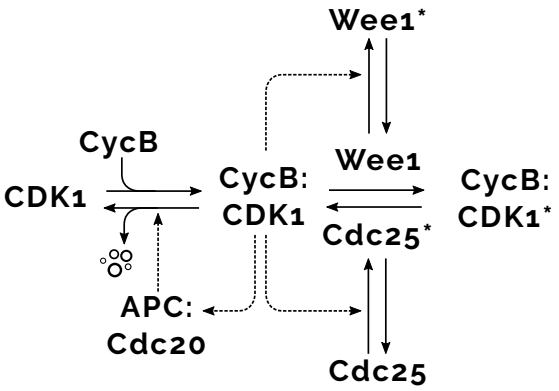


Figure 1.2: Cell Cycle Oscillator Control Network - Xenopus Egg Extract

ligase is a multisubunit complex and depends on co-activators to promote its activity towards specific classes of substrates, which it polyubiquitylates and thus targets for proteasomal degradation [9, 10]. The exit from mitosis is initiated by the activation of APC/C with its co-activator Cdc20, which targets cyclin B for degradation [10, 11, 12]. This lowers the activity of cyclin B:CDK1. However, it also lowers the activity of APC/C:Cdc20, whose activity depends on regulatory phosphorylation of the APC/C-core by cyclin B:CDK1 [13]. Before the next M-phase, cyclin B steadily accumulates until it reaches a critical threshold at which CDK1 gets abruptly activated.

A sharp threshold is established by a dual positive feedback circuit of cyclin B:CDK1 on its activity. In addition to binding of regulatory cyclins, CDK1 activity depends on the removal of inhibitory phosphorylations (T14, and Y15), conferred by the kinases Wee1 and Myt1, and removed by the phosphatase Cdc25 (figure 1.2) [14, 15, 16]. CDK1 and Wee1 are locked in a double-negative feedback loop - they are mutual antagonists. At low CDK1 activity, Wee1 gains the upper hand, and CDK1 is mostly present in its phosphorylated form. At high CDK1 activity, Wee1 is inhibited [17], and Cdc25 - which is activated by CDK1- phosphorylation [18, 19] - becomes more effective at removing the phosphorylation on CDK1.

1.0.3 Bistability

The dual positive feedback loops establish a bistable switch [20]. Within a specific range of cyclin B levels, CDK1 can be either in its active or its inactive form. Whether CDK1 is active or not is entirely dependent on the history of the cell. In other words, the mechanism establishes two distinct cyclin B-thresholds for getting into M-phase and CDK1-inactivation. Due to the self-stabilising mechanisms

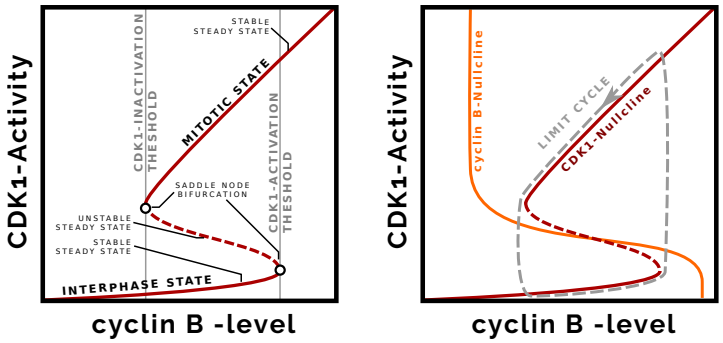


Figure 1.3: Bistability and Limit Cycle Oscillators - Diagram illustrating features of the phase space of the system depicted in 1.2 **Left:** The nullcline for CDK1 activity as a function of cyclin B is bistable and exhibits hysteresis, establishing different thresholds for entry and exit into mitosis. **Right:** Phase portrait depicting the stable states of cyclin B as a function of CDK1 activity and of CDK1 as a function of cyclin B. The system supports limit cycle oscillations.

that surround cyclin B:CDK1, the entry-threshold is higher than the exit threshold [20].

Bistability is a well-characterised property of certain dynamic systems. Fundamental requirements for bistability are **positive feedback** (either positive of double-negative feedback circuits) and sufficient **nonlinearity** of the interactions, both of which are properties of the network detailed in figure 1.2. Systems exhibit bistability if - for a certain range of parameter k - there exist two stable steady states of any variable in the system that are separated by an unstable steady state. Varying the control parameter k allows us to draw the change in the steady states of the system as a function of k. The **phase plane** in the left panel figure 1.3 shows how the steady states of CDK1 activity change as the level of cyclin B is varied as parameter. The solid lines depict the stable steady states. These are separated by an unstable branch. At certain values of k, the unstable branch and a stable branch collide and create a so-called **saddle node bifurcation**. Saddle node bifurcations mark the transition between a bistable domain (two stable steady states of the system coexist for a given k) and a mono-stable domain, and thus mark the transition thresholds between the two states.

Bistable systems exhibit a range of characteristic properties, which serve as unintuitive predictions and can be used like fingerprints to test whether a system truly exhibits bistability. Originally proposed to govern the cell cycle in *Xenopus laevis* early embryo extracts by Novak and Tyson [20], predictions stemming from bistability have been confirmed experimentally over the past years. The three most prominent are:

- **Hysteresis** - The difference in thresholds for changing between the two steady states [21, 22].
- **Critical slowing-down** - Close to the bifurcation points, the transition between the two states is characteristically slow. This can be observed in time-course-simulations and was confirmed by Sha *et al.* [21] for the early embryo of *Xenopus laevis*.
- **Excitability** - Bistable systems create excitable media. In unmixed media, waves of chemical activity that trigger the transition between the two states propagate faster than the diffusion limit [23].

1.0.4 Checkpoints

In somatic cells, the cell cycle does not strictly behave like a free-running oscillator, but allows for additional levels of control that regulate the commitment to growth and the duration of the gap phases by integrating intra- and extra-cellular cues. So-called checkpoints reinforce the correct order of cell cycle events by delaying the progression in the cell cycle in response to biochemical stimuli that signal unmet requirements for progression into the next phase [24, 25]. These mechanisms allow the cell to monitor the completion of a stage and confer the cell cycle with the fidelity required for innumerable repetitions: They coordinate the cell cycle with growth to maintain cell size, ensure that chromosomes are duplicated only once per cycle and warrant accurate distribution of the duplicated chromosomes to the daughter cells. Formally, checkpoints consist of: a surveillance mechanism, which checks for errors; an error correction machinery, which acts in response to problems detected by the surveillance mechanism; a checkpoint enforcement mechanism, which delays progression until successful completion of the corresponding phase.

Three major cell cycle transitions are regulated by checkpoints [26]: The **Restriction Point control** is a mechanism active during G1, at which the cell becomes committed to the cell cycle. G1 is extended through the activity of an additional APC/C-regulatory sub-unit called Cdh1. It becomes the major regulator of APC/C during mitotic exit and suppresses the re-accumulation of cyclins until extra-cellular signals appear that trigger the accumulation of G1/S-cyclins that are not targeted by APC/C:Cdh1, and in turn inhibit Cdh1. The **G2/M checkpoint**, delays entry into mitosis by potentiating Wee1 activity and weakening Cdc25 activity in response to DNA-damage [27, 28]. The third checkpoint is the so-called **Mitotic Checkpoint** and it ensures correct division of DNA between daughter cells.

2

Mitosis

After completion of S-phase, cells contain two complete sets of chromatids, and a pair of centrosomes. Corresponding chromatids are called sister chromatids and are held together by ring-shaped protein complexes called cohesin [29]. In mitosis, the cell faces the challenge of dividing the chromatids correctly between the nascent daughter cells. Broadly speaking, there are two different strategies that eukaryotic cells employ to tackle this challenge [1]: Yeasts undergo so-called *closed mitosis*. Here, sister chromatids are segregated within an intact nucleus, before the nucleus elongates and becomes pinched in two by the dividing cytoplasm. Metazoans on the other hand, perform an *open mitosis*, where the cellular architecture changes more profoundly to facilitate segregation of sister chromatids. Open mitosis proceeds as follows:

Prophase is the first phase of mitosis, and sets the stage for the division of DNA. It begins with the condensation of chromatin [31], the fragmentation of the Golgi apparatus [32] and loss of cohesion between sister chromatids along the arms of the chromosomes [33]. Next the centrosomes move to opposing poles of the cell and begin to organise a bipolar array of microtubules that will constitute the mitotic spindle [34, 35]. The nuclear envelope disassembles to expose the chromosomes to spindle microtubules (**Nuclear Envelope Breakdown, NEBD**) [36, 37].

In the following **Prometaphase**, chromosomes are captured by the mitotic spindle. The spindle microtubules undergo cycles of growth and shrinkage and gradually invade the centre of the cell. Moreover, microtubules nucleate from the chromatid masses. In a stochastic search and capture process, microtubules become attached to kinetochores [38, 39] - large protein complexes that assemble at the

[1] This is a simplification. For a more nuanced discussion of the topic, see [30]

centromeres of each chromosome in early prometaphase and act as microtubule binding interfaces [40].

Metaphase begins when all corresponding sister chromatids have become connected to opposite poles of the mitotic spindle. As a result of the dynamics of the mitotic spindle, pairs of sister chromatids are subject to equal drag from both poles of the mitotic spindle, and thus become oriented in the equatorial plane of the cell. On a phenotypic level metaphase is characterised by chromosomes that have become *bi-orientated* and have thus formed a *metaphase plate*, but it appears otherwise uneventful.

In contrast, the onset of **Anaphase** is quite dramatic: Suddenly, the centromeric cohesin is lost in a synchronous manner across all pairs of sister chromatids [41], and they are pulled apart by the mitotic spindle (Anaphase A). Overlapping spindle microtubules from opposing poles that remain in the centre of the cell begin to interact and form the so-called central spindle, adding a third organising centre to the spindle [42] (Anaphase B). Meanwhile, the centrosomes begin to move further apart assisting in the separation of the sister chromatids.

Anaphase is followed by **Telophase**, where the cell repackages the chromatids and prepares the division of the cytoplasm: The nuclear envelope, whose disassembly marked the entry into prometaphase, becomes reassembled on the surface of the de-condensing chromatin [36, 43, 44]. In the meantime the cell uses the overlapping microtubules that constitute the central spindle to determine the middle of the cell and triggers the assembly of a contractile, actin-myosin ring along its equator, and the spindle becomes disassembled [45].

With the completion of telophase, mitosis has ended. To complete cell division, the cell is left with the task of dividing its cytoplasm. During **Cytokinesis**, the actin-myosin ring along the equator of the cell directs the ingression of the so-called *cleavage furrow*. This process depends on active contraction of the ring and deposition of membrane components to enable its increase in surface area. More and more membrane is pulled in on the division plane and the cytoplasm eventually divides in two. [45, 46]

> Even this very superficial description of the fundamental events in mitosis leaves us to wonder how the cell manages to sufficiently resolve the underlying events in time: If the formation of attachments between spindle microtubules and kinetochores is intrinsically stochastic, how can the cell reliably achieve correct attachments of corresponding sisters to opposing poles? How is the cleavage of cohesin prevented until it is certain that sister chromatids will be correctly divided between the two daughter cells? How is the reassembly of the nuclear envelope

delayed until the sister chromatids have been separated, and how is it coordinated with the de-condensation of chromatin? How does the cell make sure that cytokinesis happens after mitosis?

To address these questions, it is necessary to focus on the operational level, as well as the control system. Thus, we will first turn to the mitotic spindle, the cellular structure that drives many facets of nuclear division, before we focus on global molecular regulation of mitosis.

2.1 The Mitotic Spindle

The mitotic spindle is a complex and highly dynamic assembly of microtubules, centrosomes, kinetochores, motor proteins and other regulatory factors. The very processes that give rise to the mitotic spindle establish a division axis, and promote the capture and segregation of sister chromatids. Our discussion will first focus on constituents of the mitotc spindle, which are both structural as well as regulatory, before we turn to processes that orchestrate assembly of the spindle and are in turn subject to regulation by the mitotic control system.

2.1.1 Parts

What does it take to build a spindle?

2.1.1.1 Microtubules

Microtubules (figure 2.1 D) are cytoskeletal protein filaments that are formed by the polymerisation of $\alpha\beta$-tubulin heterodimers. They thus have an end whose face exposes only β-tubulin units (the so-called (+)-end), whereas the face on the other end exposes only α-tubulin units (the (-)-end). The (+)-ends can dynamically switch between growth and shrinkage (**dynamic instability**) [47]. This process depends on the phosphorylation state of the guanosine bound to the β-tubulin: (+)-end tubulin units in their GDP-bound form are more likely to become de-polymerised than tubulin units which are associated with GTP. The rate of shrinkage is modulated by GTPases and varies through the cell cycle; in mitosis it is larger than in interphase, giving rise to microtubules that are shorter on average.

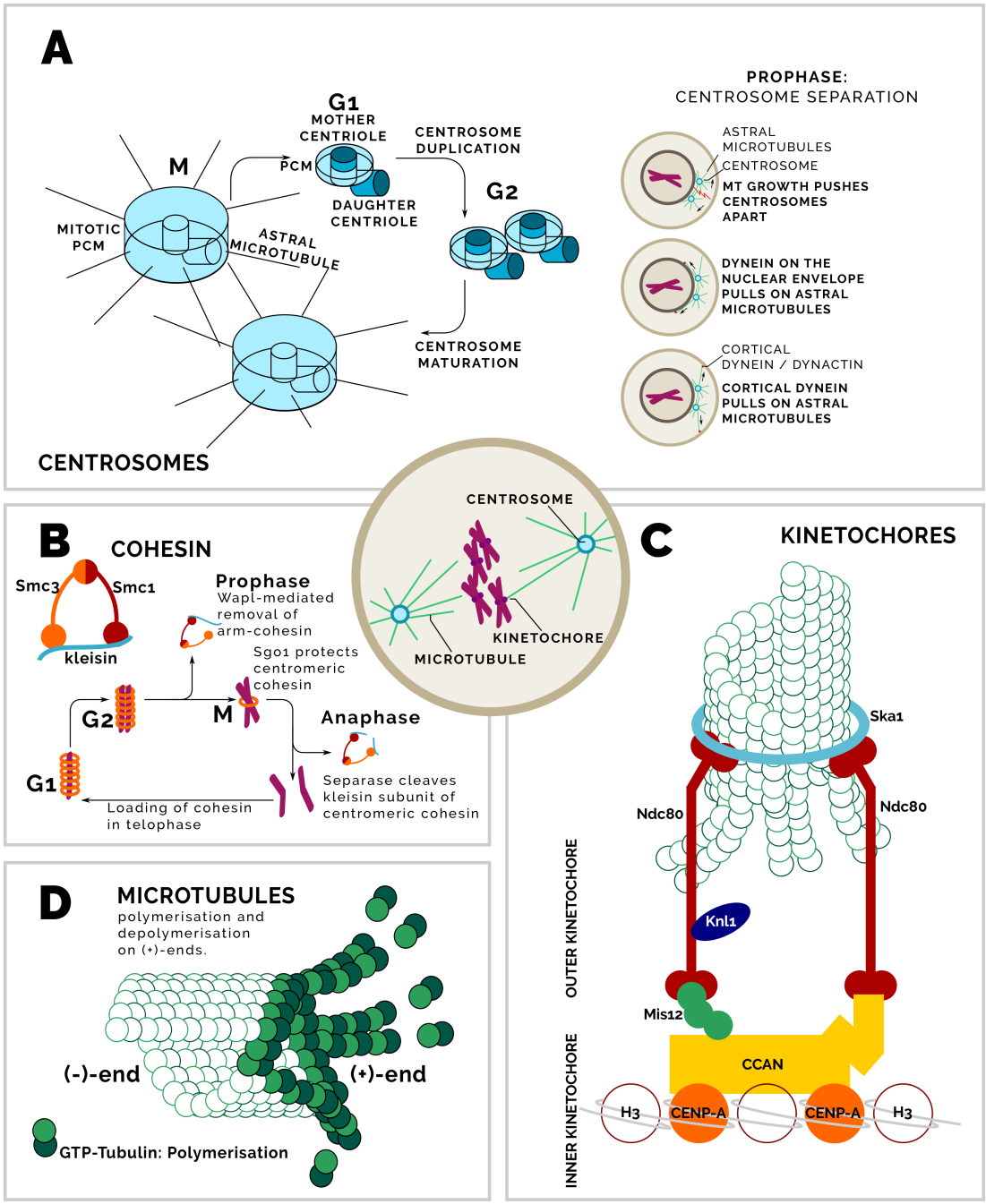


Figure 2.1: Constituents of a mitotic spindle - Overview of the cellular substructures involved in the assembly of the mitotic spindle. **A** The centrosome cycle, and processes directing centrosome separation in prophase. **B:** The cohesin complex, loading and removal of cohesin throughout the cell cycle. **C:** Components of the kinetochore. **D:** Dynamic instability of microtubules.

2.1.1.2 Centrosomes

Centrosomes[1] are the key microtubule organising centres in animal cells and thus play a crucial role in the assembly of the mitotic spindle. They consist of two centrioles (the so-called **mother and daughter centriole**), which are surrounded by a dense network of proteins called the pericentriolar matrix (**PCM**) that includes proteins required for the anchoring and nucleation of microtubules - notably γ-tubulin [49] and pericentrin. In meiosis, bipolar spindles are assembled without centrosomes, whereas in mitosis, centrosomes serve as organising centres in the formation of bipolar spindles. Like DNA, centrosomes are replicated in the S-phase of the cell cycle. Their duplication is tightly controlled; the presence of more than two centrosomes leads to the formation of multi-polar spindles and contributes to genome instability [50, 51, 52].

In interphase, the PCM forms a thin layer around the mother centriole. Upon entry into mitosis, centrosomes maturate in a process that depends on the activity of the mitotic kinases **Plk1** [48, 53] and **Aurora A** [54] and entails recruitment of constituents of the PCM onto a networked scaffold structure that assembles around the mother centriole [55]. This enlargement of the PCM allows the centrosome to nucleate and anchor a dense radial array of so-called astral microtubules. In prophase, the pair of centrosomes begins to separate. The precise mechanistic details of this process are still unclear. However it has been shown to exploit the presence of the nuclear envelope and rely on the concerted action of the cytoskeleton and motor proteins (figure 2.1 A): Growth of microtubules is thought to be a key factor in the early stages of centrosome-separation. Very short microtubule fibres buckle less than long fibres. Thus, the opposing growth-direction of microtubules emanating from the centrosomes is likely to generate a considerable force [56] that can push centrosomes apart [57]. In addition, the kinesin-5 motor **Eg5** is recruited to the centrosome and the surrounding astral microtubules. Eg5 cross-links and mediates sliding of anti-parallel microtubules, thus assisting in the separation of centrosomes [58]. As astral microtubules grow towards the cortex of the cell, they interact with cortically anchored **dynein**. The (-)-end directed mobility of dynein can generate a pulling force that assists in the separation of centrosomes [59, 60]. Moreover, dynein has been shown to localise to the nuclear envelope as early as G2, and may contribute to centrosome separation in a similar manner [61].

[1] Relevant reviews [35, 48]

2.1.1.3 Kinetochores

Kinetochores[1] (figure 2.1 C) are complex protein structures that mediate the attachment of chromosomes to microtubules [62]. In vertebrates they consist of over 100 sub-units, each of which are present in more than one copy. These constituents can be grouped into three functional classes: **inner kinetochore** components that provide a platform for the centromere-specific assembly of kinetochores, and provide the interface with DNA; **outer kinetochore** components that collectively mediate binding of microtubules; and **regulatory components**.

Core components of the inner kinetochore include **CENP-A** and members of the constitutive centromere-associated network (**CCAN**). The histone H3 variant CENP-A that forms nucleosomes in centromeric regions provides centromere identity in most organisms, and is required for the localisation of kinetochore components in most eukaryotes, with the notable exception of kinetoplastids [64]. The CCAN is composed of numerous sub-complexes and provides a selective binding interface between CENP-A and constituents of the outer kinetochore. CENP-C, the largest component of the inner kinetochore, has been proposed to act as a molecular "blueprint" of inner kinetochore assembly [65] and it provides a binding interface for components of the outer kinetochore.

The **Mis12**, **Knl1** and **Ndc80**-complexes form the so-called **KMN-network** that mediates microtubule binding in the outer kinetochore. The tetrameric complex Mis12 plays a central role in the organisation of the KMN-network, as it forms contacts with CENP-C at the inner kinetochore, Ndc80 and Knl1 [66]. Ndc80 consists of four sub-units (Hec1, Nuf2, Spc24, and Spc25) and forms an elongated ($\simeq 55\ nm$ long) coiled-coil structure. It constitutes the endpoint of the microtubule-binding interface [67, 68]. In addition to its part in the KMN-network, Ndc80 has been shown to directly interact with CENP-TW components of the CCAN network [69].

End-on attachments are formed through electrostatic interactions between an unstructured, N-terminal tail of the Ndc80-component Hec1, which is positively charged and a negatively-charged, C-terminal tail of tubulin [70, 71, 72]. In addition, the **Ska1**-complex forms ring-like oligomeric assemblies around microtubules and maintains kinetochore attachments with de-polymerising microtubules [73].

Human kinetochores contain numerous copies of the outer kinetochore components. Historically, it has been assumed that these form discrete microtubule binding sites, each interacting with a single microtubule-fibre. However, recent experimental and theoretical work suggests that the interaction between microtubule-

[1] Relevant reviews [62, 63]

binding proteins in the outer kinetochore form a structurally less-constrained "molecular lawn" [74].

2.1.1.4 Cohesin

Cohesin[1] (figure 2.1 B) is a large ring-shaped protein complex that is pivotal to the correct division of DNA among the daughter cells. It keeps corresponding sister chromatids physically linked to each other, thereby encoding topologically the lineage of each of the 92 chromatids of human mitotic cells. Thus cohesion of sister chromatids provides the logic for successful distribution of DNA during nuclear division: Sister chromatids are kept together from the time of duplication until they become attached to opposite poles of the mitotic spindle. Once all sister chromatids have become attached to opposing poles of the mitotic spindle, cohesin is cleaved, and the sister chromatids are segregated to opposite poles of the mitotic spindle.

Cohesin is a tetrameric complex consisting of two "structural maintenance of chromosomes" sub-units (**Smc1** and **Smc3**), a **kleisin** sub-unit (Scc1 or Rad21 in human) and an associated factor - Pds5 [75]. Smc1 and Smc3 are each characterised by a central hinge domain around which the proteins form back-folded coiled-coil domains ending in an ATPase head that is composed of the N- and C-terminal domains of the proteins. Smc1 and Smc1 are directly connected via their hinge domain. Their ATPase-domains are connected via the kleisin component. Thus, Smc1, Smc3 and kleisin form a ring-like structure [75].

In vertebrates, cohesin becomes associated with DNA as early as the telophase of the preceding cell cycle. Loading of cohesin onto initially intertwined replicating DNA occurs in S-phase; it is mediated by loading factors (Eco1) and establishes sister chromatid cohesion. Upon chromosome condensation in prophase, a large proportion of cohesin associated with chromosome arms is removed by the **Prophase-pathway** [33], which is promoted by mitotic phosphorylation (Plk1 and Aurora B) [76]. This process involves opening of the ring at the junction of Smc3 and kleisin, and is mediated by **Wapl** and **Plk1**. At the centromeres, **shugoshin** (Sgo1 and Sgo2) and **PP2A:B56** become localised through local activity of **Aurora B** and protect cohesin from prophase-pathway-mediated removal [77].

This process ensures that sister chromatid cohesion is maintained until anaphase onset, when a second pathway promotes removal of cohesin via the cleavage of the kleisin sub-unit. At anaphase onset, a kleisin-specific protease called

[1] Relevant review [29]

separase is activated upon APC/C:Cdc20-driven degradation of its inhibitory chaperone **securin**.

2.1.2 ORGANISATION

HOW DOES THE SPINDLE COME TOGETHER?

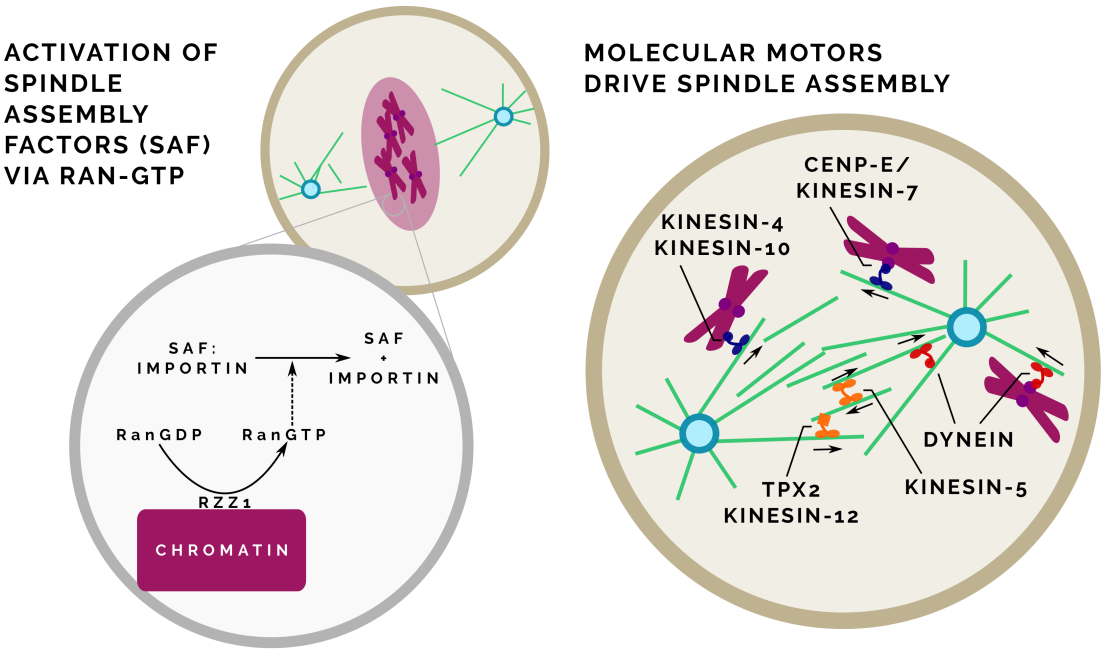


Figure 2.2: Organising Principles Driving Spindle Assembly - **Left panel:** Activation of spindle assembly factors by Ran-GTP. **Right panel:** Role of motor proteins in spindle assembly.

It is tempting to view spindle assembly[1] as a process that is characterised by a clear division of roles: active microtubules and passive kinetochores. This view informed the so-called **search and capture hypothesis** [38], which was inspired by the discovery of the dynamical instability of microtubules [47].

However, entirely stochastic search and capture driven by microtubular growth and shrinkage alone has been shown to be insufficient for efficient spindle formation [79], and since the postulation of the search and capture mechanism, many layers of regulation have been discovered that contribute to the organisation of the mitotic spindle: The coordinated interplay of chromatin, centrosomes, kinetochores, microtubules, signalling molecules, motor proteins and cellular architecture renders spindle assembly an impressive feat of self-organisation.

Strikingly, many spindle regulators are proteins that are structurally or functionally associated with the nuclear pores in interphase [80] - most notably **RanGTP** and

[1] Relevant reviews [35, 78]

karyopherins, which play important roles in the assembly of the mitotic spindle. In Interphase, RanGTP and karyopherins regulate nuclear import and export. Ran is a small protein that exists in two nucleotide-bound forms - RanGTP and RanGDP. The inter-conversion between the two forms is regulated by the nucleotide exchange factors RCC1 and RanGAP, whose distinct cellular localisation gives rise to a sharp spatial separation between the GTP- and GDP-bound forms of the otherwise freely diffusible Ran. The nuclear protein RCC1 catalyses the conversion of RanGDP to RanGTP. RanGAP promotes the reverse reaction. In mammalian cells it is localised to the cytoplasmic side of nuclear pore complexes. The basis for the regulation of nuclear import and export by Ran is its modulation of binding interactions between karyopherins and their cargo. In the nucleus, the more abundant RanGTP promotes the dissociation of cargo proteins carrying a nuclear localisation signal from importin. Conversely, RanGDP promotes cargo-release from exportins in the cytoplasm. Similar to its role in nuclear transport, RanGTP stimulates the release of NLS-carrying cargoes from importin in mitosis (figure 2.2, left panel), whose activity is inhibited when associated with importin. The localisation of RCC1 on chromatin persists after breakdown of the nuclear envelope and gives rise to a cloud of RanGTP that surrounds the chromosomes [81]. This results in a localised release of many NLS-carrying **spindle assembly factors**, which promote microtubule polymerisation and organisation [82, 83].

One such spindle assembly factor is **TPX2** [82, 84, 85]: It activates **Aurora A** and targets it to microtubules [86, 87, 88], thus contributing to centrosome maturation; it stimulates microtubule growth by activating the **Augmin**-complex [89]; and it interacts with homo-dimeric motors from the **kinesin-12** family - such as **Hklp2/Kif15** - via their leucine-zipper domain, and targets them to microtubules [58]. MKlp2 interacts with chromosomes via **Ki67** and contributes to the assembly of a bipolar spindle [90]. Moreover Hklp2 is believed to be able to bind to microtubules directly via its motor domain, an interaction that could lead to cross-linking between microtubules. The (+)-end directed motor activity of kinesin-12 would thus contribute to anti-parallel sliding of microtubules emanating from opposite poles and would thus facilitate the assembly of a bipolar spindle. In this role, members of the kinesin-12 family are believed to act redundantly with members of the aforementioned kinesin-5 family, such as **Eg5** [58]. These form homo-tetramers that can cross-link microtubules directly and promote anti-parallel sliding. Interestingly, Eg5 was shown to be activated by RanGTP and regulated by **Aurora A** [88, 91].

In contrast, motors that promote (-)-end direct transport, such as **dynein** and members of the **kinesin-14**-family, contribute to the coherence of the spindle by

driving pole-ward transport of microtubules. This allows for kinetochore-associated microtubules (**K-fibres**) to be incorporated into the spindle and promotes focusing of the microtubule-structure around the spindle poles [92].

Both chromosome arms and kinetochores interact with microtubules. These interactions are mediated through molecular motors. This increases the likelihood of an initial capture of chromosomes by the mitotic spindle and promotes the congression of the chromatids in the centre of the spindle. So-called **lateral attachments** are formed between kinetochores and the sides of microtubules. The (-)-end directed activity of dynein promotes the transport of chromosomes to the spindle poles when attachments with astral microtubules are formed in the periphery of the spindle. Lateral attachments that are formed in the centre of the spindle have to be resolved to end-on attachments. This process requires (+)-end directed transport of kinetochores via CENP-E (a member of the kinesin-7 family) [93, 94, 95, 96]. In addition, chromokinesins of the kinesin-4 (**Kif4/Hklp1**) and kinesin-10 (**Kid/NOD**) families promote the ejection of chromosome arms from the spindle poles through (+)-end directed transport processes (figure 2.2 right panel) [97].

Taken together, the processes that give rise to the mitotic spindle facilitate the assembly of a bipolar structure, promote the localisation of the chromatin to the equatorial plane of the cell, focus microtubules towards the centrosomes and bias the growth of microtubules towards the chromatin. Yet for mitosis to succeed, one sister out of each pair has to be distributed to each daughter cell. This requires that sisters are attached to opposite poles of the mitotic spindle, and that the onset of anaphase be delayed until correct attachment has been achieved.

2.2 Molecular Control of Mitosis

> *Nothing in mitosis makes sense, except in the light of post-translational modification.* - This contextual re-appropriation of the famous quote by the Russian evolutionary biologist Theodosius Dobzhansky will constitute the theme for a broader discussion of the molecular control of mitosis. For fundamentally, all events of mitosis are regulated by a balance of mitotic kinases and their counter-acting phosphatases, as well as by ubiquitylation-directed proteolysis. Pathways underpinning early mitotic events are activated through phosphorylation by mitotic kinases such as **cyclin B:CDK1**, **Aurora A**, **Aurora B** and **Plk1**, which are most active early in mitosis [98]. On the other hand, processes underlying late mitotic events are inhibited by mitotic phosphorylation. They become activated by phosphatases, most notably **Cdc14** (in budding yeast) and phos-

phatases belonging to the protein phosphatase family (PPP) - most prominently **PP1**, **PP2A:B55**, and **PP2A:B56**, whose activities are potentiated at the end of mitosis [99, 100, 101].

The meta-to-anaphase transition constitutes a turning point in mitosis as it marks the transition between the kinase/phosphatase signalling domains. It is regulated by the mitotic checkpoint (often referred to as spindle assembly checkpoint)[1] - a feedback control system that works through the coupled action of an **error monitoring and correction module** and a **checkpoint enforcement/effector module**, and integrates signals from the mitotic spindle with the kinase-phosphatase control system.

The defining event in the initiation of exit from mitosis is the activation of the E3-ubiquitin ligase **APC/C** by its co-activator **Cdc20**, which targets **securin** and **cyclin B** for degradation, and thereby triggers the separation of sister chromatids, and the inactivation of CDK1 [10, 11, 12]. The enforcement mechanism of the mitotic checkpoint acts by producing an inhibitor that selectively inhibits the activity of APC/C towards its early anaphase substrates. It blocks the activation of APC/C:Cdc20 before all chromosomes have become bi-oriented by producing the mitotic checkpoint complex (**MCC**). The Mitotic Checkpoint thus ensures that all sister chromatids can be correctly divided among the nascent daughter cells, before their segregation is initiated and the cell exits from mitosis [102, 103].

The error correction module and checkpoint enforcement module are intimately interlinked: The error correction mechanism destabilises incorrect attachments and produces unattached kinetochores. In turn, unattached kinetochores act as assembly platforms for MCC, and thus act as a signal to the checkpoint enforcement module. Moreover, many upstream activators of the mitotic checkpoint regulate components of both systems, and are themselves subject to checkpoint-driven protection from inactivation.

To enable a structured discussion of the mitotic checkpoint in light of complicated interdependencies, the following overview of our current knowledge about the underlying molecular mechanisms will follow the flow of information in the system and begin with the formation and correction of attachments at the level of error correction and lead on to a discussion of the checkpoint enforcement module.

[1] The terminology in the field is riddled with ambiguity: Mitotic checkpoint and spindle assembly checkpoint are often used interchangeably. In this work, mitotic checkpoint will refer to the control system that is composed of enforcement module and error correction / surveillance mechanism, in line with the definition given above.

2.3 Error Correction

2.3.1 Quality

What constitutes "correct" attachments?

A configuration of end-on kinetochore-microtubule attachments, where kinetochores of sister chromatids are connected to opposite poles of the mitotic spindle is termed **amphitelic** attachment. Incorrect configurations do not satisfy this connectivity-condition, they include: **monotelic** attachment - only one sister is attached to the spindle, **syntelic** attachment - both sisters are attached to microtubules emanating from the same spindle-pole, and **merotelic** attachment - one sister is attached to both poles of the mitotic spindle (figure 2.3, bottom-left).

These different types of attachment are exposed to the dynamism of spindle microtubules in different ways: The shrinkage of attached microtubules along with pole-ward, motor-mediated transport results in a pulling force that is directed away from the equatorial plane of the cell and points towards the spindle poles. Anchoring of the spindle poles in the cellular cortex as well as anti-parallel sliding of overlapping microtubules counteract this force and maintains the structure of the spindle [104].

The pole-directed force develops tension along the binding interface between microtubules and kinetochores. For a pair of sister chromatids, the resulting pulling force is asymmetric in the case of monotelic, syntelic and merotelic attachments, and symmetric in the case of amphitelic attachment. This asymmetry in tension is exploited by the error correction mechanism, which uses it to detect and correct faulty attachments: It couples tension-dependent structural changes in the kinetochore with a sharp kinase activity gradient that phosphorylates and thus destabilises kinetochore microtubule interactions that lack tension [105, 106].

2.3.2 The Conductor

What effects error correction?

At the heart of the error correction mechanism sits the **chromosomal passenger complex (CPC)**[1], which localises to the inner kinetochore in early mitosis, before re-localising to the spindle mid-zone in anaphase. It consists of the Ser/Thr-kinase **Aurora B**, the regulatory components **Survivin** [108] and **Borealin** [109], as well as the scaffold component **INCENP** [110, 111]. Survivin, Borealin and the N-terminus of

[1] Relevant review: [107]

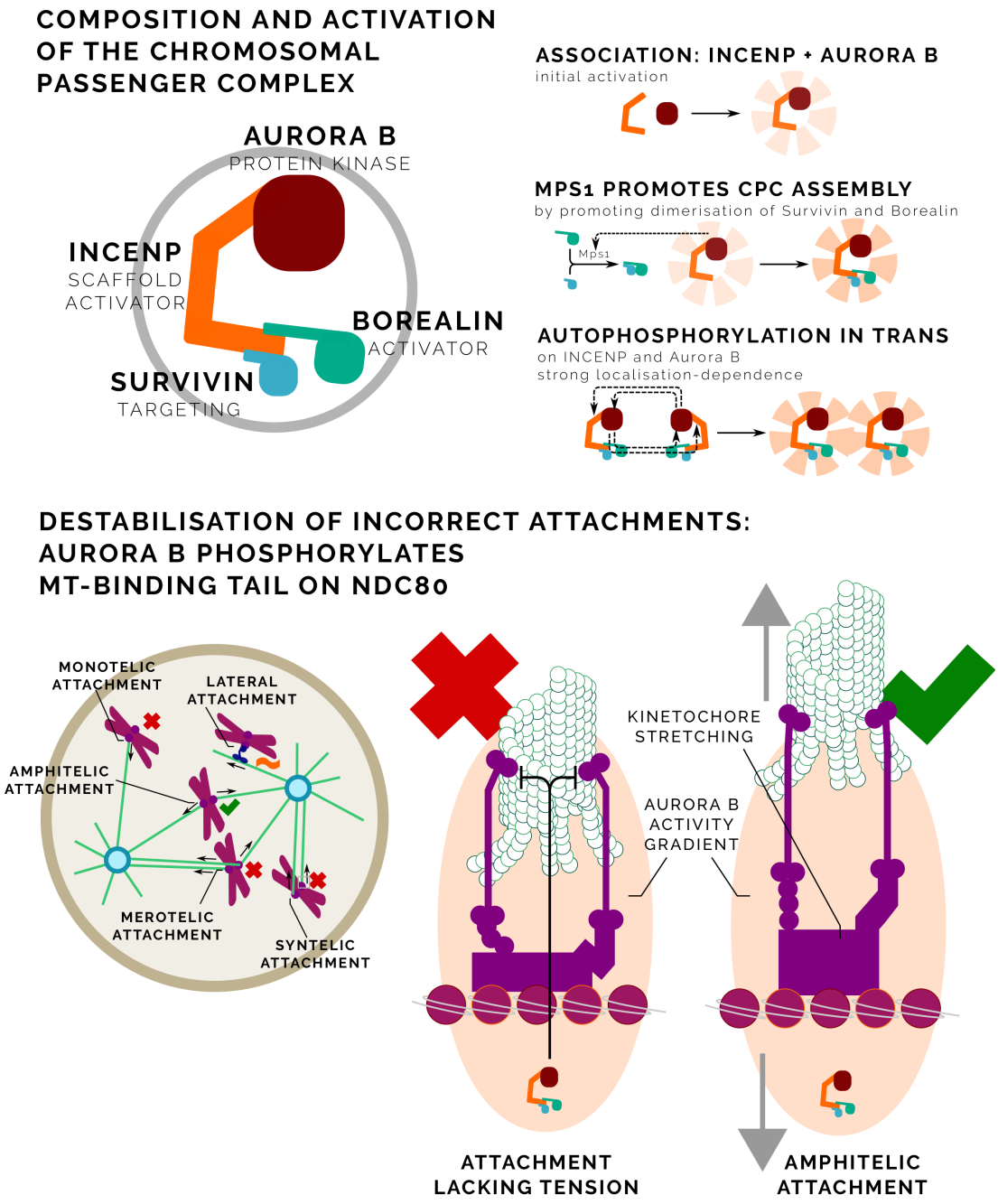


Figure 2.3: Error Correction - **Top:** Composition of the chromosomal passenger complex, and mechanisms leading to its activation. **Bottom-Left:** Types of microtubule-kinetochore attachments. **Bottom-Right:** Illustration of the tension dependent mechanism leading to structural deformations in the kinetochore that stabilise kinetochore-microtubule attachments.

INCENP form the localisation module, which is required for the correct localisation of the CPC in early mitosis and in anaphase [112]. The central domain of INCENP forms a linker to the kinase module of the CPC, which is composed of the conserved IN-box in the C-terminal region of INCENP and Aurora B [113].

INCENP has been likened to cyclins in its role as a stoichiometric activator of Aurora B. Regulation and activation of Aurora B is a complex process that is characterised by numerous feedback mechanisms: Association between INCENP and Aurora B is believed to be the crucial initial step in the activation of Aurora B. It confers Aurora B with some basal activity that is subsequently potentiated by autophosphorylation of the CPC on both INCENP (on its C-terminal TSS-motif) [114] and Aurora B (on T232 in the T-loop of its kinase domain) [115]. Both phosphorylations are believed to act in *trans* [116], providing a mechanism for a strong effect of increasing local concentration on Aurora B activity.

This localisation-driven auto-activation becomes fully potentiated in early mitosis, when the CPC plays a crucial role in the regulation of chromatin architecture, sister chromatid cohesion and in the definition of the centromere [117]: Aurora B activity recruits condensin [118] and **Bub1**. The latter phosphorylates H2A (H2A-pS121) in the vicinity of centromeres [119], recruits shugoshin 1 (**Sgo1**) and PP2A:B56 to the chromatin, and protects centromeric cohesin from Wapl-mediated removal. In turn, Sgo1 is an important interaction partner of the CPC [120, 121]. Similarly, Aurora B activity at the centromeres contributes to the accumulation of **Haspin** [122], which phosphorylates H3 (H3-pT3) and enables binding of Survivin [123].

Aurora B activity itself is subject to regulation by mitotic kinases. **Cyclin B:CDK1** phosphorylates multiple sites on Survivin that promote the interaction of the CPC with Sgo1 and thus target it to centromeric chromatin [124]. An immuno-depletion study in *Xenopus laevis* egg extracts [125] and a study employing a small-molecule inhibitor in HeLa cells [126] suggest that a basal level of Aurora B is required to localise the checkpoint kinase **Mps1** to the kinetochore. In turn, Mps1 phosphorylates T230 on Borealin to promote CPC assembly and Aurora B activation [127]. On the other hand, CDK1 and Aurora B phosphorylations on INCENP (T59) suppress the interaction of the CPC with MKlp2 that targets the CPC to the mid-zone of the spindle in anaphase [128, 129, 130, 131].

Aurora B activity is antagonised by **PP1** and **PP2A:B56**, whose local activity is tightly controlled throughout mitosis. PP1 localises to kinetochores through its interaction with Knl1, and is targeted to bulk chromatin by its regulatory sub-unit **CDCA8** (Repo-man). The latter interaction is inhibited in early mitosis by CDK1-

phosphorylation of Repo-man [132]. PP2A:B56 is enriched at unattached kinetochores, through the Aurora B-dependent recruitment to centromeric Sgo1 and Sgo2 [133].

2.3.3 Correction

How are attachments corrected?

Aurora B phosphorylates multiple sites in the KMN-network and at the kinetochore-microtubule interface; most notably, the positively charged tail of Ndc80 that directly interacts with a negatively charged tail of tubulin, Knl1 and Mis12 as well as Ska1 [67, 134, 135, 136]. These phosphorylations synergistically impair the interaction with microtubules and thus destabilise attachments. In addition, Aurora B promotes the accumulation of the microtubule depolymerase MCAK, but at the same time suppresses its activity through phosphorylation. The precise role of this incoherent feed-forward loop remains unclear, but it has been implicated in the promotion of spindle assembly via non-kinetochore-attached microtubules close to the chromatin and may have a role in the destabilisation of merotelic attachments.

Both PP1 and PP2A:B56 play a role in antagonising Aurora B in the context of error correction: PP1 antagonises Aurora B by removing phosphorylations on Knl1 [137], whereas PP2A:B56 associated with Sgo1 removes Aurora B phosphorylations on MCAK [77].

Taken together, the interplay of kinase and phosphatase activity, the potentiation of Aurora B activities through localisation and the control of CPC-assembly by mitotic kinases give rise to an abrupt activation of the CPC in mitosis and contribute to spatial gradients of Aurora B activity that are fundamental to its role as the effector of error correction that modulates kinetochore-microtubule attachments in response to lack of tension. [105, 106, 138, 139] Indeed, recently, it has been shown that a bistability inherent in the kinase-phosphatase regulation of Aurora B activity enables the development of sharp spatial patterns of Aurora B activity [140].

2.3.4 Detection

How is tension transduced?

Such sharp spatial patterns of Aurora B activity cooperate with tension-dependent deformations of the kinetochore and collectively give rise to an error correction mechanism that destabilises incorrect attachments. Using targeted Förster Resonance Energy Transfer (FRET) experiments, the kinetochore was shown to undergo

considerable stretching upon bi-orientation, displacing the Aurora B phosphorylation targets by approximately 20 nm compared to their position within the kinetochore in an unattached or tensionless state. [105, 106, 134, 141]

Furthermore, the dynamic instability of microtubules is critical to the tension sensing mechanism, as attachments between kinetochores and stabilised microtubules - such as upon treatment with Taxol - activate the error correction. In a recent study in budding yeast [142], Ndc80 and the yeast analogue of Ska1 - Dam1 - have been shown to act in a non-linear force coupling mechanism, whereby the end of both polymerising, as well as of de-polymerising microtubules attached to kinetochores give rise to deformations in the kinetochores and are thus capable of silencing error correction: On de-polymerising microtubules, curling microtubule filaments pull Dam1 and Ndc80 towards the poles of the spindle, resulting in pulling forces directed towards the poles. On the other hand, the centromere-directed push generated by polymerising microtubules similarly leads to a deformation of the centromere, which similarly results in drag forces on Ndc80 and Dam1 [142].

2.3.5 Focus

How are syntelic and merotelic attachments corrected?

In addition to the Aurora B-driven error correction machinery, other mechanisms exist that contribute to the formation of correct attachments. Syntelically attached chromosomes frequently become transported towards the spindle poles that are characterised by high activity of Aurora A due to localisation. Although it was originally thought that Aurora A and Aurora B perform entirely distinct functions, Aurora A has recently been shown to contribute to error correction by phosphorylating components of the outer kinetochore in the proximity of the spindle poles, and thus destabilising syntelic attachments [143].

Merotelic attachments occur frequently in the early stages of mitosis. If not corrected, they can be a major contributor to chromosomal defects. The low frequency at which merotelic attachments are observed at the meta-to-anaphase onset suggests that active mechanisms exist that are capable of converting attachments from merotelic to amphitelic [144]. However, resolution of merotelic attachments does not entail the generation of unattached kinetochores, rendering direct control by the error correction machinery less plausible. Evidence in fission yeast suggests that spindle elongation may contribute to the correction of merotely by changing the force balance on the mitotic spindle [145]. In addition, a recent study comparing the properties of kinetochores in fission yeast and Ptk1-cells concluded that

changes in the visco-elastic response of the kinetochore to merotelic attachments actively contribute to their conversion to amphitelic attachments [146]. However, a mechanistic basis for the correction of merotelic attachments remains elusive.

2.4 The Mitotic Checkpoint Enforcement Mechanism

Besides their role in mediating attachments with microtubules, kinetochores serve as assembly sites for MCC - the effector of the mitotic checkpoint [1] - and render the production of MCC sensitive to attachment. MCC is a multi-subunit complex composed of **Mad2**, **Cdc20**, **Bub3** and **BubR1** and acts as an inhibitor of APC/C:Cdc20 (figure 2.4 B).

2.4.1 Target

What is inhibited by the checkpoint; and what not?

The anaphase promoting complex/cyclosome (APC/C) is a 1.5 MDa multi-subunit protein complex that localises to the nucleus in interphase, and becomes associated with the spindle during mitosis. Besides being required for the separation of sister chromatids in anaphase, APC/C is fundamental for the initiation of S-phase and the maintenance of G1. As an E3 ubiquitin ligase, it operates by assembling ubiquitin chains on its substrates, which make them recognisable by the 26S proteasome, and thus targets them for degradation (figure 2.4 A). As such, its activity depends on E1 (ubiquitin-activating enzyme) and E2 (ubiquitin-conjugating enzyme, such as Ube2S and UbcH10) co-factors that enable efficient ubiquitylation of substrates, and is antagonised by de-ubiquitylating enzymes such as Usp44. Recently, APC/C along with its E2 co-activators has been shown to engage in a distinct catalytic architecture that promotes processive multi-ubiquitylation of its substrates, whereas a different conformation is adopted for chain elongation [149].

In addition to regulation at the level of ubiquitylation itself, the co-activators Cdc20 and Cdh1 associate with APC/C, and allow it to recognise, bind and ubiquitylate cell-cycle-phase specific substrates, via specific degron sequences. Cdc20 associates with APC/C early in mitosis and remains its predominant co-activator until the end of anaphase, when Cdh1 takes over the role of APC/C co-activator [150]. Whereas APC/C:Cdc20 has a limited range of substrates and drives entry into anaphase by targeting cyclin B and securin for degradation [151], APC/C:Cdh1 is characterised by a much broader range of substrates - among them Cdc20, Plk1,

[1] Relevant reviews: [147, 148]

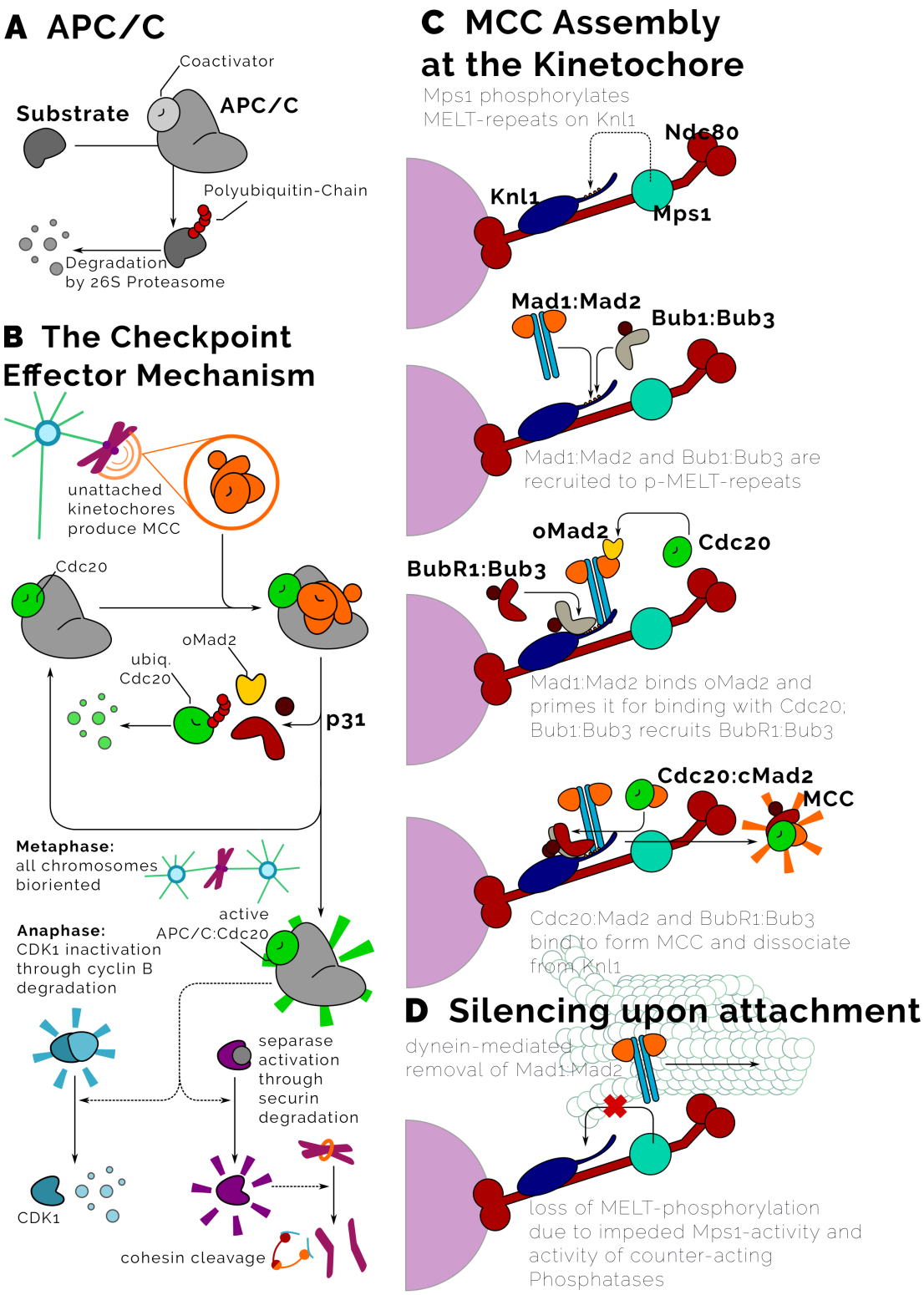


Figure 2.4: The Mitotc Checkpoint Effector Mechanism - Working Principles and Inhibitor Assembly

and Aurora A and B. It drives mitotic exit and keeps the activity of mitotic activators low throughout G1 [150].

As the dominant driver of anaphase onset, APC/C associated with Cdc20 is subject to control by the mitotic checkpoint, and inhibited by MCC. However, this does not mean that APC/C is entirely inactive during a checkpoint arrest. Independently of inhibition by the checkpoint, core APC/C targets cyclin A for degradation by the proteasome.

Activity of APC/C is regulated by post-translational modification of components of the core complex, as well as of the co-activators: It has long been established that mitotic kinases hyper-phosphorylate APC/C. This has led to the hypothesis that APC/C is activated by CDK1 phosphorylation [150]. Recent studies have demonstrated a molecular mechanism, whereby CDK1 activates APC/C by phosphorylating its core components APC1 and APC3 in a loop-region required for Cdc20-binding, and thus increases its capacity to bind its co-activator [13, 152].

Cdc20 itself may be subject to control by mitotic phosphorylation: Cdc20 is cooperatively phosphorylated by Bub1 and Plk1. The precise role of these phosphorylations remains unclear, but seems indicative of modulating the interaction between APC/C:Cdc20 and Ube2S [153]. On the other hand, Cdh1 carries multiple CDK1-phosphorylation sites that inhibit binding to APC/C [150].

In summary, the activatory phosphorylation of APC/C by CDK1, as well as the inactivation of cyclin A by free APC/C and cyclin B by APC/C:Cdc20 give rise to a negative feedback loop. However, the situation is complicated by the incoherent feed-forward loop through which CDK1 activity influences the activity of APC/C:Cdh1. On one hand, CDK1 activates APC/C, but on the other it inhibits the binding of Cdh1 to APC/C. This inhibition of Cdh1 is crucial to allow Cdc20 - itself a substrate of Cdh1 - to specifically activate APC/C towards its early anaphase substrates. In turn, activation of APC/C by Cdc20 is inhibited by MCC - the effector of the mitotic checkpoint, and rendered conditional on bi-orientation of chromosomes.

2.4.2 Assembly

How is MCC made?

The assembly of MCC (figure 2.4 C) is a multi-step process and depends on the activity of a set of regulatory enzymes that do not become incorporated into MCC. Crucially, it depends on the activity of **Aurora B** kinase, the kinase **Mps1** and is also subject to regulation by **cyclin B:CDK1**. The dependence of MCC assembly on Aurora B- and CDK1 activity is likely funnelled through Mps1 whose activity is

regulated by direct phosphorylation, and by localisation: A study in *Xenopus laevis* egg extracts has identified the CDK1-phosphosite pS283 on Mps1 to be required for full catalytic activity of Mps1, while leaving its localisation unaffected [154]. Correct recruitment of Mps1 to the kinetochores is regulated by Aurora B. Mps1 and Aurora B engage in positive feedback by mutually activating each other. As briefly mentioned above, Mps1 phsophorylates T230 on Borealin and contributes to assembly of the CPC [127]. In turn, basal activity of Aurora B is required for the localisation of Mps1 to the kinetochore [125, 126]. At the kinetochore, Ndc80 acts as a receptor for Mps1 [155, 156], and allows it to phosphorylate multiple Met-Glu-Leu-Thr (**MELT**) motifs on **Knl1** [157, 158, 159].

The Bub1:Bub3 complex fulfils an important scaffolding function at the kinetochore. The kinase **Bub1** (which also plays an important role in Sgo1-mediated protection of centromeric cohesin) forms a complex with the MCC-component **Bub3**, Bub1:Bub3 is recruited to kinetochores in prometaphase and localises to Knl1 upon phosphorylation of its MELT-motifs [160, 161]. Independently of Bub1's kinase activity, Knl1-localised Bub1:Bub3 acts as mediator in the assembly of MCC bringing into close proximity the sub-complexes that constitute MCC: It promotes the localisation of the structurally similar BubR1:Bub3 to the kinetochore [162, 163], as well as the catalytic assembly of ***C*-Mad2:Cdc20** at the kinetochore [164].

Mad2 exists in two stable conformations, termed open (***O*-Mad2**) and closed (***C*-Mad2**), which can be associated with distinct pools of Mad2: Free, unbound Mad2 is predominantly present in its open conformation, whereas the closed conformation is adopted in complex with either Mad1 or Cdc20 [165, 166]. Both Mad2-binding partners present a short, linear Mad2-recognition motif, whose interaction with a C-terminal region of Mad2 (often referred to as the "safety belt") entail the conformational switch from *O*-Mad2 to *C*-Mad2 and hetero-dimerisation [167]. Mad1 and Mad2 form a hetero-tetrameric complex and associate stably throughout the cell cycle in 2:2 stoichiometry [167]. In interphase, the complex is associated with the nuclear pore [168], whereas it becomes recruited to Bub1:Bub3 at unattached kinetochores in early mitosis [164]. In addition, the **RZZ**-complex (Rod-Zwilch-ZW10) was shown to recruit Mad1:*C*-Mad2 to unattached kinetochores [169].

At the kinetochore, Mad1:*C*-Mad2 is believed to act as a catalyst, facilitating the association between *O*-Mad2 and Cdc20: In vitro, *O*-Mad2 and Cdc20 have been shown to undergo complex formation spontaneously, however the rate of formation of the resulting *C*-Mad2:Cdc20 hetero-dimer became markedly accelerated in the presence of Mad1:*C*-Mad2 [170, 171]. This observation underlies the **"template model"** [147, 172], which posits that association of *O*-Mad2 with kinetochore

tethered Mad1:*C*-Mad2 lowers the activation energy for the conformational switch that accompanies the complex formation between Mad2 and Cdc20 [170]. Historically, the scope of the template model was much wider in stating that any complex containing *C*-Mad2 could catalyse the production of *C*-Mad2:Cdc20 [173]. However, both experimental, and theoretical studies have highlighted that such unconstrained catalysis would impede the capacity of the signalling system to turn off [170]. The formation of *C*-Mad2:Cdc20 heterodimers in itself reduces the availability of the APC/C-co-activator Cdc20 that is required to initiate early anaphase. Although this sequestration of Cdc20 plausibly contributes to the inhibition of APC/C by MCC, it is unlikely to be the predominant inhibitory mode [163].

Assembly of a fully functional APC/C-inhibitor that acts as a pseudo-substrate of APC/C:Cdc20 crucially depends on the association of *C*-Mad2:Cdc20 with the BubR1:Bub3 hetero-dimer. It is believed that the co-localisation of *C*-Mad2:Cdc20 and BubR1:Bub3 facilitates the efficient formation of MCC, however recent evidence suggests that the recruitment of BubR1:Bub3 to the kinetochore is not strictly required for MCC formation [174].

2.4.3 Initiation

Is all MCC produced at kinetochores?

MCC assembly at the kinetochores allows the checkpoint to delay anaphase onset in response to lack of attachment. However, this does not mean that all MCC is made at kinetochores. Recently, nuclear pores were shown to play a crucial role in the assembly of a pool of MCC as early as interphase. This interphase-MCC determines the minimal time it takes for a cell to pass through prometaphase and metaphase, and prevents bypassing of the checkpoint due to slow activation kinetics of the checkpoint. [168]

2.4.4 Structure

How are the components of MCC connected?

BubR1 is the largest component of MCC and rich in functional motifs that facilitate its interaction with the other MCC components. It contains two KEN-boxes (KEN1 and KEN2) - short recognition motifs that act as degrons for APC/C:Cdc20-mediated proteasomal degradation, as well as a D-box motif that fulfils a similar role in the substrate recognition of APC/C:Cdc20. Similarly to Bub1, BubR1 contains a Bub3-binding domain (GLEBS-motif), which is required for its interaction with Bub3, as well as a proximal helix structure that promotes its association with Bub1:Bub3.

A crystal structure of fission yeast MCC, provides insight into the molecular contacts within the complex [175]: The safety-belt on Mad2 wraps around the Mad2-recognition motif on Cdc20, the N-terminal KEN1 in BubR1 (called Mad3 in fission yeast) interacts with the WD40 β-propeller structure of Cdc20 and an α-helix on its binding partner Mad2. In addition, the proximal tetratricopeptide repeat (TPR) repeat on BubR1 contacts Cdc20, as well as Mad2, giving rise to a stable MCC core structure. Notably, fission yeast MCC does not contain Bub3, and a truncated form of BubR1 that did not contain KEN2 was used in the study.

2.4.5 Identity

What is the effector of the checkpoint?

Detailed insight into the structure of MCC nonwithstanding, the composition of the SAC effector has come under scrutiny in recent years. The stoichiometry of the constituents in the effector complex has long been assumed to be equimolar, however new evidence suggests that MCC associated with APC/C contains twice as much Cdc20 as BubR1 and Bub3. Based on the presence of two KEN-boxes, it had been hypothesised that BubR1 supports the interaction with two molecules of Cdc20, and that this capacity may play an important role in checkpoint signalling [176]. This hypothesis was confirmed experimentally in a recent study employing recombinant MCC and systematic mutagenesis [177]: Core MCC (consisting of Mad2, Cdc20 and BubR1 in 1:1:1 stoichiometry) can bind a second Cdc20 in a structurally distinct manner. Whereas Cdc20 in the core complex requires the presence of the Mad2-interaction motif, binding of the second Cdc20 is independent of the Mad2-interaction motif and instead requires the presence of BubR1's KEN2-box and its adjacent D-box. Furthermore, the authors went on to show that the interaction between core MCC (Mad2:Cdc20:BubR1) with a second Cdc20 is essential for penetrance of APC/C inhibition by the checkpoint, and the likely mechanism, whereby MCC inhibits APC/C that is already associated with Cdc20 and thus preactivated. These findings have recently been corroborated by two structural studies confirming the presence of two molecules of Cdc20 in the APC/C:MCC complex [178, 179].

Furthermore, Mad2 has been shown to be sub-stoichiometric in these complexes [180]. This observation has led the field to question the precise identity of the inhibitor of APC/C:Cdc20. In vitro experiments suggest that a complex consisting of BubR1, Bub3 and Cdc20 (often referred to as BBC) may in fact be the effective inhibitor of APC/C. However, the study has shown that efficient synthesis of the BBC requires the initial formation of MCC, which then decomposes to BBC.

2.4.6 Turnover

How does the antagonism between APC/C and MCC play out?

Far from being a static interaction, where the MCC acts as a stoichiometric inhibitor and merely occupies the active site of APC/C, inhibition of APC/C by MCC is a highly dynamic process, and subject to control on various levels. Whereas MCC is often referred to as a pseudo-substrate of APC/C, evidence supporting the ubiquitylation of MCC's Cdc20 subunit by APC/C qualifies MCC as a full-fledged substrate of APC/C. This process has been shown to depend on the APC/C-subunit APC15 [181, 182]. It is believed that ubiquitylation of Cdc20 destabilises MCC, leads to its dis-assembly and may lead to the proteasomal degradation of Cdc20. Evidence showing that a stable checkpoint arrest requires protein synthesis, corroborates this hypothesis. Thus, APC/C may directly control the turnover of MCC through ubiquitylation.

Secondly, an APC/C-independent pathway regulates the turnover of MCC via p31^{comet} and the AAA-ATPase TRIP13 . p31^{comet} is a structural homolog of Mad2 and was shown to bind to Cdc20 and displace Mad2 from MCC. The extraction of Mad2 from MCC is catalysed cooperatively by p31^{comet} and TRIP13. The latter promotes the conformational change from *C*-Mad2 to *O*-Mad2, thereby replenishing the pool of *O*-Mad2 required for checkpoint signalling [183, 184, 185]. This displacement is believed to compromise the stability of MCC and contribute to efficient silencing of the checkpoint [186, 187, 188]. This hypothesis is supported by recent data, which suggest that the activity of p31 is suppressed by mitotic phosphorylation [189, 190]; however, the precise identity of the phosphorylating kinase remains unclear.

2.4.7 Termination

How is the checkpoint turned off?

Thus far, the discussion of the mitotic checkpoint enforcement module has focused on how kinetochores produce a molecule that inhibits APC/C:Cdc20. We shall now turn to the question as to how production of the inhibitor is terminated upon formation of attachments (figure 2.4 D). Several signalling pathways contribute to silencing of the checkpoint: Dynein-mediated stripping of Mad1:Mad2 from the kinetochores [191, 192], a mechanical switch on Mps1 activity [193, 194], as well as by the mitotic phosphatases PP1 [195] and PP2A:B56 [196].

Preventing the removal of Mad1:Mad2 by artificially tethering it to the kinetochore is sufficient to produce a stable checkpoint arrest even if all chromosomes

have been bi-oriented [197, 198, 199]. Thus, removal of Mad1:Mad2 plays a central role in the termination of checkpoint signalling. Retention of Mad1:Mad2 at the kinetochore is antagonised by a dynein-mediated process that strips Mad1:Mad2 from the kinetochore through active transport along attached microtubules. At the kinetochore, the RZZ-complex (Rod-Zwilch-ZW10) and Spindly cooperate in the recruitment of dynein. In contrast to the Bub1:Bub3-associated pool, a pool of Mad1:Mad2 is associated with the RZZ-complex [169]. Upon attachment of microtubules, the (-)-directed movement of dynein strips Mad1:Mad2 from the kinetochore and reduces the rate of MCC production [191, 192].

In addition to the initiation of active transport processes upon attachment, the establishment of stable attachments tips the balance of kinase-phosphatase activity in favour of de-phosphorylation. Recent experiments have demonstrated a direct competition between Mps1 activity and microtubule attachments. The precise mechanism for this competition remains to be elucidated, yet models involving displacement of Mps1 from the kinetochore, as well as models based on steric hindrance have been proposed. [193, 194, 200]

2.5 Anaphase and Beyond

> To conclude this overview, our discussion will now focus on the events that trigger anaphase after chromosome bi-orientation, and how exit from mitosis is regulated on a global level by the mitotic control system.

2.5.1 Departure

What happens when the checkpoint is turned off?

With the bi-orientation of the last unattached kinetochore, MCC assembly slows down to a rate that is no longer able to sustain inhibition of APC/C. APC/C:Cdc20 becomes active and targets cyclin B and securin for degradation. The degradation of securin activates separase and allows it to cleave cohesin's kleisin subunit, thus resolving sister chromatid cohesion. Cleavage of cohesin initiates the separation of sister chromatids, which get pulled towards opposing poles of the mitotic spindle. The segregation of sister chromatids is accompanied by the formation of the central spindle by overlapping microtubules in the centre of the cell. The chromosomal passenger complex relocates to the central spindle.

Surprisingly, securin is not essential in mammalian cells [201]. This is likely due to additional inhibitory interactions such as cyclin B:CDK1 acting as a stoichiometric

inhibitor for separase. Separase can exist in two conformations - one (cis) susceptible to inhibition by cyclin B:CDK1, the other refractory (trans). In the presence of securin, separase predominantly exists in its trans-form. Upon release from securin, a CDK1 phosphorylation-specific peptidyl-prolyl cis/trans isomerase Pin1 can trigger the conformational change from trans-separase to cis-separase, rendering it susceptible to inhibition by cyclin B:CDK1, and refractory to re-inhibition by securin [202].

2.5.2 Relay

How is the decision to exit from mitosis broadcast?

The degradation of cyclin B and securin constitutes the crucial trigger for the onset of anaphase. The loss of cyclin B reduces the activity of CDK1, whose phosphorylation of many substrates was crucial in maintaining the mitotic state, by either activating their mitosis-specific function, or inhibiting their function required for exit from mitosis. To perform a successful exit from mitosis, these phosphorylations have to be removed in orderly fashion, sequentially initiating central spindle formation, relocation of the chromosomal passenger complex, spindle elongation, determination of the abscission plane, nuclear envelope reformation and cytokinesis. In metazoans phosphorylations of key CDK1-substrates are removed by the phosphatases PP2A:B55 and PP1 [99, 100, 203].

In turn, these phosphatases are subject to control by CDK1 activity: The phosphorylation of T230 on PP1 by CDK1 inhibits its activity and promotes the binding of PP1 with phosphorylated inhibitor 1. Activation of PP1 relies on auto-de-phosphorylation on T230 and subsequent inactivation of inhibitor 1 by de-phosphorylation [204]. PP2A:B55, on the other hand, is inhibited via the ENSA-Greatwall pathway: CDK1 activates the kinase Greatwall (MASTL) [205]. Greatwall in turn phosphorylates ENSA and ARPP19 [206, 207], which act as pseudo-substrate inhibitors of PP2A:B55 through unfair competition - they associate very strongly with PP2A:B55, but are turned over slowly [208]. Thus, activation of PP2A:B55 requires the inactivation of Greatwall, and the de-phosphorylation of ENSA/ARPP19. These interactions give rise to a timer module that delays activation of PP2A:B55 for some time after APC/C:Cdc20 activation and subsequent separase release, and thus ensures that cytokinesis is initiated after chromosome segregation [101]. Recent experiments in *Xenopus laevis* egg extracts suggest that PP1 plays a crucial role in the activation of PP2A:B55 by removing the activatory auto-phosphorylation on Greatwall [209].

3

Systems-Level Perspective

> Having discussed signalling pathways that give rise to the mitotic checkpoint in detail, we shall now turn to properties that characterise the signalling system as a whole and to questions pertaining to the terminology and conceptual representation of the checkpoint system.

3.1 Models

The mitotic checkpoint has been the subject of a wide range of theoretical studies in recent years. Based on the models developed in these studies, they can be classified into three groups: biophysical models focussing on the mechanics of spindle formation [210, 211], models investigating the spatial dynamics of checkpoint signalling [173, 212], and models focussing on the on the role of molecular feedback mechanisms in checkpoint signalling [213, 214, 215]. The work presented herein is in the tradition of the latter category.

The fundamental premise of this discussion is that the mitotic checkpoint can be conceptualised as a molecular signalling system. This assumption is buried deep within the narratives of virtually all discussions on the topic. On the surface, it appears to be stating the obvious: Cells have evolved systems of molecules that act together to translate an input into an output, in order to process some form of biochemical information about the cell or its environment and act in response to it. However, it should be noted that by accepting the concept, a purpose-directedness is introduced. To enable a clear discussion of this issue, let us introduce some basic terminology on molecular signalling systems first: Molecular signalling systems respond to a well-defined chemical stimulus that acts as signal (input). The signal triggers state-dependent molecular changes within the signalling system that eventually give rise to a response (output). The state of the system determines the input-output mapping, may depend on alternative inputs - such as the activity of upstream regulators - and may be history-dependent.

This concept does not pose a problem in itself, and has proven useful in reasoning about biological systems in various contexts. Yet, it gives rise to a set of challenging problems related to the description of the matter at hand, as input (signal) and output (response), as well as the notion of "purpose" of the system, are highly sensitive to the definition of the system-boundaries.

3.2 Boundaries

Can we do better than to reason based on entirely binary logic?

Frequently, discussions about the mitotic checkpoint assume that checkpoint enforcement module and error correction are entirely separable entities. Yet, is it right to view error correction and checkpoint enforcement as distinct and separate systems?

Let us briefly review the key points from the discussion of the molecular basis of both error correction and checkpoint signalling: Whereas it is tempting to assign clear roles to Aurora B (in error correction) and Mps1 (in checkpoint effector signalling), both modules are closely interlinked at the level of upstream regulators, and the roles of cyclin B:CDK1, Mps1 and Aurora B in error correction and production of the checkpoint effector are difficult to separate: Cyclin B:CDK1 and Mps1 are involved in the assembly of the CPC and thus influence the local activity of Aurora B at the kinetochore. In turn, Aurora B is required for the localisation of Mps1 at the kinetochore, and cyclin B:CDK1 activates Mps1 through phosphorylation. Moreover, checkpoint activity ensures sustained activity of cyclin B:CDK1 by protecting it from proteasomal degradation.

Qualitatively, these interactions strongly suggest that a conceptual separation of error correction and checkpoint enforcement modules is not at all justified. However, such reasoning leaves an important determinant unaccounted for: Many experiments that inform our insight into molecular interactions correspond to endpoint measurements and disregard how components of the systems interact in time - error correction and the checkpoint effector may act at entirely different timescales, and thus behave as if independent; a positive interaction may vastly outpace a competing negative interaction between the same components with respect to the time it takes for each to take effect, giving rise to counter-intuitive activity patterns over time. Purely qualitative reasoning based on a binary description of the molecular interactions fails in such instances.

The work presented in this thesis is based on a strategy that complements biological intuition and targeted experiments with quantitative, mathematical models.

These models represent signalling networks as systems of coupled rate equations that express how activities of key components of the network change over time and in response to certain stimuli. The parameters used in these equations correspond to rate constants for reaction steps, or may directly represent an input signal. They are chosen to bring the model into agreement with experimental data. Subsequently, time-course simulations derived from the models are analysed to yield predictions that are testable under new experimental conditions, which can in turn inform an improved instance of the model. Thus, the strategy lends itself to cycles of iterative refinement through data-driven modelling and model-driven experimentation.

Furthermore, the analysis of steady states of the system can provide a natural framework for the discussion of systems-level properties: Attractors - such as stable steady states - impose structure onto the abstract space representing possible states of the system (phase space). Thus, an analysis of the phase space can give rise to a clear terminology to describe a system, its fuzzy boundaries, behaviour and capacities.

The fundamental hypothesis that underpins the checkpoint-related work presented in the following chapter is that the checkpoint is regulated by a bistable switch. Bistability was touched upon in chapter 1; we shall now briefly recapitulate the key characteristics of a bistable switch, and will then relate them to systems-level properties relevant for the mitotic checkpoint: A system exhibits bistability if, for a range of input-signal strengths (represented by a parameter), there exist two stable steady states separated by an unstable steady state. At certain strengths of input signal, the unstable and stable steady states merge and form a saddle node bifurcation, marking the boundary of the bistable regime: At these points, two coexistent stable steady states appear. Stable and unstable steady states are distinguished based on their surrounding vector fields (figure 3.1, left panel). The vector field around stable steady states points towards them, whereas the vector field points away from unstable steady states. Thus, for a system-state that is not a steady state, the system will become attracted towards the closest stable steady state and repelled by the closest unstable steady states. In other words: **stable steady states** form basins of attraction (**valleys**) that are separated by **unstable steady states** (**mountain ranges**). A thus partitioned phase space can be used to define clear terms that describe the checkpoint system: The positions of **saddle node bifurcations** with respect to the input signal marks the thresholds for **engagement** and **disengagement** of the system (figure 3.1, middle panel). The **threshold for disengagement** of the checkpoint control system corresponds to its

sensitivity. Global activity of the system is best defined based on the capacity of the system to become engaged. Here, the position of the unstable saddle node as a function of the input signal marks the boundary between an **active** and an **inactive** checkpoint control system.

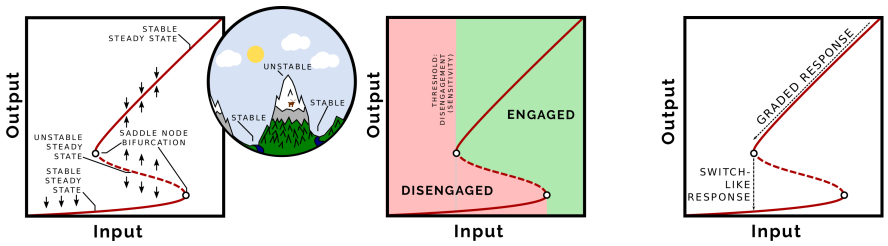


Figure 3.1: A bistable switch and basic terminology of control systems - A schematic illustration of a bistable switch, and how it can give rise to basic terminology in the context of the mitotic checkpoint

Having defined the terminology in terms of properties of the dynamical system, the task remains of clarifying it in the context of experimental insight. Questions relating to the nature of the signal, the sensitivity to the signal, the inactivation of the checkpoint and its irreversibility have a long history in the field. Many of these questions have been debated heavily over the past decade. In most cases a clear answer is still pending, and the underlying issues still constitute major controversies. The following discussion will motivate the presentation of the original research presented in this thesis.

3.3 Signal

Is it lack of tension or lack of attachment that turns the checkpoint on?

Let us assume that the error correction mechanism and thecheckpoint enforcement module can be treated as separate systems: Do they respond to distinct signals? - Does the error correction strictly respond to tension, whereas the checkpoint enforcement mechanism answers to attachment alone?

At the level of error correction, the attenuation of Aurora B activity by "tension" - kinetochore deformations induced by microtubule growth and shrinkage (intra-kinetochore stretch) and tension across the centromeres (inter-kinetochore stretch) - has become increasingly well established in recent years. It has become supplemented with insight into the underlying molecular mechanisms, revealing a complex force-coupling mechanism that underpins the capacity of the error correction to detect faulty attachments.

On the other hand, the stripping of Mad1:Mad2 from attached microtubules provides a mechanistic basis for how the production of MCC is stopped upon attachment of a kinetochore. Experiments showing that tethering Mad1:Mad2 to bi-oriented chromosomes is sufficient to sustain MCC production further corroborates this mechanism. Yet, local activity of Mps1 at the kinetochore was recently shown to be modulated by deformations in the kinetochore (intra-kinetochore stretch) [193, 194]. These deformations are induced by the attachment of microtubules, so they could easily be attributed to the concept of an attachment-based signal.

However, close consideration of the arguments reveals potentially overlapping definitions: Deformations of the kinetochore in response to attachment also feature in the coarse-grained definition of the tension-based signal to which the error correction machinery responds. What are the differences between tension and attachment, and where should a line be drawn?

In models that incorporate a description of the error correction mechanism, this issue will be addressed by allowing for checkpoint effector activity to be modulated by attachments, as well as by a mechanism that depends on the deformation of kinetochores. Subsequent parametrisation of the model based on targeted experiments will be used to interpret the individual contributions in the framework of the model.

3.4 Sensitivity

How many unattached kinetochores does it take to make the checkpoint signal?

A potential cross-talk with error correction notwithstanding, the response of checkpoint effector signalling to unattached kinetochores is well characterised. In a study using live-cell imaging and laser micromanipulation in PtK1 cells, a single kinetochore was shown to be sufficient to delay the onset of anaphase [103]. This finding is often invoked as evidence for an entirely switch-like response of the checkpoint enforcement mechanism to unattached kinetochores: The checkpoint is assumed to be fully active - producing MCC at close to the maximal possible rate - until the last kinetochore has become attached, when the rate of MCC production abruptly drops. However, recent evidence suggests that view has to be revised:

In a careful study of the kinetics of checkpoint signalling using live-cell imaging and laser microsurgery in HeLa cells, Dick and Gerlich [216] revealed that the capacity of the checkpoint to become re-engaged in response to a single kinetochore that becomes unattached in metaphase decays towards anaphase. Moreover, they

estimated the rate of MCC production as a function of the number of unattached kinetochores, revealing a dependence that - albeit non-linear - does not resemble a simple step-function.

In a subsequent study on RPE1 cells, Collin *et al.* [217] investigated localisation of Mad2 to the kinetochore and the degradation of endogenous, tagged cyclin B in the context of different spindle poisons (the Eg5-inhibitor DMA, the microtubule-stabilising drug Taxol and the microtubule-de-polymerising drug Nocodazole). They show that treatment of cells with these different drugs induces different extents of Mad2-localisation at the kinetochore, resulting in a reduced assembly of MCC and weaker inhibition of APC/C.

These findings suggest that the response of the checkpoint to unattached kinetochores is graded, which is often interpreted as being inconsistent with a toggle switch model. Thus, is it even plausible that the mitotic checkpoint may be regulated by a bistable switch? An assumed inconsistency between switch-like behaviour and a partially graded response is a common misconception about bistable switches. - Indeed, systems that exhibit bistability support a graded response over a certain range of input signals (figure 3.1, right panel). Whereas the observed gradedness imposes constraints on the behaviour of a bistable switch, it does not disqualify it as such.

3.5 Irreversibility

What prevents the checkpoint from signalling in anaphase?

The principle that a bistable switch underpins mitotic checkpoint control becomes a particularly attractive concept in the context of irreversibility. Irreversible inactivation can naturally emerge from the hysteresis inherent in bistable systems, if the saddle-node bifurcation that establishes a threshold for reactivation lies in a physically not realisable regime. Thus, bistability may indeed present itself as the most parsimonious model for the mitotic checkpoint, as models that exhibit a response that is strictly graded are not capable of explaining irreversible inactivation.

Irreversibility becomes a pressing question at the onset of anaphase: Upon cohesin cleavage, inter-kinetochore tension - a major contributor in suppressing error correction - is lost. If error correction in particular, or checkpoint signalling as a whole were not silenced at this point, microtubule-kinetochore attachments could become destabilised in the process of sister chromatid segregation. Were

the checkpoint enforcement mechanism still active, production of MCC and inhibition of APC/C would entail. This scenario frames the so-called anaphase problem, which asks: How is reactivation of the checkpoint avoided at the onset of anaphase?

Far from being a simple question, close consideration of the anaphase problem reveals that it stages a set of challenging problems: Does cohesin cleavage induce a sufficiently strong change in kinetochore dynamics to trigger reactivation of the error correction machinery? If so, what changes at the molecular level to prevent reactivation of error correction after anaphase onset? How are the underlying molecular changes coordinated with the onset of anaphase?

Over the past decade, numerous studies have addressed various aspects of the problem: Induced premature cleavage of cohesin during metaphase was shown to destabilise attachments and to trigger re-synthesis of MCC [131, 218], thus confirming the fundamental premise of the anaphase problem, that cohesin cleavage bears the potential to reactivate error correction. In their study on fission yeast, Kamenz *et al.* [219] report that re-engagement of checkpoint-signalling is slow compared to the time-scale of progression through anaphase, and therefore functions as a safety mechanism against a resurgence of APC/C-inhibition in anaphase. However, the role of this mechanism in higher eukaryotes remains unclear, as the checkpoint clearly retains the power to transiently inhibit APC/C when challenged with the detachment of a single kinetochore in metaphase [216, 220]. A different line of evidence highlights the role of the relocation of the CPC in the inactivation of the error correction machinery: Depletion of MKlp2 led to retention of the chromosomal passenger complex at kinetochores in anaphase, and resulted in reactivation of the checkpoint effector components BubR1 and Bub1 [130].

Critically, phosphorylation by cyclin B:CDK1 prevents the MKlp2-dependent relocalisation of the chromosomal passenger complex [128, 129, 130, 131]. Using non-degradable mutants of cyclin B:CDK1, sustained activity of CDK1 was shown to induce aberrant "pseudo"-anaphases characterised by de-stabilised microtubule-kinetochore attachments and reactivation of MCC synthesis and concomitant APC/C inhibition [221, 222]. Conversely, it was demonstrated that cells arrested in metaphase through proteasomal inhibition by MG132 only show a checkpoint response to microtubule de-polymerisation if CDK1 activity is kept high, but fail to mount a checkpoint response when CDK1 is inhibited with flavopiridol [221, 222].

From these findings, a picture emerges, whereby cyclin B:CDK1 activity is fundamental in managing error correction: Its sustained activity is required to maintain CPC activity at the kinetochores, and the degradation of cyclin B coordinates inactivation of error correction with anaphase onset.

3.6 Finality

What happens when correct attachments cannot be achieved, and what if things go wrong?

In addition to its coordinating role in error correction, cyclin B:CDK1 appears to have a crucial function in maintaining checkpoint effector signalling: Microtubule de-polymerising drugs such as Nocodazole and Colchicine are widely used in experiments aimed at isolating effects at the level of the checkpoint effector signalling from error correction. In the absence of microtubules, the spindle cannot assemble. Thus, kinetochores remain persistently unattached, allowing the investigation of the checkpoint effector signalling system in a persistently active state. In this case, the mitotic checkpoint delays the progression in mitosis for many hours. However the "arrest" is not indefinite: Numerous studies have described so-called mitotic slippage - a phenomenon where checkpoint control is eventually bypassed and the cell progresses into an aberrant anaphase that leads to aneuploidy (a condition characterised by aberrant numbers of chromosomes that contributes to genome instability and cancer). In PtK1 cells and human RPE1 cells, mitotic slippage was shown to occur via slow proteasomal degradation of cyclin B in the presence of an engaged mitotic checkpoint [223]. Recent evidence suggests that the cellular pool of cyclin B needs to be actively replenished via de-novo synthesis in order to sustain a checkpoint arrest over many hours, and that exogenous expression of cyclin B can delay mitotic slippage [224].

Taken together, these findings suggest that cyclin B:CDK1 activity is fundamental in sustaining the activity of both modules of the mitotic checkpoint throughout prometaphase and metaphase, and that the proteasomal degradation of cyclin B:CDK1 coordinates irreversible inactivation of the mitotic checkpoint with the onset of anaphase. The role of cyclin B in sustaining a mitotic arrest in the persistent presence of unattached kinetochores suggests that a critical activity of cyclin B:CDK1 is needed to sustain signalling of the checkpoint enforcement module.

4

Costly Crosstalk

The work presented in this chapter was conducted in collaboration with Mihailo Mirkovic (MM) and Raquel A. Oliveira (RAO) at Institutio Gulbenkian de Ciencia in Lisbon, Portugal. The underlying experiments were designed by RAO and MM, and carried out by MM. In 2015, it was published in Cell Reports [225].

How can we conceptualise the coupling between the error correction and checkpoint enforcement modules? The importance of a clear conceptual framework and the implications thereof on notions such as the signal have been discussed in detail in the preceding chapter. From this discussion, it has emerged that a clear separation of the subsystems that constitute the mitotic checkpoint is problematic, for they share intimate interdepencies at the level of mitotic kinases. Moreover, error correction and the checkpoint effector appear closely coupled in terms of their respective in- and outputs: Error correction produces unattached kinetochores, which serve as input to the checkpoint effector. In turn, an active checkpoint effector prevents inactivation of mitotic kinases that are crucial for the activity of error correction and the checkpoint effector.

However, this does not imply that the subsystems are entirely indistinguishable: The capacity of the tension-dependent error correction machinery to integrate the attachment-status of both sister chormatids - and to destabilise attachments accordingly - relies on the existence of a mechanism that mechanically couples sister chromatids. Sister chromatids are physically linked through the cohesin complex, which couples the spindle-forces that act on sister chromatids upon attachment of both sisters. Therefore, sister chromatid cohesion enables the development of tension between the sister chromatids (inter-kinetochore tension) upon amphitelic attachment. Indeed, cohesin-defects are associated with aneuploidy and cells with un-replicated

chromosomes or cells subjected to premature loss of cohesin show aberrant mitoses, characterised by eventual mitotic exit in spite of lack of bi-orientation.

Thus, by eliminating inter-kinetochore tension, premature artificial cleavage of cohesin can provide a promising experimental route towards the systems-level investigation of the interplay of the checkpoint enforcement mechanism and error correction.

4.1 Data

4.1.1 Experimental System

The basis for this study is a tool for the acute removal of cohesin in *Drosophila melanogaster* third instar larvae through cleavage of its Rad21 (kleisin) subunit using an exogenous protease (tobacco etch virus [TEV]) [218]. In this system, the expression of TEV is inducible by heat-shock treatment of the larvae at $37°C$ for $45\ min$. To study the mitotic checkpoint, larval brains were dissected and prepared for immunofluorescence or live-cell imaging of neuroblasts (stem cells that give rise to the central nervous system).

4.1.2 Timing of Mitosis

To assess the capacity of the checkpoint to respond to premature loss of sister chromatid cohesion, we compared the duration of mitosis (from nuclear envelope breakdown [NEBD] to nuclear envelope reformation [NEF]) in cells that exclusively contain TEV-sensitive cohesin under the following conditions:

- ***00***: wild-type, untreated
- ***0h***: wild-type, heat-shock treated
- ***a***: heat-shock treated; expression of TEV, premature loss of sister chromatid cohesion
- ***b***: Colchicine-treated ($100\ \mu M$); Colchicine is a drug that de-polymerises microtubules in a similar manner to Nocodazole
- ***ab***: combined heat-shock treatment and Colchicine addition ($100\ \mu M$)

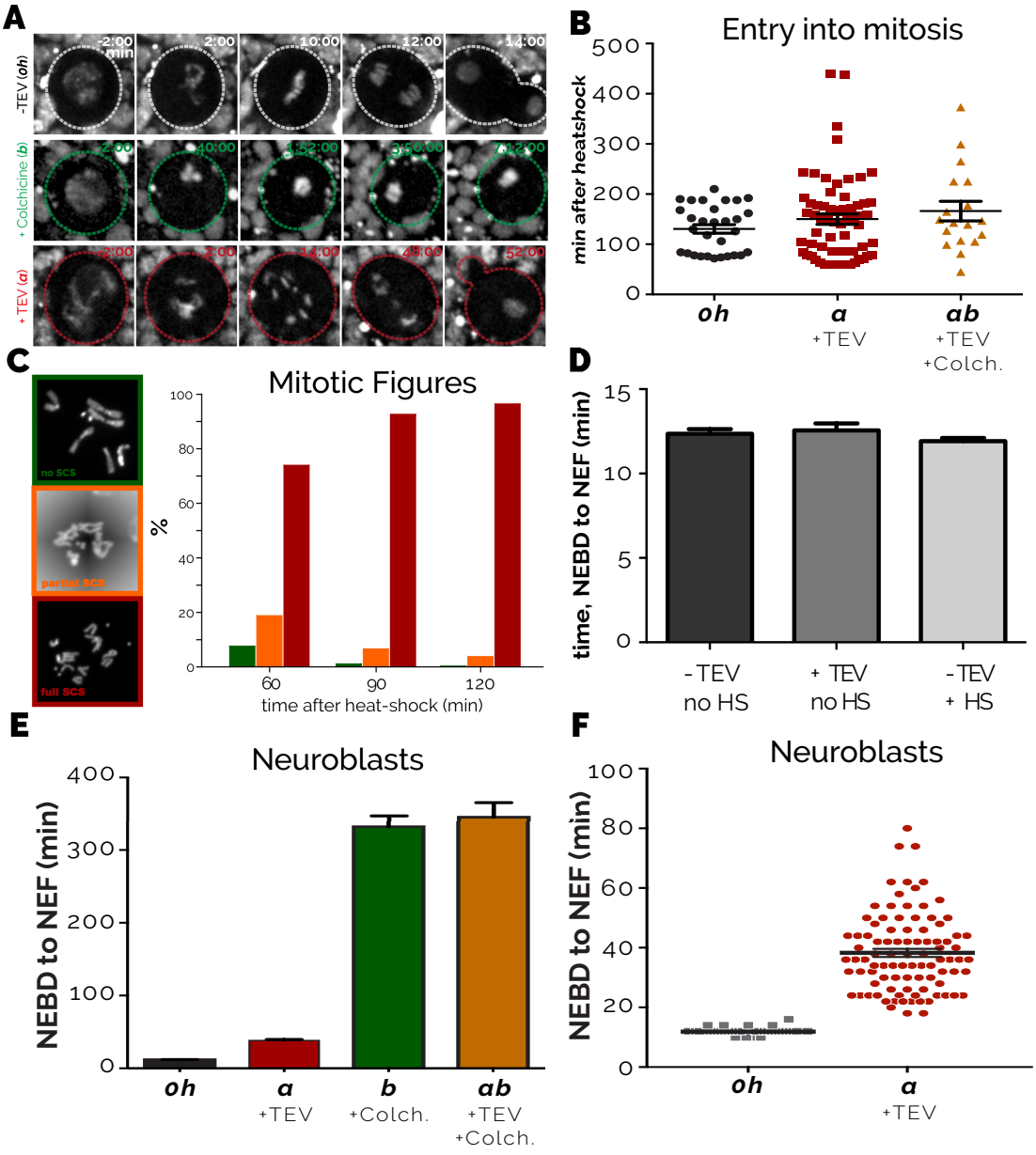


Figure 4.1: Mitotic Timing - (**A**) Images of dividing *Drosophila* neuroblasts from heat-shocked wild-type strains (***Oh***), wild-type strains treated with 100 μM Colchicine (***b***), and neuroblasts upon induced cohesin cleavage (***a***). (**B**) Time of entry into mitosis after heat-shock in the indicated experimental conditions. Mitosis is not observed within the first 60 min after heat-shock. The treatments have no effect on the time of mitotic entry after heat-shock. (**C**) Quantification of sister chromatid separation upon heat-shock treatment. (**D**) Time of mitosis (NEBD to NEF) in three different control conditions. (**E**) Average duration of mitosis (NEBD to NEF). (**F**) Comparison of mitotic timing between heat-shocked control cells (***Oh***) and cells subjected to cohesin cleavage (***b***). *Figure adapted from [225].*

Table 4.1: Comparison of duration of mitosis in different treatments depicted in figure 4.1 E

abbreviation	treatment	NEBD to NEF (min)	n (cells)	N (brains)
00	wild-type, untreated	12 ± 00	62	6
0h	wild-type, heat-shock treated	12 ± 00	41	4
a	heat-shock treated; expression of TEV	38.3 ± 13.1	93	8
b	colchicine-treated	330	57	6
ab	heat-shock, TEV, colchicine treatment	340	15	2

Upon heat-shock, cells delayed mitotic entry for $148 \pm 75\ min$ ($n = 113$ cells, $N = 14$ brains)[1] (figure 4.1 B, C); this enabled us to assess the effect of premature sister chromatid separation (PSCS) in the same cell cycle.

Whereas control cells (***00*** $n = 61, N = 6$ and ***0h***, $n = 41, N = 4$)) (figure 4.1 D) took $12\ min$ to complete mitosis, premature loss of sister chromatid cohesion (***a***, $n = 93, N = 8$) resulted in markedly longer mitoses ($38.3 \pm 13.1\ min$) (figure 4.1 E,F). Strikingly, cells treated with colchicine (***b***, $n = 57, N = 6$) (figure 4.1 E) remained arrested in mitosis for significantly longer times ($330\ min$). An additive effect of TEV-expression and colchicine treatment was not observed (***ab*** $n = 15, N = 2$).

These results indicate that the mitotic checkpoint in *Drosophila* neuroblasts is highly effective at responding to lack of attachments as a consequence of microtubule de-polymerisation (figure 4.1 E and table 4.1). However the short delay observed upon premature sister chromatid separation indicates that the checkpoint fails to respond robustly to this situation. We therefore hypothesised that transient kinetochore-microtubule attachments can form after premature sister chromatid separation. Since amphitelic attachments cannot be achieved, the lack of opposing pulling forces triggers the eventual destabilisation of these attachments by the error correction. From this simple model, one would predict robust mitotic arrest upon premature sister chromatid separation. Yet the data on mitotic timing suggests that the mitotic checkpoint fails to respond robustly to separated sister chromatids.

4.1.3 Aurora B Localisation

Recent evidence suggests that localisation and activity of Aurora B become compromised upon depletion of cohesin [226]. Thus, we next investigated whether artificial cleavage of cohesin perturbs Aurora B localisation in our experimental system.

[1] n - total number of individual cells, N - number of independent experiments

We prepared spreads from larval brains that were either treated with colchicine (***b***), or subjected to heat-shock-induced TEV-cleavage of cohesin (***a***), and measured Aurora B localisation and the related haspin-mediated phosphorylation of H3T3 relative to the centromere marker CID by means of immuno-staining.

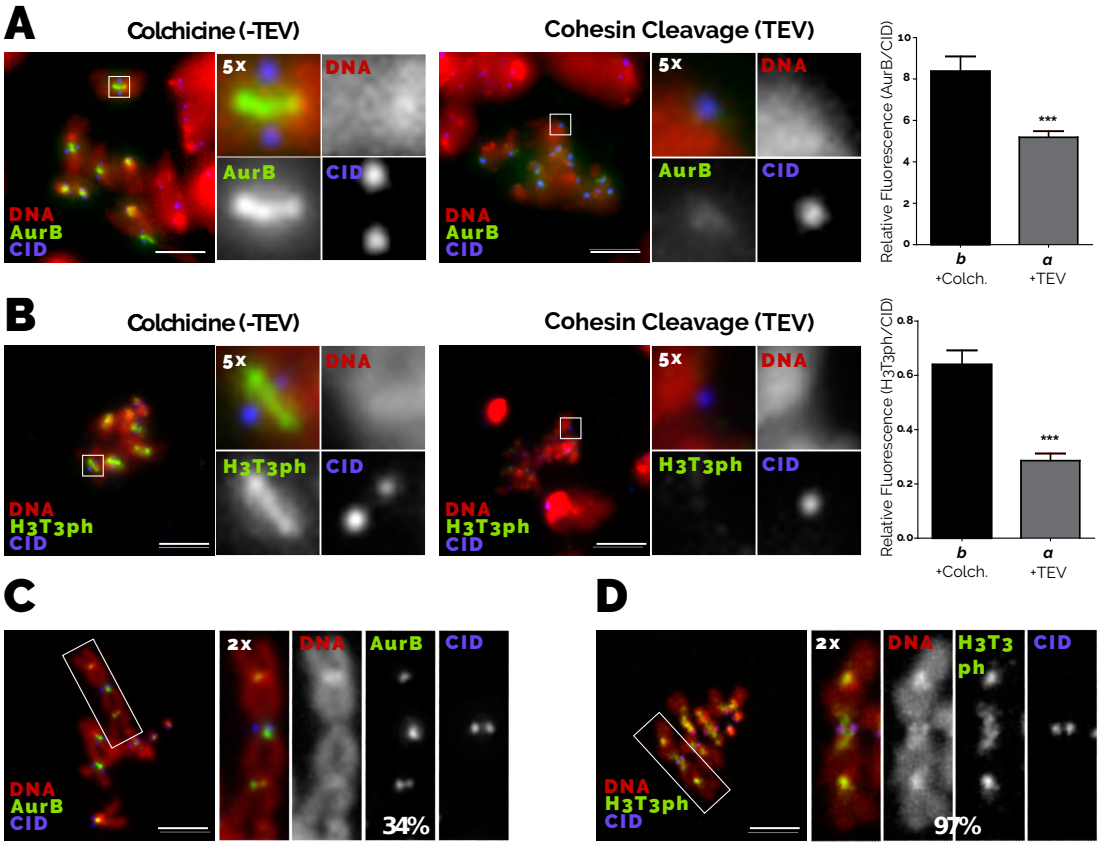


Figure 4.2: Aurora B Localisation Upon Cohesin Cleavage - Spreads of larval brains from wild-type and cohesin-cleaved strains immuno-stained for Aurora B (**A**) and H3T3ph (**B**). DNA is shown in red and CID in blue. Right graph depicts relative fluorescence intensity in the centromere vicinity in each experimental condition. (**C,D**) Spreads from larval brains from C(2)EN strains immuno-stained for Aurora B (C) and H3T3ph (D) demonstrating their localisation at ectopic hetero-chromatin sites, despite the absence of a proximal centromere (labelled with CID in blue). Numbers indicate the percentage of ectopic sites containing Aurora B/phH3T3. Scale bars are 5 μm. *Figure adapted from [225]*

Quantification of the relative fluorescence of Aurora B at centromeres showed that 40% less Aurora B localised to the centromere upon cleavage of cohesin (***a***) relative to colchicine-treated cells with intact cohesin (***b***) (figure 4.2 A). Similarly, haspin phosphorylation on histone H3 was reduced by 50% (figure 4.2 B). Interestingly, cohesin cleavage resulted in a specific reduction of Aurora B activity in the vicinity of centromeres, but not at ectopic chromatin sites (figure 4.2 C,D).

4.1.4 Stabilisation of Attachments

To investigate how the reduced activity of Aurora B affects the error correction mechanism, we conducted a quantitative analysis of chromosome movement in cells expressing the EGFP-tagged centromere marker CID (EGFP-CID) subjected to premature cohesin cleavage (***a***). Upon automated image-segmentation, centromeres were classified into three categories based on their spatial overlap in consecutive frames during imaging: No-overlap, corresponding to fast movement; two frames overlap; and three frames overlap, corresponding to slow movement (figure 4.3 A, B).

At NEBD, approximately six in ten kinetochores showed no overlap between two consecutive frames, three in ten kinetochores overlapped in two consecutive frames, and only one in ten kinetochores overlapped in three or more frames (Figure 4.3 B, C). Moreover, the high degree of chromatin movement is accompanied by oscillatory movements of the chromatin between spindle poles. Whereas the proportion of non-overlapping kinetochores decreased over time, the proportion of kinetochores found to overlap in three or more consecutive frames increased linearly (Figure 4.3 B, C). At the end of mitosis, one third of kinetochores overlapped in three or more consecutive frames, and an equal proportion of kinetochores overlapped in two consecutive frames (Figure 4.3 B, C).

4.1.5 Aurora B Inhibition

The data presented above suggest that the high degree of chromatin movement results from cycles of attachment and error correction-mediated destabilisation due to lack of tension. To test this hypothesis, we assessed timing of mitosis and motility of chromatin upon acute inhibition of Aurora B in cells subjected to premature cleavage of cohesin (***a***), treatment with colchicine (***b***) or a combination of the two treatments (***ab***).

Addition of the Aurora B inhibitor binucleine 2 [227] to cells ($n = 33, N = 3$) subjected to premature loss of cohesin (***a***) shortened the moderate arrest observed without the addition of an inhibitor (approximately $40\ min$) further, and resulted in an abrupt mitotic exit in $7.5 \pm 0.5\ min$ (Figure 4.3 E). Furthermore, chromatin movement was strongly reduced upon addition of the inhibitor (Figure 4.3 D). Conversely, cells treated with binucleine 2 in the absence of microtubules (***b*****:** $n = 26, N = 5$; ***ab*****:** $n = 20, N = 3$) arrested in mitosis for $50 - 80\ min$ (Figure 4.3 E).

These data suggest that whereas cleavage of cohesin compromises the localisation of Aurora B, the retained activity of Aurora B is sufficient to transiently inhibit

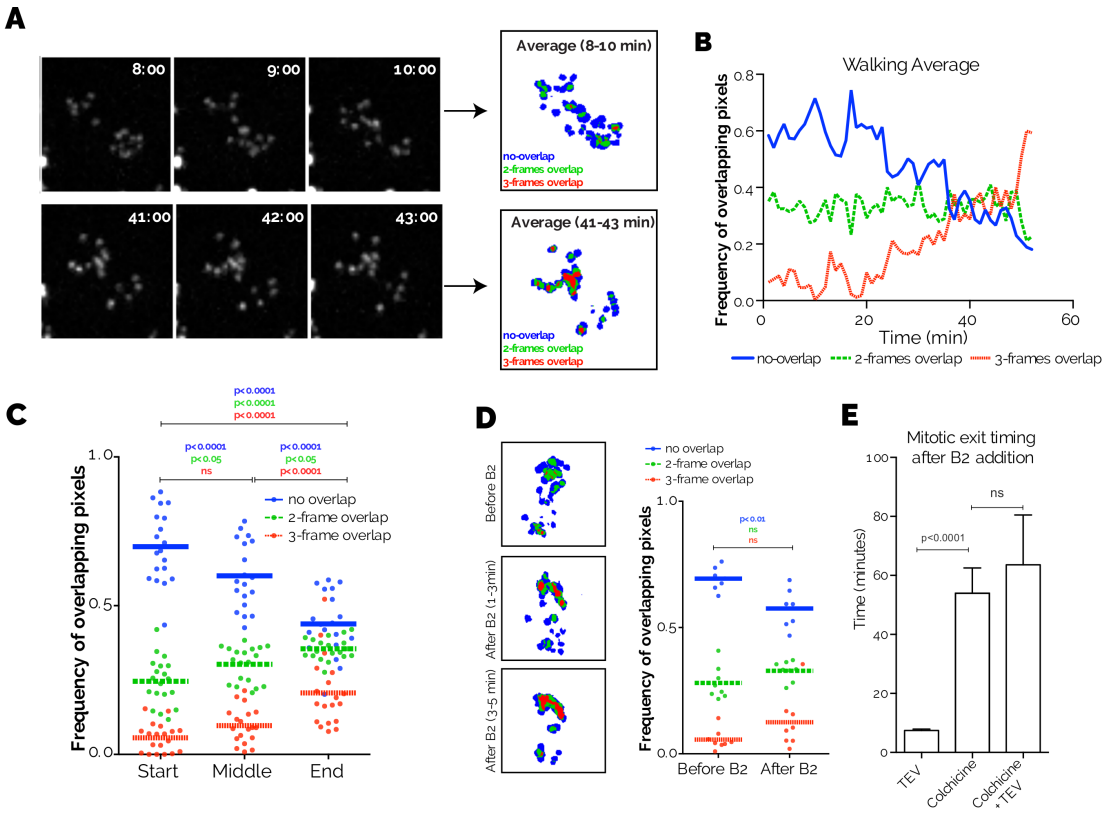


Figure 4.3: Characterisation of Chromatin Movement - (**A**) Stills from live-cell imaging of CID-EGFP-expressing neuroblasts upon cohesin cleavage ($t_0 = NEBD$). Right panel represents average of the binary images of 3 consecutive frames used to estimate centromere displacements - blue, non-overlapping pixels; green, 2 out of 3 frame overlap; red, 3 frame overlap. (**B**) Frequency of overlapping pixels to estimate centromere displacement (as in A), throughout mitosis with PSCS. (**C**) Centromere displacement at different times of arrest upon TEV-mediated cohesin cleavage: start: 6-10 min after NEBD; end: $6 - 10\ min$ before anaphase onset; middle: $5\ min$ at the midpoint of the arrest ($n = 23, N = 3$); p = adjusted p-value by two-way ANOVA; (**D**) Centromere displacement before and after addition of the AurB inhibitor binucleine 2 (final concentration: $25\ \mu M$); binucleine 2 was added 6-10 minutes after NEBD and centromere displacement was measured immediately after until anaphase onset ($n = 8, N = 3$); p = adjusted p-value by two-way ANOVA; (**E**) Mitotic exit time after binucleine 2 addition in TEV-cleavage ($n = 33, N = 3$), colchicine treatment ($n = 26, N = 5$) and colchicine + TEV ($n = 20, N = 3$) experiments ($mean \pm SEM$). *Figure adapted from [225].*

progression into anaphase upon premature cleavage of cohesin. The differential effect observed for cells treated with binucleine 2 in the presence and absence of microtubules, can be explained through the dual role of Aurora B in the two subsystems of the mitotic checkpoint: In the absence of microtubules attachments cannot be formed, and any effect of Aurora B inhibition is likely due to its role in checkpoint effector signalling; whereas the inhibition of Aurora B in colchicine-treated cells shortened the duration of mitosis relative to colchicine-treated cells with otherwise unperturbed Aurora B activity (figure 4.3 E) - cells still took approximately $60\ min$ to exit mitosis. This suggests that removing the Aurora B-mediated phosphorylations relevant for checkpoint effector signalling is kinetically slow. Upon premature cleavage of cohesin in the presence of microtubules, the much faster exit from mitosis must therefore be due to an additional process. As microtubules are present in this case, a role of error correction is likely. This line of reasoning is supported by our data on chromatin movement, where the reduced mobility of chromatin upon binucleine 2 addition renders error correction weaker in destabilising attachments, providing a plausible explanation for the accelerated mitotic exit upon premature sister chromatid separation.

4.1.6 Types of Attachments Upon Loss of Cohesin

Taken together, our analyses suggest that kinetochore-microtubule attachments become progressively stabilised in cells subjected to premature sister chromatid separation. Three explanations appear most plausible for this: As previously shown for cells undergoing mitosis with un-replicated chromosomes, stable attachments could arise from the accumulation of merotelic attachments [228]. Alternatively, attachments could become stabilised as a consequence of tension generated in the absence of cohesin, such as by cytoplasmic drag on chromatids. Lastly, attachments could become stabilised abnormally in the absence of maximal tension.

To distinguish between these scenarios, we analysed the attachments in more detail. Brains expressing the chromatin marker HisH2Av-mRFP1 and the kinetochore marker Cid-EGFP were incubated with $1:10000$ Sir-Tub probes in order to visualise microtubules, and subsequently squashed for imaging. We quantified the prevalence of different configurations of attachments in cells sampled randomly between NEBD and NEF. Thus, prevalence represents a mean frequency of observation throughout mitosis (figure 4.4 A). To classify types of attachments, we distinguish between unattached kinetochores, end-on attachments, lateral attachments and merotelic attachments.

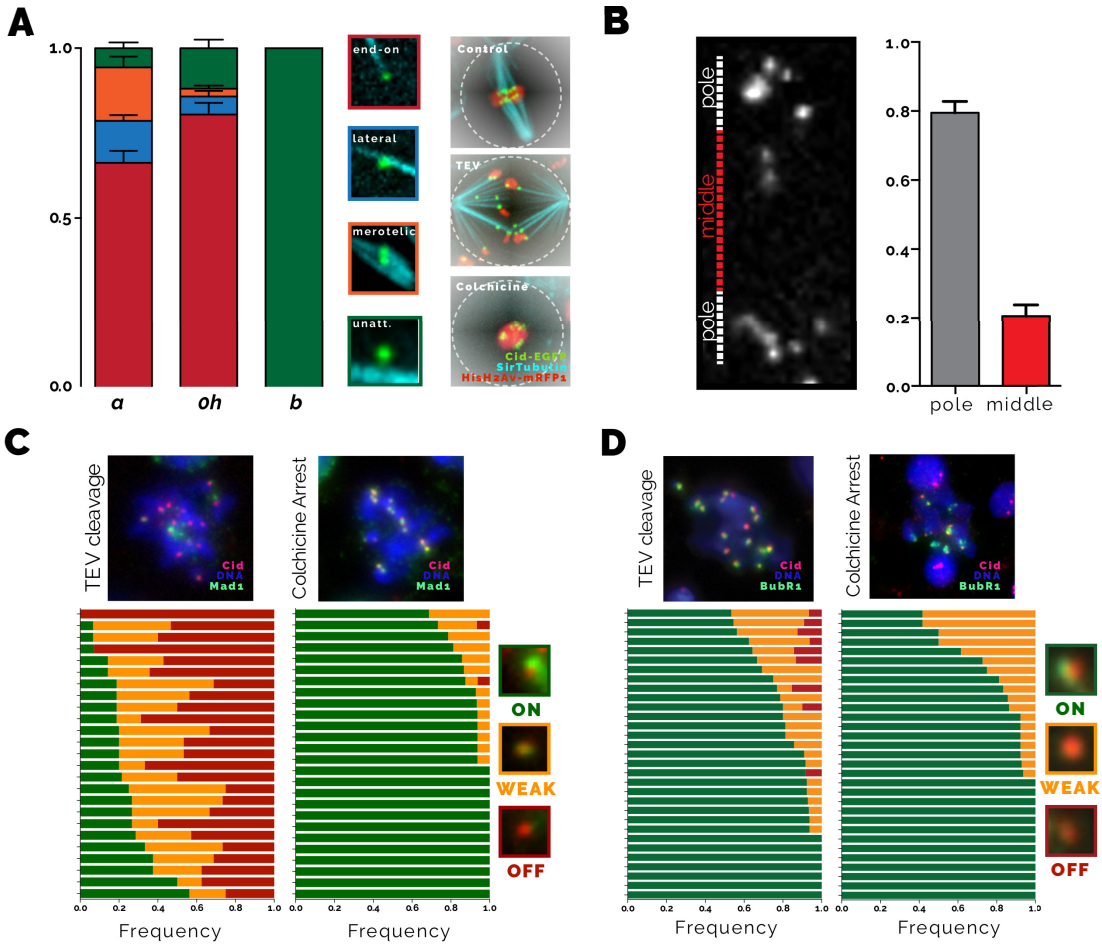


Figure 4.4: Characterisation of Attachment-Types - (**A**) Frequency of kinetochore attachment observed after cohesin cleavage; brains expressing HisH2Av-mRFP1 (red) and Cid-EGFP (green) were shortly incubated with $1:10,000$ Sir-Tub probes (Cyan) before brain squash; graph shows average attachment profile for controls (prometaphase and metaphase cells), cohesin-cleaved and colchicine-treated NBs (n>25 NBs; (N=3)). (**B**) Centromere distribution at the time of mitotic exit in cohesin-cleaved NBs; for each image, the segregation plane, determined based on the two most distal centromeres, was divided into two equally-sized regions as exemplified. (**C**) and (**D**) Spreads from larval brains from colchicine-arrested and cohesin-cleaved cells immunostained for Mad1 (**C**) and BubR1 (**D**) (in green). DNA is shown in blue and CID in red. Graph depicts relative frequency of kinetochores containing no, low, and high levels of Mad1/BubR1. Note that in contrast to colchicine-arrest, cohesin cleavage leads to reduced levels of Mad1 at kinetochores and a high asynchrony between the different analysed cells (each at random points of the arrest). In contrast, BubR1 is mostly present at significant levels in all kinetochores of the analysed cells. *Figure adapted from [225].*

In cells treated with colchicine (***b***), 100% of kinetochores were unattached, whereas in cells undergoing unperturbed mitosis (***Oh***) on average 80% of kinetochores were attached in an end-on manner, 12% of kinetochores were unattached, 6% of kinetochores were laterally attached, and 2% showed merotelic attachments. In contrast, in cells subjected to premature cleavage of cohesin (***a***) 66% of kinetochores showed end-on attachments, 6% of kinetochores were unattached, 12% of kinetochores showed lateral attachment and 16% of attachments were merotelic. Thus, compared to unperturbed mitosis, unattached kinetochores and end-on attachments were less prevalent, whereas merotelic and lateral attachments were more frequent under TEV treatment.

4.1.7 Chromatin Positioning

The relatively low proportion of merotelic attachments in the case of premature sister chormatid separation suggests that the accumulation of merotelic attachments is not the major contributor to the stabilisation of attachments. However, were merotelic attachments to accumulate over time, they could explain the progressive stabilisation of attachments. In this case, the accumulation of merotelic attachments would position the chromatin in the vicinity of the segregation plane upon anaphase onset. To test this hypothesis, we quantified the positions of centromeres at mitotic exit by means of live-cell imaging on cells subjected to premature cohesin cleavage (***a***, $n = 20, N = 4$) (figure 4.4 B). We found that 80% of centromeres were positioned close to the spindle poles, whereas 20% were indeed positioned in the proximity of the segregation plane. Furthermore, the centromeres positioned close to the segregation plane appeared stretched, consistent with the idea of being bound to both poles of the mitotic spindle. Thus, the accumulation of merotelic attachments towards mitotic exit is not a key driving force in the stabilisation of attachments observed in cells undergoing mitosis with separated sister chromatids.

4.1.8 Localisation of Mad2 and BubR1

To further corroborate these findings, we monitored levels of Mad2-EGFP and BubR1-EGFP on kinetochores over time. Due to constraints in the imaging protocol and the short duration of prometaphase in control cells, my collaborators were unable to measure levels of Mad2-EGFP and BubR1-EGFP in control cells. However, it is well established that Mad2 localises to unattached kinetochores and is quickly removed

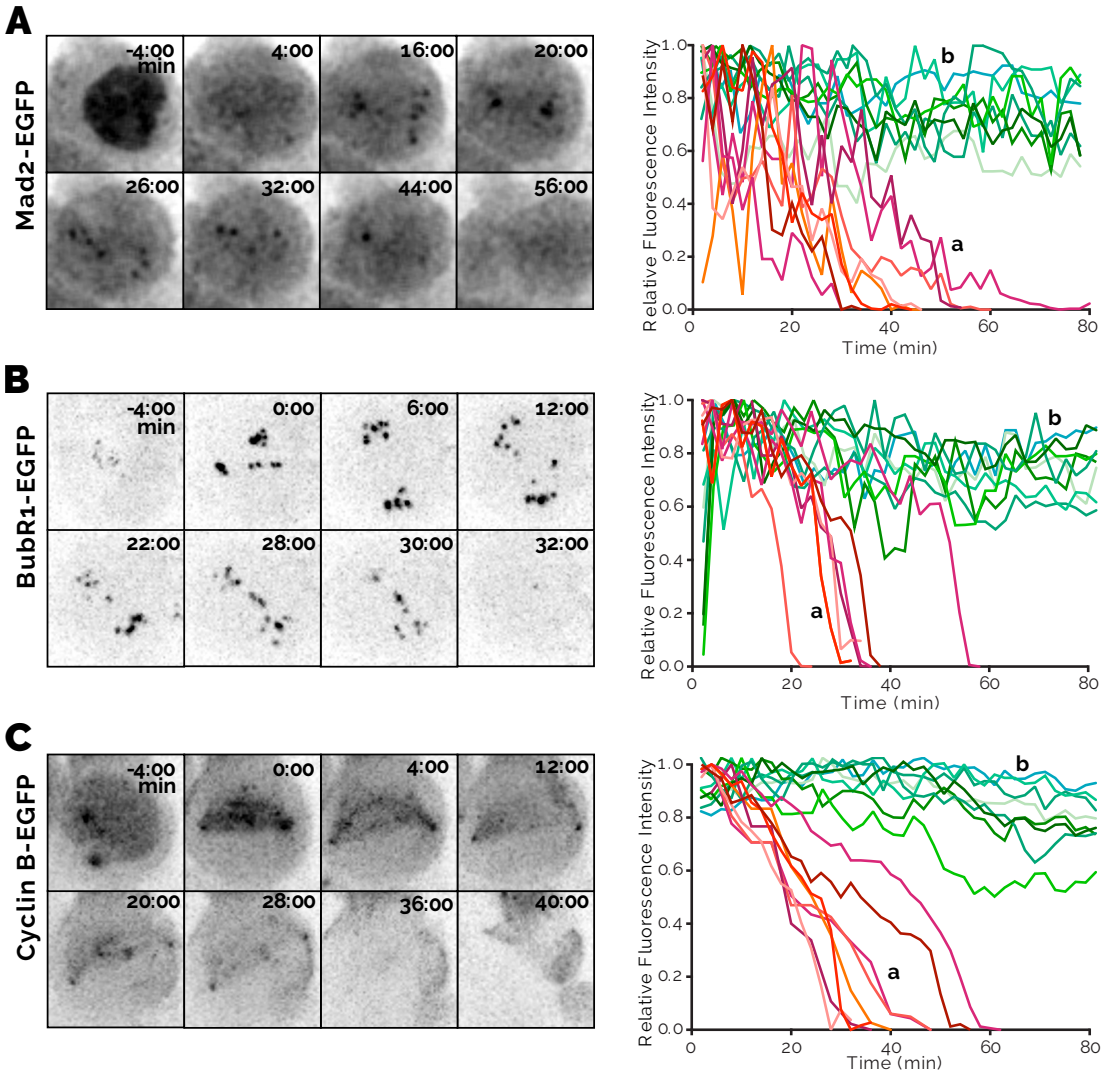


Figure 4.5: Timecourse-Imaging of Mad2, BubR1 and Cyclin B - (**A-C**) Stills from live-cell imaging of Mad2-GFP (**A**), BubR1-GFP (**B**) and cyclin B-GFP (**C**) during the mitotic delay induced by cohesin cleavage. Times are relative to NEBD; scale bar = 5 μm. The graphs depict relative fluorescence intensity of Mad2-GFP (**A**), BubR1-GFP (**B**) and cyclin B-GFP (**C**) in cohesin cleavage (red) and colchicine-arrested (green) cells, normalised to the maximum value within each dataset. Times are relative to NEBD; *Figure adapted from [225].*

upon formation of end-on attachments [229, 230]. On the other hand, BubR1 localises to the kinetochore, but is retained on kinetochores until they come under tension through the formation of amphitelic attachments [229, 230].

Our experimental data (figure 4.5 A,B) show that kinetochores show significant levels of Mad2-EGFP and BubR1-EGFP right after cleavage of cohesin. However, the maximal level observed after cohesin cleavage is about one third of the level observed upon colchicine treatment. Whereas Mad2-EGFP levels show a steady decline over time, and completely disappear shortly before the onset of anaphase, levels of BubR1-EGFP decay more slowly, and show a pronounced step-like decline concomitant with anaphase onset. Conversely, in cells treated with colchicine the localisation of Mad2-EGFP and BubR1-EGFP is stable over time, consistent with a robust checkpoint arrest. Strikingly, Mad2-EGFP levels fluctuate heavily over time, whereas the BubR1-EGFP signal shows little variation.

The distinct localisation patterns observed for Mad2-EGFP and BubR1-EGFP support the idea that attachments become abnormally stabilised throughout the progression through mitosis. Furthermore, the fluctuations in Mad2-EGFP levels at kinetochores suggest that individual chromatids undergo repeated cycles of attachment and detachment, consistent with the kinetochore tracking data presented above.

4.1.9 Degradation of Cyclin B

What can explain this unexpected stabilisation of attachments upon premature loss of cohesin, and what are its implications on checkpoint signalling? Recent findings suggest that the inhibitory activity of the checkpoint is proportional to its signalling strength [216, 217]. Therefore, gradual stabilisation of attachments over time could lead to a gradually reduced capacity of the checkpoint to produce MCC, and concomitant partial activation of APC/C.

To test a possible activation of APC/C we monitored levels of cyclin B-GFP over time, comparing its degradation pattern upon premature cohesin cleavage with control cells and cells treated with colchicine (figure 4.5 C). In the presence of colchicine, cyclin B levels remain high throughout the imaging period of $1.5\ h$ and fluctuate around the level observed at NEBD. In control cells, cyclin B degradation follows a characteristic sigmoidal pattern: For the initial $5\ min$ after NEBD, cyclin B levels remain at the level measured at NEBD, before the degradation of cyclin B accelerates and it becomes rapidly degraded. Conversely, cells subjected

to premature loss of sister chromatid cohesion show a bi-phasic degradation pattern, characterised by significant initial degradation of cyclin B at an intermediate rate followed by an accelerated degradation concomitant with anaphase onset.

Cyclin B is a key substrate of APC/C:Cdc20 and protected from degradation by the mitotic checkpoint. Our findings suggest that premature loss of sister chromatid cohesion and the concomitant progressive stabilisation of attachments lead to a premature, partial activation of APC/C that drives the partial degradation of cyclin B prior to anaphase onset.

4.2 Model

The activity of cyclin B:CDK1 is crucial in maintaining the mitotic state, and cyclin B:CDK1 potentially influences checkpoint signalling at the level of error correction and the enforcement mechanism. To investigate how the partial degradation of cyclin B observed upon premature sister chromatid separation affects checkpoint signalling, we formulated three instances of a mathematical model of checkpoint signalling that incorporate different degrees of feedback control within the checkpoint control mechanism, and contrast simulations of these models with the experimental data presented above.

The models share a common structure expressed by the *core* model, which is composed of two modules: The error correction module (EC) describes the formation of attachments between microtubules ($[MT]$) and microtubule binding sites on kinetochores ($[MBS]$); the destabilisation of attachments by centromeric Aurora B ($[AurB_c]$), which is attenuated by tension the kinetochore; and the effect of cohesin on tension formation and Aurora B localisation. In turn, the checkpoint enforcement module (CE) describes APC/C-dependent degradation of cyclin B, and the inhibition of this process by MCC that is produced at unattached microtubule binding sites.

In the *core* model, signalling of the checkpoint enforcement module is strictly downstream of the error correction module, and we assume that the activity of cyclin B:CDK1 does not influence the rate of MCC-production. In the *single-feedback* model, we consider the role of cyclin B:CDK1 and Aurora B in the assembly of MCC, introducing a double negative feedback loop in the checkpoint enforcement mechanism and strengthening the coupling between the error correction module and the checkpoint enforcement module through the introduction of the Aurora B effect on MCC assembly. The *dual-feedback* model builds on the *single-feedback*

model: We assume that the error correction and checkpoint enforcement modules mutually activate each other by introducing a cyclin B:CDK1-dependency in the activation of Aurora B.

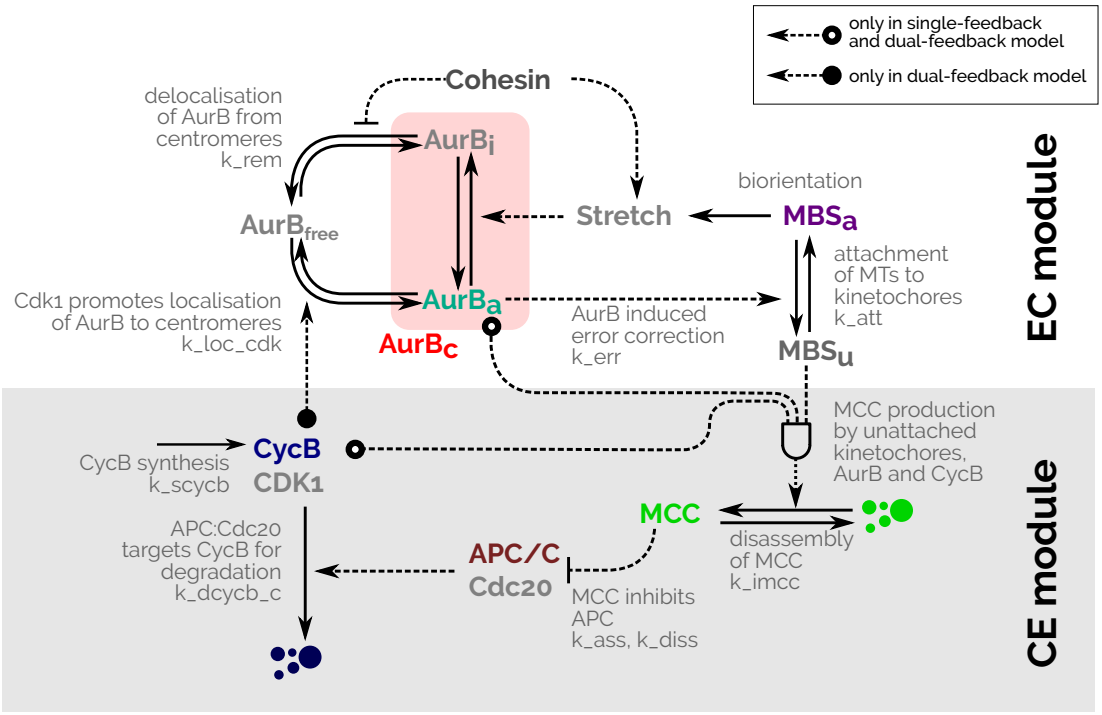


Figure 4.6: Wiring Diagram of the Model - Detailed molecular interaction network of EC and CE: The EC module operates at centromeres/kinetochores and it uses Aurora B activity to destabilise MT-KT attachments and thereby generates unattached MT-binding sites at KTs (MBSu) as an output of the EC module. Unattached MT binding sites of the KT signal to the SAC module by catalysing the production of Mitotic Checkpoint Complexes (MCC). MCC inhibition of APC/C-dependent cyclin B degradation regulates CDK1 activity, which is the output of the CE module. By promoting localisation of Aurora B at centromeres, CDK1 activity represents an input of EC. *Figure adapted from [225].*

4.2.1 Construction

Figure 4.6 shows the qualitative interactions underlying the error-correction (EC) and checkpoint effector (CE) modules. These were first converted into reaction-rate equations in the form of a system of coupled ordinary differential equations (ODEs), and parametrised for model simulations to reproduce the timing of mitosis and degradation patterns of cyclin B observed for cells undergoing unperturbed mitosis, as well as for cells treated with colchicine. To capture the inherent stochasticity in the formation of attachments, I then converted the deterministic,

ODE-based model into a stochastic model, and compared simulations for cells undergoing mitosis upon premature cleavage of cohesin with the corresponding experimental data.

In the following section, I will first discuss in detail the assumptions that informed the construction of the model using the deterministic model, and conclude with an account of how the deterministic model was converted into a stochastic model.

4.2.1.1 Aurora B Localisation

I assume that a major determinant of Aurora B activity is the localisation of Aurora B molecules at kinetochores. Thus, I consider Aurora B molecules ($[AurB_T]$) distributed between two forms: centromeric ($[AurB_c]$) and other cellular compartments ($[AurB_T] - [AurB_c]$). The models describe the localisation of Aurora B at centromeres ($[AurB_c]$) as a combination of cyclin B:CDK1-independent ($k_{loc} = 3\ min^{-1}$) and -dependent ($k_{loc,CDK} = 5\ min^{-1} AU^{-1}$ only in the *single-* and *dual feedback* models) processes.

$$\frac{d[AurB_c]}{dt} = (k_{loc} + k_{loc,CDK} \cdot [CDK1]) \cdot ([AurB_T] - [AurB_c]) - k_{rem} \cdot [AurB_c] \quad (4.1)$$

$[AurB_c]$ dissociation from centromeres follows first order kinetics with a rate constant of $k_{rem} = 2.5\ min^{-1}$ and $k_{rem} = 10\ min^{-1}$ in the presence and in the absence of cohesins, respectively. The rationale behind the choice of a higher rate in the absence of cohesin was to efficiently recapitulate our observation that the removal of cohesin disrupts the localisation, resulting in a 50% reduction in the levels and activity of Aurora B at the centromere. The kinetic parameters of AurB localisation are summarised in table 4.2. In case of CDK1-driven localisation (*dual-feedback model*), the steady state fraction of AurB at centromeres during prophase ($[CDK1] = 1$) is given by

$$\frac{[AurB]_c}{[AurB_T]} = \frac{k_{loc,CDK} \cdot [CDK1]}{k_{loc,CDK} \cdot [CDK1] + k_{rem}} \quad (4.2)$$

This corresponds to 0.666 and 0.333 in the presence and in the absence of cohesins, respectively. We choose the total level of $[AurB]$ to be 1.5 AU. Consequently, the level of the centromeric pool ($[AurB_c]$) is 1 AU at the beginning of normal mitosis.

4.2.1.2 Attachments

The rate of MT-KT attachments is proportional to MT-density (represented by the parameter $[MT]$) and the number of unattached MT binding sites at kinetochores ($[MBS_T] - [aMBS]$):

$$\frac{d[aMBS]}{dt} = k_{att} \cdot [MT] \cdot ([MBS_T] - [aMBS]) - k_{err} \cdot \frac{[AurB_a]}{1 + [BN2]} \cdot [aMBS] \quad (4.3)$$

Here, $[BN2]$ corresponds to the concentration of AurB inhibitor (binucleine 2) relative to its IC50 value. Using 20-fold AurB inhibition ($[BN2] = 19$) in the *dual-feedback model* reduces the length of TEV-induced mitosis ($\simeq 45\ min$) to about $9\ min$ (simulation not shown), consistent with the corresponding experiment.

4.2.1.3 Aurora B activity

To capture a tension-dependent effect in our model, we assume that only a fraction of centromeric AurB ($[AurB_a]$) can destabilise MT-KT attachments at kinetochores ($[aMBS]$). The "active" form of Aurora B ($[AurB]_a$) is reduced by MT-KT attachments ($[aMBS]$) according to a Hill-function ($N = 4$, $J = 0.4$).

$$[AurB]_a = [AurB_c] \cdot (1 - Stretch \cdot \frac{[aMBS]^N}{J^N + [aMBS]^N}) \quad (4.4)$$

The value of the $Stretch$ parameter is chosen to be one in the presence of sister chromatid cohesion. Thus, we assume that amphitelic attachments between sister chromatids are formed efficiently, and stabilised effectively through cooperative action of neighbouring microtubule attachment sites.

To model cells undergoing mitosis upon precocious sister chromatid separation, we assume that the value of $Stretch$ is reduced considerably to $Stretch = 0.15$. This choice of parameter is based on our findings that single chromatids were often found attached to the spindle, as well as on the potential role of intra-kinetochore stretch in the termination of checkpoint signalling [105, 106, 231, 232].

The rate constant of MT-KT attachment was chosen to be of similar magnitude ($k_{att} = 0.5\ min^{-1}$) to detachment ($k_{err} = 0.66\ min^{-1}AU^{-1}$), which guarantees that kinetochores only become saturated with microtubule attachments if the activity of Aurora B is reduced through the Stretch-dependent effect. In order to simulate the effect of spindle disruption by colchicine, MT was set to zero.

4.2.1.4 APC/C

The cellular level of APC/C is assumed to be constant ($[APC_T] = 1\ AU$) during mitosis and distributed between active, free ($[APC]$) and inactive, MCC-bound ($[APCMCC]$) forms. The level of active $[APC]$ is decreased by rapid $[MCC]$ binding and increased by dissociation and dis-assembly of $[MCC]$ [214].

$$[APCMCC] = [APC_T] - [APC] \tag{4.5}$$

$$\frac{d[APC]}{dt} = (k_{diss} + k_{imcc}) \cdot [APCMCC] - k_{ass} \cdot [APC] \cdot [MCC_{free}] \tag{4.6}$$

Association ($k_{ass} = 200\ min^{-1}AU^{-1}$) and dissociation ($k_{diss} = 0.01\ min^{-1}$) rate constants are chosen to describe a tight binding of MCC and APC/C [233]. The level of the limiting MCC component (labelled by $[MCC_T]$) is assumed to be in excess over APC/C ($[MCC_T] = 1.2 > [APC_T]$), which is a necessary requirement for stoichiometric inhibition [234].

4.2.1.5 MCC

The assembled MCC could be associated with APC/C ($[APC_T] - [APC]$) or present in a free form ($[MCC_{free}]$). $[MCC_{free}]$ is produced by unattached KTs from the pool of free MCC sub-units at a rate proportional to the level of the limiting component ($[preMCC]$). In the two feedback-models, the rate of production of $[MCC_{free}]$ is proportional to both $[AurB_a]$ and $[CDK1]$ activities, because these kinases activate checkpoint proteins at the kinetochore. The level of $[MCC_{free}]$ is decreased by binding to APC/C (k_{ass}) and by dis-assembly of the complex ($k_{imcc} = 0.5\ min^{-1}$) and it is increased by dissociation from the MCC:APC complex (k_{diss}):

$$[preMCC] = [MCC_T] - [MCC_{free}] - [APC_T] + [APC] \tag{4.7}$$

$$[AurB_{a,EF}] = \frac{[AurB_a]/(1 + [BN2])}{J_{amc} + [AurB_a]/(1 + [BN2])} \tag{4.8}$$

$$\begin{aligned}\frac{d[MCC_{free}]}{dt} = {} & (k_{amcc} + k_{amcc,kin} \cdot [CDK1] \cdot [AurB_{a,EF}]) \cdot [uMBS] \cdot [preMCC] \\ & + k_{diss} \cdot [APCMCC] - k_{ass} \cdot [APC_{free}] \cdot [MCC_{free}] - k_{imcc} \cdot [MCC_{free}]\end{aligned} \tag{4.9}$$

The kinetic parameters of MCC production are summarised in table 4.2.

Table 4.2: Kinetic parameters used in the three model instances

parameter	basic model	single-feedback model	dual-feedback model
$k_{loc}(min^{-1})$	3	3	0
$k_{loc,CDK}(min^{-1}AU^{-1})$	0	0	5
$k_{rem}(min^{-1})$	2.5, 10 (TEV)	2.5, 10 (TEV)	2.5, 10 (TEV)
$k_{err}(min^{-1}AU^{-1})$	0.66	0.66	0.66
N	4	4	4
J	0.4	0.4	0.4
$k_{att}(min^{-1})$	0.5, 0 (Colch)	0.5, 0 (Colch)	0.5, 0 (Colch)
$k_{ass}(min^{-1}AU^{-1})$	200	200	200
$k_{diss}(min^{-1})$	0.01	0.01	0.01
$k_{amcc}(min^{-1}AU^{-1})$	10	0	0
$k_{amcc,kin}(min^{-1}AU^{-3})$	0	15	15
$k_{imcc}(min^{-1})$	0.5	0.5	0.5
J_{amc}	0.1	0.1	0.1
$k_{scycb}(AUmin^{-1})$	0.004	0.004	0.004
$k_{dcycb}(min^{-1})$	0.004	0.004	0.004
$k_{dcycb,apc}(min^{-1}AU^{-1})$	0.5	0.5	0.5
$[APC_T]\ (AU)$	1	1	1
$[MCC_T]\ (AU)$	1.2	1.2	1.2
$[AurB_T]\ (AU)$	1.5	1.5	1.5

The low sensitivity of the checkpoint enforcement mechanism to Aurora B inhibition (our data, figure 4.3 E and [126]) suggests an efficient activation of checkpoint-proteins by Aurora B, which we describe with a hyperbolic ("saturating") function using a small "saturation-constant" ($J_{amc} = 0.1$). Therefore after a 20-fold ($[BN2] = 19$) inhibition the residual 5% activity of Aurora B kinase could maintain a third of the MCC production rate. These parameter values reduce the length of colchicine-induced mitotic arrest upon Aurora B inhibition, to about $60min$ (simulation not shown) in the dual-feedback model, consistent with the corresponding experiment.

4.2.1.6 Cyclin B and CDK1

Cyclin B ($CycB$) is synthesised at a constant rate ($k_{scycb} = 0.004\ AUmin^{-1}$) and associates rapidly with CDK1 present in excess, therefore the level of cyclin B determines

CDK1 activity via

$$[CDK1] = \frac{CycB}{1 + [RO]} \tag{4.10}$$

where $[RO]$ corresponds to the concentration of CDK inhibitor (roscovitine) relative to its IC50 value. CDK1 is inactivated by cyclin B degradation which has a small, APC/C-independent ($k_{dcycb} = 0.004\ min^{-1}, t_{\frac{1}{2}} \simeq 170\ min$) and a large, APC/C-dependent rate constant ($k_{dcycb,apc} = 0.5\ min^{-1}AU^{-1} = t_{\frac{1}{2}} \simeq 1.4\ min$):

$$\frac{d[CycB]}{dt} = k_{scycb} - (k_{dcycb} + k_{dcycb,apc} \cdot [APC]_{free}) \cdot [CycB] \tag{4.11}$$

The steady state level of cyclin B in the absence of APC/C activity (interphase) is $\frac{k_{scycb}}{k_{dcycb}}$, which we set to one by choosing the rate of cyclin B synthesis (k_{scycb}) identical to k_{dcycb} ($k_{dcycb} = 0.004\ min^{-1}$; $k_{scycb} = 0.004\ min^{-1}AU$).

Interactive Notebook - Deterministic Model (static version)

4.2.2 Implementation

The model was simulated by Gillespie's Stochastic Simulation Algorithm (SSA)[1] after converting the rate of elementary reactions into propensity functions [236].

The initial conditions of numerical simulations are obtained from a steady state calculated from the corresponding deterministic model without MT-binding to KTs ($[MT] = 0$) and lack of APC/C activity ($k_{dcycb,apc} = 0\ min^{-1}AU^{-1}$), which corresponds to an interphase situation. The start of numerical simulations corresponds to nuclear envelope breakdown when the mitotic spindle starts to capture kinetochores and APC/C is activated by cyclin B:CDK1, which is captured by setting $[MT] = 1$ and $k_{dcycb,apc} = 0.5\ min^{-1}AU^{-1}$.

The stochastic simulations follow the number of molecules in a total volume (V_T) of 10^4 units. V_T is divided into a smaller (V_x) and a larger (V_{nx}) compartment in order to follow a single sister kinetochore of a chromosome (normal mitosis)/sister chromatid (TEV-induced mitosis) and the collection of all the kinetochores within the cell, respectively. Since Drosophila somatic cells have 16 sisterchromatids, the small volume is V_x = V_T/16 = 625 units while V_{nx} = 15VT/16 = 9375 units. The components of the checkpoint enforcement module are assumed to be more abundant than the components of error correction. Since we set the level of $[APC_T] = 1\ AU$ and $[MCC_T] = 1.2\ AU$, these molecules are represented in the volume of $10^4\ units$

[1] For a recent review of the algorithm and its applications please refer to [235].

by 10^4 copies and $1.2 \cdot 10^4$ copies, respectively. The choice of $k_{scycb} = k_{dcycb}$ sets the initial number of cyclin B molecules to 10^4. Zero- and second-order rate-constants of the deterministic (concentration) models were scaled by volume and relative protein abundance.

We assume 11 microtubule-binding sites (MBS) on each sister kinetochore [237], which gives 176 binding sites on 16 sister kinetochores; therefore we set the parameter $[MBS_{tot}] = 0.0176$. By choosing $[AurB_T] = 0.15\ AU$ the total number of Aurora B molecules is $1.5 \cdot 10^3$, which are distributed between centromeric and free pools. At the beginning of mitosis, two-thirds ($\sim 10^3$) and one-third (~ 500) AurB molecules are bound to centromeres in the presence and in the absence of cohesins, respectively (see above). These centromeric AurB molecules are distributed randomly among eight chromosomes and 16 sisterchromatids. Therefore on average $\sim 60 (= 1000/16)$ and $\sim 30 (= 500/16)$ AurB molecules are acting on a single sister kinetochore in the presence and in the absence of cohesins, respectively.

4.2.3 Simulations

Figure 4.7 shows representative stochastic simulations for the three model instances (A: core model, B: single-feedback model, C: dual-feedback model). Time-course simulations of control cells and cells subjected to premature cohesin cleavage are shown side-by-side. Simulations of the checkpoint enforcement module are shown in the grey boxes on the left hand side of each panel. Corresponding simulations of the error correction module are shown on the right hand side, where the upper pair of plots depicts simulations for an individual kinetochore, and the lower pair of plots shows the global behaviour of the error correction module.

4.2.3.1 Core Model

Interactive Notebook - Core Model (stochastic) (static version)

In this study, the core model constitutes our starting point in the mathematical exploration of signalling dynamics of the mitotic checkpoint. Here (figure 4.7 panel A) - with checkpoint effector signalling strictly downstream of error correction - the behaviour of cells undergoing unperturbed mitosis is nicely recapitulated. The model simulations show a sharp sigmoidal degradation of cyclin B at the meta-to-anaphase transition that corresponds well with our experimental data (figure 4.5

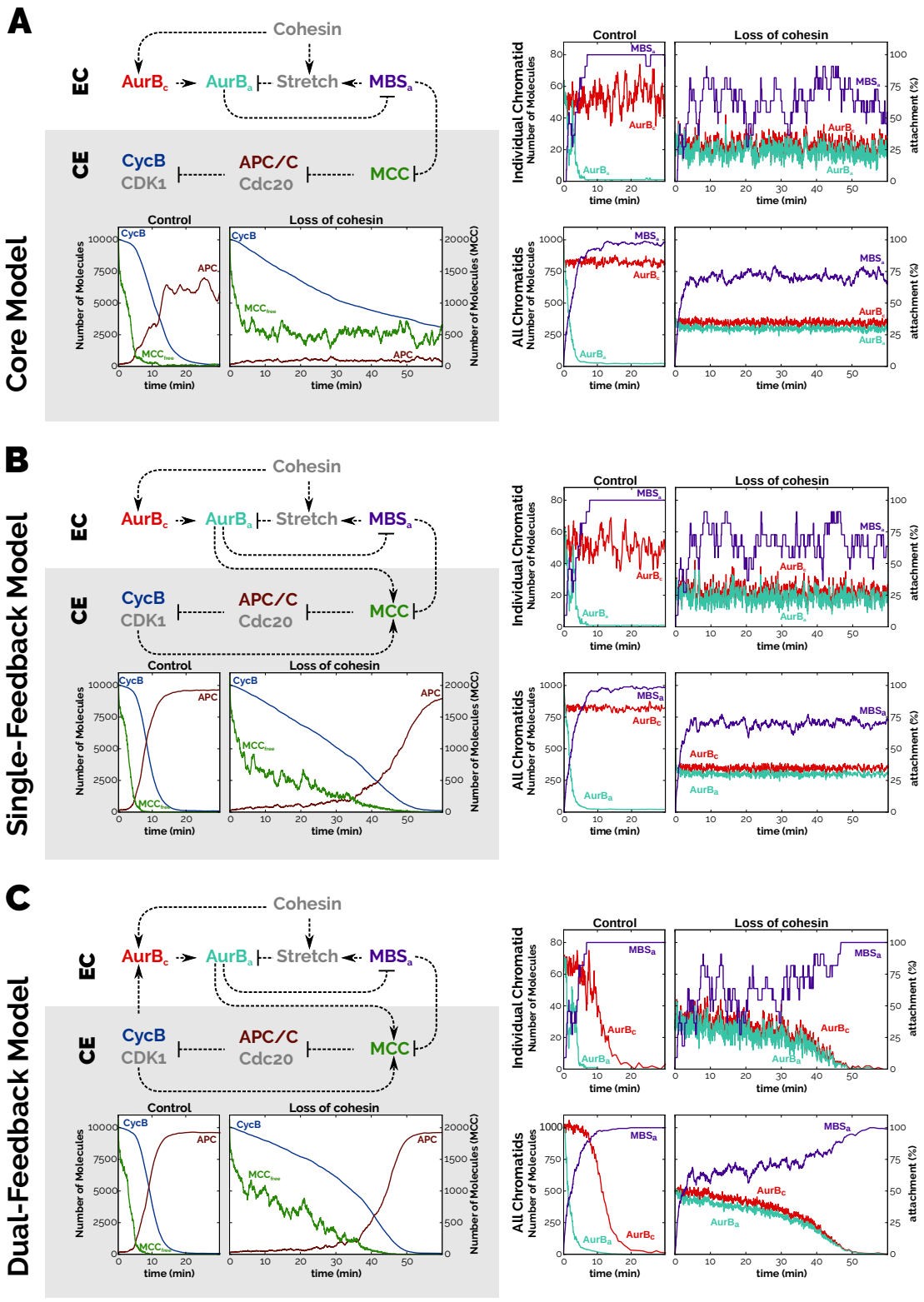


Figure 4.7: Model Simulations - Three different scenarios for the interaction between the CE and EC; each panel shows a molecular-influence diagram (top left), along with stochastic simulations for control and PSCS cells. Simulations show changes of key components of the EC and CE modules over time (t_0 = NEBD). For the EC module, simulations depict the behaviour of an individual chromatid (top) and all chromatids (bottom).

panel C). However, neither the timing of mitosis nor the observed degradation patterns for cyclin B are reproduced accurately in the simulation of cohesin removal. Here, the model predicts a prolonged mitotic arrest and a cyclin B timecourse characterised by slow degradation of cyclin B lacking the pronounced acceleration observed in the experiments. Moreover, simulations of the error correction module show that, overall, 75% of microtubule-binding sites become attached relatively quickly (purple curve, lower sub-panel), yet individual kinetochores show persistent fluctuations in their attachment state (purple curve, upper sub-panel), indicating a sustained activity of the error correction module. As a consequence of the persistent activity of the error correction module, unattached microtubule-binding sites are present in sufficient number to catalyse the production of MCC and inhibit APC/C.

4.2.3.2 Single-Feedback Model

> **Interactive Notebook - Single-Feedback Model (stochastic)** (static version)

The experimental data for cyclin B degradation (figure 4.5 panel C) in cells undergoing mitosis upon premature cleavage of cohesin show a clear bi-phasic degradation pattern characterised by an initial phase of slow degradation, followed by a distinct acceleration and faster degradation that presumably coincides with a switch-like activation of APC/C. To account for this behaviour, I introduced a CDK1- and Aurora B-dependency in the assembly of MCC. To this end, only the parameters governing MCC assembly had to be changed, maintaining good agreement with the experimental controls (figure 4.7 panel B). The kinase-independent rate constant of MCC assembly was set to zero, whereas the rate constant corresponding to the kinase-dependent reaction was set to 15 $min^{-1}AU^{-1}$.

Notably - whereas timing and pattern of cyclin B degradation were largely unchanged for control cells - the introduction of the feedback in the checkpoint enforcement module resulted in a considerably more stable activation of APC/C at the onset of anaphase (dark red curves in figure 4.7 panels A and B). Moreover, by introducing feedback control within the checkpoint enforcement module, model simulations were able to recapitulate the temporal pattern of cyclin B degradation observed in cells subjected to premature cleavage of cohesin. However, since the introduced effects act downstream of error correction, the dynamics within the EC were unaffected: Globally, an attachment of 75% of microtubule binding sites was

reached within 5 min. However, at individual kinetochores, the microtubule binding sites continued to fluctuate between attached and unattached states.

4.2.3.3 Dual-Feedback Model

Interactive Notebook - Dual-Feedback Model (stochastic) (static version)

The experimental characterisation of kinetochore-microtubule attachments upon premature cleavage of cohesin (figure 4.3) clearly suggests that even in the absence of inter-kinetochore tension, attachments become gradually stabilised, leading to the accumulation of stable end-on attachments. Feedback control between the error correction and checkpoint effector subsystems would be a plausible scenario to account for this observation. To express this effect in the context of the present mathematical model, I rendered the localisation of Aurora B dependent on CDK1 activity by setting the rate constant for the constitutive localisation of Aurora B to the centromere to zero, and increasing the rate constant for the corresponding CDK1-dependent reaction to 5 $min^{-1}AU^{-1}$.

Thus parametrised, the agreement of simulations with control data was retained, whereas the capacity of the model to capture the behaviour of TEV-treated cells was greatly improved (figure 4.7 panel C): The feedback between the two subsystems enhanced the bi-phasic character of the degradation pattern observed in the cyclin B simulations. Furthermore, simulations of the error correction module were able to recapitulate the progressive stabilisation of kinetochore-microtubule attachments. The simulation of a sub-volume corresponding to an individual kinetochore reveals that the feature of fluctuating attachment states is indeed retained in this model. However the gradual degradation of cyclin B driven by basal activity of APC/C slowly reduces the pool of centromeric Aurora B. In turn, this gradually reduces the pool of Aurora B that can act in error correction, dampening the fluctuations, until attachments become fully stabilised.

4.2.4 Model Analysis

4.2.4.1 The Effect of Stretch

The formulation of the tension-dependence in the error correction module of the model gives the $Stretch$ parameter special importance. To ensure robustness of

any predictions formulated on the basis of the model, I performed a series of stochastic simulations to compare the dynamics of cyclin B degradation and APC/C activation for different values of the stretch parameter (figure 4.8).

Leaving the parameter-set otherwise unchanged, varying the parameter in increments of 0.2 shows that the sustained mitotic arrest in the TEV-cleavage case is a robust interpretation of the core-model simulations if cohesin cleavage in TEV-treated cells results in a reduction of tension of more than 20%. For the single-feedback model, varying the stretch parameter influences the timing of mitosis, and the degradation only shows a distinct bi-phasic character for parameter-values below 0.2. Similarly, timing of mitosis is strongly affected by the stretch parameter in the dual feedback model. However, the bi-phasic character of the cyclin B degradation patterns remains more pronounced for higher values of the parameter. Interestingly, for this model the effect of inherent stochasticity on mitotic timing becomes stronger with smaller values of stretch, as illustrated by the partially overlapping timecourses corresponding to stretch values of 0.2 and 0.0.

Thus, fundamental predictions of the model are not sensitive to the stretch parameter in an unexpected manner, and consequently assumptions regarding the precise extent of the reduction of tension upon TEV-treatment do not restrict the validity of the model.

4.2.4.2 Cyclin B Degradation Pattern

In the discussion thus far, I have stressed the importance of an agreement between simulated and measured degradation patterns of cyclin B. However, thus far all statements in this context have been purely qualitative. To emphasise the distinct bi-phasic character of the cyclin B degradation patterns observed in the experiment, and directly show the model's agreement with the data, panel B in figure 4.8 shows a comparison of cyclin B degradation rates as a function of cyclin B levels. The red dots and error bars indicate calculated rates from the experimental data, whereas the blue lines depict calculated rates from a simulation. Note the marked increase in the rate of cyclin B degradation for lower levels of cyclin B. This feature is characteristic of a feedback in the underlying control system, for trivial kinetics would predict that the rate of a substrate's degradation decreases monotonically with the concentration of the substrate. Comparison of experimental data and simulations shows that the core model - lacking the said feedback mechanism - fails to recapitulate the experimental data, and indeed cyclin B degradation stops at

0.2 AU, as APC/C does not become activated. Interestingly, even for the single-feedback model, which includes a feedback to explain the acceleration at low cyclin B levels, the agreement between simulation and experiment is only moderate. In the context of the parameter-set, it can be presumed that the sustained destabilisation of attachments prevents a sufficiently sharp activation of APC/C. In comparison, the experimental data are best described by the dual-feedback model.

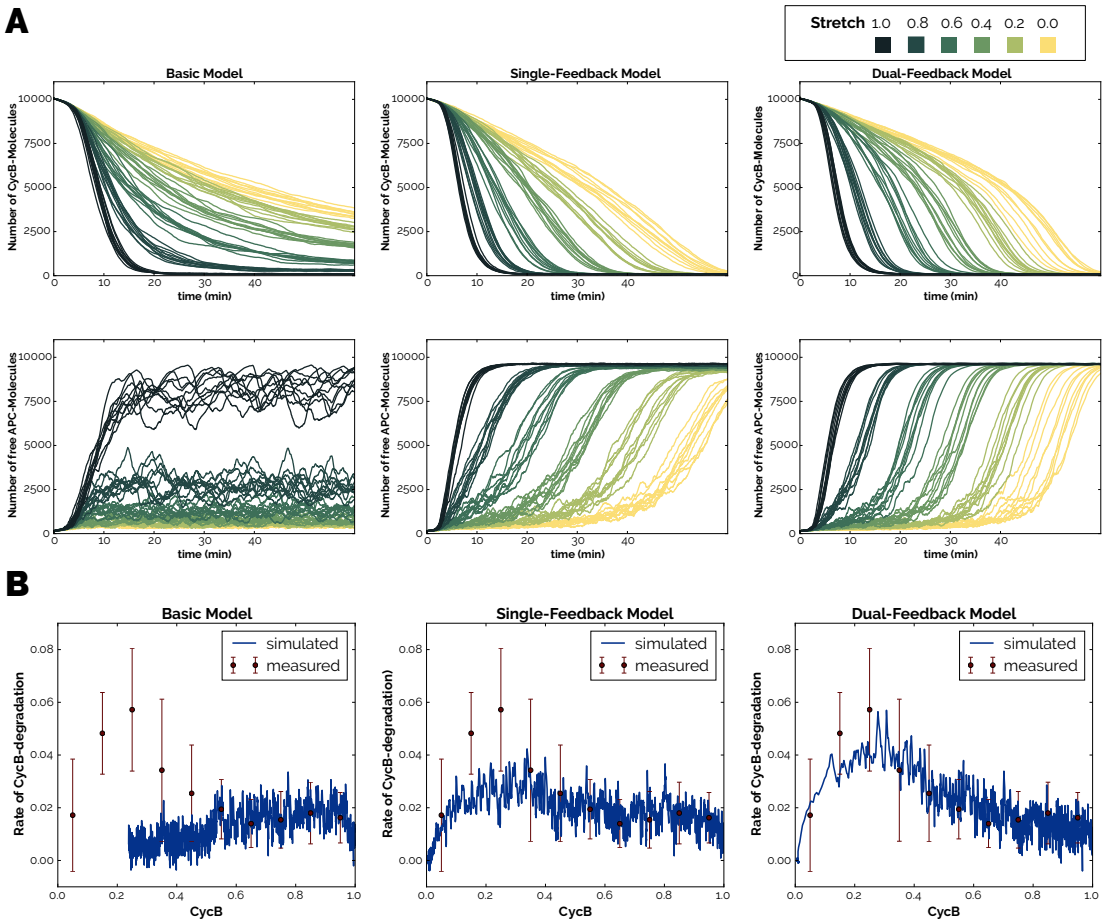


Figure 4.8: Model Analysis - (**A**) Numerical simulations of cyclin B (top row) and APC/C (bottom row) levels at different values of Stretch parameters in absence of cohesion with the three different models. (**B**) Predicted rates of cyclin B degradation after the loss of cohesins in the three model instances (blue lines) are plotted against degradation rates obtained from experimental data (red dots and error bars).

4.2.5 Prediction

Interactive Notebook - Prediction (static version)

In the dual-feedback model, cyclin B:CDK1 mediates the feedback between the checkpoint enforcement module and error correction. As a consequence, a perturbation of the activity of cyclin B:CDK1 would have dramatic consequences on the dynamics of the signalling system. To explore this intuition, I performed a series of simulations varying the activity of CDK1 in the model using the parameter *RO*, representing a CDK1 inhibitor, and analysed these simulations in terms of mitotic timing [1] as a function of maximal CDK1 activity after inhibition.

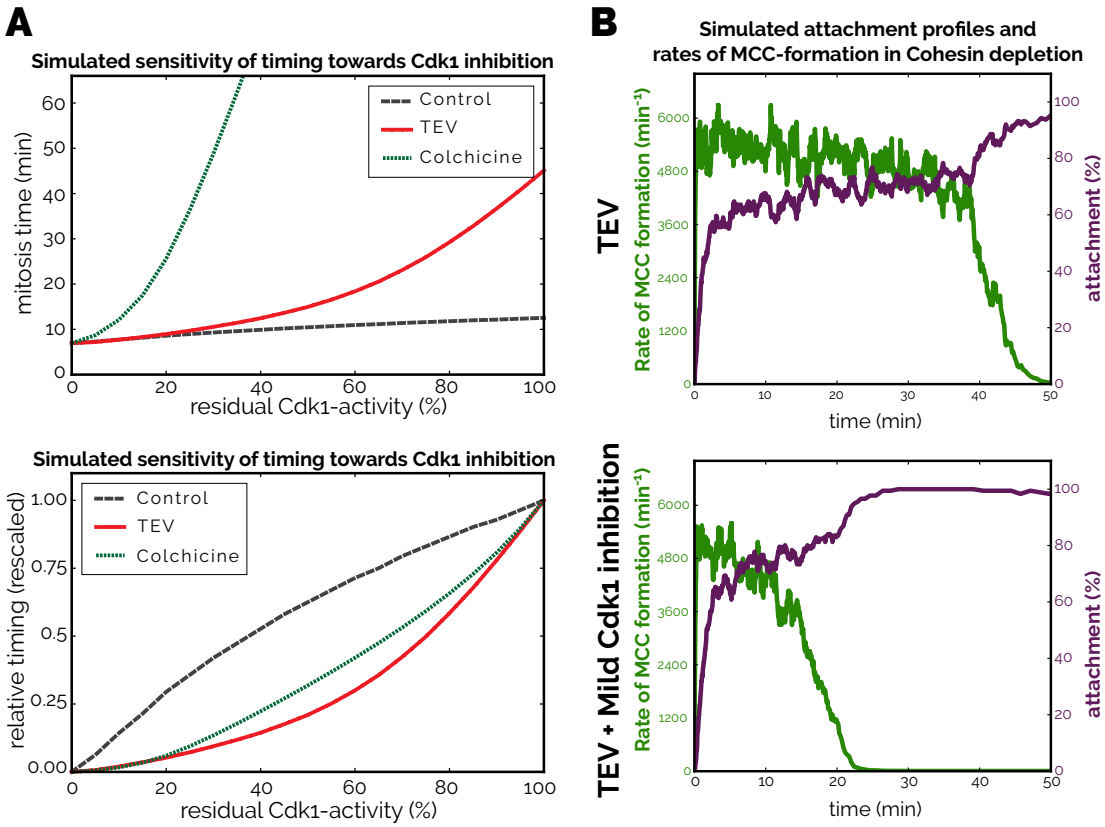


Figure 4.9: Model Predictions - (**A**) Predicted sensitivity of the Control, TEV- and Colchicine-treated cells to CDK1 inhibition. Mitotic exit timing was determined by the time cyclin B level is reduced to 10% of its initial value. (**B**) Comparison of simulated attachment profiles and rates of MCC formation for cohesin-cleaved cells with full CDK1 activity (top) and subject to 30% CDK1 inhibition (bottom).

[1] Here, mitotic timing was defined as the time it took cyclin B to drop below 10% of its level at NEBD.

Panel A in figure 4.9 shows the results of this analysis in absolute and relative terms. The model predicts that the effect of CDK1 inhibition on control cells should be minor, advancing the onset of anaphase by a maximum of 4 minutes for maximal CDK1 inhibition. Conversely, the effect of CDK1 inhibition is predicted to be much more pronounced for TEV- and colchicine-treated cells. For cells undergoing mitosis with precociously cleaved cohesin, the model predicts that the time from NEBD to NEF should be reduced by 50% upon inhibiting 25% of CDK1. Whereas in the case of colchicine-treated cells, 35% inhibition of CDK1 should shorten the time comparably. For both treatments, cells can be said to be hypersensitive to CDK1 inhibition.

Notably, in the case of TEV-treated cells, the model predicts that CDK1 inhibition should accelerate the stabilisation of attachments: Panel B in figure 4.9 shows simulations comparing global attachment profiles and rate of MCC formation for cells undergoing mitosis with precociously cleaved cohesin in the absence and presence of a mild dose (30% inhibition) of CDK1 inhibitor. The simulations clearly demonstrate that use of a mild CDK1 inhibition should accelerate the stabilisation of attachments and advance the concomitant silencing of the checkpoint enforcement module in time.

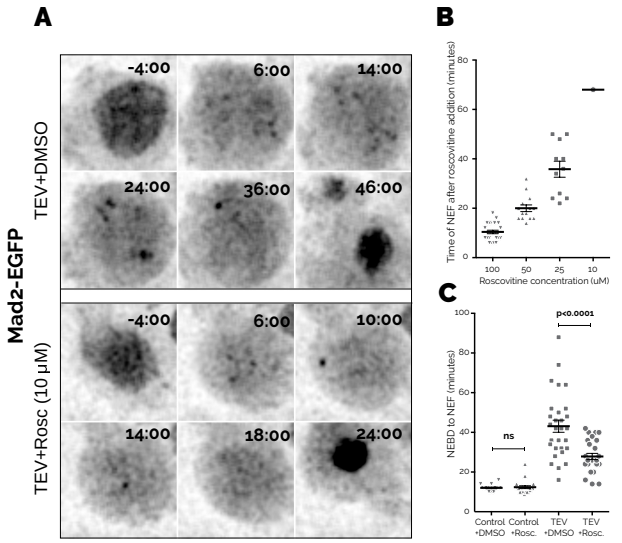


Figure 4.10: Validation of Predictions - (**A**) Stills from live-cell imaging of Mad2-GFP during the mitotic delay induced by TEV-mediated cohesin cleavage with and without incubation with $10 \mu M$ roscovitine. Times are relative to NEBD; scale-bar: $5\ \mu m$; (**B**) Time of mitotic exit observed upon addition of different doses of roscovitine to colchicine-arrested brains within 2 hours. (**C**) Mitosis duration in wild-type and TEV-mediated cohesin cleavage larval neuroblasts, with and without prior incubation with $10\ \mu M$ roscovitine; p, adjusted p-value by One-way ANOVA;

4.2.6 Validation

These insights provided a set of testable predictions that were tested experimentally to validate the mathematical model, and substantiate the claim that feedback between error correction and checkpoint effector accounts for the lack of a robust checkpoint response in the case of cells undergoing mitosis with precociously separated sister chromatids.

To test whether TEV-treated cells indeed display hypersensitivity to CDK1 inhibition, we first tested the response of cells treated with colchicine to different doses of the CDK1-Inhibitor roscovitine (figure 4.10 panel B). Whereas the addition of 100 μM roscovitine efficiently abolished the colchicine-induced mitotic arrest and lead to exit from mitosis within 10 min (24 cells out of 24 exited), only one in 24 cells was observed to exit mitosis within 80 min upon treatment with 10 μM roscovitine. Control cells incubated with 10 μM roscovitine were found to enter and progress through mitosis with unperturbed timing (figure 4.10 panel C). Conversely, the addition of 10 μM roscovitine to TEV-treated cells lead to a significant reduction in the timing of mitosis.

The model postulates that this effect arises from the accumulation of stabilised kinetochore-microtubule attachments and the concomitant decrease in checkpoint effector signalling; in other words, a lower rate of MCC production. To test this prediction experimentally, we used live-cell imaging to compare the localisation of Mad2-EGFP at kinetochores in PSCS-cells treated with either DMSO or 10 μM roscovitine. Representative stills from the live-cell imaging shown in figure 4.10 panel A demonstrate that spots indicating the localisation of Mad2 to unattached kinetochores disappear sooner upon roscovitine treatment, significantly shortening the mitotic delay imposed by the checkpoint.

4.3 Discussion

4.3.1 Findings

This work shows that the mitotic checkpoint fails to respond robustly to the precocious removal of sister chromatid cohesion, which is a major contributor to tension. Using a strategy that combines mathematical modelling and targeted experiments, we show that the poor response of the mitotic checkpoint to removal of cohesin can be attributed to two major findings:

Firstly, attachments of single chromatids to the mitotic spindle are not immediately corrected by the error correction machinery. This finding may be attributed to kinetic effects within the error correction mechanism, and the existence of additional factors - such as polar ejection forces, or cytoplasmic drag on chromatids - that stabilise attachments in the absence of tension. The partial stabilisation of attachments of individual chromatids results in a decreased rate of MCC synthesis, as indicated by the reduced localisation of Mad2 to kinetochores. In turn, the reduced rate of synthesis of MCC results in a compromised efficacy of the checkpoint enforcement mechanism in inhibiting APC/C, which leads to partial degradation of cyclin B.

Secondly, we find that the partial degradation of cyclin B compromises CDK1 activity, which feeds back in to the error correction mechanism, rendering it progressively less effective at destabilising attachments of individual chromatids to the mitotic spindle. This promotes a further loss in efficacy of the checkpoint mechanism, which percolates through the system, until the anaphase inhibitory capacity of the checkpoint is lost completely, and checkpoint control collapses, allowing the onset of an erroneous anaphase.

4.3.2 Interpretation

This coupling of the checkpoint enforcement mechanism and error correction machinery through a positive feedback stabilises the high CDK1 state in cells undergoing unperturbed mitosis. The demonstrated high sensitivity of both subsystems to CDK1 activity may facilitate the efficient and timely inactivation of the checkpoint system prior to anaphase, and is likely to contribute to the avoidance of a reactivation of the checkpoint when cohesion is lost at anaphase onset. However, our experimental system employing artificial cleavage of cohesin prior to mitosis appears to uncover the cost of this marriage of stabilisation of the active state of the checkpoint and its efficient inactivation: a compromised capacity of the system to detect and respond to a situation where the error correction machinery cannot be satisfied, due to the amplification of the kinetically slow response of the error correction throughout the control system.

4.3.3 Limitations

In this study, *Drosophila* neuroblasts were used, and it remains to be shown that our findings equally apply to the mitotic checkpoint in mammalian cells. Here, scaling poses a particular challenge: *Drosophila* has a low number of chromosomes,

making it more prone to inactivate the checkpoint upon cohesin cleavage within a testable time-frame. A higher number of chromosomes may lead to a longer period of checkpoint activity, as indicated in a study on mouse embryos, which delay mitotic exit for over 17 hours upon cohesin cleavage [238]. Nevertheless, the regulatory network described here is highly conserved across species, predicting that even mammalian cells with prematurely separated sister chromatdis will eventually satisfy the checkpoint.

Our mathematical representation of the tension-dependent attenuation of centromeric Aurora B and the isolation of a single kinetochore as a sub-volume of the overall reaction volume may be seen as unorthodox or too simplistic. Indeed the fundamental premise of representing a spatially heterogeneous system and localisation effects therein by a compartmentalised, yet well-mixed system may be subject to criticism. However, the simplicity of the model makes it more accessible to scrutiny, and the good agreement with the experimental data along with the confirmed predictions of the model gives us confidence in its validity.

4.3.4 Contextualisation

This analysis highlights the importance of considering error correction and the checkpoint enforcement mechanism as subsystems that cooperate to give rise to the mitotic checkpoint, instead of treating them as entirely separate entities. The implications of this conceptual frame-shift are far-reaching. Usually, microtubule depolymerising drugs such as colchicine or nocodazole are used to probe dynamics of the mitotic checkpoint in a persistently active state. Along with the checkpoint dynamics of control cells, these dynamics are then used as points of reference in reasoning about the behaviour of the checkpoint under a variety of perturbations. However, with the absence of attachments in such cases, said cost of coupling the checkpoint effector and the error correction is not incurred: the slow timescale at which erroneous attachments are corrected by the error correction - which would affect any system capable of forming attachments - does not affect signalling in the checkpoint effector system. Therefore, such perturbations effectively isolate checkpoint effector signalling from error correction signalling, and thus *hyper-activate* the checkpoint system, rather than activating it to an extent that would directly correspond to its activity in unperturbed mitosis.

5

Disengagement and Inactivation

The work presented in this chapter was conducted in collaboration with Amalie Dick (AD) and Daniel Gerlich (DG) at IMBA Vienna, Austria. The underlying experiments were designed by DG and AD, and carried out by AD. A manuscript about this project is in preparation.

The previous chapter has highlighted the importance of detailed dynamical studies in the context of mitotic checkpoint signalling: We have shown that the response of the mitotic checkpoint to premature loss of cohesin in *Drosophila* neuroblasts is best explained by a model in which the checkpoint enforcement module and the error correction mechanism cooperate through a positive feedback mechanism. Our analysis suggests that in cells undergoing unperturbed mitosis, this systems-level feedback mechanism, along with a CDK1-mediated double-negative feedback loop within the checkpoint enforcement mechanism ($CDK1 \rightarrow MCC \dashv APC/C \dashv CDK1$) is likely to stabilise the checkpoint-active state, and contribute to efficient and irreversible inactivation of the checkpoint at the onset of anaphase by rendering the system hypersensitive to CDK1 activity.

This account sheds light on a solution as to how mammalian cells may avoid the anaphase problem, and opens a route to understanding how they may be able to combine crucial systems-level characteristics of checkpoint signalling that superficially appear incompatible: The capacity of the checkpoint effector to generate a strong response to a weak signal requires sufficient amplification of the signal at the level of MCC assembly to robustly block APC/C-activation [102]. Classic experiments on PtK1 cells show that the duration of metaphase is short and subject to very little variability, independent of the duration of prometaphase, which can be very variable [103]. In order to explain this rapid disengagement of the checkpoint in metaphase in light of very variable duration of prometaphase, either sufficiently fast turnover of MCC or a highly non-

linear signal-response relationship (many kinetochores produce MCC at the same rate as few kinetochores) have to be invoked. Both cases are likely to negatively affect sensitivity of the checkpoint. This apparent incompatibility may be resolved through the presence of a CDK1-centred feedback loop within the checkpoint enforcement module, which results in a slowing down of the assembly of MCC or an acceleration of the dis-assembly of MCC as cyclin B gets degraded.

Moreover, such a mechanism would account for apparent irreversibility in the inactivation of the checkpoint upon acute detachment of chromosomes in metaphase: When challenged with the detachment of kinetochores by means of laser microsurgery in metaphase, HeLa cells show a transient period during which they are capable of re-inhibiting APC/C, but lose this capacity prior to the onset of anaphase [216]. Similarly, addition of Taxol to HeLa cells in metaphase was shown to re-activate the checkpoint and re-inhibit APC/C [220].

Two recent studies by Vazquez-Novelle *et al.* [222] and Rattani *et al.* [221] demonstrated a direct link between the activity of cyclin B:CDK1 and the activity of the checkpoint in mammalian cells: Using a non-degradable mutant of cyclin B, they show that sustained activity of CDK1 in anaphase leads to a reactivation of the mitotic checkpoint, destabilisation of kinetochore-microtubule attachments and chromosome scattering. Moreover, Vazquez-Novelle *et al.* [222] demonstrate that cells that were arrested in metaphase, through proteasomal inhibition by MG132 only show a checkpoint response to microtubule de-polymerisation if CDK1 activity is kept high, but fail to reactivate when CDK1 is inhibited with flavopiridol. Importantly, in this case the response of the system should be independent of error correction, suggesting that irreversibility may indeed be a feature of the checkpoint enforcement mechanism itself.

In this framework, the progression from prometaphase to anaphase at the level of the checkpoint is best described as a two stage process, entailing disengagement of the checkpoint - the transition from an actively-signalling state to a state where MCC is no longer produced, but where the system retains its sensitivity and capacity to become re-engaged - and inactivation of the checkpoint, where the capacity to become re-engaged is lost. Both stages entail the crossing of characteristic thresholds: A threshold specifying the sensitivity to unattached kinetochores in the case of disengagement, and a CDK1 activity threshold for inactivation (figure 5.1).

5.1 Data

The studies mentioned above provide some support for the hypothesis that a CDK1 threshold renders inactivation of the checkpoint enforcement module irreversible. Yet, the lack of temporal resolution and binary nature of the perturbation in these works limits the validity of conclusions that may be drawn and leaves crucial questions un-addressed. Whereas the recruitment of neither Mad2 nor BubR1 alone

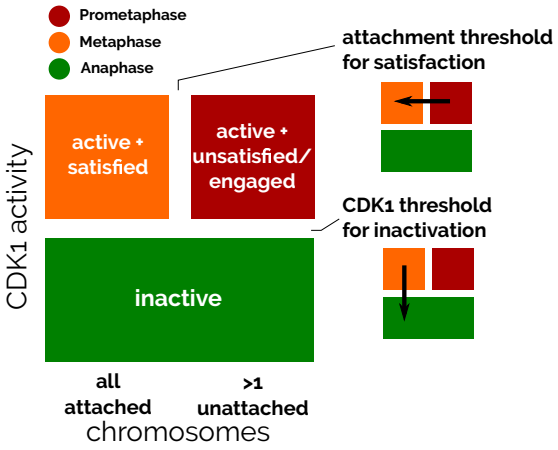


Figure 5.1: Conceptual Framework: Classification of qualitative states of checkpoint signalling - In prometaphase, the checkpoint is active and engaged, i.e. producing MCC in response to unattached kinetochores (red). As the cell enters metaphase, all chromosomes become bi-oriented, a sensitivity threshold is crossed and the checkpoint disengages. It retains the capacity to become re-engaged, however it is no longer actively producing MCC (orange). As cyclin B levels, and CDK1 activity drop, the checkpoint becomes inactivated at, or prior to the onset of anaphase. Its capacity to become reengaged is lost.

represents a sufficient condition for active production of MCC, each of them represents a necessary condition for checkpoint signalling. From these observations of Vazquez-Novelle *et al.* [222], it can be safely concluded that the inhibition of CDK activity terminates checkpoint control. Yet, it cannot be concluded that in the converse case the checkpoint is actively producing MCC, given that recruitment of Mad2 to kinetochores is necessary but not sufficient for checkpoint signalling.

In the hypothesis formulated above, I postulate a discrete threshold in CDK1 activity that lies within the range of activity of CDK1 crossed at the onset of anaphase, and controls inactivation of the checkpoint. The experiments by Vazquez-Novelle *et al.* [222] demonstrate a dependence, but do not directly support a CDK1 threshold for the inactivation of the checkpoint, as a single dose of CDK inhibitor does not permit any conclusions in this context. Moreover, treatment of cells with flavopiridol likely affects the activity of other cyclin-dependent kinases. This further restricts conclusions that can be drawn about a CDK1-specific threshold for checkpoint activity.

5.1.1 Experimental System

Whereas the recruitment of Mad2 to kinetochores can only be used as a proxy for the activity of the checkpoint, the degradation dynamics of the two early anaphase

substrates of APC/C:Cdc20 - cyclin B and securin - provide more direct information about the activity of the checkpoint. We therefore devised a quantitative live-cell imaging assay following the degradation dynamics of fluorescently-tagged reporters of early anaphase substrates of APC/C:Cdc20. In recent years, HeLa has been the cell line of choice in studies investigating the mitotic checkpoint in human cells. However, researchers are increasingly transitioning towards using RPE1 cells, as it represents a non-cancerous human cell line, and is not partially polyploid as is HeLa. To investigate the dynamics of the mitotic checkpoint while accounting for this transition, we use two previously published cell lines: HeLa cells expressing securin-mEGFP from a BAC construct controlled by the endogenous promoter, first described in [216]; and RPE1 cells expressing endogenously tagged cyclin B1-Venus, first described in [217].

5.1.2 High Doses of CDK1 Inhibitor

Cells were treated with 100 ng/mL nocodazole for up to 20 h and arrested in prometaphase. Subsequently, 13.3 μM of the CDK1-specific inhibitor RO-3306 was added to the HeLa cells, and 20.0 μM or 10.0 μM was added to RPE1 cells, using an automated fluid-handling device. Degradation kinetics of total cyclin B1-Venus and securin-mEGFP were measured in circular regions of wide-field time lapse images and corrected for bleaching, as previously described in [216]. The timecourse data were aligned to the time of RO-3306 addition and normalised to the average signal intensity over the 12 min prior to drug addition.

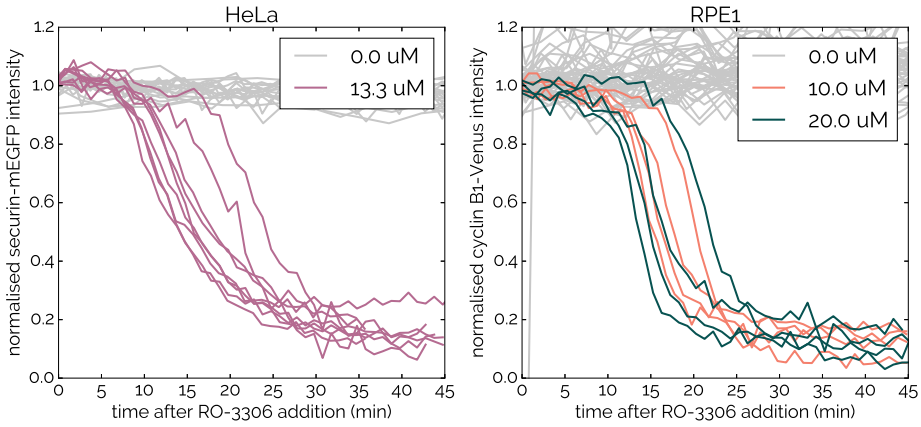


Figure 5.2: Addition of high doses of RO-3306 to nocodazole-treated cells - **Left:** Degradation of securin-mEGFP in HeLa-Kyoto cells treated with 100 ng/mL nocodazole upon addition of 13.3 μM RO-3306. **Right:** Degradation of cyclin B1-Venus in hTert-RPE1 cells treated with 100 ng/mL nocodazole upon addition of 20 μM or 10 μM RO-3306

In nocodazole-arrested HeLa cells treated with $13.3\ \mu M$ RO-3306 ($n = 9, N = 2$) (figure 5.2 left panel) the degradation of securin-mEGFP begins $5\ min$ after the addition of RO-3306, becomes accelerated over the next $5\ min$, and proceeds at maximal rate over the following $5\ min$, before it begins to slow down. After $30 - 35\ min$ normalised securin-mEGFP intensities reach a steady state of $0.15 - 0.2$. The degradation of cyclin B1-Venus in nocodazole-arrested RPE1 cells treated with $20.0\ \mu M$ ($n = 4, N = 1$) or $10.0\ \mu M$ ($n = 4, N = 1$) (figure 5.2 right panel) RO-3306 follows a similar pattern.

Although the degradation patterns of securin-mEGFP and cyclin B1-Venus in the two cell lines is sigmoidal, the degradation of cyclin B1-Venus in the RPE1 cells appears sharper than the degradation of securin-mEGFP in HeLa cells. For both cell types, high doses of RO-3306 appear to terminate the production of MCC with little or no delay in the presence of unattached kinetochores, and a dose-dependence could not be observed for RPE1 cells. The cyclin B1-Venus degradation patterns resulting from the use of the two different doses of RO-3306 appear indistinguishable.

5.1.3 Intermediate Doses of CDK1 Inhibitor

This lack of any apparent dose-dependence suggests that the inhibitor concentrations used over-titrate CDK1 activity. Over-titration of CDK1 is consistent with a complete inhibition of CDK1 as well as with the inhibition of CDK1 activity beyond a required activity threshold for checkpoint signalling.

To better distinguish between these two possibilities, we moved to lower doses of RO-3306 ($3.3\ \mu M$ and $2.5\ \mu M$ for HeLa cells and $3.0\ \mu M$ and $2.5\ \mu M$ for RPE1 cell). Moreover, we extended the imaging time after RO-3306 accordingly, in order to detect potential delays in the onset of degradation.

The timecourses depicted in figure 5.3 show pronounced differences between the two cell types. The degradation of securin-mEGFP in HeLa cells treated with $3.3\ \mu M$ RO-3306 ($n = 16, N = 2$) (figure 5.3 top panel) follows a bi-phasic pattern, characterised by a slow initial degradation, followed by accelerated degradation. Interestingly, the data appear to cluster into two distinct groups: Eight cells initiate rapid degradation of securin between $25\ min$ and $75\ min$ after RO-3306 addition, whereas the other eight cells do not initiate accelerated degradation of securin until $110\ min$ after the addition of RO-3306. Cells from both experimental repeats were found in both groups. Notably, the initial rate of securin degradation before the

onset of accelerated degradation of securin does not vary considerably between the two groups.

The degradation of securin-mEGFP in HeLa cells treated with 2.5 μM RO-3306 ($n = 20, N = 2$) (figure 5.3 bottom panel) appears more varied. Eight cells show degradation patterns similar to those displayed by cells treated with 3.3 μM RO-3306; six cells fall into the faster category, whereas two cells follow the slow degradation pattern. The remaining twelve cells are indistinguishable from cells treated with nocodazole alone, and do not initiate considerable degradation of securin-mEGFP within 150 min.

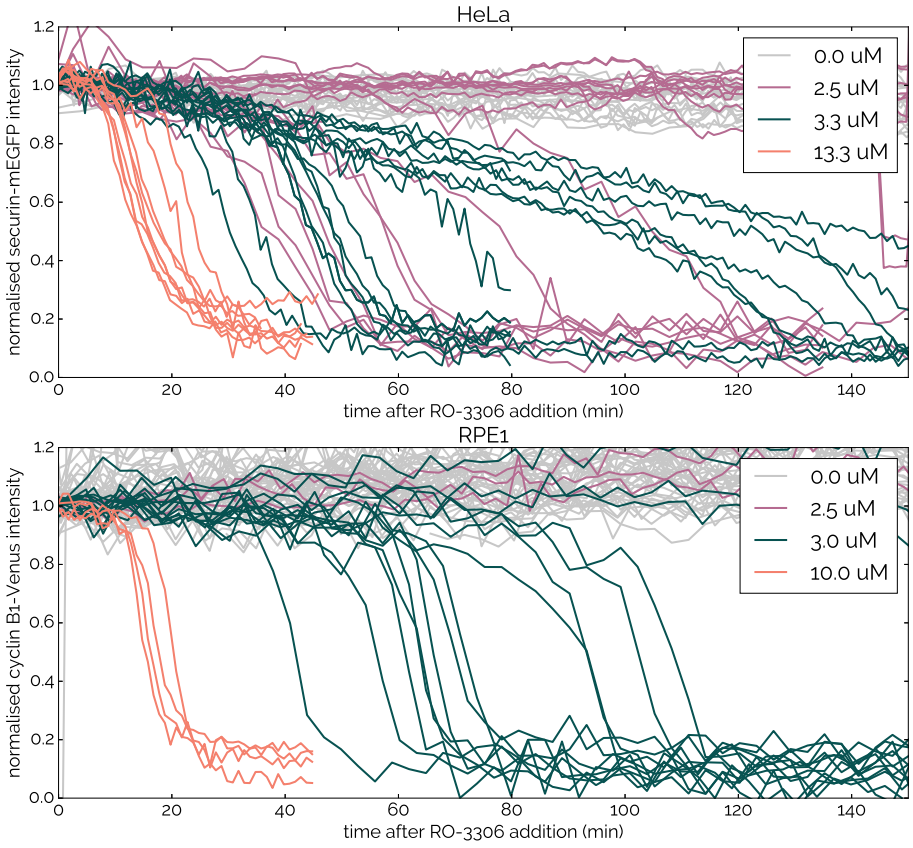


Figure 5.3: Addition of medium doses of RO-3306 to nocodazole-treated cells - **Top:** Degradation of securin-mEGFP in HeLa-Kyoto cells treated with 100 ng/mL nocodazole upon addition of 13.3 μM, 3.3 μM and 2.5 μM RO-3306 **Bottom:** Degradation of cyclin B1-Venus in hTert-RPE1 cells treated with 100 ng/mL nocodazole upon addition of 10 μM, 3.0 μM and 2.5 μM RO-3306.

The response of RPE1 cells to the addition of comparable doses of RO-3306 is markedly different. When treated with 3.0 μM RO-3306 ($n = 15, N = 2$), the

degradation of cyclin B1-Venus in twelve cells shows a strong bi-phasic pattern, characterised by an initial phase ($40 - 90\ min$) of almost constant cyclin B levels, before rapid degradation of cyclin B sets in. Only two cells treated with $3.0\ \mu M$ RO-3306 do not initiate the degradation of cyclin B within $150\ min$ after the addition of RO-3306. Similarly, the addition of $2.5\ \mu M$ RO-3306 ($n = 3, N = 1$) did not trigger the degradation of cyclin B1-Venus within $150\ min$ after the addition of RO-3306.

The pronounced binary response of the degradation of cyclin B to inhibition of CDK1 observed for RPE1 cells suggests that activity of the checkpoint, indicated by inhibition of APC/C, indeed depends on CDK1 activity in a non-linear manner, and is characterised by a distinct CDK1 activity threshold. Notably, the degradation of cyclin B has a strong sigmoidal character and accelerated degradation sets in at near maximal levels of cyclin B. The stark difference in timing between this case and cells treated with a higher dose of CDK1-inhibitor can be attributed to a critical slowing-down phenomenon. Assuming that cyclin B is the major determinant of CDK1 activity at this stage of mitosis [1], our cyclin B1-Venus degradation data are inconsistent with an entirely graded response of checkpoint activity to CDK1 activity. In the latter case, weaker and weaker inhibition of CDK1 would be expected to result in partial activation of APC/C and lead to a pattern of cyclin B degradation characterised by initially slow degradation of cyclin B1 that becomes gradually accelerated until a break-point is reached, when all CDK1 activity is lost.

If it is indeed the case that the activity of the checkpoint depends on the activity of CDK1 in a switch-like manner, why do the data for the degradation of securin-mEGFP in HeLa cells not show a similar pattern? Assuming that the securin-mEGFP employed in this context is a perfect reporter for cyclin B, the degradation pattern for securin-mEGFP in HeLa cells would lend stronger support to the hypothesis that the activity of the checkpoint depends on CDK1 activity in a much more graded manner; a situation where partial inhibition of CDK1 results in partial activation of APC/C, and the rate of degradation of the early anaphase substrates gradually accelerates until a break-point is reached, when either all CDK1 activity is lost, or a non-zero threshold is crossed.

5.1.4 Long-term imaging of cells treated with nocodazole

Due to the different nature of the two reporters used in this study - cyclin B1 is endogenously tagged and very abundant, whilst securin is expressed from a BAC-

[1] Early in mitosis, cyclin A plays a relevant role in the activation of CDK1, however it gets degraded throughout prometaphase in a manner not regulated by the checkpoint.

construct and less abundant - this discrepancy may be an artefact resulting from the experimental setup. Securin and cyclin B have been shown to be degraded following similar dynamics in unperturbed mitosis. However, processes governing synthesis and degradation of the two different reporters, as well as the corresponding un-tagged proteins, may behave very differently during prolonged arrest in prometaphase. To investigate how the levels of securin and cyclin B behave in a prolonged arrest in prometaphase, we treated cells with $100\ ng/mL$ nocodazole and followed the intensity of securin-mEGFP (HeLa) and cyclin B1-Venus (RPE1) for up to $2400\ min$.

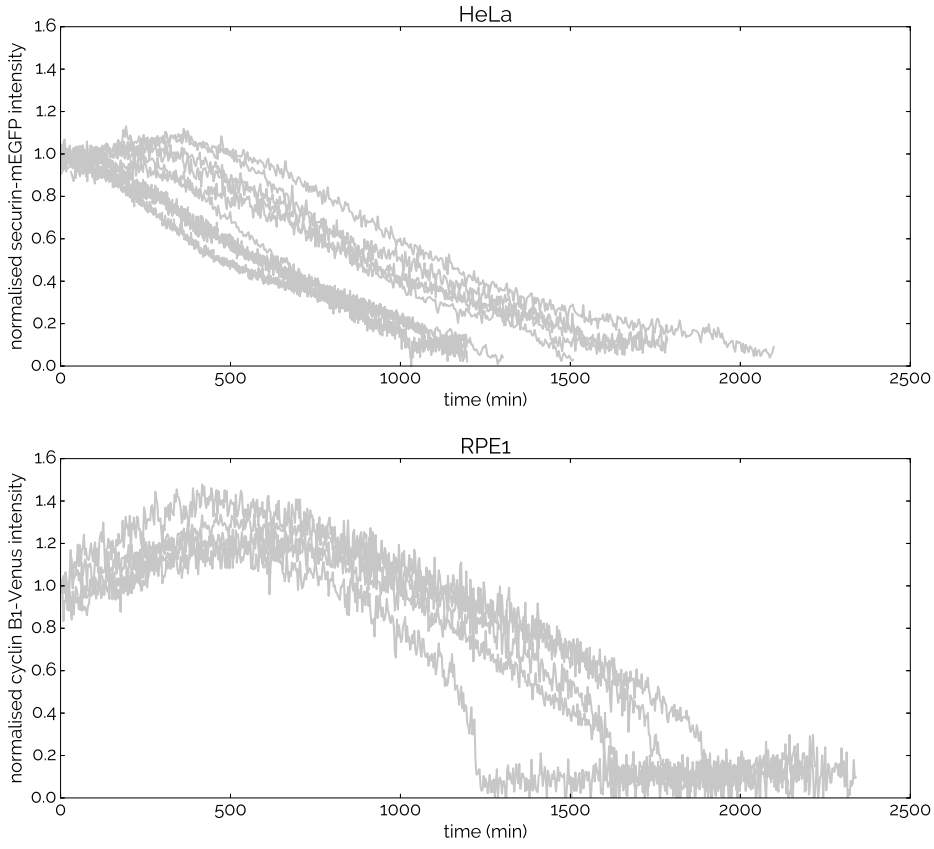


Figure 5.4: Treatment with nocodazole alone - **Top:** Degradation of securin-mEGFP in HeLa-Kyoto cells treated with $100\ ng/mL$ nocodazole. **Bottom:** Degradation of cyclin B1-Venus in hTert-RPE1 cells treated with $100\ ng/mL$ nocodazole.

In HeLa cells treated with $100\ ng/mL$ nocodazole ($n = 9, N = 3$), normalised securin-eGFP intensities trace out a tri-phasic pattern in time: For the first $250 - 500\ min$ securin intensities stay constant or rise minimally, before they begin to fall

at a slow rate. Over the next $700 - 1000\ min$ the signal follows an exponential-like pattern, characterised by a declining rate of degradation, before the signal drops to around 20% of the initial intensity, when most cells show a short phase of accelerated degradation.

In RPE1 cells treated with $100\ ng/mL$ nocodazole ($n = 5, N = 2$), cyclin B1-Venus follows a similarly tri-phasic pattern. However, the features of the corresponding timecourses are distinctly different from our observation of HeLa cells: Over the first $500\ min$ cyclin B1-Venus intensities consistently increase by $20 - 40\%$ of their initial value, until they begin to fall at a slow, apparently constant rate. After an additional $700 - 1000\ min$ [1] , the signal reaches an intensity of approximately 40% relative to the signal intensity at NEBD, and the degradation of cyclin B becomes markedly accelerated. Notably, in both cell types, the accelerated degradation of the fluorescent reporter precedes chromatin de-condensation.

Apart from the necessary background correction, my collaborators also performed extensive experiments employing soluble GFP to study the effect of changes in cell morphology that accompany entry into- and exit from mitosis (data not shown). We found that the cell-rounding effect that accompanies entry into mitosis, and the cell-flattening effect that accompanies exit from mitosis, indeed influence the intensity measurements. However, neither the initial increase in cyclin B1-Venus intensities at the beginning of the experiment, nor the rapid drop in reporter intensities preceding mitotic exit, can be explained by changes in cell morphology, as this was found only to contribute to a variation of 10% signal intensity. Moreover, rounding of the cell precedes $t = 0$ in our imaging experiment, and flattening of the cell follows the accelerated degradation of the fluorescent reporters. Thus, we are confident that these features are indeed characteristic to the degradation dynamics of our fluorescent reporters and do not constitute experimental artefacts.

Interactive Notebook - Data (static version)

[1] Brito *et al.* [239] and Yang *et al.* [240] report a nocodazole dose-dependence of the duration of the mitotic arrest, and report that cells exposed to low doses of nocodazole can form functional spindles, and satisfy the checkpoint. Based on these data, one would predict that our treatment ($100\ ng/mL \simeq 300\ nM$) should induce a mitotic arrest lasting up to $10\ h$. However, we consistently found RPE1 and HeLa cells that arrested in mitosis for more than $1000\ min \simeq 16\ h$, and observed no spindle formation.

5.2 Model

The observation that our fluorescent reporters get degraded throughout a prolonged arrest in prometaphase is associated with the phenomenon of mitotic slippage, a process whereby cells bypass checkpoint control, if they are unable to produce configurations of attachments that satisfy the mitotic checkpoint. This process is driven by proteasomal degradation of cyclin B and leads to exit from mitosis in the presence of actively signalling kinetochores[1] [223].

Note that the findings of Brito and Rieder [223] and the findings by Vazquez-Novelle *et al.* [222] present potentially contradicting models on the operation of the checkpoint: Brito and Rieder find that cyclin B is almost completely degraded during slippage in RPE1 cells, and by immunofluorescence find that kinetochores still stain positive for Mad2 and BubR1 once chromatin de-condensation has set in. Considering the almost complete degradation of the cyclin B probe in these experiments, one would assume that CDK1 activity would correspondingly drop to zero. On the other hand, Vazquez-Novelle *et al.* [222] show that recruitment of Mad2 to unattached kinetochores is sensitive to inhibition of CDK, and readily removed within 15 min after addition of the inhibitor. As discussed above, the use of Mad2 localisation to assess the activity of the checkpoint is problematic, and we present the degradation dynamics of cyclin B and securin as a superior indicator of checkpoint activity.

Moreover, we believe that a hypersensitive dependence of checkpoint activity on CDK1 activity bears potential not only to reconcile this apparent contradiction, but may also account for a previously unexplained features of literature data: A characteristic acceleration in the degradation of cyclin B, which was observed in many previous studies [217, 223, 239, 240].

A hypersensitive dependence of checkpoint signalling on the activity of CDK1 would predict that the checkpoint gets inactivated after the activity of CDK1 drops below a certain threshold, resulting in an activation of APC/C:Cdc20 and accelerated degradation of its substrates cyclin B and securin. In this context, activity is to be understood as the capacity of the checkpoint control system to inhibit APC/C:Cdc20. This may include signal generation (production of MCC, as commonly probed by the localisation of Mad2 to kinetochores), but is certainly not lim-

[1] Brito and Rieder [223] use immunofluorescence experiments to substantiate their claim that the proteasomal degradation is not driven by APC/C:Cdh1. Similarly, the claim that kinetochores are actively signalling is based on end-point measurements assessing the localisation of Mad2 and BubR1 at kinetochores after chromatin de-condensation.

ited to this level, as the turnover of MCC and its affinity to APC/C:Cdc20 undoubtedly also play a role in this context.

To explore this hypothesis more formally, I devised a mathematical model that describes a generalised consensus picture of the fundamental interactions between cyclin B:CDK1, APC/C:Cdc20 and MCC in terms of a coupled system of ordinary differential equations.

5.2.1 Construction

I assume that data on the degradation of early-anaphase reporters collected for HeLa and RPE1 cells can be explained by the same underlying network. Thus, differences in the degradation dynamics of securin and cyclin B are explained by differences in the parameters governing synthesis and degradation of securin and cyclin B in the context of identical activities of APC and MCC, but do not rely on changes to the network structure. Figure 5.5 provides an overview of the molecular interactions expressed in the model. Due to the central role of cyclin B:CDK1 in the network, simulations will be overlaid onto cyclin B1-Venus data collected in RPE1 cells, and these data will be used to parametrise the model. The parameters that govern the turnover of securin are chosen to qualitatively demonstrate that the securin data for HeLa cells are indeed consistent with the cyclin B data for RPE1 cells.

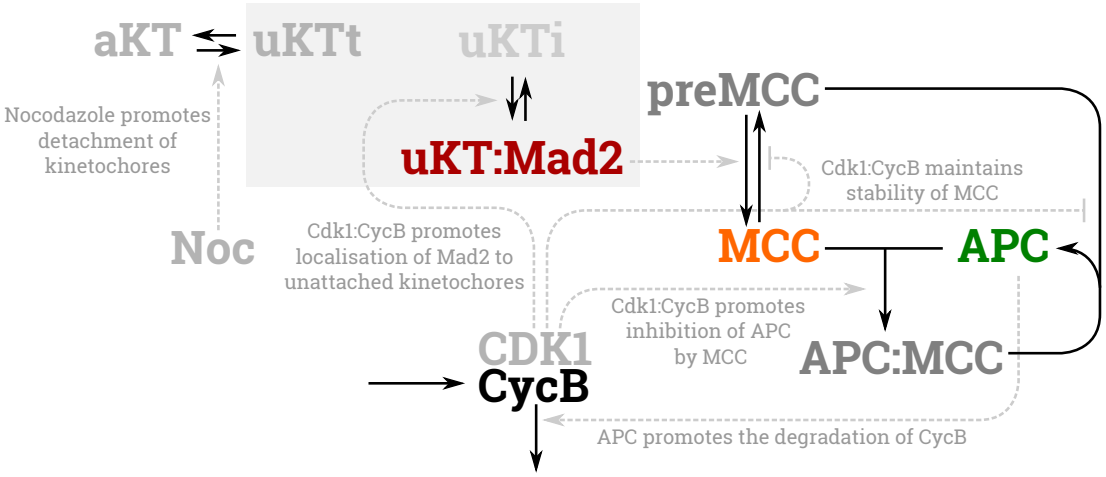


Figure 5.5: Wiring Diagram - Diagram depicting the assumptions and qualitative interactions that informed the construction of the model.

5.2.1.1 Cyclin B Synthesis and Degradation

The level of cyclin B is determined by synthesis ($k_{scycb} = 0.005\ AU\ min^{-1}$) and degradation. Degradation of cyclin B is governed by a slow constitutive process ($k_{dcycb} = 0.002\ min^{-1}$, $\tau \simeq 346\ min$) and a much faster process depending on APC/C:Cdc20 activity ($k_{dcycb,apc} = 1.5 min^{-1}\ AU^{-1}$, $\tau \simeq 0.46\ min$). To capture the initial increase of cyclin B levels observed during mitotic slippage, I assume that cyclin B does not start from steady state in the absence of APC/C ($[CycB]_{SS} = 2.5\ AU$) at the onset of prometaphase, but from a much lower point set to 1 ($[CycB]_0 = 1\ AU$). Moreover, we assume that the rate of cyclin B synthesis decays slowly over time, following an exponential function ($r_{decay} = 0.0008\ min^{-1}$, $\tau \simeq 866\ min$). This formulation is a proxy for changes in the dynamics of the system that occur during mitotic slippage. These could affect synthesis of cyclin B directly, such as the slow depletion of cyclin B-encoding RNAs, or increase the rate of proteasomal degradation that is not directly regulated by the checkpoint, such as a plausible slow activation of Cdh1.

$$\frac{d[CycB]}{dt} = k_{scycb} \cdot e^{-r_{decay} \cdot t} - (k_{dcycb} + k_{dcycb,apc} \cdot [APC]_{free}) \cdot [CycB] \tag{5.1}$$

5.2.1.2 CDK1 activity

I assume that cyclin B associates rapidly with CDK1 and therefore directly determines the activity of CDK1. To account for the inhibition of CDK1, cyclin B levels are divided by a term that expresses the activity of a CDK1 inhibitor $[Inh]$ relative to its IC_{50} value.

$$[CDK1] = \frac{[CycB]}{1 + [Inh]} \tag{5.2}$$

5.2.1.3 Securin

Securin is strictly treated as a reporter in this model. The dynamics of securin turnover follow similar kinetics to the turnover of cyclin B: Its rate of synthesis is decaying over time, and it is degraded by a slow constitutive process, and a much faster APC/C-driven process.

$$\frac{d[Sec]}{dt} = k_{ssec} \cdot e^{-r_{decay,sec} \cdot t} - (k_{dsec} + k_{dsec,apc} \cdot [APC]_{free}) \cdot [Sec] \tag{5.3}$$

5.2.1.4 Kinetochore Signalling

Kinetochores can be either unattached ($[uKT_t]$) or attached ($1 - [uKT_t]$). In simulations of unperturbed mitosis, all kinetochores are unattached at the beginning of prometaphase, and become attached following first-order kinetics ($k_{att} = 0.6\, min^{-1}$).

$$\frac{d[uKT_t]}{dt} = -k_{att} \cdot [uKT_t] \tag{5.4}$$

To model CDK1-dependent processes at the kinetochore level that lead to the formation of a catalytic platform for MCC assembly (such as the recruitment of Mad1:Mad2), we assume that unattached kinetochores can become actively signalling kinetochores ($[uKT_a]$) in a reversible process depending on CDK1 activity. The fraction of unattached, inactive kinetochores ($[uKT_t] - [uKT_a]$) is activated in a second-order process that depends on CDK1 activity ($k_a = 40\ min{-}1\ AU^{-1}$). The phosphatase-dependent reverse reaction that converts actively signalling, unattached kinetochores to inactive kinetochores is modelled via a first-order process depending on $[uKT_a]$ alone ($k_i = 40\ min^{-1}$). The corresponding steady state is $0.5\ AU$.

$$\frac{d[uKT_a]}{dt} = k_a \cdot [CDK1] \cdot ([uKt_t] - [uKT_a]) - k_i \cdot [uKT_a] \tag{5.5}$$

5.2.1.5 MCC and APC/C

I assume that the total pool of MCC components is constant ($[MCC_T] = 2.4\ AU$), and distributed between assembled MCC ($[MCC_t]$) and MCC-precursor components ($[MCC_{pre}]$).

$$[MCC_T] = [MCC]_t + [MCC_{pre}] \tag{5.6}$$

Assembled MCC ($[MCC_t]$) can either associate with $[APC]$ to form $[APCMCC]$ or it can be present in its free, unbound form ($[MCC_{free}]$). At the beginning of prometaphase, MCC is present in excess over APC/C ($[APC_T]_0 = 1.0\ AU$, $[MCC_t]_0 = 2.2\ AU$)

$$[MCC_t] = [MCC_{free}] + [APCMCC] \tag{5.7}$$

MCC is assembled from MCC-precursor components ($[preMCC]$) in a second-order process that depends on $[uKT_a]$, actively signalling, unattached kinetochores ($k_{amcc} = 100\ min^{-1}\ AU^{-1}$). I assume that both forms of assembled MCC are disassembled via the same processes, namely a constitutively active first-order process

Table 5.1: Kinetic parameters used in the model

parameter	value
$k_{scycb}(AU\ min^{-1})$	0.005
$k_{dcycb}(min^{-1})$	0.002
$k_{dcycb,apc}(min^{-1}\ AU^{-1})$	1.5
$r_{decay}(min^{-1})$	0.0008
$k_{ssec}(AU\ min^{-1})$	0.0025
$k_{dsec}(min^{-1})$	0.002
$k_{dsec,apc}(min^{-1}\ AU^{-1})$	0.75
$r_{decay,sec}(min^{-1})$	0.0016
$k_{att}(min^{-1})$	0.6
$k_{ass}(min^{-1}\ AU^{-1})$	100
$k_{ass,cdk}(min^{-1}\ AU^{-2})$	350
$k_{diss}(min^{-1})$	0.2
$k_{amcc}(min^{-1}\ AU^{-1})$	100
$k_{imcc}(min^{-1})$	0.1
$k_{imcc,p31}(min^{-1})$	0.08
J_{imcc}	0.09
N	2.6
$[APC_T]\ (AU)$	1
$[MCC_T]\ (AU)$	2.4

($k_imcc = 0.1\ min^{-1}$, $\tau \simeq 6.9$), and a second process that is inhibited by CDK1 activity ($i_{mcc,cdki}$).

$$\frac{d[MCC_t]}{dt} = k_{amcc} \cdot [preMCC] \cdot [uKT_a] - (k_{imcc} + i_{mcc,cdki}) \cdot [MCC_t] \tag{5.8}$$

The CDK1 inhibited pathway of MCC dis-assembly ($k_{imcc,p31} = 0.08\ min^{-1}$, $J_{imcc} = 0.09$, $N = 2.6$) depends on CDK1 activity in a hyperbolic manner and contributes $0.08\ min^{-1}$ to the dis-assembly of MCC if $[CDK1] = 1\ AU$, and $\simeq 39\ min^{-1}$ when [CDK1] reaches its lower steady state of $\simeq 0.033\ AU$ in the presence of full APC activation.

$$i_{mcc,cdki} = k_{imcc,p31} \cdot \frac{1}{J_{imcc}^N + [CDK1]^N} \tag{5.9}$$

The total pool of APC/C is assumed to be constant ($[APC_T] = 1\ AU$) and distributed between an inactive, MCC-bound form $[APCMCC]$ and an active, free form $[APC]$.

$$[APC_T] = [APCMCC] + [APC] \tag{5.10}$$

I assume that all APC/C is bound to MCC ($[APCMCC]_0 = 1\ AU$) at the onset of pro-metaphase. APC/C is released from the complex via dissociation of the complex into free APC/C and free MCC ($k_{diss} = 0.2\ min^{-1}$, $\tau \simeq 3.46\ min$, or via dis-assembly of MCC, as described above. In turn, free APC/C can associate with free MCC via a constitutive second-order process ($k_{ass} = 100\ min^{-1}\ AU^{-1}$) or by a process that depends on CDK1 activity ($k_{ass,cdk} = 350\ min^{-1}\ AU^{-2}$).

$$\begin{aligned}\frac{d[APC]}{dt} &= (k_{diss} + k_{imcc} + i_{imcc,cdki}) \cdot [APCMCC] \\ &-(k_{ass} + k_{ass,cdk} \cdot [CDK1]) \cdot [APC] \cdot [MCC_{free}]\end{aligned} \tag{5.11}$$

5.2.2 Implementation

Model simulations were generated using XPPjl [1], a simulation tool written in julia [2], which I developed in order to facilitate programmatic modelling of a diverse set of conditions, data analysis and plotting. To solve the system of ODEs numerically, I used a second/third-order adaptive solver for stiff problems, employing a modified Rosenbrock triple, as implemented in julia's ODE Package [3].

[1] https://github.com/novakgroupoxford/XPPjl

[2] http://julialang.org/

[3] https://github.com/JuliaDiffEq/ODE.jl

5.2.3 Simulations

Interactive Notebook - Model (static version)

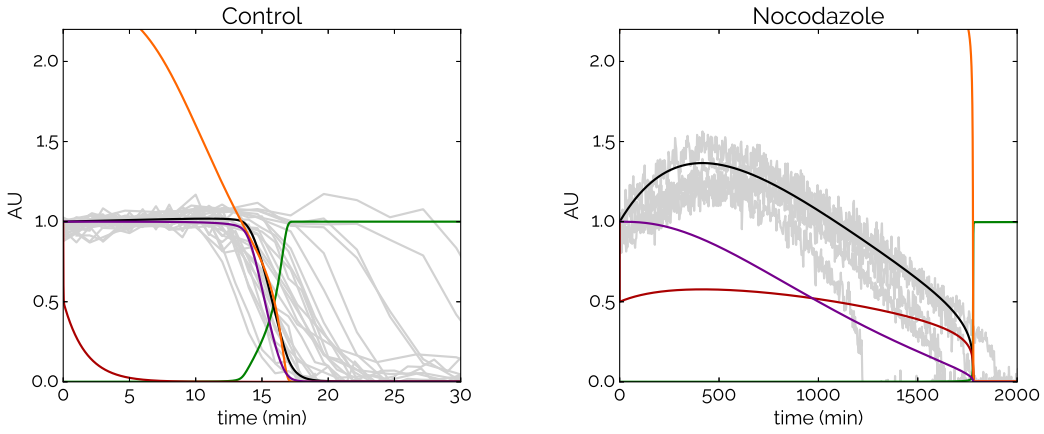


Figure 5.6: Simulation of Unperturbed Mitosis and Mitotic Slippage - **Left:** Simulation of unperturbed mitosis showing timecourses for **cyclin B**, **securin**, **total MCC**, **free APC/C** and **total uKT** contrasted with corresponding experimental data for cyclin B1-Venus in RPE1 cells ($n = 28, N = 4$) (grey timecourses). **Right:** Timecourse simulation for cells treated with $100\ ng/mL$ nocodazole, contrasted with corresponding experimental data ($n = 9, N = 3$).

5.2.3.1 Unperturbed Mitosis

I first simulated progression through unperturbed mitosis and used the model to predict timecourses for MCC and APC/C (figure 5.6 left panel). The model was conditioned on data following cyclin B1-Venus timecourses in RPE1 cells undergoing unperturbed mitosis ($n = 28, N = 4$) (grey timecourses in figure 5.6 left panel). The simulations start from nuclear envelope breakdown (NEBD), where an initial pool of pre-assembled MCC inhibits APC/C [168], all chromosomes are unattached, and CDK1 activity is high. As chromosomes become attached, the system initially maintains a robust inhibition of APC/C by replenishing an excess pool of MCC. Once all chromosomes have become attached, the assembly of MCC stops, the level of MCC falls below the level of APC/C, and the inhibition on APC/C is released. The simulations highlight the role of feedback mechanisms in governing the meta-to-anaphase transition: With APC/C becoming active, the rate of cyclin B degradation accelerates. This releases the inhibition on the pathway of fast MCC dis-assembly and renders MCC a less efficient inhibitor. Furthermore, dropping activity of CDK1

renders MCC assembly at kinetochores less efficient. APC/C activity becomes fully potentiated and the cell enters anaphase. Note that securin and cyclin B are degraded following very similar kinetics.

5.2.3.2 Nocodazole Treatment - Mitotic Slippage

To simulate prolonged treatment with a high dose of nocodazole, which results in the de-polymerisation of microtubules and prevents the formation of attachments, I set the rate at which unattached kinetochores become attached to zero ($k_{att} = 0$), and otherwise leave the model unchanged. Again, a pre-assembled pool of MCC inhibits APC/C, all kinetochores are unattached and CDK1 activity is high. For the first $500\ min$ the activity of cyclin B increases, before it begins to decline at a relatively constant rate. Securin levels do not increase initially, but show a pronounced shoulder, before slippage-degradation sets in. After $1800\ min$ a breakpoint is reached, MCC is rapidly disassembled, APC/C is activated and the remaining cyclin B and securin are rapidly degraded.

The model simulations nicely recapitulate the degradation pattern observed in a representative cell. We shall now briefly discuss the features of the model that establish this good agreement. Cyclin B starts far from its steady state and is a very slow variable. Thus, in spite of the permanently declining rate of cyclin B synthesis, levels of cyclin B initially increase, before the initial phase of slow, net degradation sets in. Notably, the phase of declining cyclin B levels is driven by the dropping rate of synthesis, as well as degradation driven by a small, but increasing activity of APC/C. The increase in the activity of APC/C results from the three-fold role of CDK1 in regulating turnover of MCC, where it promotes the assembly of MCC, as well as its association with APC/C, and inhibits a fast dis-assembly pathway. Consequently, the checkpoint grows weaker and weaker as cyclin B is degraded and the activity of CDK1 drops, while still retaining its activity. When the breakpoint is reached, the checkpoint is weakened to the extent that APC/C can overcome inhibition by MCC, and the degradation of cyclin B and securin accelerates.

The degradation patterns of securin and cyclin B are almost indistinguishable in simulations of unperturbed mitosis. However, cells spend a dramatically longer time in the checkpoint-active state when treated with nocodazole, and potential differences in the underlying dynamics become visible. In spite of the absence of direct experimental data for the degradation of securin in RPE1 cells, simulations for securin are included to demonstrate that the similar regulatory dependencies governing the degradation of cyclin B and securin can give rise to very different degradation patterns under experimental conditions that amplify slight differences

Table 5.2: Parameters: CDK1 Inhibition

[RO-3306] (μM)	Inh	$[CDK1]_{max}$
13.3	5.0	16 %
10.0	5.0	16 %
3.3	2.2	31.25 %
3.0	2.2	31.25 %
2.5	0.75	57.14 %

in the underlying rate constants. Thus, I do not make the claim that the dynamics of the checkpoint are identical in HeLa and RPE1, but merely intend to demonstrate that the apparent inconsistency in the degradation of securin and cyclin B does not necessarily exist.

5.2.3.3 Titration of CDK1 activity

Having conditioned the model to accurately recapitulate unperturbed mitosis and treatment with nocodazole, I next turned to simulate the addition of different doses of CDK1 inhibitor to cells arrested in nocodazole. As a consequence of our experimental protocol, the time that individual cells have spent in nocodazole can vary from cell to cell. To account for potential effects resulting from this variability, I first perform simulations for the treatment with nocodazole alone ($k_{att} = 0$), and stop these simulations after 1 min, 130 min, 280 min, 445 min, 640 min or 870 min. Next, the parameter expressing the inhibition of CDK1 (Inh) is changed to mimic addition of RO-3306, and the simulation is continued. Figures 5.7 and 5.8 show timecourse simulations generated with the procedure above, where the value of the inhibitor parameter was chosen to agree with the experimental data. As the experimental data were normalised to the reporter signal at the time of drug addition, the left columns in figures 5.7 and 5.8 show simulated timecourses normalised to the time of parameter change contrasted with the corresponding experimental data.

Using appropriate values for the Inh parameter (table 5.2), the normalised simulations recapitulate the experimental data for securin-mEGFP and cyclin B1-Venus reasonably well. Simulations of the experimental condition employing 3 μM RO-3306 overestimate the initial rate of cyclin B degradation upon addition of the CDK1 inhibitor, and fail to capture the two populations of timecourses observed for securin-mEGFP. Nonetheless, the overall timing, and the acceleration of the degradation of securin and cyclin B are adequately recapitulated. Interestingly, the different times

cells have spent in nocodazole can explain a large part of the variability observed in the experimental data.

The simulations in the right column of figure 5.7 reveal a curious pattern: For cells treated with a high dose of CDK1 inhibitor, the model predicts that the accelerated degradation occurs independently of the cyclin B level. Acceleration occurs after a relatively short delay that appears not to depend on the cyclin B level, rather than on the duration of the nocodazole arrest. Conversely, for cells treated with a low dose of CDK1 inhibitor, the model predicts that the acceleration should occur at a defined cyclin B level, whereas the time it takes for the acceleration to occur strictly depends on the duration of the nocodazole arrest, and appears to be independent of the cyclin B level at the time of inhibitor addition. In this framework, treatment with 3 μM of RO-3306 appears to be an intermediate case, where acceleration occurs at a consistent level of cyclin B (as in the case of a low dose), and the delay depends on the cyclin B level at the time of inhibitor addition (as in the case of a high dose).

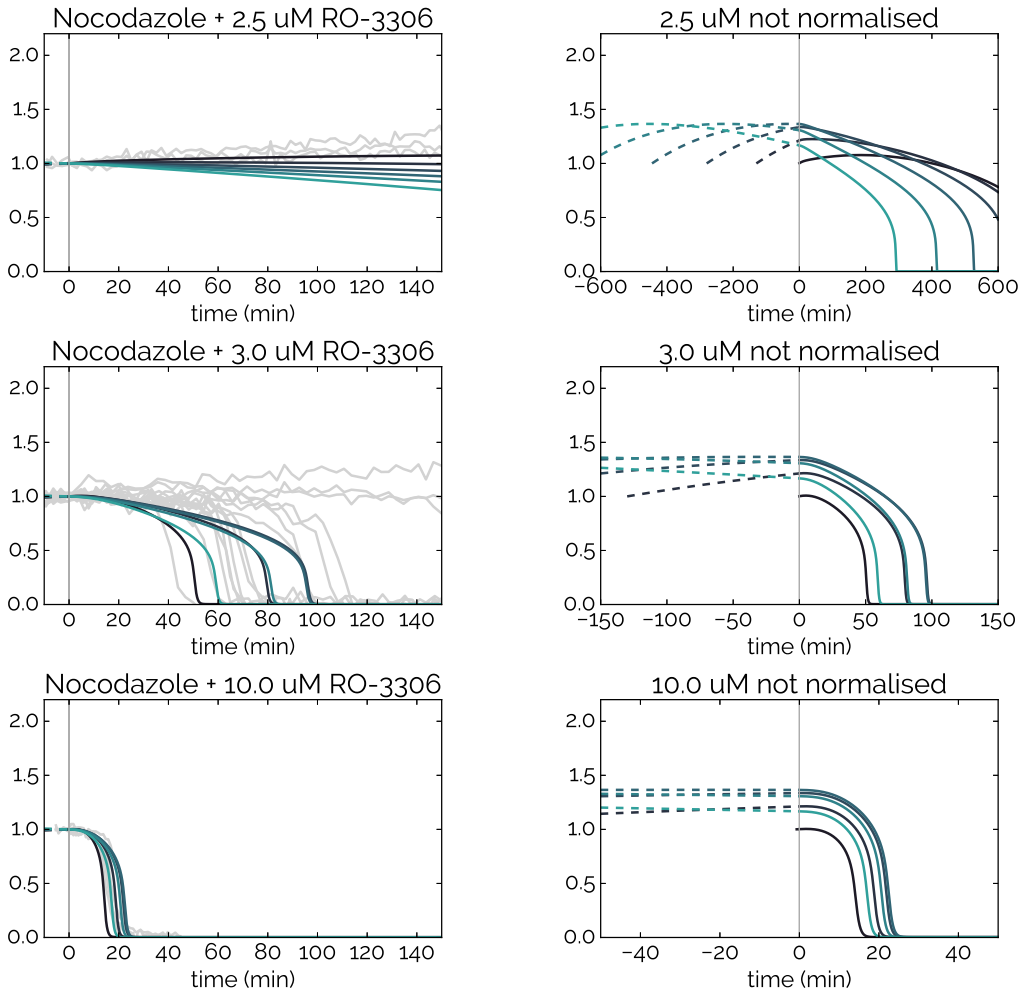


Figure 5.7: Simulation cyclin B degradation with partial Cdk1 inhbition - Simulations of cyclin B timecourses upon acute addition of CDK1 inhibitor to cells arrested in nocodazole, aligned by the time of inhibitor addition. **1**, **132**, **278**, **445**, **638**, and **841** minutes in nocodazole were simulated prior to the addition of the CDK-inhibitor. **Left Column:** Timecourses are normalised to the cyclin B level at the time of addition of the inhibitor, and corresponding experimental data are shown in grey. **Right Column:** The dashed lines show the timecourse of cyclin B prior to addition of the inhibitor.

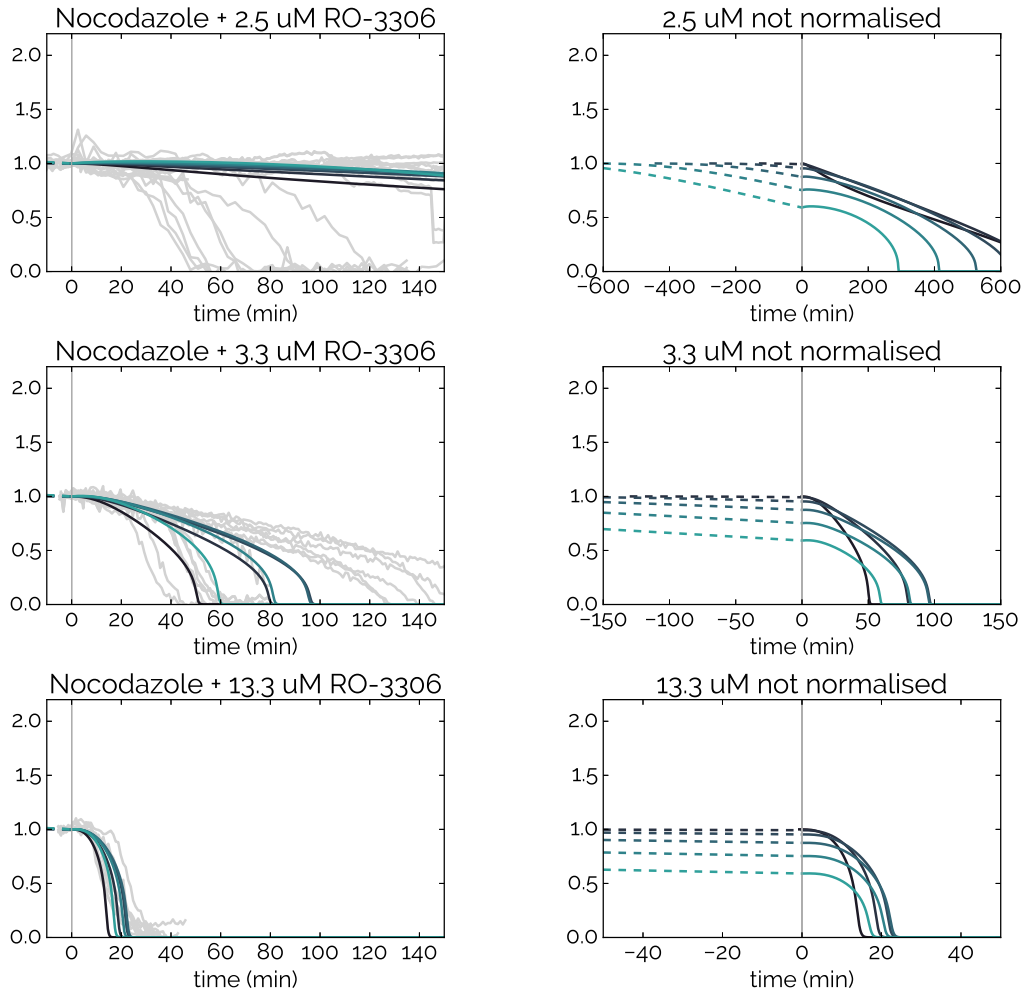


Figure 5.8: Simulation securin degradation with partial Cdk1 inhbition - Simulations of securin timecourses upon acute addition of CDK1 inhibitor to cells arrested in nocodazole, aligned by the time of inhibitor addition. **1**, **132**, **278**, **445**, **638**, and **841** minutes in nocodazole were simulated prior to the addition of the CDK-inhibitor. **Left Column:** Timecourses are normalised to the securin level at the time of addition of the inhibitor, and corresponding experimental data are shown in grey. **Right Column:** The dashed lines show the timecourse of securin prior to addition of the inhibitor.

5.2.4 Bifurcation Analysis

To investigate this unexpected behaviour further, I performed bifurcation analysis [1] on the model.

5.2.4.1 Evolution in Time

Due to the decaying rate of cyclin B synthesis and the crucial role of cyclin B:CDK1 in the system, we cannot speak of true steady states. To demonstrate this evolution in time, I converted the exponentially decaying rate of cyclin B synthesis to a fixed parameter, and treat it as a bifurcation parameter. This measure is necessary to enable the analysis of the system's steady states, and corresponds to a separation of timescales. Starting from the steady state of cyclin B corresponding to a situation where all kinetochores are unattached ($uKT_t = 1$), the programme computes how the steady state changes when the bifurcation parameter (k_{scycb}) is varied.

The resulting diagram is shown in the left panel of figure 5.9, where the black line indicates how the bistable regime changes as (k_{scycb}) is varied. For values of k_{scycb} larger than $0.0025 AU\ min^{-1}$, the system displays bistability. As k_{scycb} drops further, the bistable regime is lost.

An interesting alternative perspective on this dependence is given in the right panel of figure 5.9. Here, I converted values for k_{scycb} to time by rearranging the equation defining the decaying rate of synthesis

$$k_{scycb,t} = k_{scycb,initial} \cdot e^{-r_{decay} \cdot t} \tag{5.12}$$

to

$$t = -\frac{log(\frac{k_{scycb,t}}{k_{scycb,initial}})}{r_{decay}} \tag{5.13}$$

Notably, bistability is lost after approximately 844 min. However, most cells stably arrest in mitosis for more than 1000 min, which may be due to a persistent partitioning in the vector field governing cyclin B turnover into a slow domain (APC/C is inhibited) and a fast domain (APC/C is active).

[1] Bifurcation analysis was performed using Bard Ementrout's XPPAut tool (`http://www.math.pitt.edu/~bard/xpp/xpp.htmL`). The model was exported to an XPPAut-compatible ODE-file, which is provided under `https://github.com/el-uhu/thesis-notebooks/blob/master/Chapter5/bifurcation.ode`.

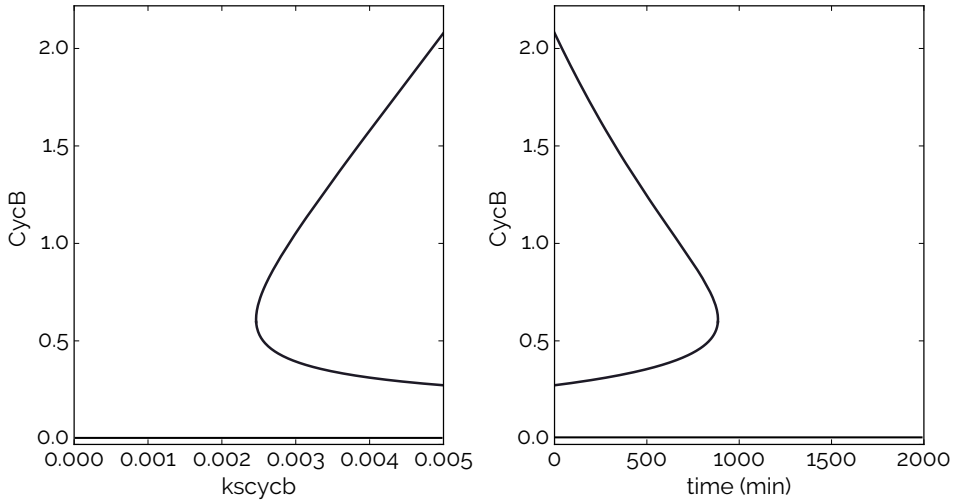


Figure 5.9: Transient Bistability - **Left:** Diagram indicating how steady states of cyclin B (black line) change as k_{scycb} is lowered. **Right:** k_{scycb} decays exponentially in the model, and can therefore be converted into time. The black line indicates how steady states of cyclin B change as a function of time, and disappear after 844 minutes.

Table 5.3: Bifurcation Diagram Snapshots: k_{scycb} and corresponding times

k_{scycb}	time (min)
0.0050	**1**
0.0045	**132**
0.0040	**278**
0.0035	**445**
0.0030	**638**
0.00255	**841**

To account for this change over time in the analysis of the system, several "snapshots" of bifurcation diagrams in terms of other bifurcation parameters were taken at a range of fixed k_{scycb} parameters (listed in table 5.3).

5.2.4.2 Sensitivity

Next, I produced a bifurcation diagram using cyclin B levels as the dynamic variable (y-Axis), and the fraction of unattached kinetochores as the bifurcation parameter (uKT_t). Figure 5.10 shows the corresponding bifurcation diagrams calculated according to the procedure above. Sensitivity towards unattached kinetochores is given as the position of the unstable steady states (shown in the figure as dashed

lines). The model exhibits exquisite sensitivity towards unattached kinetochores, as indicated in figure 5.10 by the fact that the upper saddle nodes are close to the ordinate and, for a particular value of k_{scycb}, change very little for cyclin B levels larger than 0.5. As a consequence of the evolution of the system in time, the checkpoint becomes less sensitive with increasing duration of the nocodazole arrest, which is illustrated by the semi-logarithmic plot show in the left panel of figure 5.10.

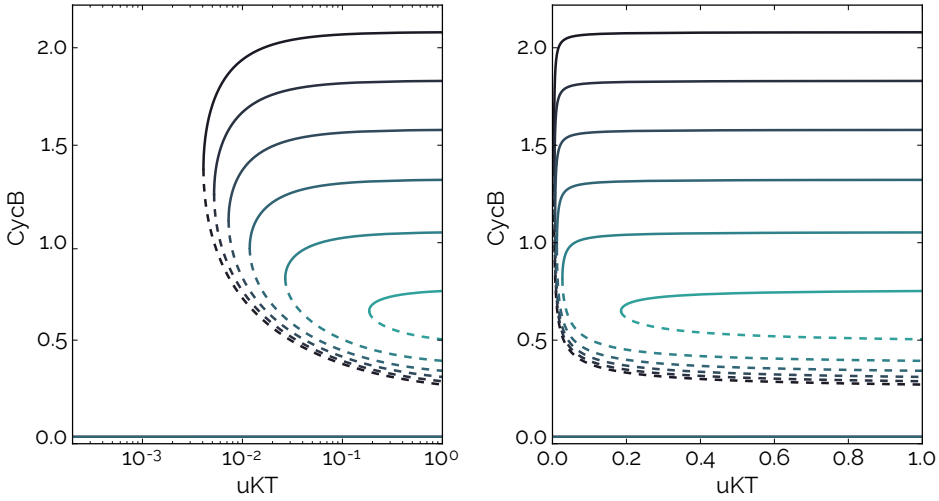


Figure 5.10: Bifurcation Diagrams: uKT vs. cyclin B - Bifurcation diagrams depicting how steady states of cyclin B change as the fraction of unattached kinetochores (uKT, treated as a parameter) varies. Stable steady states are shown as solid lines, whereas unstable steady states are represented by dashed lines. The bifurcation diagrams were computed for values of k_{scycb} corresponding to **1**, **132**, **278**, **445**, **638**, and **841** minutes in nocodazole. **Left:** Logarithmic scale; **right:** Linear scale.

5.2.4.3 CDK1 Dependence

To investigate how partial inhibition of CDK1 affects the dynamics of the checkpoint system, I used the Inh parameter as a bifurcation parameter, and generated bifurcation diagrams for the range of k_{scycb} parameters listed in table 5.3. The resulting diagrams are shown in figure 5.11. In order to facilitate interpretation, I converted the Inh parameter to the maximal possible residual CDK1 activity after inhibition according to the following equation:

$$[CDK1]_{max} = \frac{100\%}{1 + Inh} \tag{5.14}$$

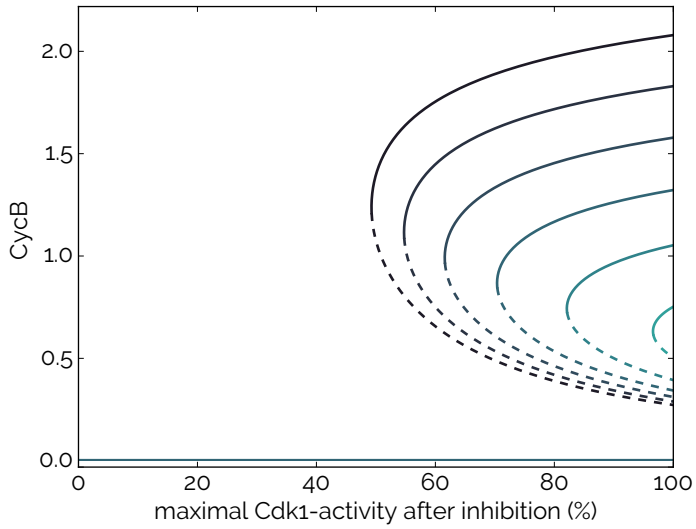


Figure 5.11: Bifurcation Diagram: maximal CDK1 activity vs. cyclin B - Bifurcation diagram indicating how the steady state of cyclin B changes as a function CDK1 inhibition. Stable steady states are shown as solid lines, whereas unstable steady states are represented by dashed lines. The Inh parameter was converted to maximal residual CDK1 activity (%) using equation 5.14. The bifurcation diagrams were computed for values of k_{scycb} corresponding to **1**, **132**, **278**, **445**, **638**, and **841** minutes in nocodazole.

Early on in the arrest, when k_{scycb} is still high, the bistable domain is maintained even if the addition of the inhibitor reduced the activity of CDK1 to just above 50%; as the rate of cyclin B synthesis (k_{scycb}) drops, the system becomes more and more sensitive to inhibition of CDK1.

This set of bifurcation diagrams provides a useful tool to reason about the unexpected response to CDK1 inhibition uncovered by simulations of cells treated with different doses of CDK1 inhibitor when arrested in nocodazole. Before the addition of CDK1 inhibitor, the maximal possible CDK1 activity is 100 %. Depending on the level of cyclin B at a given point in time, the state of the system is described by a point along the far right of the diagram in figure 5.11. Acute inhibition of CDK1 moves the state of the system towards the left.

To simulate the addition of $13.3\ \mu M$ or $10.0\ \mu M$ RO-3306, best results were obtained by choosing $Inh = 5.0$, corresponding to an inhibition of 84 % of CDK1 ($[CDK1]_{max} = 16\%$). Data for the addition of $3.3\ \mu M$ or $3.0\ \mu M$ RO-3306 were best described by choosing $Inh = 2.2$ ($[CDK1]_{max} = 31.25\%$). In both cases, the extent of CDK1 inhibition was sufficient to completely "push" the system out of the bistable regime, even if the addition of the inhibitor occurred after a very short ar-

rest in nocodazole, when the rate of cyclin B synthesis was still high. For the higher dose, the inhibition is strong enough to push the system far away from the bifurcation point, and the degradation of cyclin B becomes accelerated with only a minor delay. However, in the case of the lower dose, the system is not pushed very far from the bifurcation point. As a consequence, we observe critical slowing down in the timecourse simulation, giving rise to a delay in the accelerated degradation of cyclin B.

The situation is markedly different for cells treated with $2.5\ \mu M$ RO-3306, which were modelled with an Inh parameter set to 0.75 ($[CDK1]_{max} = 57.14\%$. Here, the extent of the inhibition was not sufficient to "push" the system completely out of the bistable regime, which means that the time it takes for cyclin B to be degraded in an accelerated fashion depends strictly on the duration of the arrest before the inhibitor was added.

5.2.5 Prediction

Crucially, in simulations describing the addition of a very low dose of CDK1 inhibitor, the time it took for cyclin B to become degraded was shortened significantly compared to the timing of pure mitotic slippage (figure 5.12 middle panel). To explore this observation in more detail, I generated simulations for an even smaller dose of CDK1 inhibitor. The top panel in figure 5.12 shows the result of a simulation generated for an inhibitor dose that reduced the maximum CDK1 activity to 71 % ($Inh = 0.4$). These simulations further substantiate the claims formulated above, and allow us to make the following prediction: Partial inhibition of CDK1 activity accelerates mitotic slippage.

5.2.6 Validation

To test this prediction, my collaborators arrested cells in nocodazole, treated them with $0.75\ \mu M$ RO-3306 ($n = 20, N = 2$), and measured the relative fluorescence of cyclin B for up to $2300\ min$ after the addition of the inhibitor. Indeed, in the majority of cells, we observed mitotic slippage-like degradation patterns that were advanced in time by $1250 - 500\ min$ (grey timecourses in the bottom panel of figure 5.12).

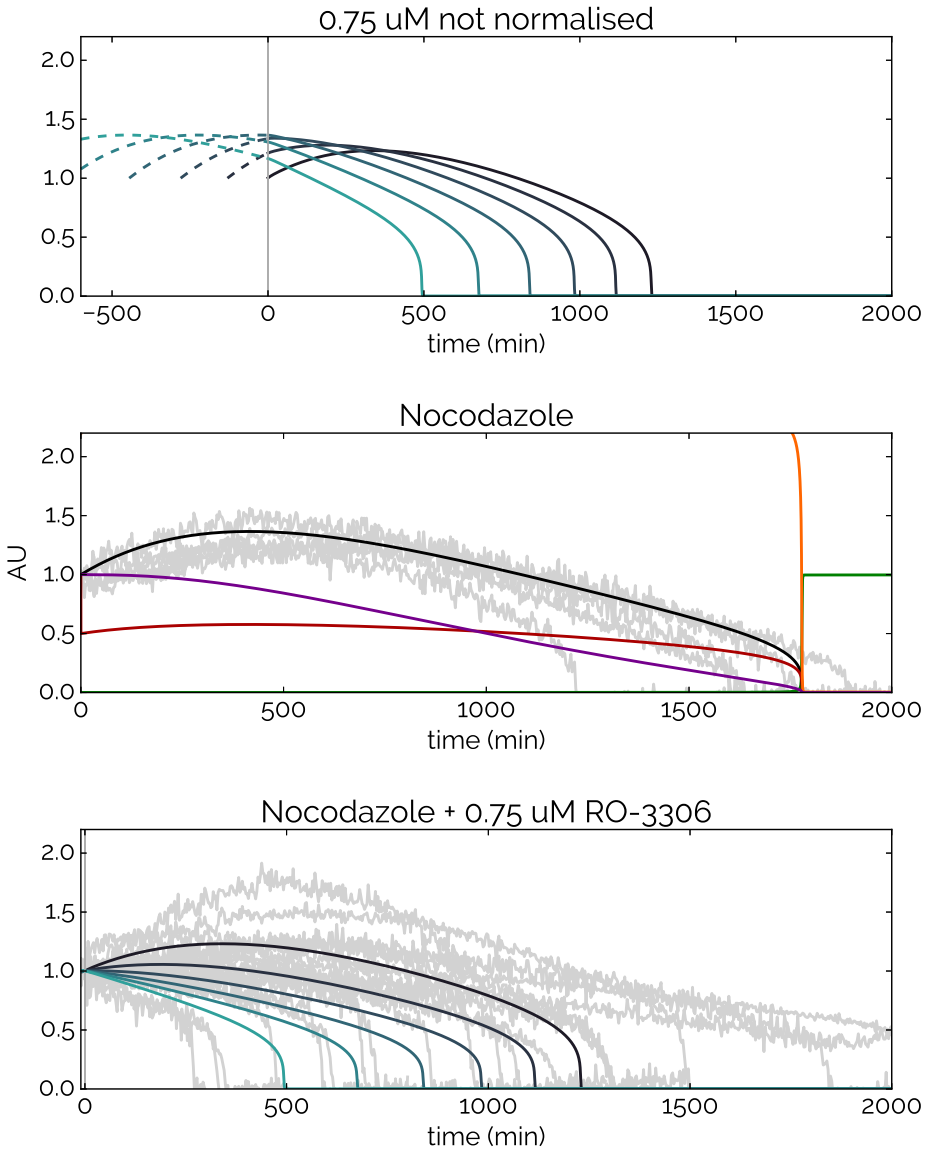


Figure 5.12: Minimal CDK1 Inhibition Accelerates Mitotic Slippage - **Top:** Simulations of cyclin B timecourses upon acute addition of a low-dose of CDK1 inhibitor ($[CDK1]_{max} = 71\%$) to cells arrested in nocodazole, aligned by the time of inhibitor addition. **1**, **132**, **278**, **445**, **638**, and **841** minutes in nocodazole were simulated prior to the addition of the CDK1 inhibitor. **Middle:** Simulation of nocodazole treatment showing timecourses for **cyclin B**, **securin**, **total MCC**, **free APC/C** and **total uKT** contrasted with corresponding experimental data of cyclin B($n = 9, N = 3$). **Bottom:** As in top panel, but timecourses are normalised to the time of inhibitor addition and contrasted with the experimental data of RPE1 cells treated them with $0.75\ \mu M$ RO-3306 ($n = 20, N = 2$). Grey timecourses depict experimerimental validation.

5.3 Discussion

Using a combination of targeted drug-treatments, quantitative live-cell imaging and mathematical modelling, we performed a comprehensive analysis of the signalling dynamics of the mitotic checkpoint. We found that the degradation patterns of fluorescently tagged cyclin B and securin observed upon acute addition of CDK1 inhibitor to HeLa and RPE1 cells arrested in nocodazole are best explained by a hypersensitive dependence of checkpoint activity on the activity of CDK1. We show that a mathematical model incorporating a CDK1-mediated double-negative feedback loop within the checkpoint enforcement mechanism ($CDK1 \rightarrow MCC \dashv APC/C \dashv CDK1$) is consistent with the experimental data and accounts for the observed hypersensitive dependence, as a characteristic phenomenon associated with the bistable switch arising from systems-level feedback within the regulatory network.

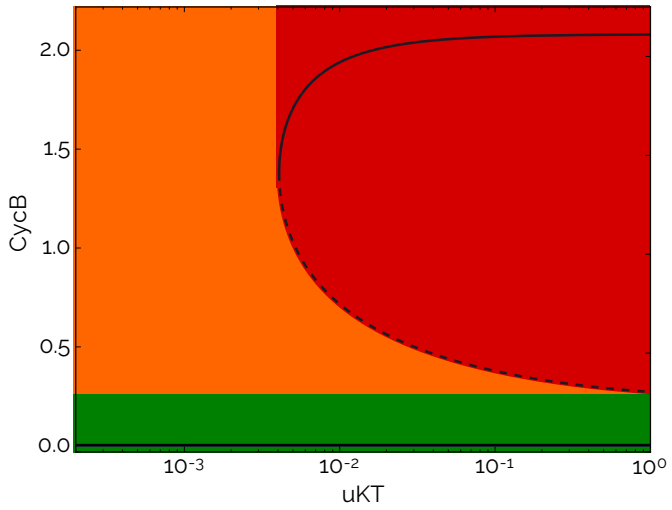


Figure 5.13: Bifurcation diagram and contextual framework - Bifurcation diagrams depicting how steady states of cyclin B change as the fraction of unattached kinetochores (uKT, treated as a parameter) varies. Stable steady states are shown as solid lines, whereas unstable steady states are represented by dashed lines. The background colours were chosen to reflect those used in figure 5.1 and illustrate the following states of the checkpoint system: **active and engaged/ unsatisfied**, **active and disengaged/ satisfied**, **inactive**,

Whereas our study is limited to cells that are unable to form attachments due to the treatment with a high dose of nocodazole, our model carries significant explanatory power to reconcile apparently contradictory findings pertaining to the anaphase problem and mitotic slippage, and bears significance for cells undergoing unperturbed mitosis.

The bistable switch provides a framework from which a qualitative description of the states of the signalling system (figure 5.13), and quantitative predictions pertaining to the transition between these states emerge naturally. Treating cells with nocodazole represents a limit-case of checkpoint signalling. For this case, we find a threshold of CDK1 activity (corresponding to the unstable steady state (dashed line) at $uKT = 1$ in figure 5.13), which - when crossed - drives the inactivation of the checkpoint. This transition has to be considered irreversible, because all kinetochores are unattached in this case (the signal is maximal) and no additional increase in signal strength to drive the reactivation of the checkpoint is possible. The bistable switch hypothesis allows us to generalise this finding, and formulate the prediction that the same threshold should be operational in cells undergoing unperturbed mitotic progression. Crossing of the unstable branch in the bifurcation diagram as kinetochores become attached (change in the x-dimension in figure 5.13) may satisfy the checkpoint, but the capacity to become re-engaged, by detaching a fraction of kinetochores and horizontally crossing the unstable branch again, is retained as long as cyclin B levels are high enough. From this vantage point, the findings by Dick and Gerlich [216] that cells challenged in metaphase with the detachment of individual kinetochores have a transient capacity to re-engage, which is lost at some point in metaphase, may be interpreted as a consequence of experimentally tracing out the unstable branch of the bifurcation diagram. As such, a bistable switch may contribute to the avoidance of the anaphase problem. Recent findings by Kamenz *et al.* [219] suggest that slow kinetics of reactivation, rather than a defined threshold, are responsible for the avoidance of the anaphase problem. In this context, the hypothesis that the mitotic checkpoint is regulated by a bistable switch presents a vantage point where slow kinetics of reactivation and thresholds are not presented as opposing concepts, but rather as two coexisting facets of the system's dynamics.

6

Dispatch

The work presented in this chapter was conducted in collaboration with Michael Cundell (MC), Ricardo Nunes Bastos (RNB), Elena Poser (EP), James Holder (JH), Shabaz Mohammed (SM), Bela Novak (BN) and Francis Barr (FB) at the Department of Biochemistry, University of Oxford. It was published in 2016 in the Journal of Cell Biology [241]. The underlying experiments were designed by MC, RNB, SM and FB, and carried out by MC, RNB, EP and JH. I developed and performed the model-driven data analysis of the bulk phosphoproteomics data, and worked with FB on the analysis of the results. BN developed the model for the electrostatic interaction between PP2A:B55 and its substrates. This chapter presents the data analysis in detail, and provides an overview of the work following the data analysis.

Exit from mitosis is initiated with the disengagement of the mitotic checkpoint. Yet, to successfully complete cell division, a diverse set of processes - such as the formation of a central spindle, chromatin de-condensation, nuclear envelope reformation and the reassembly of the Golgi apparatus - have to be tightly controlled in an integrated spatial and temporal fashion. How is the singular event corresponding to the decision to exit mitosis dispatched to initiate these processes?

At a molecular level, mitotic exit is understood to be regulated by proteolysis, as well as phosphorylation and de-phosphorylation. Phosphatases from the PPP-family are known to play a crucial role in mitotic exit and cooperate to produce a precisely timed wave of phosphatase activity that strictly follows chromatin disjunction: A holo-enzyme, consisting of protein phosphatase 2A (PP2A) and a B55-family regulatory subunit, is kept inactive throughout mitosis by the B55-ENSA-Greatwall-pathway: Greatwall-MASTL kinase is activated through phosphorylat-

ion by cyclin B:CDK1 and phosphorylates ENSA and ARPP19. Phosphorylated ENSA and ARPP19 act as inhibitors of PP2A:B55 via unfair competition: They associate tightly in phosphorylated form and get de-phosphorylated following slow first-order kinetics [208]. Throughout mitosis, Greatwall-MASTL maintains a pool of phosphorylated ENSA and ARPP19 in excess over PP2A:B55, therefore keeping it inhibited. With the APC/C:Cdc20-driven degradation of cyclin B, the rate of Greatwall-MASTL phosphorylation drops and Greatwall-MASTL gets inactivated by PP1. PP2A:B55 gains the upper hand and de-phosphorylates ENSA and ARPP19, releasing itself from its inhibition. This pathway generates a delay that ensures that the activation of PP2A:B55 follows chromatin disjunction [101].

PP2A:B55 has been shown to regulate the anaphase spindle protein PRC1, and has been implicated in the control of the reassembly of the Golgi apparatus via GM130. Yet, its importance plausibly extends beyond these two substrates: Removal of the ENSA-Greatwall inhibitory pathway leads to constitutively active PP2A:B55, which results in a mitotic catastrophe, premature assembly of the central spindle and precocious cytokinesis. In spite of its central role in orchestrating mitotic exit, very few substrates of PP2A:B55 are known. Moreover, our understanding of how it recognises its substrates is incomplete.

6.1 Data

6.1.1 Theoretical Premise

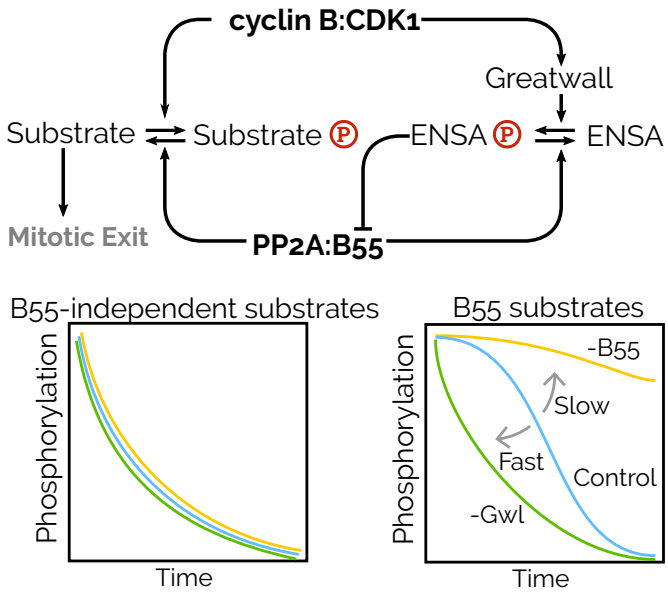


Figure 6.1: Theoretical Premise - Expected Phosphorylation Profiles for PP2A:B55-dependent and -independent substrates

To gain a better understanding of the precise role of PP2A:B55 in orchestrating exit from mitosis, to identify novel substrates of PP2A:B55 and to elucidate the molecular basis for how it recognises its substrates, we conducted a comprehensive study of the mitotic phospho-proteome. In the design of this study, we exploited theunique dynamic features of the PP2A:B55-ENSA-Greatwall pathway:

The activity of PP2A:B55 towards its substrates is inhibited by the presence of phosphorylated ENSA and ARPP19. ENSA and ARPP19 are present in excess over PP2A:B55. Following the inactivation of Greatwall-MASTL, PP2A:B55 first has to de-phosphorylate ENSA and ARPP19 in order to become fully active. Therefore, substrates of PP2A:B55 should display delayed de-phosphorylation kinetics manifested through a characteristic shoulder in their phosphorylation profile over time. Moreover, de-phosphorylation profiles of PP2A:B55 substrates should be sensitive to perturbations affecting the activatory subunit B55, and Greatwall-MASTL. Reduced levels of the activatory subunit B55 should reduce the activity of PP2A:B55 towards its substrates and result in a further delay of substrate de-phosphorylation. On the other hand, reduced levels of Greatwall-MASTL should lower the steady state level of phosphorylated ENSA in the cell, leading to accelerated de-phosphorylation of PP2A:B55 substrates and abolishment of the characteristic delay.

Thus, substrates of PP2A:B55 are expected to show a characteristic dynamic response in their phosphorylation profiles under unperturbed conditions, B55 depletion and depletion of Greatwall-MASTL. Conversely, substrates that are subject to regulation by other phosphatases are expected to behave similarly under these three conditions (figure 6.1).

6.1.2 Experimental Setup

Based on this theoretical premise, we developed a protocol to study the phosphoproteome of whole-cell extracts of HeLa cells in a time-resolved manner. We compared cells from a phosphatase-active control condition (Control), with phosphatase-hypo-active cells (B55) where B55 was depleted via RNAi, and phosphatase-hyper-active cells (Gwl), where Greatwall-MASTL was depleted by RNAi.

6.1.2.1 Preparation of Cell Extracts and de-phosphorylation Assay

Cells were transfected with siRNA duplexes targeting luciferase (Control), B55 regulatory sub-units (PPPR2AD) (B55) or MASTL (Gwl) for 54h, before they were incubated with $100 ng\ \mu L$ nocodazole for 18h to arrest cells in mitosis. Following wash-

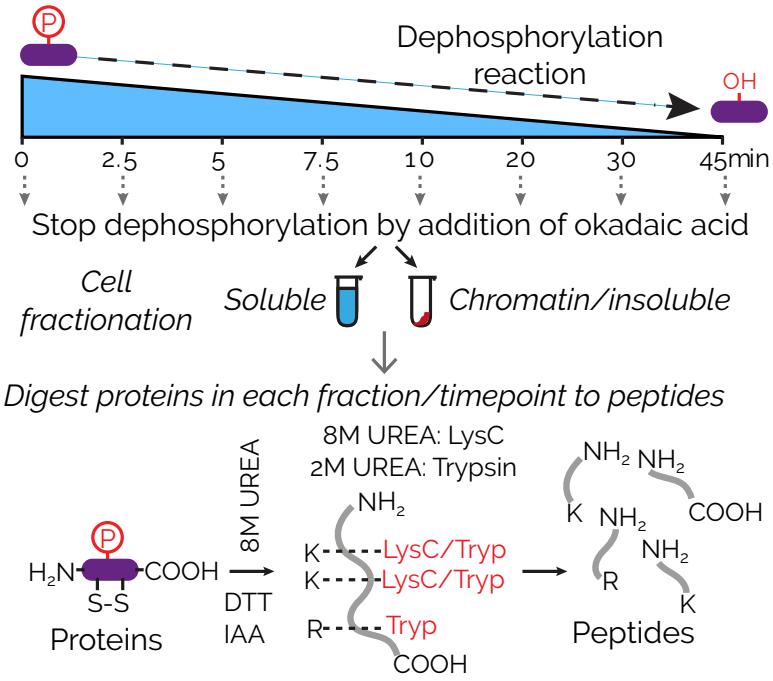


Figure 6.2: In Vitro de-phosphorylation Assay and Sample Preparation

out of nocodazole with ice-cold PBS, cells from each condition were split into two aliquots and lysed on ice.

For one aliquot, the lysis buffer was supplemented with 2 μM of the phosphatase inhibitor ocadaic acid, to capture the state of the phospho-proteome before activation of the phosphatase. These samples were subsequently treated as timepoint $t = 0\ min$. From the other aliquot, samples were taken after 2.5 min, 5.0 min, 7.5 min, 10.0 min, 20 min, 30 min and 45 min, and supplemented with 2 μM ocadaic acid to stop the de-phosphorylation reaction. Subsequently, all samples were separated into chromatin and soluble fractions by means of centrifugation for 15 min at 20000 g_{av}, 4°C, before they were snap-frozen and stored at −80°C.

Supernatant samples were thawed, and protein precipitated with trichloroacetic acid for 1 h on ice, before centrifugation for 5 min at 20000 g_{av}, 4°C. Precipitated proteins were washed with acetone and solubilised in 8 M urea. Chromatin samples were re-suspended in 50 mM ammonium bicarbonate solution, and solubilised in 8 M urea.

All samples were reduced using 4 mM DTT for 25 min at 56°C, and alkylated using 8 mM iodoacetamide incubation in the dark for 30 min. Proteins were then digested with lysyl endopeptidase (4 h at 37°C), followed by trypsin (12 h at 37°C). Digestions were quenched by acidification with 5% formic acid.

6.1.2.2 Phosphoproteomics Labelling Strategy

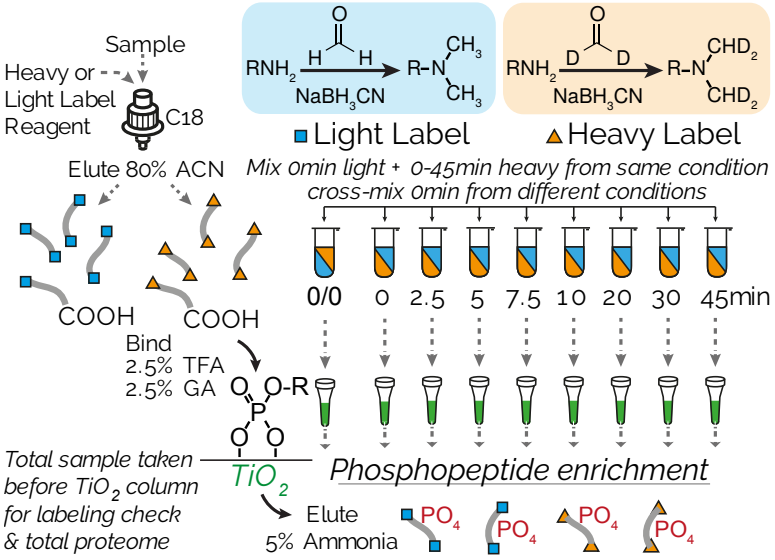


Figure 6.3: SILAC-Labelling Strategy

Only a small fraction of the overall proteome is phosphorylated, dramatically decreasing the likelihood of observing phosphorylated peptides in the mass spectrometer. To alleviate this problem and to enable quantitative assessment of the extent of phosphorylation over time, we devised a strategy entailing the labelling of peptides corresponding to all sampled timepoints and peptides corresponding to timepoint $t = 0$ with isotopically distinct labels followed by phospho-peptide enrichment.

To this end, tryptic peptides (equivalent to $0.32\ mg$ to $2.5\ mg$ of total supernatant protein) were bound to SepPak C18-reverse phase columns, and subjected to on-column dimethyl labelling [242]: Peptides from all timepoints of the de-phosphorylation assay were labelled with cyanoborohydride and deuterated formaldehyde (heavy label). One aliquot of the $0\ min$ timepoint was labelled with formaldehyde and cyanoborohydride (light label). The labelling resulted in a mass increase of $28\ Da$ per primary amine for the light label, and $32\ Da$ per primary amine for the heavy label. $200\mu g$ of heavy- and light-labelled samples were mixed, resulting in samples containing heavy- and light-labelled peptides. All samples were subsequently enriched for phospho-peptide using microspin columns packed with titanium dioxide ($34\ g$ for $5\ min$).

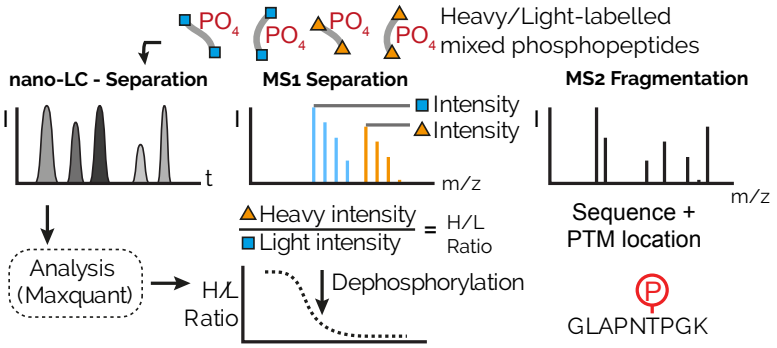


Figure 6.4: Proteomics Pipeline and Preliminary Data Processing

6.1.2.3 Proteomics Pipeline

Thus, quantification of the phosphorylation of a peptide at any of the sampled time-points (heavy label) was possible by comparing the mass spectrometry signal intensity of the heavy-labelled phosphorylated peptide with the corresponding light-labelled phosphorylated peptide ($t = 0$) within the same sample.

Liquid chromatography (LC) was performed using an EASY-nano-LC 1000 system. Phospho-peptides were initially trapped on a Reposil-Gold 120 C18 ($3\ \mu m$, $0.012 \mu m$ pores, $0.1\%\ [vol/vol]$ formic acid in water) guard at constant pressure ($500\ bar$), and separated on an EASY-Spray column headed at $45°C$ using a $3\ h$ linear $8 - 30\%\ [vol/vol]$ acetonitrile gradient and constant $200\ nl/min$ flow rate.

An EASY-Spray nano-electrospray ion source was used to introduce the peptides into an Orbitrap Elite mass spectrometer. Spectra were acquired with resolution 30000 m/z range $350 - 1500 \cdot 10^6$ AGC target, maximum injection time $250\ ms$. The 20 most abundant peaks were fragmented using CID (AGC target $5 \cdot 10^3$, maximum injection time $100\ ms$) or ETD (AGC cation and anion target $5 \cdot 10^3$ and $2 \cdot 10^5$, respectively, maximum injection time $100\ ms$, normalised collision energy 35%) in a data-dependent decision tree method.

Peptide identification and quantitation of heavy to light phospho-peptide ratios were then performed using MaxQuant [243, 244].

6.2 Model-Driven Data-Analysis

This phospho-proteomics approach yielded a dataset comprising entries for 46802 phospho-peptides. Each entry contained data on the position of the phosphorylation within the corresponding protein, the ratio of measured intensities of the corresponding heavy- and light-labelled species, as well as quality measures, such

as calculated experimental errors and identification probabilities. The aim of the analysis of these data was to render this complex dataset more accessible, by first extracting the good quality data from the full dataset, and by subsequently clustering them, to identify substrates of PP2A:B55 in an automated and reproducible manner.

To this end, I developed a model-driven data analysis strategy. Data were first cleaned and filtered based on general quality criteria. Then a mathematical model was fitted to each entry within this cleaned-up dataset. By expressing the fundamental hypothesis that informed the experimental design in terms of coupled ordinary differential equations, parameters underlying the model, along with a suitable objective function, could then be used as numeric measures of B55 substrate character. The following section will first detail the pre-processing steps employed to clean up and filter the raw dataset, and then describe the model, the parametrisation strategy, as well as the results of this analysis.

6.2.1 Preparation of the Dataset

In the initial stage of data analysis, I focused on transforming the output-table generated by MaxQuant into a dataset that would be more amenable to analysis by means of a mathematical model. To this end, data for different timepoints, experimental conditions and experimental repeats corresponding to a particular peptides were aggregated and organised.

6.2.1.1 Pre-processing

> **Interactive Notebook - Preprocessing** (static version)

In order to facilitate access to the data in the MaxQuant-Table using a simple query routine, some columns were renamed: For multiple measurements of a quantity, MaxQuant attaches a number to the end of the column header. This breaks the naming pattern otherwise followed, where information on the type of data is followed by the experiment identifier. To address this problem, the column names are changed by moving these numbers before the experiment identifiers.

6.2.1.2 Extracting Data from the MaxQuant-Table

Interactive Notebook - Extracting (static version)

In order to analyse the timecourses, I extracted timecourse data from the columns containing information on the normalised Heavy-over-Light Ratio: Means and standard errors are calculated across the different experimental repeats. Furthermore, I extracted the relevant cross-mixing data, information on the gene name and protein ID of the peptide, as well as information on the position of the phosphorylation site in the sequence of the corresponding protein. To account for potential differences between the behaviour of a peptide in the supernatant and in the pellet fraction, they are treated separately: If a peptide was measured in both fractions, it is recorded as two separate entries.

6.2.1.3 Summarisation and Cleaning of the Dataset

Interactive Notebook - Cleaning (static version)

The detection of a peptide by the mass spectrometer is an inherently stochastic process. Thus, signals are not detected for every peptide at every point in time. This presents a considerable challenge to the model-driven analysis: Further downstream in the analysis pipeline, the objective function is used to assess the agreement between model simulation and experimental data, in order to determine the parameter set that best describes the data in an automated fitting routine. A simple mean-square deviation was chosen as the objective function. It measures the distances between the experimental data and the simulation at the sampled timepoints, and aggregates these distances to a single value. If the number of measured datapoints varies greatly between different peptides, the parametrisation routine may yield inconsistent results, and the comparability of parameter sets may thus be compromised. An approach that would directly account for distinct patterns of missing data by clustering the data sets based on the patterns, and considering the clusters separately was considered impractical, as the number of different patterns was too large:

On the other hand, whereas individual values are frequently missing, the dataset is robust towards them due the timecourse nature of the experimental data. Moreover, it was desirable to retain as much of the potentially useful data as possible for further analysis.

Table 6.1: Patterns of missing data

Timepoints per condition	8
Conditions	3
Total timepoints, N	24
Possible states, s	2 (data present, data absent)
Number of possible patterns	$s^N = 2^{24} = 16777216$

Table 6.2: Summary of filtering steps

	total peptides	unique peptides
Extracted	46802	23401
Data for t =0	9658	8236
More than 4 data points present	9069	7743
Sufficient cross-mixing data	7446	6450
Timepoints in range	7424	6432
Gene name information present	7391	6410

To balance these requirements, I reduced the extracted dataset to its fittable subset, using the following strategy based on general quality criteria:

- Discard entries with missing data at timepoint 0.
- Discard entries with fewer than four timepoints.
- Discard entries lacking cross-mixing data relative to the control condition..
- Discard entries with normalised ratios larger than 10.
- Discard entries lacking gene name or protein identifier information.

The total number of peptides after each cleaning step, as well as the number of unique peptides (no discrimination between substrate and pellet samples) are shown in table 6.2.

6.2.1.4 Curation of the Dataset

After reducing the dataset to its fittable subset, annotations from the Panther database[1] and information of the sequence of the whole protein were added to the table.

[1] `http://www.pantherdb.org/`

6.2.2 The Model

Interactive Notebook - Model (static version)

I next devised a simple mathematical model to describe the de-phosphorylation of a phosphorylated substrate by PP2A:B55 and another, unspecified phosphatase (figure 6.5). The model is built on the following assumptions:

1. At time $t = 0$ substrates are maximally phosphorylate; CDK1 and MASTL are inactive.
2. A substrate can be de-phosphorylated following second-order kinetics. De-phosphorylation is catalysed by PP2A:B55 and an unspecified phosphatase, PPX.
3. PPX is assumed to be constitutively active, whereas PP2A:B55 is regulated by binding to its pseudo-substrate ENSA.
4. Unlike other substrates, ENSA is de-phosphorylated slowly when bound in complex with PP2A:B55. ENSA de-phosphorylation from the complex follows first order kinetics [208, 245].
5. The amount of PP2A:B55:pENSA complex is maximal at $t = 0$ and corresponds to the abundance of the limiting component.
6. Depletion of B55 by means of RNAi affects the activity of PP2A:B55, but leaves PPX unaffected.
7. Depletion of MASTL by means of RNAi reduces the pool of phosphorylated ENSA available at $t = 0$.

The network of interactions shown in figure 6.5 was converted into a system of coupled ordinary differential equations (equation 6.1) and associated algebraic equations (equation 6.1).

6.2.2.1 System of ODEs

$$\begin{aligned} \frac{dENSA_{p,total}}{dt} &= -k_{cat} \cdot B55 : ENSA_p \\ \frac{dB55{:}ENSA_p}{dt} &= k_{ass} \cdot B55_{free} \cdot ENSA_{p,free} - (k_{diss} + k_{cat}) \cdot B55 : ENSA_p \\ \frac{dSubstrate_p}{dt} &= -(k_{independent} + k_{B55} \cdot B55_{free}) \cdot Substrate_p \end{aligned} \tag{6.1}$$

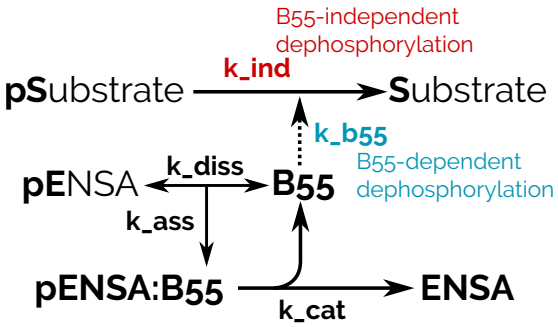


Figure 6.5: Wiring Diagram of the de-phosphorylation Model - Phosphorylated ENSA ($ENSA_p$) binds with free PP2A:B55 ($B55$). The complex formation is governed by the association and dissociation rate constants k_{ass} and k_{diss}. Phosphorylated substrates are de-phosphorylated in a process independent of PP2A:B55 (k_{ind}) and in a manner depending on free PP2A:B55 (k_{B55})

6.2.2.2 Algebraic Equations

$$\begin{aligned} B55_{free} &= B55_{total} - B55 : ENSA_p \\ ENSA_{p,free} &= ENSA_{p,total} - B55 : ENSA_p \end{aligned} \tag{6.2}$$

6.2.2.3 Model States

To capture the three different treatments, *Control*, *B55 depletion* and *Gwl depletion*, I assume three distinct states of the model that are realised by informed changes of parameters and initial conditions.

Initial values for $ENSA_{p,total}$ and $Substrate_p$ are set equal to the corresponding abundance at $t = 0$ in the experimental data, relative to the *Control* condition. Thus, the abundance of a substrate other than ENSA is assumed to be 1 under control conditions. For the B55- and MASTL-depletion conditions, I use the cross-mixing data to adjust the initial value. To capture the *B55 depletion* case, an additional parameter *depletion* is introduced, which accounts for the reduced activity of $B55_{total}$.[1]

6.2.2.4 Parameters

- k_{ass}, second-order rate constant for the association of $ENSA_p$ and PP2A:B55.
- k_{diss}, first-order rate constant for the dissociation of the $ENSA_p$:PP2A:B55 complex.

[1] As MASTL does not feature explicitly in the model, the effect of MASTL-depletion is reflected in the initial value of $ENSA_{p,total}$, and no dedicated parameter is needed.

- k_{cat}, first-order rate constant for the de-phosphorylation of ENSA$_p$ from the complex.
- k_{ind}, second-order rate constant for the PP2A:B55-independent, de-phosphorylation of Substrate$_p$ by a constitutively active phosphatase.
- k_{B55}, second-order rate constant for the PP2A:B55-dependent de-phosphorylation of Substrate$_p$.
- *depletion*, parameter reflecting the reduction in B55 activity achieved by B55 depletion.
- $B55_{total}$, parameter reflecting the abundance of PP2A:B55 relative to ENSA$_{p,total,t=0}$.
  - $B55_{total,Control} = B55_{total,GWL} = B55_{total}$
  - $B55_{total,B55} = B55_{total} \cdot depletion$

6.2.2.5 Initial conditions

- $ENSA^{sim}_{p,total,condition,t=0} = ENSA^{data}_{p,condition,t=0}$
- $Substrate^{sim}_{p,condition,t=0} = Substrate^{data}_{p,condition,t=0}$
- $B55 : ENSA_{p,condition,t=0} = min(B55_{total,condition}, ENSA_{p,total,conditiont=0})$

6.2.3 Parametrisation Strategy for the Model Core

The role of ENSA$_p$ in inhibiting PP2A:B55 is well-established, and B55-dependent de-phosphorylation of pT481 on PRC1 is well-characterised [101]. Timecourse data for the relative abundance of ENSA phosphorylated on S67 are interpreted to reflect the total pool of phosphorylated ENSA in the system (i.e. both free and PP2A:B55-bound ENSA$_p$). Timecourse data on the relative abundance of PRC1 phosphorylated on T481 reflect the abundance profile of a well-established substrate of PP2A:B55.

To estimate the activity profile of PP2A:B55 towards its substrates in a robust manner, timecourses for the ENSA and PRC1 are considered jointly: Timecourse simulations ($t = [0, 2.5, 5.0, 7.5, 10, 20, 30, 45]\ min$) of ENSA$_{p,total}$ and Substrate$_p$ are compared with the corresponding experimental data by calculating the mean square deviation across all conditions (c = [Control, B55, GWL]) in both data sets (d = [ENSA$_{p,total}$, Substrate$_p$]):

$$o(P) = \frac{\sum_d \sum_c \sum_t (y^{data}_{c,t,d} - y(P)^{sim}_{c,t,d})^2}{2 \cdot \sum_d \sum_c \sum_t (1)} \tag{6.3}$$

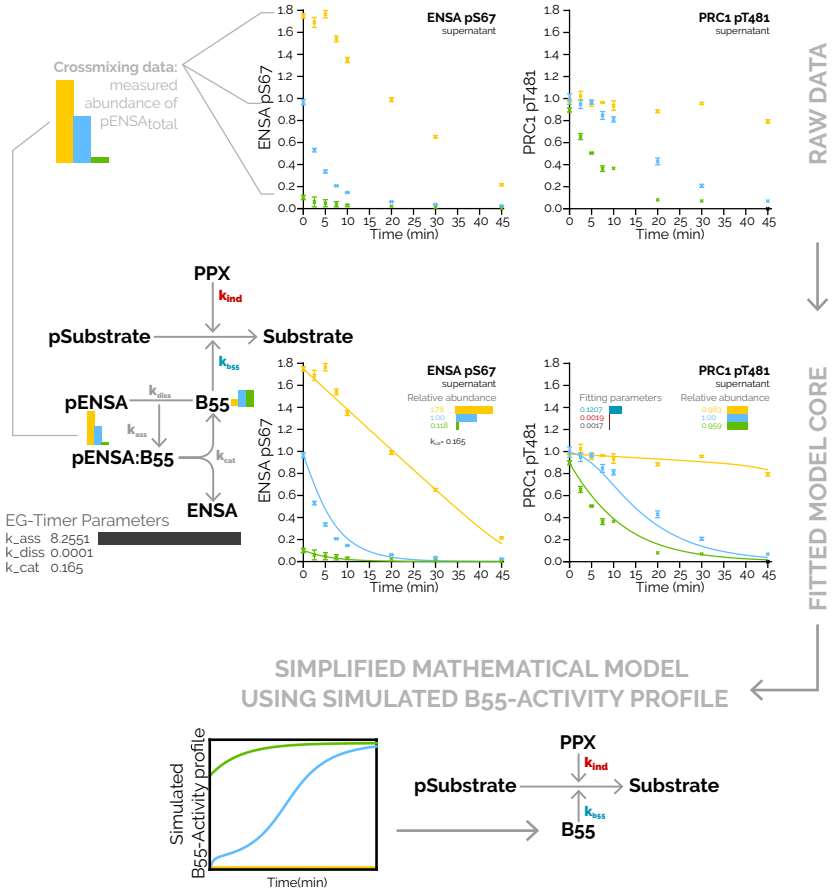


Figure 6.6: Parametrisation of the model core - Experimental data for the de-phosphorylation of the PP2A:B55-inhibitor ENSA$_p$ and the well-validated PP2A:B55-substrate PRC1 pT481 are jointly considered to fit the model. Timecourse data are corrected based on the cross-mixing data that for B55- and MASTL-depletion indicate abundance of the phosphorylated peptide at $t = 0$ relative to the control condition. The model is fitted to the data using a box-constrained interior point algorithm. From the optimal parameter set an activity profile for B55 is calculated (timecourses indicated in the bottom section of the figure).

Crosses indicate means of experimentally measured heavy-over-light intensities across the experimental repeats, error bars indicate the corresponding standard error. Simulations are shown as solid lines. Color code: **Conditions:** Control, B55 depletion, MASTL depletion; **Fitting parameters:** k_{B55}, k_{ind}; **Value of the objective function:** $o(P)$

Table 6.3: Summary of filtering steps

parameter	value	unit
k_{ass}	8.2251	$min^{-1}\ AU^{-1}$
k_{diss}	0.0001	min^{-1}
k_{cat}	0.1650	min^{-1}
$B55_{total}$	0.7303	AU
$depletion$	0.3099	
$k_{ind,\ PRC1\ pT481}$	0.0019	$min^{-1}\ AU^{-1}$
$k_{B55,\ PRC1\ pT481}$	0.1207	$min^{-1}\ AU^{-1}$
$o(P)$	0.0017	

At the optimal parameter set P, the objective function $o(P)$ becomes minimal. An interior-point algorithm for box-constrained minimisation problems was used to find the optimal parameter set. The parametrisation strategy is illustrated in figure 6.6. The set of parameters determined using this approach are listed in table 6.3

6.2.4 Global Parametrisation Strategy

Observations on the abundance of individual phosphorylated peptides in the data-set stem from the same set of experiments that informed the parametrisation of the model core. I therefore assumed that each peptide should be exposed to the activity of *PP2A:B55* as determined by the model core. Assuming that the de-phosphorylation of substrates other than ENSA does not significantly reduce the activity of PP2A:B55, we can reduce the model to the *Substrate-Sub-module* (figure 6.6 bottom section) and treat the B55 activity as input data. I obtain the B55 activity from simulations of the model core using the optimal parameter set.

Integrating the differential equation for Substrate$_p$,

$$\frac{dSubstrate_p}{dt} = -(k_{independent} + k_{B55} \cdot B55_{free}) \cdot Substrate_p \tag{6.4}$$

gives an expression for the abundance of the phosphorylated substrate at a given point in time (t) that depends on t and the integral of B55 activity between $t = 0$ and t:

$$Substrate_p(t) = exp(-k_{ind} \cdot t - k_{B55} \cdot \int_0^t B55(t)dt) \tag{6.5}$$

This integral can be approximated by the rectangle method:

$$\int_0^t B55(t)dt \simeq \sum_{t=0}^{t_{end-1}} (t_{i+1} - t_i) \cdot B55(t_i) \tag{6.6}$$

The expression for the abundance of a phosphorylated substrate therefore becomes:

$$Substrate_p(t) \simeq exp(-k_{ind} \cdot t - k_{B55} \cdot \frac{t \cdot \sum_{t=0}^{t} B55(t)}{\sum_{t=0}^{t} 1}) \tag{6.7}$$

Using this expression and an interior-point algorithm for box-constrained minimisation problems, the dataset comprising thousands of timecourses for potential B55-dependent substrates can be fitted in a very efficient manner, as it no longer relies on the system of ODEs to be solved repeatedly. The global parametrisation strategy is illustrated in figure 6.7.

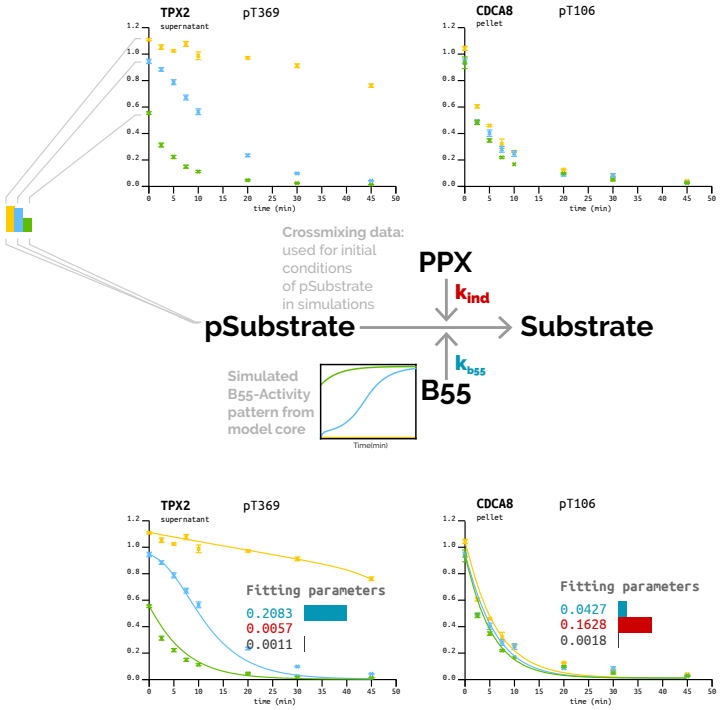


Figure 6.7: Phospho-proteome-wide fitting of the simplified model to timecourse data - The calculated activity profile of B55 is used as an input in a reduced formalisation of the mathematical model. This simplified model is fitted to the timecourse data of each peptide using a box-constrained interior point algorithm. Crosses indicate means of experimentally measured heavy-over-light intensities across the experimental repeats, error bars indicate the corresponding standard error. Simulations are shown as solid lines. Color code: **Conditions:** Control, B55 depletion, MASTL depletion; **Fitting parameters:** k_{B55}, k_{ind}; **Value of the objective function:** $o(P)$

6.2.5 Substrate Identification

To identify substrates that are de-phosphorylated by PP2A:B55, the following strategy is employed:

- Consider only peptides with a reasonable agreement between simulation and experimental data, set to $o(k_{ind}, k_{B55}) < 0.005$.
- Consider only peptides with a B55-dependent de-phosphorylation rate k_{B55} greater than 0.
- Consider only peptides whose k_{B55} is larger than their k_{ind}.
- Reduce the list to only consider peptides whose k_{B55} lies in the top 15-percentile.

Figure 6.8 provides an overview of the result of the classification.

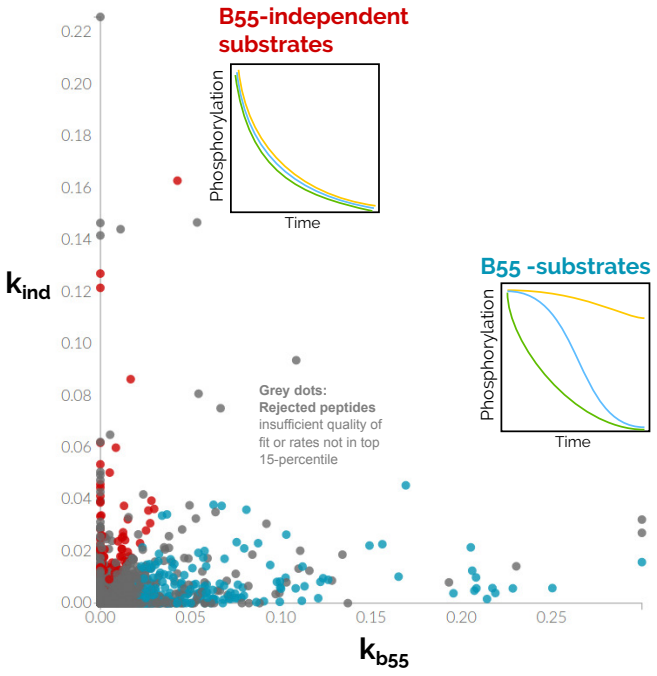


Figure 6.8: Substrate Identification - The dataset is partitioned based on the parameters obtained from model-fitting. Each dot corresponds to a peptide. Grey dots correspond to peptides that have not been clearly assigned. Peptides represented by blue dots have been assigned as high-confidence substrates of PP2A:B55. Peptides represented by red dots have been assigned to the group of high-confidence PP2A:B55-independent substrates.

6.3 Results

Interactive Visualisation

6.3.1 Categorisation of peptides

To assess the reliability of this approach, I first tested whether the model-driven data analysis pipeline categorised well-known B55-dependent substrates correctly. Unsurprisingly, the model-driven analysis recovered PRC1-pT481 (figure 6.9, left panel) as a substrate, which was included in the global fitting step as a test case. Furthermore, the well-known PP2A:B55-substrate Cdc20-pS41 (figure 6.9, right panel) featured in the group of high-confidence substrates.

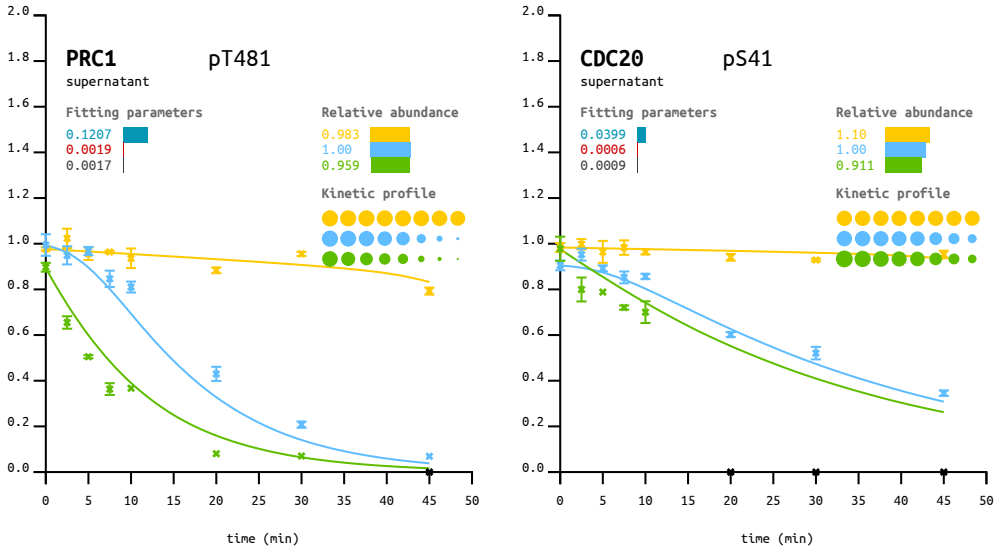


Figure 6.9: Known B55 Substrates - Crosses indicate means of experimentally measured heavy-over-light intensities across the experimental repeats, error bars indicate the corresponding standard error. Simulations are shown as solid lines. Color code: **Conditions:** Control, B55 depletion, MASTL depletion; **Fitting parameters:** k_{B55}, k_{ind}; **Value of the objective function:** $o(P)$

Many previously unidentified substrates of PP2A:B55 and novel sites on known substrates featured prominently in the group of high-confidence PP2A:B55 substrates: We identified a novel phosphorylation site on PRC1, pT470 ($k_{B55} = 0.2142\, min^{-1}\, AU^{-1}$) that is regulated by PP2A:B55. Figure 6.10 provides an overview of the entire group of high confidence B55 substrates. Notably, the substrates that are de-phosphorylated fall into two groups: Spindle proteins (figure 6.12), such as PRC1, the Aurora A

regulator TPX2, NUMA1, MAP7, NUSAP1 and SKA3, and nuclear pore proteins (figure 6.13), such as NDC1, LEMD1, POM121C, TMPO, NUP98 and NUP153. In terms of de-phosphorylation kinetics, the two groups appear as clusters, and de-phosphorylation of spindle proteins precedes de-phosphorylation of nuclear pore proteins.

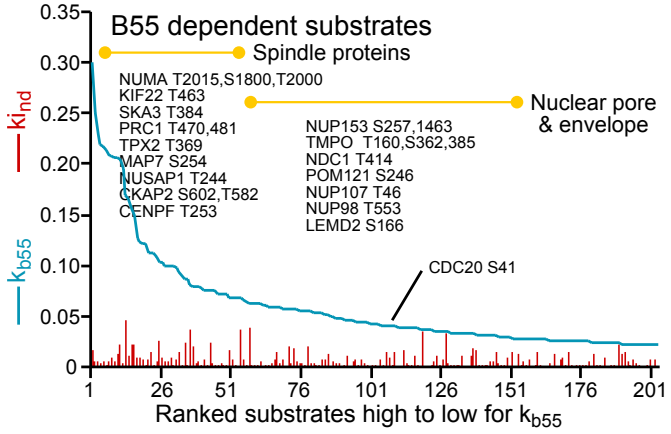


Figure 6.10: High-Confidence B55 Substrates - The group of substrates of PP2A:B55 identified with high confidence are ranked by k_{B55}.

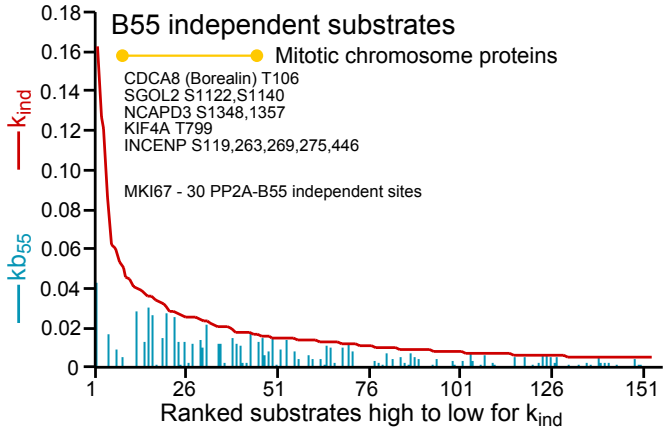


Figure 6.11: High-Confidence B55-independent Substrates - The group of peptides found to be regulated independently of PP2A:B55 are ranked by k_{ind}.

Using an analogous approach to our classification of high-confidence PP2A:B55-dependent substrates, we were able to define phospho-peptides that are de-phosphorylated in a manner independent of PP2A:B55 (figure 6.11). Strikingly, many of the proteins found to be de-phosphorylated fastest in this group are proteins that commonly associate with mitotic chromosomes (figure 6.14), such as shugoshin 2 (SGOL2), the chromosome surfactant MKI67 [246], the CPC components Borealin (CDCA8) and INCENP, and the condensin component NCAPD3.

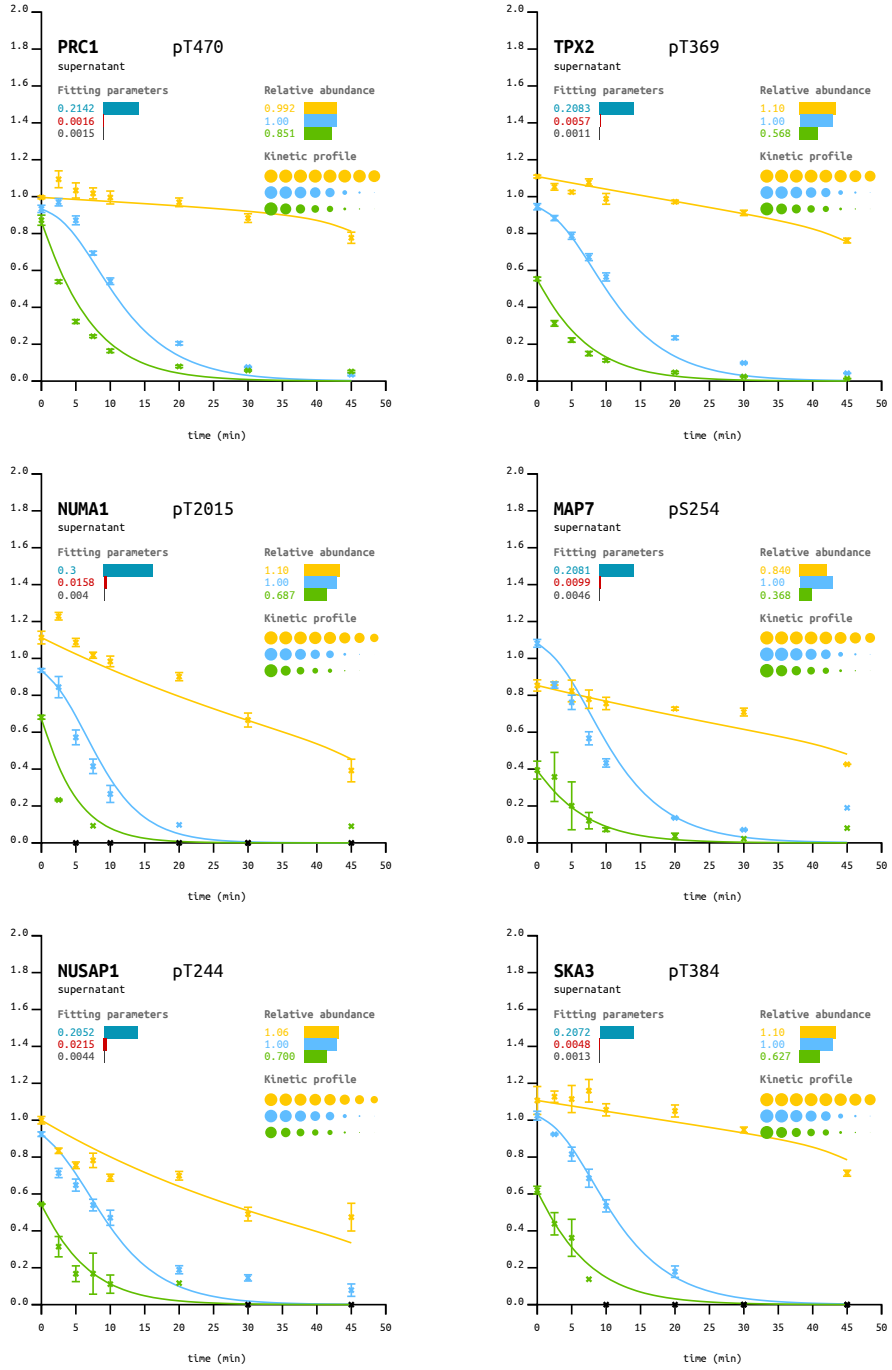


Figure 6.12: Novel B55 Substrates: Spindle proteins - Crosses indicate means of experimentally measured heavy-over-light intensities across the experimental repeats, error bars indicate the corresponding standard error. Simulations are shown as solid lines. Color code: **Conditions:** Control, B55 depletion, MASTL depletion; **Fitting parameters:** k_{B55}, k_{ind}; **Value of the objective function:** $o(P)$

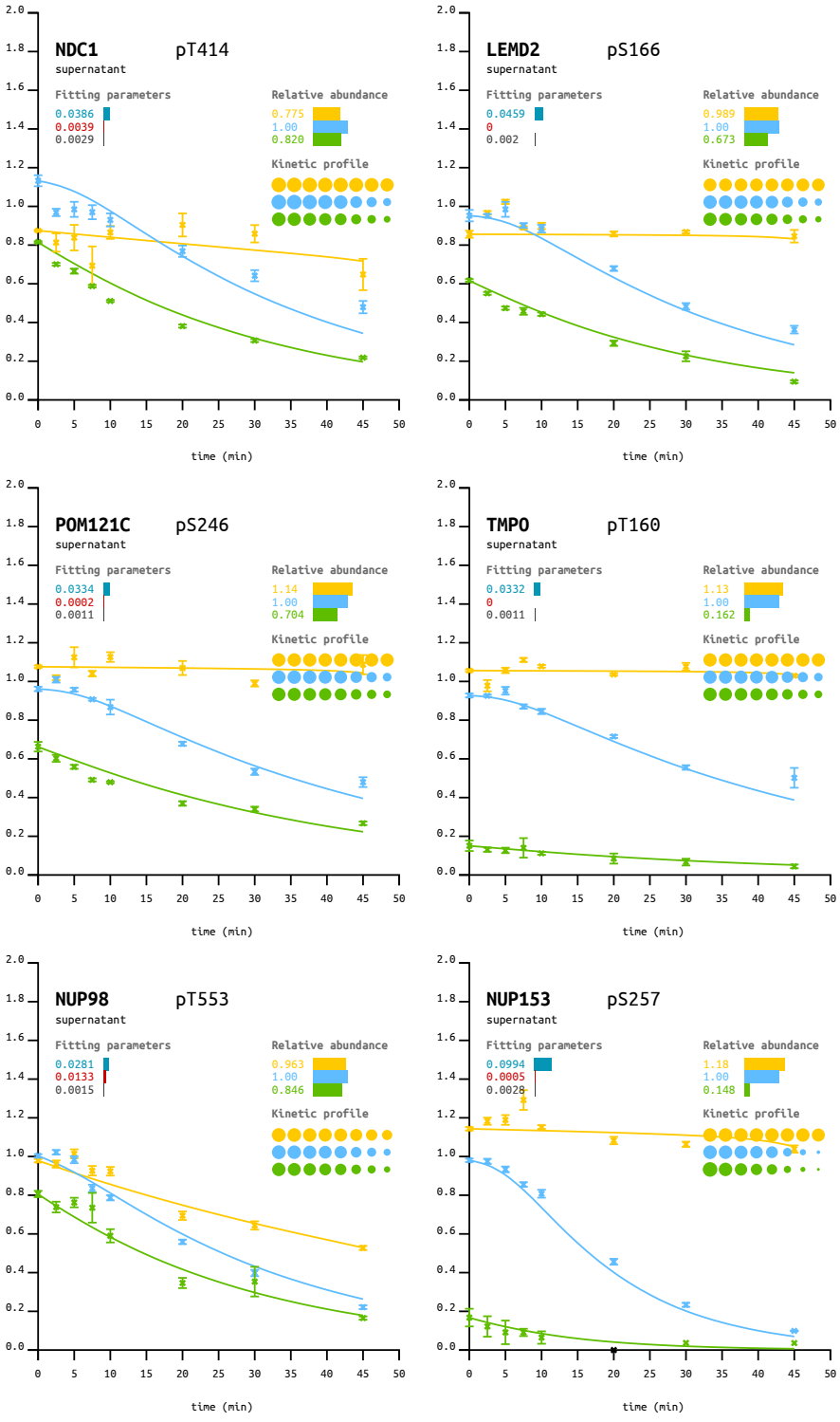


Figure 6.13: Novel B55 Substrates: Nuclear pores - Crosses indicate means of experimental measuredly heavy-over-light intensities across the experimental repeats, error bars indicate the corresponding standard error. Simulations are shown as solid lines. Color code: **Conditions:** Control, B55 depletion, MASTL depletion; **Fitting parameters:** k_{B55}, k_{ind}; **Value of the objective function:** $o(P)$

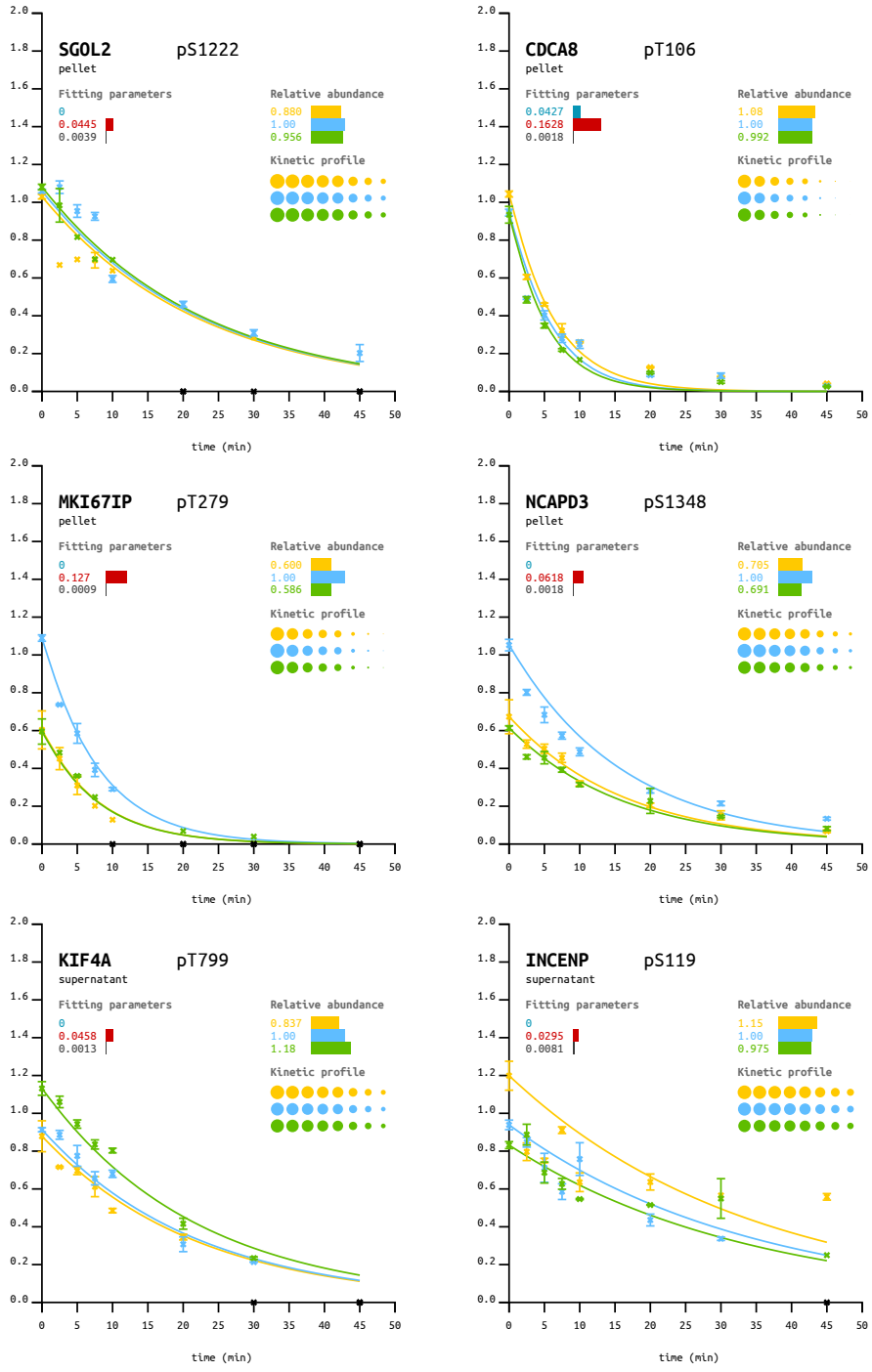


Figure 6.14: Novel B55-independent Substrates: - Crosses indicate means of experimentally measured heavy-over-light intensities across the experimental repeats, error bars indicate the corresponding standard error. Simulations are shown as solid lines. Color code: **Conditions:** Control, B55 depletion, MASTL depletion; **Fitting parameters:** k_{B55}, k_{ind}; **Value of the objective function:** $o(P)$

6.3.2 Recognition Motif

Following this qualitative analysis of our results, we next tried to identify common, sequence-level properties of the group of high-confidence PP2A:B55 substrates. To this end, I extracted information on the composition of the amino acid sequence 25 residues upstream and 10 residues downstream of the phosphorylation site (36 residues in total) from the curated dataset. The resulting list of sequence windows around the phosphorylation site was compared against a similar list derived from the total mitotic phospho-proteome. We used the sequence analysis tool IceLogo [247] to calculate factors expressing the enrichment of particular amino acids at specific positions around the phosphorylation site regulated by PP2A:B55.

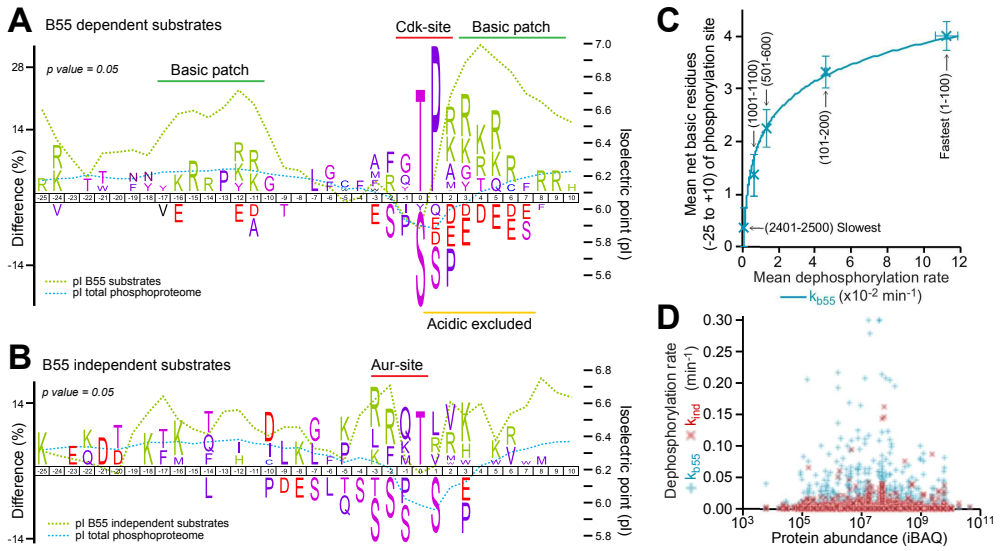


Figure 6.15: Bipartite poly-basic recognition motif - (A) A 36-amino acid sequence centred on the phosphorylated residue for the high confidence B55-dependent (203 peptides) and (B) -independent (153 peptides) substrates was compared against the experimentally determined total cell phospho-proteome data (23,131 peptides) using IceLogo with P = 0.05. Plots for substrate-enriched and excluded amino acids and average isolectric point (pI, green dotted line) and the total cell phospho-proteome (blue dotted line) within this sequence window are shown. (C) Mean B55-dependent dephosphorylation rates for the fastest (1-100) and progressively slower groups of ranked substrates as a function of the mean number of net basic residues. Error bars indicate the SEM (n = 100) for the different ranked groups of substrates. (D) Initial B55-dependent (blue, +) and independent (red, x) dephosphorylation rates for the top 2,960 peptides ranked by k_{B55} as a function of protein abundance calculated using intensity-based absolute quantification (iBAQ) from a total mitotic cell proteome dataset. *Reproduced from [241].*

Our candidate substrates of PP2A:B55 display a strong enrichment of threonine

Table 6.4: Frequency of phosphorylated amino acid

phosphorylated amino acid	frequency B55 substrates	frequency mitotic phospho-proteome
pT	55%	25%
pS	45%	73%
pY	<1%	<2%

over serine as the phosphorylated amino acid. The corresponding frequencies are listed in table 6.4. Moreover, the sequence analysis (figure 6.15 panel A) around the phosphorylation site revealed an enrichment of positively charged, basic residues flanking the phosphorylation site. In turn, acidic residues are excluded immediately downstream of the phosphorylation site. The CDK1 consensus motif (pS/pT-P-X-R/K) [248] is highly enriched in the group of high-confidence PP2A:B55 substrates. Conversely, peptides that were classified as high-confidence PP2A:B55-independent substrates (figure 6.15 panel B) show a markedly different pattern most similar to an Aurora B recognition motif [248].

6.3.3 Electrostatic Control of Dephosphorylation Kinetics

Noteably, the bipartite poly-basic region is not itself a feature of the CDK1 consensus site, suggesting that it may play a role in dephosphorylation by PP2A:B55. To explore this idea, we ranked all peptides in our dataset for which $k_{B55} > 0$, grouped them into sets of one hundred peptides and determined the group-wise average k_{B55} (figure 6.15 panel C). The group containing the peptides with the 100 highest k_{B55} has the highest net number of basic residues, as groups get progressively slower, the number of net basic residues decreases non-linearly. No direct relationship between rate of dephosphorylation (k_{B55} as well as k_{ind}) and protein abundance was found (figure 6.15 panel D).

To test the role of charge in modulating PP2A:B55-driven dephosphorylation kinetics directly, my collaborators selected PRC1 as a model substrate, generated a graded series of mutants of the full-length protein, carrying fewer and fewer basic residues in the four basic patches around pT470 and pT481 (figure 6.16 panel A), and tested dephosphorylation of these mutants *in vitro* using an assay first described in [101] (figure 6.16 panels B and C), as well as by mass spectrometry (figure 6.16 panel D). We found that the initial rate of dephosphorylation drops with decreasing number of basic residues in the four basic patches, and displays sigmoidal characteristics with a threshold of around four basic residues (blue crosses, figure 6.16 panel E).

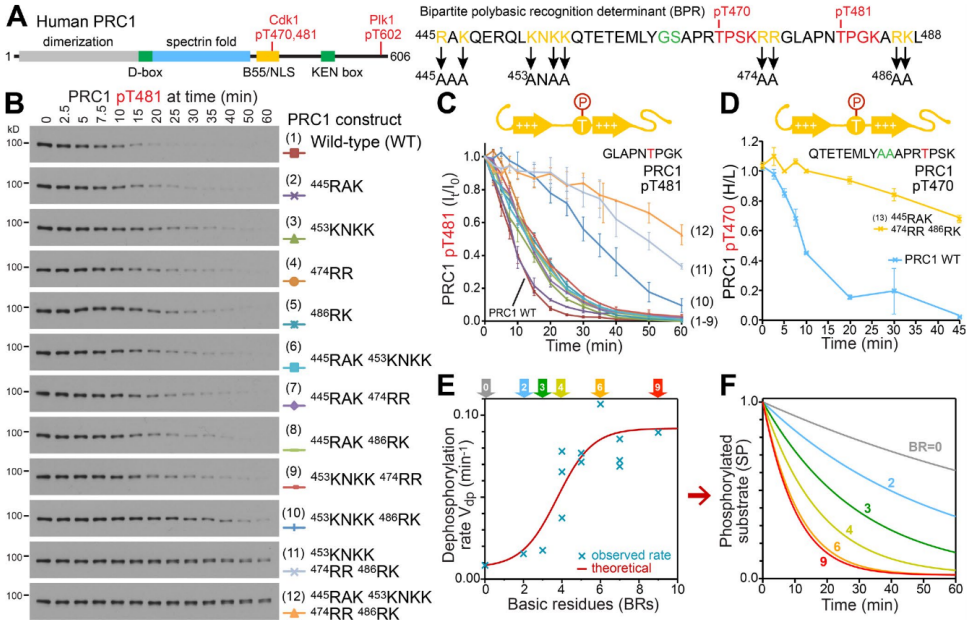


Figure 6.16: Dephosphorylation rate is encoded by the bipartite poly-basic recognition motif - (A) A schematic of human PRC1 based on structural data [249, 250] with phosphorylation sites for CDK1 and Plk1 [251], D- and KEN-box destruction motifs, and a putative NLS. Alanine-scanning mutations were introduced at basic residues (BRs) in B55 BPR and putative NLS region as marked in the sequence below the schematic. BRs within the consensus CDK1 phosphorylation sites (red) were not mutated, since this compromises phosphorylation. To allow analysis of T470 dephosphorylation, the GS sequence (green) at position 465/466 was mutated to AA, creating a unique peptide that could be differentiated from the endogenous protein by mass spectrometry. (B) PRC1 pT481 CDK1 site dephosphorylation of GFP-tagged wild-type PRC1 (1) and the series of single and combined basic patch mutants (2-12) was followed by Western blotting. (C) PRC1 pT481 dephosphorylation for all samples numbered as in B; error bars indicate SEM (n = 3 independent experiments). (D) PRC1 pT470 dephosphorylation profiles for the endogenous wild-type and BPR/GS mutant PRC1 extracted from mass spectrometry data; error bars indicate SEM (n = 2). (E) The effect of BRs within the BPR on the dephosphorylation of PRC1 mutants described in B and C. Initial rate versus BR. Experimental data (observed rate, blue x) and kinetic equation (solid curve, red). (F) Numerical simulations of dephosphorylation kinetics with representative BR values. *Reproduced from [241].*

6.3.3.1 Mathematical Model

The ultra-sensitive dependence of the initial rate of dephosphorylation on the number of basic residues adjacent to the phosphorylation site suggests that the basic residues cooperate in increasing the affinity of the substrate to PP2A:B55. To formulate this idea in the framework of Michaelis-Menten kinetics, we[1] devised a simple mathematical model: Equation 6.8 defines the initial rate of dephosphorylation (V_{dp}) when the relative concentration of the substrate is scaled to 1. Both V_{max} and K_M are normalised by the initial substrate concentration.

$$V_{dp} = \frac{V_{max}}{1 + K_M} \tag{6.8}$$

We assume that basic residues in the vicinity of the phosphorylation site reduce the dissociation rate of the PP2A:B55 in a cooperative manner. This effect is described using an Arrhenius term that expresses a dependency of the activation energy of the dissociation step on the number of basic residues. Expressed this way, we separate K_M into two terms: The first term is constant $K_M^{'} = \frac{k_{cat}+k_{dis}^{'}}{k_{ass}}$ and depends on a basic-residue-independent rate constant for the dissociation step ($k_{dis}^{'}$). The second term depends on the number of basic residues:

$$K_D^{BR} \cdot e^{\frac{-E \cdot BR}{RT}} = \frac{k_{dis}^{BR}}{k_{ass}} \cdot e^{\frac{-E \cdot BR}{RT}} \tag{6.9}$$

Here, $K_D^{BR} = \frac{k_{dis}^{BR}}{k_{ass}}$ describes the maximal equilibrium rate constant in the absence of basic residues. The resulting equation takes the form:

$$V_{dp} = k_{dp}^{'} + \frac{V_{max}}{1 + K_M^{'} + K_D^{BR} \cdot e^{\frac{-E \cdot BR}{RT}}} \tag{6.10}$$

where a small constitutive rate constant is added for B55-independent dephosphorylation ($k_{dp}^{'}$). This expression was fitted to the experimental data shown in figure 6.16 panel E. The red solid line in figure 6.16 panel E was calculated using theparameters listed in table 6.5.

To simulate dephosphorylation timecourses (shown in figure 6.16 panel F) for the different mutants of PRC1, we converted equation 6.10 into ordinary differential equation 6.11, which was solved using numerical integration.

$$\frac{d[PRC1]}{dt} = -k_{dp}^{'} \cdot [PRC1] - \frac{V_{max} \cdot [PRC1]}{[PRC1] + K_M^{'} + K_D^{BR} \cdot e^{\frac{-E \cdot BR}{RT}}} \tag{6.11}$$

Taken together, the data from the PRC1 mutation series experiment and the insight gained through this mathematical model suggest that the bipartite poly-basic

[1] this work was primarily performed by Bela Novak

Table 6.5: Parameters for the electrostatic model

parameter	value
E_a	$2.5\ kJ \cdot mol^{-1}$
R	$8.315\ kJ \cdot mol^{-1} \cdot K^{-1}$
T	$244\ K\ (4^{\circ}C)$
$V_{max,PRC1}$	$0.426\ AU min^{-1}$
$K^{'}_{M,PRC1}$	$4\ AU$
$K^{BR}_{D,PRC1}$	$300\ AU$
$k^{'}_{dp,PRC1}$	$0.007\ min^{-1}$

recognition motif encodes an electrostatic signal that gives rise to differential kinetics of dephosphorylation by PP2A:B55.

6.3.4 Validation In Vivo

To confirm that the bipartite poly-basic recognition motifs indeed play a role *in vivo*, recruitment of two PRC1 mutants (mutants 11 and 12 in figure 6.16) to the spindle in anaphase was tested by means of live-cell imaging of GFP-tagged PRC1 (data not shown). Whereas wild-type PRC1 is nuclear in G2 cells and recruited to the central spindle 4 minutes into anaphase, mutant 11 lacking two BPRs and mutant 12 lacking all BPRs showed delayed dynamics of recruitment to the spindle, and were recruited to a lesser extent. Moreover, both mutants failed to become localised to the nucleus in G2 cells, pointing at an interesting relationship between the PP2A:B55-recognition motif and the nuclear localisation signal of PRC1 (NLS) that although functionally distinct appear to overlap.

The role of the bipartite poly-basic recognition motif was further generalised *in vivo* by live-cell imaging of a mutant of the newly discovered PP2A:B55-substrate TPX2. Dephosphorylation of pT369 in a mutant lacking basic residues in the bipartite poly-basic recognition motif is slowed down 20-fold *in vitro*. Consistent with this finding, this mutant failed to localise to the spindle following PRC1 recruitment (expected wild-type behaviour) and was directly imported into the nucleus in telophase. Interestingly, the CDK1 site pT369 lies adjacent to an importin-α binding domain.

6.3.5 Recognition Determinant

To better define how PP2A:B55 recognises its substrates in a manner depending on the number of basic residues flanking the substrate's phosphorylation site, my collaborators mutated acidic residues on the surface of the phosphatase regulatory subunit B55. These residues form an acidic cleft which plausibly interacts electrostatically with a substrate's basic residues. Mutation of the ten conserved acidic residues to alanine revealed that dephosphorylation of PRC1 pT481, as observed in an *in vitro* assay by means of western blotting, was greatly reduced. Moreover, the recruitment of PRC1 to the central spindle *in vivo* was greatly attenuated upon transfection of the B55 DE/A muntant and knock-down of the endogenous B55. These results provide evidence supporting our postulated model, which states that the rate of dephosphorylation of substrates of PP2A:B55 is modulated by electrostatic interactions between bipartite poly-basic recognition motifs flanking the phosphorylation site and an acidic interface at the PP2A:B55 regulatory subunit B55.

6.3.6 Amino Acid Preference

To explain the considerable enrichment of phospho-threonine in our group of high-confidence PP2A:B55 substrates over the total phospho-proteome, my collaborators then investigated the effect of mutating PRC1's T481 to S481. Strikingly, whereas the mutation did not abolish dephosphorylation altogether, by substituting threonine with serine the dephosphorylation rate was greatly reduced. Still, a large fraction of fast, high-confidence PP2A:B55 substrates were serine-phospho-peptides. How can these observations be reconciled? Comparison of the sequence motifs of serine- and threonine-phospho-peptides in the group of high-confidence PP2A:B55 substrates revealed that fast phospho-serine substrates contain aromatic, or bulky hydrophobic and acidic residues immediately upstream of the phosphorylation site. Indeed, substitution of YFD into the sequence upstream of pS470/pS481 in the mutant PRC1 recovered wild-type-like dephosphorylation kinetics.

6.3.7 ENSA Revisited

Our findings relating to the modulation of the association-dissociation equilibrium between PP2A:B55 and its substrates by means of electrostatic interaction driven by substrate-level basic residues and acidic residues on B55, and the effect of the

nature of the phosphorylated amino acid on the dephosphorylation rate, shed an interesting perspective on how the activity of PP2A:B55 is regulated throughout mitosis by the same fundamental principles: Interpreted in the framework of Michaelis-Menten kinetics, any substrate of an enzyme can be considered an inhibitor of the enzyme, provided it tightly associates with the enzyme (second-order process) followed by a relatively slow catalytic turnover (first-order process). Indeed, tight association between ENSA and PP2A:B55 is supported by the fact that ENSA contains a higher number of basic residues in the vicinity of its phosphorylation site pS67 than any other substrate identified in our screen. Employing a similar mutation strategy as applied to PRC1, my collaborators were able to show that a reduction in basic residues around the phosphorylation site slows down dephosphorylation of $ENSA_p$. Moreover, serine rather than threonine is phosphorylated at the relevant phosphorylation site, potentially accounting for the slow, first-order catalytic step. For an ENSA pS67T mutant, the presented framework would predict accelerated dephosphorylation of ENSA, potentially compromising its efficacy as an inhibitor of PP2A:B55 activity. Unfortunately, we were not able to test this prediction directly, as the ENSA pS67T mutant did not show detectable phosphorylation.

6.4 Discussion

6.4.1 Heuristic

Modern studies in systems biology rely heavily on high-throughput experimental techniques that produce comprehensive data sets. Such data sets - as the dataset that represented the starting point for this study - pose new challenges to the analysis: More data do not generally translate to more insight. When relatively rare events are of interest, the meaningful signal may be obscured by noise. Increasingly, assumption-free approaches are used to extract novel insights from these studies by identifying patterns in the dataset. However, by definition unbiased, assumption-free methods are poorly positioned to account complex prior knowledge into the data analysis.

The approach presented in this chapter provides a complementary approach to assumption-free methods and is based on a search heuristic. The fundamental hypothesis that informed the design of the experiment was expressed as a mathematical model describing the dynamics of dephosphorylation of a substrate under the chosen experimental conditions.

By fitting the model to the data, timecourses could be described by two parameters expressing the rate of PP2A:B55-dependent and -independent dephosphorylation, thus compressing the data in a manner that can be meaningfully interpreted. Crucially for a proteomics experiment that is intrinsically prone to generating data sets with missing data, this model-driven approach to data analysis is robust towards missing datapoints. Through representing the data by means of a model describing the dynamics of the system, I was able to adequately account for the timecourse nature of the data. This strengthened the overall analysis, as uncertainties associated with individual datapoints could be contextualised based on preceding and following datapoints.

6.4.2 Generalisable Design Implications

The ability to account for timecourse data as related data deriving from an underlying process changing in time, rather than a non-related series of datapoints; the capacity to compress complex data in a meaningful manner; and the possibility to apply an informed hypothesis to comprehensive data sets can maximise the utility of high-throughput studies in studying biological systems, by using a model-driven approach to data analysis. The use of dynamical models as search heuristics in high-throughput studies has implications on the design of experiments and models.

6.4.2.1 Model Constraints

Questions of generality and scalability of the mathematical model become relevant when attempting to use models as heuristics in analysing high-throughput data sets: The model that was used in this study consists of two modules: a specific core module, which describes the regulation of the activity of PP2A:B55 by the BEG pathway, and a general module describing the dephosphorylation of an arbitrary substrate by a PP2A:B55-dependent and a PP2A:B55-independent process.

The dataset included data on the dephosphorylation of ENSA, which were used to parametrise the core module and precondition the model for its application throughout the dataset. The preconditioning allowed for sufficient complexity in the core module to accurately describe the BEG pathway. Due to non-linear dependence of PP2A:B55 activity on the relative levels $ENSA_p$, the core module demands a dedicated parametrisation step during the preconditioning. Note that non-linearities are absent in the general module describing substrate dephosphorylation. The rate equation for the phosphorylated substrate scales linearly with the concentration of

the phosphorylated substrates. It is robust towards normalisation of the substrate concentration, and rate parameters are comparable between different substrates even if their initial concentrations differ.

6.4.2.2 Experimental Design

Correspondingly, I would argue that non-linear dependencies between data (input) and predicted activity (output) generally require dedicated experiments to yield the corresponding parameters, whereas modules within the model, where the rate equation scales linearly with the quantity of interest can generally be "broadcast".

Extension of the model to account for additional determinants of the activity or abundance of the quantity of interest, such as the effect of kinases on the abundance of phosphorylated substrate, have to be parametrised using a separate experiment, in order to reduce the data-dependency of the general module to that which is directly observable in the high-throughput dataset.

Embracing an automated optimisation routine for the parametrisation of the model is a fundamental requirement for this approach to succeed. Such optimisation routines rely on objective functions that measure the agreement between simulation and experimental data. Unevenly spaced timepoints in a timecourse experiment render the choice of a suitable objective function difficult, as they carry different weights of evidence. The process of accounting for varying weights of evidence in the objective function lacks a generally accepted method and is thus prone to introducing implicit assumptions into the analysis. This becomes particularly problematic when faced with varying patterns of missing data that demand a flexible re-allocation of weights in the objective function. Consequently, experimental design based on evenly spaced timepoints should be considered preferable.

6.4.3 Summary

This study represents a comprehensive investigation of substrates of PP2A:B55 at mitotic exit. In our analysis, we first identified a broad range of PP2A:B55 substrates based on their characteristic dephosphorylation patterns under control conditions, hypo- and hyper-activation of PP2A:B55. By analysing the amino acid sequences flanking the phosphorylation sites in these substrates, we were able to identify a non-linear dependence of PP2A:B55-driven rate of dephosphorylation on the basicity of the amino acid sequence in the vicinity of the phosphorylation sites controlled by PP2A:B55. We then demonstrated a direct effect of basicity on the rate of

dephosphorylation by PP2A:B55 *in vitro*, by mutating basic amino acids in the vicinity of the phosphorylation site to alanine and observing slower rates of dephosphorylation. The data are supported by a mathematical model in which Michaelis-Menten-like dephosphorylation kinetics *in vitro* are accelerated by electrostatic interactions between substrates and PP2A:B55 that affect the dissociation equilibrium of the enzyme-substrate complex. In turn, this model is supported by data that shows reduced rates of PRC1 pT481 dephosphorylation upon mutating acidic residues in the catalytic B55 subunit of the PP2A:B55 complex.

As such, it provides important insight into how cells control the events underpinning mitotic exit in time. The role of basic residues around the phosphorylation site in encoding rates of dephosphorylation has strong predictive power and may enable future studies in the field to directly manipulate activation and inactivation times of PP2A:B55-dependent processes at mitotic exit. Furthermore, our findings hint at a general principle whereby a single enzyme can control a broad range of substrates in a time-resolved manner through modulation of the dissociation equilibrium of enzyme-substrate complex by the composition of the substrate's recognition motif.

7

Conclusions

Throughout chapters 1 and 2, I developed a view of mitosis that emphasises the role of post-translational modification in its regulation. I laid out key conceptual challenges associated with the the regulation of mitosis in chapter 3, and discussed the utility of dynamical systems theory in biological studies employing data-driven modelling and model-driven experimentation aimed at resolving these problems. Each of the three projects discussed in chapters 4-6 represents a distinct realisation of this methodological concept, and presents us with different perspectives on mitotic regulation.

7.1 Boundaries & Signal

In chapter 4, I focussed on the question of system boundaries. Using a combination of model-driven experiments and data-driven modelling, my collaborators and I were able to place into the broader context of crosstalk between the error correction mechanism and the checkpoint enforcement mechanism the counter-intuitive experimental finding that the mitotic checkpoint in *Drosophila* neuroblasts responds poorly to premature loss of sister-chromatid cohesion. We found that our experimental data is best explained by a models whereby error correction and the checkpoint enforcement mechanism cooperate by mutually activating each other. However, the crosstalk between the two subsystems incurs a cost: A failure to robustly sustain checkpoint activity when sister chromatid cohesion is lost. This effect results from the slow correction of incorrect attachments, which weakens the checkpoint enforcement mechanism. This allows APC/C to become partially active, and further weakens the checkpoint overall. The resulting model of the mitotic checkpoint in *Drosophila* neuroblasts allowed us to accurately predict how the

system would respond to partial inhibition of CDK1, lending further support to this finding.

7.2 Irreversibility & Finality

In chapter 5, I elaborate on the role of of CDK1 in checkpoint signalling. Building on previous studies, my collaborators developed a quantitative live-cell imaging assay to probe the response of the checkpoint to partial inhibition of CDK1 in two human cell-lines. By experimentally focusing on the degradation dynamics of the two APC/C:Cdc20 substrates cyclin B and securin, we were able to observe a hypersensitive dependence of the activity of the checkpoint on the activity of CDK1. The subsequent analysis of the data by means of modelling revealed a connection between the characteristic degradation patterns observed in our experiments and the phenomenon of mitotic slippage, which was confirmed by experimentally testing the prediction of the model that partial inhibition of CDK1 accelerates mitotic slippage. Using bifurcation analysis of the model, I was able to rationalise this finding, lending support to the notion that a characteristic threshold inactivates the checkpoint at the onset of anaphase, and thereby contributes to the avoidance of the anaphase problem.

To lend further support to the conceptual framework developed in chapter 5, futher experiments need to be conducted. The live-cell imaging protocol investigating the response of nocodazole arrested cells to partial inhibition of CDK1 should be extended to allow for quantification of the localistion of Mad2 to kinetochores in parallel to the quantification of cyclin B levels. This is necessary to be able to claim that mitotic slippage corresponds to a collapse of checkpoint signalling rather than a bypassing of it, as previously claimed by Brito *et al.* [223]. In this context a knockout of the APC/C co-activator Cdh1 would be particularly helpful, as it is the prime candidate to drive a possible bypassing of the mitotic checkpoint.

7.3 Sensitivity

Due to its character as hallmark of the mitotic checkpoint, models of the mitotic checkpoint have to explain sensitivity of the checkpoint to single unattached kinetochores in order to be deemed valid. As a consequence of the limited scope of the experimental data presented in this thesis, the question of sensitivity was only marginally addressed, and demands more attention in future work. In the context

of the model presented in chapter 5, it would be particularly interesting to perform simulations recapitulating the data presented in [216]. Moreover, the bistable switch hypothesis presents a strong prediction that sensitivity of the checkpoint should become reduced when levels of cyclin B drop. A cell line co-expressing tagged cyclin B and Mad2 would be well-suited to test this prediction based on an experimental protocol similar to the laser microsurgery experiments presented by Dick and Gerlich [216].

However, the question of how sensitivity is best addressed in the context of a mathematical model remains to be resolved. Current models of the mitotic checkpoint, including the one presented in chapter 5, assume that attachment state of kinetochores or microtubule binding sites can be represented by a continuous variable. However, the number of kinetochores in cells is discrete, and recent findings on microtubule binding sites in human cells suggest that they display a remarkable degree of cooperativity. Therefore, it may be more appropriate to model the mitotic checkpoint as an ensemble of partially coupled switches.

7.4 Beyond the Mitotic Checkpoint

In chapter 6, I presented a complementary use of a mathematical model in a systems-biological study. By expressing the theoretical premise of a proteomics experiment designed to identify novel substrates of PP2A:B55 as a simple, reducible mathematical model, I was able to design a data-analysis pipeline to identify new substrates of PP2A:B55 in an automated manner. This constituted the crucial, rate-limiting step in this study. It enabled the subsequent identification of a general principle, whereby the rate of PP2A:B55-driven dephosphorylation at mitotic exit is electrostatically encoded in its substrates.

References

[1] Ron Sender, Shai Fuchs, and Ron Milo. **Are We Really Vastly Outnumbered? Revisiting the Ratio of Bacterial to Host Cells in Humans**. *Cell*, **164**(3):337–340, 28 January 2016. 1

[2] David Owen Morgan. *The cell cycle : principles of control*. Primers in biology. New Science Press Ltd in association with Oxford University Press, London, 2007. 1, 2

[3] Joseph R Pomerening, Sun Young Kim, and James E Ferrell, Jr. **Systems-level dissection of the cell-cycle oscillator: bypassing positive feedback produces damped oscillations**. *Cell*, **122**(4):565–578, 26 August 2005. 2

[4] Andrew W Murray. **Recycling the cell cycle: cyclins revisited**. *Cell*, **116**(2):221–234, 23 January 2004. 2

[5] V Simanis and P Nurse. **The cell cycle control gene cdc2+ of fission yeast encodes a protein kinase potentially regulated by phosphorylation**. *Cell*, **45**(2):261–268, 25 April 1986. 2

[6] S Moreno, J Hayles, and P Nurse. **Regulation of p34cdc2 protein kinase during mitosis**. *Cell*, **58**(2):361–372, 28 July 1989. 2

[7] B Durkacz, A Carr, and P Nurse. **Transcription of the cdc2 cell cycle control gene of the fission yeast Schizosaccharomyces pombe**. *EMBO J.*, **5**(2):369–373, February 1986. 2

[8] T Evans, E T Rosenthal, J Youngblom, D Distel, and T Hunt. **Cyclin: a protein specified by maternal mRNA in sea urchin eggs that is destroyed at each cleavage division**. *Cell*, **33**(2):389–396, June 1983. 2

[9] D O Morgan. **Regulation of the APC and the exit from mitosis**. *Nat. Cell Biol.*, **1**(2):E47–53, June 1999. 4

[10] Jan-Michael Peters. **The anaphase promoting complex/cyclosome: a machine designed to destroy**. *Nat. Rev. Mol. Cell Biol.*, **7**(9):644–656, September 2006. 4, 17

[11] M Glotzer, A W Murray, and M W Kirschner. **Cyclin is degraded by the ubiquitin pathway**. *Nature*, **349**(6305):132–138, 10 January 1991. 4, 17

[12] R W King, R J Deshaies, J M Peters, and others. **How proteolysis drives the cell cycle**. *Science*, 1996. 4, 17

[13] Suyang Zhang, Leifu Chang, Claudio Alfieri, Ziguo Zhang, Jing Yang, Sarah Maslen, Mark Skehel, and David Barford. **Molecular mechanism of APC/C activation by mitotic phosphorylation**. *Nature*, 27 April 2016. 4, 25

[14] Mark J Solomon, Michael Glotzer, Tina H Lee, Michel Philippe, and Marc W Kirschner. **Cyclin activation of p34 cdc2**. *Cell*, **63**(5):1013–1024, 1990. 4

[15] M J Solomon, T Lee, and M W Kirschner. **Role of phosphorylation in p34cdc2 activation: identification of an activating kinase**. *Mol. Biol. Cell*, **3**(1):13–27, January 1992. 4

[16] Carl Smythe and John W Newport. **Coupling of mitosis to the completion of S phase in Xenopus occurs via modulation of the tyrosine kinase that phosphorylates p34 cdc2**. *Cell*, **68**(4):787–797, 1992. 4

[17] Z Tang, T R Coleman, and W G Dunphy. **Two distinct mechanisms for negative regulation of the Wee1 protein kinase**. *EMBO J.*, **12**(9):3427–3436, September 1993. 4

[18] A Kumagai and W G Dunphy. **Regulation of the cdc25 protein during the cell cycle in Xenopus extracts**. *Cell*, **70**(1):139–151, 10 July 1992. 4

[19] I Hoffmann, P R Clarke, M J Marcote, E Karsenti, and G Draetta. **Phosphorylation and activation of human cdc25-C by cdc2–cyclin B and its involvement in the self-amplification of MPF at mitosis**. *EMBO J.*, **12**(1):53–63, January 1993. 4

[20] B Novak and J J Tyson. **Numerical analysis of a comprehensive model of M-phase control in Xenopus oocyte extracts and intact embryos**. *J. Cell Sci.*, **106 (Pt 4)**:1153–1168, December 1993. 4, 5

[21] Wei Sha, Jonathan Moore, Katherine Chen, Antonio D Lassaletta, Chung-Seon Yi, John J Tyson, and Jill C Sible. **Hysteresis drives cell-cycle transitions in Xenopus laevis egg extracts**. *Proceedings of the National Academy of Sciences*, **100**(3):975–980, 2003. 6

[22] Joseph R Pomerening, Eduardo D Sontag, and James E Ferrell, Jr. **Building a cell cycle oscillator: hysteresis and bistability in the activation of Cdc2**. *Nat. Cell Biol.*, **5**(4):346–351, April 2003. 6

[23] Jeremy B Chang and James E Ferrell, Jr. **Mitotic trigger waves and the spatial coordination of the Xenopus cell cycle**. *Nature*, **500**(7464):603–607, 29 August 2013. 6

[24] L H Hartwell and T A Weinert. **Checkpoints: controls that ensure the order of cell cycle events**. *Science*, **246**(4930):629–634, 3 November 1989. 6

[25] A W Murray. **Creative blocks: cell-cycle checkpoints and feedback controls**. *Nature*, **359**(6396):599–604, 15 October 1992. 6

[26] A Murray. **Cell cycle checkpoints**. *Curr. Opin. Cell Biol.*, **6**(6):872–876, December 1994. 6

[27] R B Painter and B R Young. **Radiosensitivity in ataxia-telangiectasia: a new explanation**. *Proc. Natl. Acad. Sci. U. S. A.*, **77**(12):7315–7317, December 1980. 6

[28] T A Weinert and L H Hartwell. **The RAD9 gene controls the cell cycle response to DNA damage in Saccharomyces cerevisiae**. *Science*, **241**(4863):317–322, 15 July 1988. 6

REFERENCES

[29] K Nasmyth and C H Haering. **Cohesin: its roles and mechanisms**. *Annu. Rev. Genet.*, 2009. 7, 13

[30] Cpc De Souza and S A Osmani. **Mitosis, not just open or closed**. *Eukaryot. Cell*, 2007. 7

[31] Tatsuya Hirano. **Condensins: organizing and segregating the genome**. *Curr. Biol.*, **15**(7):R265–75, 12 April 2005. 7

[32] Antonino Colanzi, Christine Suetterlin, and Vivek Malhotra. **Cell-cycle-specific Golgi fragmentation: how and why?** *Curr. Opin. Cell Biol.*, **15**(4):462–467, August 2003. 7

[33] I C Waizenegger, S Hauf, A Meinke, and J M Peters. **Two distinct pathways remove mammalian cohesin from chromosome arms in prophase and from centromeres in anaphase**. *Cell*, **103**(3):399–410, 27 October 2000. 7, 13

[34] Sharat Gadde and Rebecca Heald. **Mechanisms and molecules of the mitotic spindle**. *Curr. Biol.*, **14**(18):R797–805, 21 September 2004. 7

[35] Marvin E Tanenbaum and René H Medema. **Mechanisms of centrosome separation and bipolar spindle assembly**. *Dev. Cell*, **19**(6):797–806, 14 December 2010. 7, 11, 14

[36] Stephan Güttinger, Eva Laurell, and Ulrike Kutay. **Orchestrating nuclear envelope disassembly and reassembly during mitosis**. *Nat. Rev. Mol. Cell Biol.*, **10**(3):178–191, March 2009. 7, 8

[37] Joël Beaudouin, Daniel Gerlich, Nathalie Daigle, Roland Eils, and Jan Ellenberg. **Nuclear envelope breakdown proceeds by microtubule-induced tearing of the lamina**. *Cell*, **108**(1):83–96, 11 January 2002. 7

[38] M Kirschner and T Mitchison. **Beyond self-assembly: from microtubules to morphogenesis**. *Cell*, **45**(3):329–342, 9 May 1986. 7, 14

[39] Valentin Magidson, Christopher B O'Connell, Jadranka Lončarek, Raja Paul, Alex Mogilner, and Alexey Khodjakov. **The spatial arrangement of chromosomes during prometaphase facilitates spindle assembly**. *Cell*, **146**(4):555–567, 19 August 2011. 7

[40] Iain M Cheeseman, Joshua S Chappie, Elizabeth M Wilson-Kubalek, and Arshad Desai. **The conserved KMN network constitutes the core microtubule-binding site of the kinetochore**. *Cell*, **127**(5):983–997, 1 December 2006. 8

[41] S Hauf, I C Waizenegger, and J M Peters. **Cohesin cleavage by separase required for anaphase and cytokinesis in human cells**. *Science*, **293**(5533):1320–1323, 17 August 2001. 8

[42] Yasuhiro Kurasawa, William C Earnshaw, Yuko Mochizuki, Naoshi Dohmae, and Kazuo Todokoro. **Essential roles of KIF4 and its binding partner PRC1 in organized central spindle midzone formation**. *EMBO J.*, **23**(16):3237–3248, 18 August 2004. 8

[43] N Chaudhary and J C Courvalin. **Stepwise reassembly of the nuclear envelope at the end of mitosis**. *J. Cell Biol.*, **122**(2):295–306, July 1993. 8

[44] Paola Vagnarelli, Susana Ribeiro, Lau Sennels, Luis Sanchez-Pulido, Flavia de Lima Alves, Toon Verheyen, David A Kelly, Chris P Ponting, Juri Rappsilber, and William C Earnshaw. **Repo-Man coordinates chromosomal reorganization with nuclear envelope reassembly during mitotic exit**. *Dev. Cell*, **21**(2):328–342, 16 August 2011. 8

[45] Juan Pablo Fededa and Daniel W Gerlich. **Molecular control of animal cell cytokinesis**. *Nat. Cell Biol.*, **14**(5):440–447, May 2012. 8

[46] Francis A Barr and Ulrike Gruneberg. **Cytokinesis: placing and making the final cut**. *Cell*, **131**(5):847–860, 30 November 2007. 8

[47] T Mitchison and M Kirschner. **Dynamic instability of microtubule growth**. *Nature*, **312**(5991):237–242, 1984. 9, 14

[48] Paul T Conduit, Zhe Feng, Jennifer H Richens, Janina Baumbach, Alan Wainman, Suruchi D Bakshi, Jeroen Dobbelaere, Steven Johnson, Susan M Lea, and Jordan W Raff. **The centrosome-specific phosphorylation of Cnn by Polo/Plk1 drives Cnn scaffold assembly and centrosome maturation**. *Dev. Cell*, **28**(6):659–669, 31 March 2014. 11

[49] M Moritz, M B Braunfeld, J W Sedat, B Alberts, and D A Agard. **Microtubule nucleation by gamma-tubulin-containing rings in the centrosome**. *Nature*, **378**(6557):638–640, 7 December 1995. 11

[50] Michel Bornens. **The centrosome in cells and organisms**. *Science*, **335**(6067):422–426, 27 January 2012. 11

[51] Christian Arquint, Anna-Maria Gabryjonczyk, and Erich A Nigg. **Centrosomes as signalling centres**. *Philos. Trans. R. Soc. Lond. B Biol. Sci.*, **369**(1650):20130464, 5 September 2014. 11

[52] Paul T Conduit, Alan Wainman, and Jordan W Raff. **Centrosome function and assembly in animal cells**. *Nat. Rev. Mol. Cell Biol.*, **16**(10):611–624, October 2015. 11

[53] Naoki Oshimori, Miho Ohsugi, and Tadashi Yamamoto. **The Plk1 target Kizuna stabilizes mitotic centrosomes to ensure spindle bipolarity**. *Nat. Cell Biol.*, **8**(10):1095–1101, October 2006. 11

[54] Kazuhisa Kinoshita, Tim L Noetzel, Laurence Pelletier, Karl Mechtler, David N Drechsel, Anne Schwager, Mike Lee, Jordan W Raff, and Anthony A Hyman. **Aurora A phosphorylation of TACC3/maskin is required for centrosome-dependent microtubule assembly in mitosis**. *J. Cell Biol.*, **170**(7):1047–1055, 26 September 2005. 11

[55] Jeffrey B Woodruff, Oliver Wueseke, and Anthony A Hyman. **Pericentriolar material structure and dynamics**. *Philos. Trans. R. Soc. Lond. B Biol. Sci.*, **369**(1650), 5 September 2014. 11

[56] Marileen Dogterom, Jacob W J Kerssemakers, Guillaume Romet-Lemonne, and Marcel E Janson. **Force generation by dynamic microtubules**. *Curr. Opin. Cell Biol.*, **17**(1):67–74, February 2005. 11

[57] E N Cytrynbaum, J M Scholey, and A Mogilner. **A force balance model of early spindle pole separation in Drosophila embryos**. *Biophys. J.*, **84**(2 Pt 1):757–769, February 2003. 11

[58] Marvin E Tanenbaum, Libor Macůrek, Aniek Janssen, Erica F Geers, Mónica Alvarez-Fernández, and René H Medema. **Kif15 cooperates with eg5 to promote bipolar spindle assembly**. *Curr. Biol.*, **19**(20):1703–1711, 3 November 2009. 11, 15

[59] S Busson, D Dujardin, A Moreau, J Dompierre, and J R De Mey. **Dynein and dynactin are localized to astral microtubules and at cortical sites in mitotic epithelial cells**. *Curr. Biol.*, **8**(9):541–544, 23 April 1998. 11

[60] Denis L Dujardin and Richard B Vallee. **Dynein at the cortex**. *Curr. Opin. Cell Biol.*, **14**(1):44–49, February 2002. 11

[61] Marvin E Tanenbaum, Anna Akhmanova, and René H Medema. **Dynein at the nuclear envelope**. *EMBO Rep.*, **11**(9):649, September 2010. 11

[62] Iain M Cheeseman. **The kinetochore**. *Cold Spring Harb. Perspect. Biol.*, **6**(7):a015826, July 2014. 12

[63] Marion E Pesenti, John R Weir, and Andrea Musacchio. **Progress in the structural and functional characterization of kinetochores**. *Curr. Opin. Struct. Biol.*, **37**:152–163, April 2016. 12

[64] Bungo Akiyoshi and Keith Gull. **Discovery of unconventional kinetochores in kinetoplastids**. *Cell*, **156**(6):1247–1258, 13 March 2014. 12

[65] Kerstin Klare, John R Weir, Federica Basilico, Tomasz Zimniak, Lucia Massimiliano, Nina Ludwigs, Franz Herzog, and Andrea Musacchio. **CENP-C is a blueprint for constitutive centromere–associated network assembly within human kinetochores**. *J. Cell Biol.*, **210**(1):11–22, 6 July 2015. 12

[66] Emanuela Screpanti, Anna De Antoni, Gregory M Alushin, Arsen Petrovic, Tiziana Melis, Eva Nogales, and Andrea Musacchio. **Direct binding of Cenp-C to the Mis12 complex joins the inner and outer kinetochore**. *Curr. Biol.*, **21**(5):391–398, 8 March 2011. 12

[67] Gregory M Alushin, Vincent H Ramey, Sebastiano Pasqualato, David A Ball, Nikolaus Grigorieff, Andrea Musacchio, and Eva Nogales. **The Ndc80 kinetochore complex forms oligomeric arrays along microtubules**. *Nature*, **467**(7317):805–810, 14 October 2010. 12, 21

[68] Gregory M Alushin, Vivek Musinipally, Daniel Matson, John Tooley, P Todd Stukenberg, and Eva Nogales. **Multimodal microtubule binding by the Ndc80 kinetochore complex**. *Nat. Struct. Mol. Biol.*, **19**(11):1161–1167, November 2012. 12

[69] Karen E Gascoigne, Kozo Takeuchi, Aussie Suzuki, Tetsuya Hori, Tatsuo Fukagawa, and Iain M Cheeseman. **Induced ectopic kinetochore assembly bypasses the requirement for CENP-A nucleosomes**. *Cell*, **145**(3):410–422, 29 April 2011. 12

[70] Ronnie R Wei, Jawdat Al-Bassam, and Stephen C Harrison. **The Ndc80/HEC1 complex is a contact point for kinetochore-microtubule attachment**. *Nat. Struct. Mol. Biol.*, **14**(1):54–59, January 2007. 12

[71] Claudio Ciferri, Sebastiano Pasqualato, Emanuela Screpanti, Gianluca Varetti, Stefano Santaguida, Gabriel Dos Reis, Alessio Maiolica, Jessica Polka, Jennifer G De Luca, Peter De Wulf, Mogjiborahman Salek, Juri Rappsilber, Carolyn A Moores, Edward D Salmon, and Andrea Musacchio. **Implications for kinetochore-microtubule attachment from the structure of an engineered Ndc80 complex**. *Cell*, **133**(3):427–439, 2 May 2008. 12

[72] Stephanie A Miller, Michael L Johnson, and P Todd Stukenberg. **Kinetochore attachments require an interaction between unstructured tails on microtubules and Ndc80 Hec1**. *Curr. Biol.*, **18**(22):1785–1791, 2008. 12

[73] Julie P I Welburn, Ekaterina L Grishchuk, Chelsea B Backer, Elizabeth M Wilson-Kubalek, John R Yates, 3rd, and Iain M Cheeseman. **The human kinetochore Ska1 complex facilitates microtubule depolymerization-coupled motility**. *Dev. Cell*, **16**(3):374–385, March 2009. 12

[74] Anatoly V Zaytsev, Lynsie J R Sundin, Keith F DeLuca, Ekaterina L Grishchuk, and Jennifer G DeLuca. **Accurate phosphoregulation of kinetochore–microtubule affinity requires unconstrained molecular interactions**. *J. Cell Biol.*, **206**(1):45–59, 7 July 2014. 13

[75] Christian H Haering, Jan Löwe, Andreas Hochwagen, and Kim Nasmyth. **Molecular architecture of SMC proteins and the yeast cohesin complex**. *Mol. Cell*, **9**(4):773–788, April 2002. 13

[76] Rita Gandhi, Peter J Gillespie, and Tatsuya Hirano. **Human Wapl is a cohesin-binding protein that promotes sister-chromatid resolution in mitotic prophase**. *Curr. Biol.*, **16**(24):2406–2417, 19 December 2006. 13

[77] Tomoya S Kitajima, Takeshi Sakuno, Kei-Ichiro Ishiguro, Shun-Ichiro Iemura, Tohru Natsume, Shigehiro A Kawashima, and Yoshinori Watanabe. **Shugoshin collaborates with protein phosphatase 2A to protect cohesin**. *Nature*, **441**(7089):46–52, 4 May 2006. 13, 21

[78] Rebecca Heald and Alexey Khodjakov. **Thirty years of search and capture: The complex simplicity of mitotic spindle assembly**. *J. Cell Biol.*, **211**(6):1103–1111, 21 December 2015. 14

[79] R Wollman, E N Cytrynbaum, J T Jones, T Meyer, and others. **Efficient chromosome capture requires a bias in the 'search-and-capture'process during mitotic-spindle assembly**. *Curr. Biol.*, 2005. 14

[80] Douglass J Forbes, Anna Travesa, Matthew S Nord, and Cyril Bernis. **Nuclear transport factors: global regulation of mitosis**. *Curr. Opin. Cell Biol.*, **35**:78–90, August 2015. 14

[81] Petr Kaláb, Arnd Pralle, Ehud Y Isacoff, Rebecca Heald, and Karsten Weis. **Analysis of a RanGTP-regulated gradient in mitotic somatic cells**. *Nature*, **440**(7084):697–701, 30 March 2006. 15

[82] Oliver J Gruss and Isabelle Vernos. **The mechanism of spindle assembly: functions of Ran and its target TPX2**. *J. Cell Biol.*, **166**(7):949–955, 27 September 2004. 15

[83] Amnon Harel and Douglass J Forbes. **Importin beta: conducting a much larger cellular symphony**. *Mol. Cell*, **16**(3):319–330, 5 November 2004. 15

[84] T Wittmann, M Wilm, E Karsenti, and I Vernos. **TPX2, A novel xenopus MAP involved in spindle pole organization**. *J. Cell Biol.*, **149**(7):1405–1418, 26 June 2000. 15

REFERENCES

[85] O J Gruss, R E Carazo-Salas, C A Schatz, G Guarguaglini, J Kast, M Wilm, N Le Bot, I Vernos, E Karsenti, and I W Mattaj. **Ran induces spindle assembly by reversing the inhibitory effect of importin alpha on TPX2 activity**. *Cell*, **104**(1):83–93, 12 January 2001. 15

[86] Richard Bayliss, Teresa Sardon, Isabelle Vernos, and Elena Conti. **Structural basis of Aurora-A activation by TPX2 at the mitotic spindle**. *Mol. Cell*, **12**(4):851–862, October 2003. 15

[87] Thomas A Kufer, Erich A Nigg, and Herman H W Silljé. **Regulation of Aurora-A kinase on the mitotic spindle**. *Chromosoma*, **112**(4):159–163, December 2003. 15

[88] Ming-Ying Tsai, Christiane Wiese, Kan Cao, Ona Martin, Peter Donovan, Joan Ruderman, Claude Prigent, and Yixian Zheng. **A Ran signalling pathway mediated by the mitotic kinase Aurora A in spindle assembly**. *Nat. Cell Biol.*, **5**(3):242–248, March 2003. 15

[89] Sabine Petry, Aaron C Groen, Keisuke Ishihara, Timothy J Mitchison, and Ronald D Vale. **Branching microtubule nucleation in Xenopus egg extracts mediated by augmin and TPX2**. *Cell*, **152**(4):768–777, 14 February 2013. 15

[90] David Vanneste, Masatoshi Takagi, Naoko Imamoto, and Isabelle Vernos. **The role of Hklp2 in the stabilization and maintenance of spindle bipolarity**. *Curr. Biol.*, **19**(20):1712–1717, 3 November 2009. 15

[91] A Wilde, S B Lizarraga, L Zhang, C Wiese, N R Gliksman, C E Walczak, and Y Zheng. **Ran stimulates spindle assembly by altering microtubule dynamics and the balance of motor activities**. *Nat. Cell Biol.*, **3**(3):221–227, March 2001. 15

[92] C E Walczak, I Vernos, T J Mitchison, E Karsenti, and R Heald. **A model for the proposed roles of different microtubule-based motor proteins in establishing spindle bipolarity**. *Curr. Biol.*, **8**(16):903–913, 1998. 16

[93] Tarun M Kapoor, Michael A Lampson, Polla Hergert, Lisa Cameron, Daniela Cimini, E D Salmon, Bruce F McEwen, and Alexey Khodjakov. **Chromosomes can congress to the metaphase plate before biorientation**. *Science*, **311**(5759):388–391, 20 January 2006. 16

[94] Shang Cai, Christopher B O'Connell, Alexey Khodjakov, and Claire E Walczak. **Chromosome congression in the absence of kinetochore fibres**. *Nat. Cell Biol.*, **11**(7):832–838, July 2009. 16

[95] Yumi Kim, Andrew J Holland, Weijie Lan, and Don W Cleveland. **Aurora kinases and protein phosphatase 1 mediate chromosome congression through regulation of CENP-E**. *Cell*, **142**(3):444–455, 6 August 2010. 16

[96] James Bancroft, Philip Auckland, Catarina P Samora, and Andrew D McAinsh. **Chromosome congression is promoted by CENP-Q- and CENP-E-dependent pathways**. *J. Cell Sci.*, **128**(1):171–184, 1 January 2015. 16

[97] C Wandke, M Barisic, R Sigl, V Rauch, and others. **Human chromokinesins promote chromosome congression and spindle microtubule dynamics during mitosis**. *J. Cell Biol.*, 2012. 16

[98] E A Nigg. **Mitotic kinases as regulators of cell division and its checkpoints**. *Nat. Rev. Mol. Cell Biol.*, **2**(1):21–32, January 2001. 16

[99] Mathieu Bollen, Daniel W Gerlich, and Bart Lesage. **Mitotic phosphatases: from entry guards to exit guides**. *Trends Cell Biol.*, **19**(10):531–541, October 2009. 17, 31

[100] Claudia Wurzenberger and Daniel W Gerlich. **Phosphatases: providing safe passage through mitotic exit**. *Nat. Rev. Mol. Cell Biol.*, **12**(8):469–482, August 2011. 17, 31

[101] Michael J Cundell, Ricardo Nunes Bastos, Tongli Zhang, James Holder, Ulrike Gruneberg, Bela Novak, and Francis A Barr. **The BEG (PP2A-B55/ENSA/Greatwall) Pathway Ensures Cytokinesis follows Chromosome Separation**. *Mol. Cell*, **52**(3):393–405, 7 November 2013. 17, 31, 100, 110, 121

[102] C L Rieder, A Schultz, R Cole, and G Sluder. **Anaphase onset in vertebrate somatic cells is controlled by a checkpoint that monitors sister kinetochore attachment to the spindle**. *J. Cell Biol.*, **127**(5):1301–1310, 1 December 1994. 17, 70

[103] C L Rieder, R W Cole, A Khodjakov, and G Sluder. **The checkpoint delaying anaphase in response to chromosome monoorientation is mediated by an inhibitory signal produced by unattached kinetochores**. *J. Cell Biol.*, **130**(4):941–948, August 1995. 17, 36, 70

[104] S Inoué and E D Salmon. **Force generation by microtubule assembly/disassembly in mitosis and related movements**. *Mol. Biol. Cell*, **6**(12):1619–1640, December 1995. 18

[105] Thomas J Maresca and Edward D Salmon. **Intrakinetochore stretch is associated with changes in kinetochore phosphorylation and spindle assembly checkpoint activity**. *J. Cell Biol.*, **184**(3):373–381, 9 February 2009. 18, 21, 22, 55

[106] Kazuhiko S K Uchida, Kentaro Takagaki, Kazuki Kumada, Youko Hirayama, Tetsuo Noda, and Toru Hirota. **Kinetochore stretching inactivates the spindle assembly checkpoint**. *J. Cell Biol.*, **184**(3):383–390, 9 February 2009. 18, 21, 22, 55

[107] Mar Carmena, Michael Wheelock, Hironori Funabiki, and William C Earnshaw. **The chromosomal passenger complex (CPC): from easy rider to the godfather of mitosis**. *Nat. Rev. Mol. Cell Biol.*, **13**(12):789–803, December 2012. 18

[108] Zuojun Yue, Ana Carvalho, Zhenjie Xu, Xuemei Yuan, Stefano Cardinale, Susana Ribeiro, Fan Lai, Hiromi Ogawa, Elisabet Gudmundsdottir, Reto Gassmann, Ciaran G Morrison, Sandrine Ruchaud, and William C Earnshaw. **Deconstructing Survivin: comprehensive genetic analysis of Survivin function by conditional knockout in a vertebrate cell line**. *J. Cell Biol.*, **183**(2):279–296, 20 October 2008. 18

[109] Reto Gassmann, Ana Carvalho, Alexander J Henzing, Sandrine Ruchaud, Damien F Hudson, Reiko Honda, Erich A Nigg, Dietlind L Gerloff, and William C Earnshaw. **Borealin a novel chromosomal passenger required for stability of the bipolar mitotic spindle**. *J. Cell Biol.*, **166**(2):179–191, 2004. 18

[110] C A Cooke, M M Heck, and W C Earnshaw. **The inner centromere protein (INCENP) antigens: movement from inner centromere to midbody during mitosis**. *J. Cell Biol.*, **105**(5):2053–2067, November 1987. 18

[111] A Arockia Jeyaprakash, Ulf R Klein, Doris Lindner, Judith Ebert, Erich A Nigg, and Elena Conti. **Structure of a Survivin–Borealin–INCENP Core Complex Reveals How Chromosomal Passengers Travel Together**. *Cell*, **131**(2):271–285, 19 October 2007. 18

[112] Ulf R Klein, Erich A Nigg, and Ulrike Gruneberg. **Centromere targeting of the chromosomal passenger complex requires a ternary subcomplex of Borealin, Survivin, and the N-terminal domain of INCENP**. *Mol. Biol. Cell*, **17**(6):2547–2558, June 2006. 20

[113] R R Adams, S P Wheatley, A M Gouldsworthy, S E Kandels-Lewis, M Carmena, C Smythe, D L Gerloff, and W C Earnshaw. **INCENP binds the Aurora-related kinase AIRK2 and is required to target it to chromosomes, the central spindle and cleavage furrow**. *Curr. Biol.*, **10**(17):1075–1078, 7 September 2000. 20

[114] John D Bishop and Jill M Schumacher. **Phosphorylation of the carboxyl terminus of inner centromere protein (INCENP) by the Aurora B Kinase stimulates Aurora B kinase activity**. *J. Biol. Chem.*, **277**(31):27577–27580, 2 August 2002. 20

[115] Reiko Honda, Roman Körner, and Erich A Nigg. **Exploring the functional interactions between Aurora B, INCENP, and survivin in mitosis**. *Mol. Biol. Cell*, **14**(8):3325–3341, August 2003. 20

[116] Fabio Sessa, Marina Mapelli, Claudio Ciferri, Cataldo Tarricone, Liliana B Areces, Thomas R Schneider, P Todd Stukenberg, and Andrea Musacchio. **Mechanism of Aurora B activation by INCENP and inhibition by hesperadin**. *Mol. Cell*, **18**(3):379–391, 29 April 2005. 20

[117] Yuya Yamagishi, Takashi Honda, Yuji Tanno, and Yoshinori Watanabe. **Two histone marks establish the inner centromere and chromosome bi-orientation**. *Science*, **330**(6001):239–243, 8 October 2010. 20

[118] Jesse J Lipp, Toru Hirota, Ina Poser, and Jan-Michael Peters. **Aurora B controls the association of condensin I but not condensin II with mitotic chromosomes**. *J. Cell Sci.*, **120**(7):1245–1255, 1 April 2007. 20

[119] Samantha J Williams, Ariane Abrieu, and Ana Losada. **Bub1 targeting to centromeres is sufficient for Sgo1 recruitment in the absence of kinetochores**. *Chromosoma*, 26 April 2016. 20

[120] Alexander E Kelly, Cristina Ghenoiu, John Z Xue, Christian Zierhut, Hiroshi Kimura, and Hironori Funabiki. **Survivin reads phosphorylated histone H3 threonine 3 to activate the mitotic kinase Aurora B**. *Science*, **330**(6001):235–239, 8 October 2010. 20

[121] Ewa Niedzialkowska, Fangwei Wang, Przemyslaw J Porebski, Wladek Minor, Jonathan M G Higgins, and P Todd Stukenberg. **Molecular basis for phosphospecific recognition of histone H3 tails by Survivin paralogues at inner centromeres**. *Mol. Biol. Cell*, **23**(8):1457–1466, April 2012. 20

[122] Fangwei Wang, Natalia P Ulyanova, Maike S van der Waal, Debasis Patnaik, Susanne M A Lens, and Jonathan M G Higgins. **A positive feedback loop involving Haspin and Aurora B promotes CPC accumulation at centromeres in mitosis**. *Curr. Biol.*, **21**(12):1061–1069, 21 June 2011. 20

[123] Fangwei Wang, Jun Dai, John R Daum, Ewa Niedzialkowska, Budhaditya Banerjee, P Todd Stukenberg, Gary J Gorbsky, and Jonathan M G Higgins. **Histone H3 Thr-3 phosphorylation by Haspin positions Aurora B at centromeres in mitosis**. *Science*, **330**(6001):231–235, 8 October 2010. 20

[124] Tatsuya Tsukahara, Yuji Tanno, and Yoshinori Watanabe. **Phosphorylation of the CPC by Cdk1 promotes chromosome bi-orientation**. *Nature*, **467**(7316):719–723, 7 October 2010. 20

[125] Suzanne Vigneron, Susana Prieto, Cyril Bernis, Jean-Claude Labbé, Anna Castro, and Thierry Lorca. **Kinetochore localization of spindle checkpoint proteins: who controls whom?** *Mol. Biol. Cell*, **15**(10):4584–4596, October 2004. 20, 26

[126] Stefano Santaguida, Anthony Tighe, Anna Morena D'Alise, Stephen S Taylor, and Andrea Musacchio. **Dissecting the role of MPS1 in chromosome biorientation and the spindle checkpoint through the small molecule inhibitor reversine**. *J. Cell Biol.*, **190**(1):73–87, 12 July 2010. 20, 26, 57

[127] Nannette Jelluma, Arjan B Brenkman, Niels J F van den Broek, Carin W A Cruijsen, Maria H J van Osch, Susanne M A Lens, René H Medema, and Geert J P L Kops. **Mps1 phosphorylates Borealin to control Aurora B activity and chromosome alignment**. *Cell*, **132**(2):233–246, 25 January 2008. 20, 26

[128] Ulrike Gruneberg, Rüdiger Neef, Reiko Honda, Erich A Nigg, and Francis A Barr. **Relocation of Aurora B from centromeres to the central spindle at the metaphase to anaphase transition requires MKlp2**. *J. Cell Biol.*, **166**(2):167–172, 19 July 2004. 20, 38

[129] Stefan Hümmer and Thomas U Mayer. **Cdk1 Negatively Regulates Midzone Localization of the Mitotic Kinesin Mklp2 and the Chromosomal Passenger Complex**. *Curr. Biol.*, **19**(7):607–612, 14 April 2009. 20, 38

[130] María Dolores Vázquez-Novelle and Mark Petronczki. **Relocation of the chromosomal passenger complex prevents mitotic checkpoint engagement at anaphase**. *Curr. Biol.*, **20**(15):1402–1407, 10 August 2010. 20, 38

[131] Lesia Mirchenko and Frank Uhlmann. **Sli15INCENP Dephosphorylation Prevents Mitotic Checkpoint Reengagement Due to Loss of Tension at Anaphase Onset**. *Curr. Biol.*, **20**(15):1396–1401, 10 August 2010. 20, 38

[132] Paola Vagnarelli, Damien F Hudson, Susana A Ribeiro, Laura Trinkle-Mulcahy, Jennifer M Spence, Fan Lai, Christine J Farr, Angus I Lamond, and William C Earnshaw. **Condensin and Repo-Man–PP1 co-operate in the regulation of chromosome architecture during mitosis**. *Nat. Cell Biol.*, **8**(10):1133–1142, 24 September 2006. 21

[133] Yuji Tanno, Tomoya S Kitajima, Takashi Honda, Yasuto Ando, Kei-Ichiro Ishiguro, and Yoshinori Watanabe. **Phosphorylation of mammalian Sgo2 by Aurora B recruits PP2A and MCAK to centromeres**. *Genes Dev.*, **24**(19):2169–2179, 1 October 2010. 21

[134] Julie P I Welburn, Mathijs Vleugel, Dan Liu, John R Yates, 3rd, Michael A Lampson, Tatsuo Fukagawa, and Iain M Cheeseman. **Aurora B phosphorylates spatially distinct targets to differentially regulate the kinetochore-microtubule interface**. *Mol. Cell*, **38**(3):383–392, 14 May 2010. 21, 22

REFERENCES

[135] K F DeLuca, Sma Lens, and J G DeLuca. **Temporal changes in Hec1 phosphorylation control kinetochore–microtubule attachment stability during mitosis**. *J. Cell Sci.*, 2011. 21

[136] Y W Chan, A A Jeyaprakash, E A Nigg, and others. **Aurora B controls kinetochore–microtubule attachments by inhibiting Ska complex–KMN network interaction**. *J. Cell Biol.*, 2012. 21

[137] Dan Liu, Mathijs Vleugel, Chelsea B Backer, Tetsuya Hori, Tatsuo Fukagawa, Iain M Cheeseman, and Michael A Lampson. **Regulated targeting of protein phosphatase 1 to the outer kinetochore by KNL1 opposes Aurora B kinase**. *J. Cell Biol.*, **188**(6):809–820, 22 March 2010. 21

[138] Tomoyuki U Tanaka, Najma Rachidi, Carsten Janke, Gislene Pereira, Marta Galova, Elmar Schiebel, Michael J R Stark, and Kim Nasmyth. **Evidence that the Ipl1-Sli15 (Aurora kinase-INCENP) complex promotes chromosome bi-orientation by altering kinetochore-spindle pole connections**. *Cell*, **108**(3):317–329, 8 February 2002. 21

[139] Enxiu Wang, Edward R Ballister, and Michael A Lampson. **Aurora B dynamics at centromeres create a diffusion-based phosphorylation gradient**. *J. Cell Biol.*, **194**(4):539–549, 22 August 2011. 21

[140] Anatoly V Zaytsev, Dario Segura-Peña, Maxim Godzi, Abram Calderon, Edward R Ballister, Rumen Stamatov, Alyssa M Mayo, Laura Peterson, Ben E Black, Fazly I Ataullakhanov, Michael A Lampson, and Ekaterina L Grishchuk. **Bistability of a coupled Aurora B kinase-phosphatase system in cell division**. *Elife*, **5**, 14 January 2016. 21

[141] Xiaohu Wan, Ryan P O'Quinn, Heather L Pierce, Ajit P Joglekar, Walt E Gall, Jennifer G DeLuca, Christopher W Carroll, Song-Tao Liu, Tim J Yen, Bruce F McEwen, P Todd Stukenberg, Arshad Desai, and E D Salmon. **Protein Architecture of the Human Kinetochore Microtubule Attachment Site**. *Cell*, **137**(4):672–684, 15 May 2009. 22

[142] Aussie Suzuki, Benjamin L Badger, Julian Haase, Tomoo Ohashi, Harold P Erickson, Edward D Salmon, and Kerry Bloom. **How the kinetochore couples microtubule force and centromere stretch to move chromosomes**. *Nat. Cell Biol.*, **18**(4):382–392, April 2016. 22

[143] Anna A Ye, Jovana Deretic, Christopher M Hoel, Albert W Hinman, Daniela Cimini, Julie P Welburn, and Thomas J Maresca. **Aurora A Kinase Contributes to a Pole-Based Error Correction Pathway**. *Curr. Biol.*, **25**(14):1842–1851, 20 July 2015. 22

[144] Juraj Gregan, Silvia Polakova, Lijuan Zhang, Iva M Tolić-Nørrelykke, and Daniela Cimini. **Merotelic kinetochore attachment: causes and effects**. *Trends Cell Biol.*, **21**(6):374–381, June 2011. 22

[145] Sung Hugh Choi and Dannel McCollum. **A role for metaphase spindle elongation forces in correction of merotelic kinetochore attachments**. *Curr. Biol.*, **22**(3):225–230, 7 February 2012. 22

[146] Gheorghe Cojoc, Emanuele Roscioli, Lijuan Zhang, Alfonso García-Ulloa, Jagesh V Shah, Michael W Berns, Nenad Pavin, Daniela Cimini, Iva M Tolić, and Juraj Gregan. **Laser microsurgery reveals conserved viscoelastic behavior of the kinetochore**. *J. Cell Biol.*, **212**(7):767–776, 28 March 2016. 23

[147] Andrea Musacchio and Edward D Salmon. **The spindle-assembly checkpoint in space and time**. *Nat. Rev. Mol. Cell Biol.*, **8**(5):379–393, May 2007. 23, 26

[148] Andrea Musacchio. **The Molecular Biology of Spindle Assembly Checkpoint Signaling Dynamics**. *Curr. Biol.*, **25**(20):R1002–R1018, 19 October 2015. 23

[149] Nicholas G Brown, Ryan VanderLinden, Edmond R Watson, Florian Weissmann, Alban Ordureau, Kuen-Phon Wu, Wei Zhang, Shanshan Yu, Peter Y Mercredi, Joseph S Harrison, Iain F Davidson, Renping Qiao, Ying Lu, Prakash Dube, Michael R Brunner, Christy R R Grace, Darcie J Miller, David Haselbach, Marc A Jarvis, Masaya Yamaguchi, David Yanishevski, Georg Petzold, Sachdev S Sidhu, Brian Kuhlman, Marc W Kirschner, J Wade Harper, Jan-Michael Peters, Holger Stark, and Brenda A Schulman. **Dual RING E3 Architectures Regulate Multiubiquitination and Ubiquitin Chain Elongation by APC/C**. *Cell*, **165**(6):1440–1453, 2 June 2016. 23

[150] Edgar R Kramer, Nadja Scheuringer, Alexandre V Podtelejnikov, Matthias Mann, and Jan-Michael Peters. **Mitotic Regulation of the APC Activator Proteins CDC20 and CDH1**. *Mol. Biol. Cell*, **11**(5):1555–1569, 1 May 2000. 23, 25

[151] Brian R Thornton and David P Toczyski. **Securin and B-cyclin/CDK are the only essential targets of the APC**. *Nat. Cell Biol.*, **5**(12):1090–1094, December 2003. 23

[152] Kazuyuki Fujimitsu, Margaret Grimaldi, and Hiroyuki Yamano. **Cyclin-dependent kinase 1–dependent activation of APC/C ubiquitin ligase**. *Science*, **352**(6289):1121–1124, 27 May 2016. 25

[153] Luying Jia, Bing Li, and Hongtao Yu. **The Bub1-Plk1 kinase complex promotes spindle checkpoint signalling through Cdc20 phosphorylation**. *Nat. Commun.*, **7**:10818, 25 February 2016. 25

[154] Violeta Morin, Susana Prieto, Sabrina Melines, Sonia Hem, Michel Rossignol, Thierry Lorca, Julien Espeut, Nathalie Morin, and Ariane Abrieu. **CDK-Dependent Potentiation of MPS1 Kinase Activity Is Essential to the Mitotic Checkpoint**. *Curr. Biol.*, **22**(4):289–295, 21 February 2012. 26

[155] Tongge Zhu, Zhen Dou, Bo Qin, Changjiang Jin, Xinghui Wang, Leilei Xu, Zhaoyang Wang, Lijuan Zhu, Fusheng Liu, Xinjiao Gao, Yuwen Ke, Zhiyong Wang, Felix Aikhionbare, Chuanhai Fu, Xia Ding, and Xuebiao Yao. **Phosphorylation of microtubule-binding protein Hec1 by mitotic kinase Aurora B specifies spindle checkpoint kinase Mps1 signaling at the kinetochore**. *J. Biol. Chem.*, **288**(50):36149–36159, 13 December 2013. 26

[156] Wilco Nijenhuis, Eleonore von Castelmur, Dene Littler, Valeria De Marco, Eelco Tromer, Mathijs Vleugel, Maria H J van Osch, Berend Snel, Anastassis Perrakis, and Geert J P L Kops. **A TPR domain–containing N-terminal module of MPS1 is required for its kinetochore localization by Aurora B**. *J. Cell Biol.*, **201**(2):217–231, 15 April 2013. 26

[157] Nitobe London, Steven Ceto, Jeffrey A Ranish, and Sue Biggins. **Phosphoregulation of Spc105 by Mps1 and PP1 regulates Bub1 localization to kinetochores**. *Curr. Biol.*, **22**(10):900–906, 22 May 2012. 26

[158] Lindsey A Shepperd, John C Meadows, Alicja M Sochaj, Theresa C Lancaster, Juan Zou, Graham J Buttrick, Juri Rappsilber, Kevin G Hardwick, and Jonathan B A Millar. **Phosphodependent recruitment of Bub1 and Bub3 to Spc7/KNL1 by Mph1 kinase maintains the spindle checkpoint**. *Curr. Biol.*, **22**(10):891–899, 22 May 2012. 26

[159] Yuya Yamagishi, Ching-Hui Yang, Yuji Tanno, and Yoshinori Watanabe. **MPS1/Mph1 phosphorylates the kinetochore protein KNL1/Spc7 to recruit SAC components**. *Nat. Cell Biol.*, **14**(7):746–752, July 2012. 26

[160] Veronica Krenn, Katharina Overlack, Ivana Primorac, Suzan van Gerwen, and Andrea Musacchio. **KI motifs of human Knl1 enhance assembly of comprehensive spindle checkpoint complexes around MELT repeats**. *Curr. Biol.*, **24**(1):29–39, 6 January 2014. 26

[161] Gang Zhang, Tiziana Lischetti, Daniel G Hayward, and Jakob Nilsson. **Distinct domains in Bub1 localize RZZ and BubR1 to kinetochores to regulate the checkpoint**. *Nat. Commun.*, **6**:7162, 2 June 2015. 26

[162] Janet L Burton and Mark J Solomon. **Mad3p, a pseudosubstrate inhibitor of APCCdc20 in the spindle assembly checkpoint**. *Genes Dev.*, **21**(6):655–667, 15 March 2007. 26

[163] Derek T C Lau and Andrew W Murray. **Mad2 and Mad3 cooperate to arrest budding yeast in mitosis**. *Curr. Biol.*, **22**(3):180–190, 7 February 2012. 26, 27

[164] Mark W Moyle, Taekyung Kim, Neil Hattersley, Julien Espeut, Dhanya K Cheerambathur, Karen Oegema, and Arshad Desai. **A Bub1–Mad1 interaction targets the Mad1–Mad2 complex to unattached kinetochores to initiate the spindle checkpoint**. *J. Cell Biol.*, **204**(5):647–657, 3 March 2014. 26

[165] L Sironi, M Melixetian, M Faretta, E Prosperini, K Helin, and A Musacchio. **Mad2 binding to Mad1 and Cdc20, rather than oligomerization, is required for the spindle checkpoint**. *EMBO J.*, **20**(22):6371–6382, 15 November 2001. 26

[166] Xuelian Luo, Zhanyun Tang, Josep Rizo, and Hongtao Yu. **The Mad2 spindle checkpoint protein undergoes similar major conformational changes upon binding to either Mad1 or Cdc20**. *Mol. Cell*, **9**(1):59–71, January 2002. 26

[167] Lucia Sironi, Marina Mapelli, Stefan Knapp, Anna De Antoni, Kuan-Teh Jeang, and Andrea Musacchio. **Crystal structure of the tetrameric Mad1-Mad2 core complex: implications of a 'safety belt' binding mechanism for the spindle checkpoint**. *EMBO J.*, **21**(10):2496–2506, 15 May 2002. 26

[168] Veronica Rodriguez-Bravo, John Maciejowski, Jennifer Corona, Håkon Kirkeby Buch, Philippe Collin, Masato T Kanemaki, Jagesh V Shah, and Prasad V Jallepalli. **Nuclear pores protect genome integrity by assembling a premitotic and Mad1-dependent anaphase inhibitor**. *Cell*, **156**(5):1017–1031, 27 February 2014. 26, 27, 85

[169] Virginia Silió, Andrew D McAinsh, and Jonathan B Millar. **KNL1-Bubs and RZZ Provide Two Separable Pathways for Checkpoint Activation at Human Kinetochores**. *Dev. Cell*, **35**(5):600–613, 7 December 2015. 26, 30

[170] Marco Simonetta, Romilde Manzoni, Roberto Mosca, Marina Mapelli, Lucia Massimiliano, Martin Vink, Bela Novak, Andrea Musacchio, and Andrea Ciliberto. **The influence of catalysis on mad2 activation dynamics**. *PLoS Biol.*, **7**(1):e10, 13 January 2009. 26, 27

[171] Anita Kulukian, Joo Seok Han, and Don W Cleveland. **Unattached kinetochores catalyze production of an anaphase inhibitor that requires a Mad2 template to prime Cdc20 for BubR1 binding**. *Dev. Cell*, **16**(1):105–117, January 2009. 26

[172] Anna De Antoni, Chad G Pearson, Daniela Cimini, Julie C Canman, Valeria Sala, Luigi Nezi, Marina Mapelli, Lucia Sironi, Mario Faretta, Edward D Salmon, and Andrea Musacchio. **The Mad1/Mad2 complex as a template for Mad2 activation in the spindle assembly checkpoint**. *Curr. Biol.*, **15**(3):214–225, 8 February 2005. 26

[173] Andreas Doncic, Eshel Ben-Jacob, and Naama Barkai. **Evaluating putative mechanisms of the mitotic spindle checkpoint**. *Proc. Natl. Acad. Sci. U. S. A.*, **102**(18):6332–6337, 3 May 2005. 27, 32

[174] Katharina Overlack, Ivana Primorac, Mathijs Vleugel, Veronica Krenn, Stefano Maffini, Ingrid Hoffmann, Geert J P L Kops, and Andrea Musacchio. **A molecular basis for the differential roles of Bub1 and BubR1 in the spindle assembly checkpoint**. *eLife Sciences*, **4**:e05269, 18 February 2015. 27

[175] William C H Chao, Kiran Kulkarni, Ziguo Zhang, Eric H Kong, and David Barford. **Structure of the mitotic checkpoint complex**. *Nature*, **484**(7393):208–213, 12 April 2012. 28

[176] Ivana Primorac and Andrea Musacchio. **Panta rhei: The APC/C at steady state**. *J. Cell Biol.*, **201**(2):177–189, 15 April 2013. 28

[177] Daisuke Izawa and Jonathon Pines. **The mitotic checkpoint complex binds a second CDC20 to inhibit active APC/C**. *Nature*, **517**(7536):631–634, 29 January 2015. 28

[178] Masaya Yamaguchi, Ryan VanderLinden, Florian Weissmann, Renping Qiao, Prakash Dube, Nicholas G Brown, David Haselbach, Wei Zhang, Sachdev S Sidhu, Jan-Michael Peters, Holger Stark, and Brenda A Schulman. **Cryo-EM of Mitotic Checkpoint Complex-Bound APC/C Reveals Reciprocal and Conformational Regulation of Ubiquitin Ligation**. *Mol. Cell*, **63**(4):593–607, 18 August 2016. 28

[179] Claudio Alfieri, Leifu Chang, Ziguo Zhang, Jing Yang, Sarah Maslen, Mark Skehel, and David Barford. **Molecular basis of APC/C regulation by the spindle assembly checkpoint**. *Nature*, **536**(7617):431–436, 25 August 2016. 28

[180] Joo Seok Han, Andrew J Holland, Daniele Fachinetti, Anita Kulukian, Bulent Cetin, and Don W Cleveland. **Catalytic Assembly of the Mitotic Checkpoint Inhibitor BubR1-Cdc20 by a Mad2-Induced Functional Switch in Cdc20**. *Mol. Cell*, **51**(1):92–104, 11 July 2013. 28

REFERENCES

[181] Jörg Mansfeld, Philippe Collin, Mark O Collins, Jyoti S Choudhary, and Jonathon Pines. **APC15 drives the turnover of MCC-CDC20 to make the spindle assembly checkpoint responsive to kinetochore attachment**. *Nat. Cell Biol.*, **13**(10):1234–1243, October 2011. 29

[182] S A Foster and D O Morgan. **The APC/C subunit Mnd2/Apc15 promotes Cdc20 autoubiquitination and spindle assembly checkpoint inactivation**. *Mol. Cell*, 2012. 29

[183] Esther Eytan, Kexi Wang, Shirly Miniowitz-Shemtov, Danielle Sitry-Shevah, Sharon Kaisari, Tim J Yen, Song-Tao Liu, and Avram Hershko. **Disassembly of mitotic checkpoint complexes by the joint action of the AAA-ATPase TRIP13 and p31comet**. *Proc. Natl. Acad. Sci. U. S. A.*, **111**(33):12019–12024, 19 August 2014. 29

[184] Qiaozhen Ye, Scott C Rosenberg, Arne Moeller, Jeffrey A Speir, Tiffany Y Su, and Kevin D Corbett. **TRIP13 is a protein-remodeling AAA+ ATPase that catalyzes MAD2 conformation switching**. *eLife Sciences*, **4**:e07367, 22 May 2015. 29

[185] Hoi Tang Ma and Randy Yat Choi Poon. **TRIP13 Regulates Both the Activation and Inactivation of the Spindle-Assembly Checkpoint**. *Cell Rep.*, **14**(5):1086–1099, 9 February 2016. 29

[186] Adar Teichner, Esther Eytan, Danielle Sitry-Shevah, Shirly Miniowitz-Shemtov, Elena Dumin, Jonathan Gromis, and Avram Hershko. **p31comet promotes disassembly of the mitotic checkpoint complex in an ATP-dependent process**. *Proc. Natl. Acad. Sci. U. S. A.*, **108**(8):3187–3192, 22 February 2011. 29

[187] Frederick G Westhorpe, Anthony Tighe, Pablo Lara-Gonzalez, and Stephen S Taylor. **p31comet-mediated extraction of Mad2 from the MCC promotes efficient mitotic exit**. *J. Cell Sci.*, **124**(Pt 22):3905–3916, 15 November 2011. 29

[188] Esther Eytan, Danielle Sitry-Shevah, Adar Teichner, and Avram Hershko. **Roles of different pools of the mitotic checkpoint complex and the mechanisms of their disassembly**. *Proc. Natl. Acad. Sci. U. S. A.*, **110**(26):10568–10573, 25 June 2013. 29

[189] Eunhee Choi and Hongtao Yu. **Phosphorylation propels p31comet for mitotic exit**. *Cell Cycle*, **14**(13):1997–1998, 3 July 2015. 29

[190] Min Mo, Alexei Arnaoutov, and Mary Dasso. **Phosphorylation of Xenopus p31comet potentiates mitotic checkpoint exit**. *Cell Cycle*, **14**(24):3978–3985, 17 December 2015. 29

[191] B J Howell, B F McEwen, J C Canman, D B Hoffman, E M Farrar, C L Rieder, and E D Salmon. **Cytoplasmic dynein/dynactin drives kinetochore protein transport to the spindle poles and has a role in mitotic spindle checkpoint inactivation**. *J. Cell Biol.*, **155**(7):1159–1172, 24 December 2001. 29, 30

[192] E Wojcik, R Basto, M Serr, F Scaërou, R Karess, and T Hays. **Kinetochore dynein: its dynamics and role in the transport of the Rough deal checkpoint protein**. *Nat. Cell Biol.*, **3**(11):1001–1007, November 2001. 29, 30

[193] Yoshitaka Hiruma, Carlos Sacristan, Spyridon T Pachis, Athanassios Adamopoulos, Timo Kuijt, Marcellus Ubbink, Eleonore von Castelmur, Anastassis Perrakis, and Geert J P L Kops. **Competition between MPS1 and microtubules at kinetochores regulates spindle checkpoint signaling**. *Science*, **348**(6240):1264–1267, 12 June 2015. 29, 30, 36

[194] Pavithra Aravamudhan, Alan A Goldfarb, and Ajit P Joglekar. **The kinetochore encodes a mechanical switch to disrupt spindle assembly checkpoint signalling**. *Nat. Cell Biol.*, **17**(7):868–879, July 2015. 29, 30, 36

[195] Wilco Nijenhuis, Giulia Vallardi, Antoinette Teixeira, Geert J P L Kops, and Adrian T Saurin. **Negative feedback at kinetochores underlies a responsive spindle checkpoint signal**. *Nat. Cell Biol.*, **16**(12):1257–1264, December 2014. 29

[196] Antonio Espert, Pelin Uluocak, Ricardo Nunes Bastos, Davinderpreet Mangat, Philipp Graab, and Ulrike Gruneberg. **PP2A-B56 opposes Mps1 phosphorylation of Knl1 and thereby promotes spindle assembly checkpoint silencing**. *J. Cell Biol.*, **206**(7):833–842, 29 September 2014. 29

[197] Maria Maldonado and Tarun M Kapoor. **Constitutive Mad1 targeting to kinetochores uncouples checkpoint signalling from chromosome biorientation**. *Nat. Cell Biol.*, **13**(4):475–482, April 2011. 30

[198] Edward R Ballister, Michelle Riegman, and Michael A Lampson. **Recruitment of Mad1 to metaphase kinetochores is sufficient to reactivate the mitotic checkpoint**. *J. Cell Biol.*, **204**(6):901–908, 17 March 2014. 30

[199] Timo E F Kuijt, Manja Omerzu, Adrian T Saurin, and Geert J P L Kops. **Conditional targeting of MAD1 to kinetochores is sufficient to reactivate the spindle assembly checkpoint in metaphase**. *Chromosoma*, **123**(5):471–480, October 2014. 30

[200] Zhejian Ji, Haishan Gao, and Hongtao Yu. **CELL DIVISION CYCLE. Kinetochore attachment sensed by competitive Mps1 and microtubule binding to Ndc80C**. *Science*, **348**(6240):1260–1264, 12 June 2015. 30

[201] J Mei, X Huang, and P Zhang. **Securin is not required for cellular viability, but is required for normal growth of mouse embryonic fibroblasts**. *Curr. Biol.*, **11**(15):1197–1201, 7 August 2001. 30

[202] Susanne Hellmuth, Scott Rata, Andreas Brown, Stefan Heidmann, Bela Novak, and Olaf Stemmann. **Human chromosome segregation involves multi-layered regulation of separase by the peptidyl-prolyl-isomerase Pin1**. *Mol. Cell*, **58**(3):495–506, 7 May 2015. 31

[203] Satoru Mochida and Tim Hunt. **Protein phosphatases and their regulation in the control of mitosis**. *EMBO Rep.*, **13**(3):197–203, March 2012. 31

[204] Judy Qiju Wu, Jessie Yanxiang Guo, Wanli Tang, Chih-Sheng Yang, Christopher D Freel, Chen Chen, Angus C Nairn, and Sally Kornbluth. **PP1-mediated dephosphorylation of phosphoproteins at mitotic exit is controlled by inhibitor-1 and PP1 phosphorylation**. *Nat. Cell Biol.*, **11**(5):644–651, May 2009. 31

[205] Jiangtao Yu, Yong Zhao, Zexiao Li, Simon Galas, and Michael L Goldberg. **Greatwall kinase participates in the Cdc2 autoregulatory loop in Xenopus egg extracts**. *Mol. Cell*, **22**(1):83–91, 7 April 2006. 31

[206] Satoru Mochida, Sarah L Maslen, Mark Skehel, and Tim Hunt. **Greatwall phosphorylates an inhibitor of protein phosphatase 2A that is essential for mitosis**. *Science*, **330**(6011):1670–1673, 17 December 2010. 31

[207] Aicha Gharbi-Ayachi, Jean-Claude Labbé, Andrew Burgess, Suzanne Vigneron, Jean-Marc Strub, Estelle Brioudes, Alain Van-Dorsselaer, Anna Castro, and Thierry Lorca. **The substrate of Greatwall kinase, Arpp19, controls mitosis by inhibiting protein phosphatase 2A**. *Science*, **330**(6011):1673–1677, 17 December 2010. 31

[208] Byron C Williams, Joshua J Filter, Kristina A Blake-Hodek, Brian E Wadzinski, Nicholas J Fuda, David Shalloway, and Michael L Goldberg. **Greatwall-phosphorylated Endosulfine is both an inhibitor and a substrate of PP2A-B55 heterotrimers**. *Elife*, **3**:e01695, 11 March 2014. 31, 100, 108

[209] Andreas Heim, Anja Konietzny, and Thomas U Mayer. **Protein phosphatase 1 is essential for Greatwall inactivation at mitotic exit**. *EMBO Rep.*, **16**(11):1501–1510, November 2015. 31

[210] Stuart C Schaffner and Jorge V José. **Biophysical model of self-organized spindle formation patterns without centrosomes and kinetochores**. *Proc. Natl. Acad. Sci. U. S. A.*, **103**(30):11166–11171, 25 July 2006. 32

[211] Rose Loughlin, Rebecca Heald, and François Nédélec. **A computational model predicts Xenopus meiotic spindle organization**. *J. Cell Biol.*, **191**(7):1239–1249, 27 December 2010. 32

[212] Jing Chen and Jian Liu. **Spatial-temporal model for silencing of the mitotic spindle assembly checkpoint**. *Nat. Commun.*, **5**:4795, 12 September 2014. 32

[213] Andreas Doncic, Eshel Ben-Jacob, Shmuel Einav, and Naama Barkai. **Reverse Engineering of the Spindle Assembly Checkpoint**. *PLoS One*, **4**(8):e6495, 4 August 2009. 32

[214] Enuo He, Orsolya Kapuy, Raquel A Oliveira, Frank Uhlmann, John J Tyson, and Béla Novák. **System-level feedbacks make the anaphase switch irreversible**. *Proc. Natl. Acad. Sci. U. S. A.*, **108**(24):10016–10021, 14 June 2011. 32, 56

[215] Stephanie Heinrich, Eva-Maria Geissen, Julia Kamenz, Susanne Trautmann, Christian Widmer, Philipp Drewe, Michael Knop, Nicole Radde, Jan Hasenauer, and Silke Hauf. **Determinants of robustness in spindle assembly checkpoint signalling**. *Nat. Cell Biol.*, **15**(11):1328–1339, November 2013. 32

[216] Amalie E Dick and Daniel W Gerlich. **Kinetic framework of spindle assembly checkpoint signalling**. *Nat. Cell Biol.*, **15**(11):1370–1377, November 2013. 36, 38, 51, 71, 73, 98, 132

[217] Philippe Collin, Oxana Nashchekina, Rachael Walker, and Jonathon Pines. **The spindle assembly checkpoint works like a rheostat rather than a toggle switch**. *Nat. Cell Biol.*, **15**(11):1378–1385, November 2013. 37, 51, 73, 79

[218] Raquel A Oliveira, Russell S Hamilton, Andrea Pauli, Ilan Davis, and Kim Nasmyth. **Cohesin cleavage and Cdk inhibition trigger formation of daughter nuclei**. *Nat. Cell Biol.*, **12**(2):185–192, February 2010. 38, 41

[219] Julia Kamenz and Silke Hauf. **Slow Checkpoint Activation Kinetics as a Safety Device in Anaphase**. *Curr. Biol.*, **24**(6):646–651, 17 March 2014. 38, 98

[220] P Clute and J Pines. **Temporal and spatial control of cyclin B1 destruction in metaphase**. *Nat. Cell Biol.*, **1**(2):82–87, June 1999. 38, 71

[221] Ahmed Rattani, P K Vinod, Jonathan Godwin, Kikuë Tachibana-Konwalski, Magda Wolna, Marcos Malumbres, Béla Novák, and Kim Nasmyth. **Dependency of the Spindle Assembly Checkpoint on Cdk1 Renders the Anaphase Transition Irreversible**. *Curr. Biol.*, **24**(6):630–637, 17 March 2014. 38, 71

[222] María Dolores Vázquez-Novelle, Laurent Sansregret, Amalie E Dick, Christopher A Smith, Andrew D McAinsh, Daniel W Gerlich, and Mark Petronczki. **Cdk1 Inactivation Terminates Mitotic Checkpoint Surveillance and Stabilizes Kinetochore Attachments in Anaphase**. *Curr. Biol.*, **24**(6):638–645, 17 March 2014. 38, 71, 72, 79

[223] Daniela A Brito and Conly L Rieder. **Mitotic Checkpoint Slippage in Humans Occurs via Cyclin B Destruction in the Presence of an Active Checkpoint**. *Curr. Biol.*, **16**(12):1194–1200, 20 June 2006. 39, 79, 131

[224] A L Mena, Ewf Lam, and S Chatterjee. **Sustained spindle-assembly checkpoint response requires de novo transcription and translation of cyclin B1**. *PLoS One*, 2010. 39

[225] Mihailo Mirkovic, Lukas H Hutter, Béla Novák, and Raquel A Oliveira. **Premature Sister Chromatid Separation Is Poorly Detected by the Spindle Assembly Checkpoint as a Result of System-Level Feedback**. *Cell Rep.*, **13**(3):470–478, 20 October 2015. 40, 42, 44, 46, 48, 50, 53

[226] María Carretero, Miguel Ruiz-Torres, Miriam Rodríguez-Corsino, Isabel Barthelemy, and Ana Losada. **Pds5B is required for cohesion establishment and Aurora B accumulation at centromeres**. *EMBO J.*, **32**(22):2938–2949, 13 November 2013. 43

[227] Yegor Smurnyy, Angela V Toms, Gilles R Hickson, Michael J Eck, and Ulrike S Eggert. **Binucleine 2, an isoform-specific inhibitor of Drosophila Aurora B kinase, provides insights into the mechanism of cytokinesis**. *ACS Chem. Biol.*, **5**(11):1015–1020, 19 November 2010. 45

[228] Christopher B O'Connell, Jadranka Loncarek, Polla Hergert, Antonis Kourtidis, Douglas S Conklin, and Alexey Khodjakov. **The spindle assembly checkpoint is satisfied in the absence of interkinetochore tension during mitosis with unreplicated genomes**. *J. Cell Biol.*, **183**(1):29–36, 6 October 2008. 47

[229] Elsa Logarinho, Hassan Bousbaa, José Miguel Dias, Carla Lopes, Isabel Amorim, Ana Antunes-Martins, and Claudio E Sunkel. **Different spindle checkpoint proteins monitor microtubule attachment and tension at kinetochores in Drosophila cells**. *J. Cell Sci.*, **117**(Pt 9):1757–1771, 1 April 2004. 51

[230] Eulalie Buffin, Christophe Lefebvre, Junyong Huang, Mary Elisabeth Gagou, and Roger E Karess. **Recruitment of Mad2 to the kinetochore requires the Rod/Zw10 complex**. *Curr. Biol.*, **15**(9):856–861, 10 May 2005. 51

[231] Thomas J Maresca and E D Salmon. **Welcome to a new kind of tension: translating kinetochore mechanics into a wait-anaphase signal**. *J. Cell Sci.*, **123**(Pt 6):825–835, 15 March 2010. 55

[232] Natalie J Nannas and Andrew W Murray. **Tethering sister centromeres to each other suggests the spindle checkpoint detects stretch within the kinetochore**. *PLoS Genet.*, **10**(8):e1004492, August 2014. 55

REFERENCES

[233] Jamin B Hein and Jakob Nilsson. **Stable MCC binding to the APC/C is required for a functional spindle assembly checkpoint**. *EMBO Rep.*, **15**(3):264–272, March 2014. 56

[234] Anael Verdugo, P K Vinod, John J Tyson, and Bela Novak. **Molecular mechanisms creating bistable switches at cell cycle transitions**. *Open Biol.*, **3**(3):120179, 1 March 2013. 56

[235] Daniel T Gillespie. **Stochastic simulation of chemical kinetics**. *Annu. Rev. Phys. Chem.*, **58**:35–55, 2007. 58

[236] Daniel T Gillespie. **A general method for numerically simulating the stochastic time evolution of coupled chemical reactions**. *J. Comput. Phys.*, **22**(4):403–434, 1 December 1976. 58

[237] Helder Maiato, Polla J Hergert, Sara Moutinho-Pereira, Yimin Dong, Kristin J Vandenbeldt, Conly L Rieder, and Bruce F McEwen. **The ultrastructure of the kinetochore and kinetochore fiber in Drosophila somatic cells**. *Chromosoma*, **115**(6):469–480, December 2006. 59

[238] Kikuë Tachibana-Konwalski, Jonathan Godwin, Máté Borsos, Ahmed Rattani, David J Adams, and Kim Nasmyth. **Spindle assembly checkpoint of oocytes depends on a kinetochore structure determined by cohesin in meiosis I**. *Curr. Biol.*, **23**(24):2534–2539, 16 December 2013. 69

[239] Daniela A Brito, Zhenye Yang, and Conly L Rieder. **Microtubules do not promote mitotic slippage when the spindle assembly checkpoint cannot be satisfied**. *J. Cell Biol.*, **182**(4):623–629, 25 August 2008. 78, 79

[240] Zhenye Yang, Alison E Kenny, Daniela A Brito, and Conly L Rieder. **Cells satisfy the mitotic checkpoint in Taxol, and do so faster in concentrations that stabilize syntelic attachments**. *J. Cell Biol.*, **186**(5):675–684, 7 September 2009. 78, 79

[241] Michael J Cundell, Lukas H Hutter, Ricardo Nunes Bastos, Elena Poser, James Holder, Shabaz Mohammed, Bela Novak, and Francis A Barr. **A PP2A-B55 recognition signal controls substrate dephosphorylation kinetics during mitotic exit**. *J. Cell Biol.*, 22 August 2016. 99, 120, 122

[242] Paul J Boersema, Reinout Raijmakers, Simone Lemeer, Shabaz Mohammed, and Albert J R Heck. **Multiplex peptide stable isotope dimethyl labeling for quantitative proteomics**. *Nat. Protoc.*, **4**(4):484–494, 2009. 103

[243] J Cox and M Mann. **MaxQuant enables high peptide identification rates, individualized ppb-range mass accuracies and proteome-wide protein quantification**. *Nat. Biotechnol.*, 2008. 104

[244] Jürgen Cox, Nadin Neuhauser, Annette Michalski, Richard A Scheltema, Jesper V Olsen, and Matthias Mann. **Andromeda: a peptide search engine integrated into the MaxQuant environment**. *J. Proteome Res.*, **10**(4):1794–1805, 1 April 2011. 104

[245] P K Vinod and Bela Novak. **Model scenarios for switch-like mitotic transitions**. *FEBS Lett.*, **589**(6):667–671, 12 March 2015. 108

[246] Sara Cuylen, Claudia Blaukopf, Antonio Z Politi, Thomas Müller-Reichert, Beate Neumann, Ina Poser, Jan Ellenberg, Anthony A Hyman, and Daniel W Gerlich. **Ki-67 acts as a biological surfactant to disperse mitotic chromosomes**. *Nature*, **535**(7611):308–312, 14 July 2016. 116

[247] Niklaas Colaert, Kenny Helsens, Lennart Martens, Joël Vandekerckhove, and Kris Gevaert. **Improved visualization of protein consensus sequences by iceLogo**. *Nat. Methods*, **6**(11):786–787, November 2009. 120

[248] Jes Alexander, Daniel Lim, Brian A Joughin, Björn Hegemann, James R A Hutchins, Tobias Ehrenberger, Frank Ivins, Fabio Sessa, Otto Hudecz, Erich A Nigg, Andrew M Fry, Andrea Musacchio, P Todd Stukenberg, Karl Mechtler, Jan-Michael Peters, Stephen J Smerdon, and Michael B Yaffe. **Spatial exclusivity combined with positive and negative selection of phosphorylation motifs is the basis for context-dependent mitotic signaling**. *Sci. Signal.*, **4**(179):ra42, 28 June 2011. 121

[249] Radhika Subramanian, Elizabeth M Wilson-Kubalek, Christopher P Arthur, Matthew J Bick, Elizabeth A Campbell, Seth A Darst, Ronald A Milligan, and Tarun M Kapoor. **Insights into antiparallel microtubule crosslinking by PRC1, a conserved nonmotor microtubule binding protein**. *Cell*, **142**(3):433–443, 6 August 2010. 122

[250] Radhika Subramanian, Shih-Chieh Ti, Lei Tan, Seth A Darst, and Tarun M Kapoor. **Marking and measuring single microtubules by PRC1 and kinesin-4**. *Cell*, **154**(2):377–390, 18 July 2013. 122

[251] Rüdiger Neef, Ulrike Gruneberg, Robert Kopajtich, Xiuling Li, Erich A Nigg, Herman Sillje, and Francis A Barr. **Choice of Plk1 docking partners during mitosis and cytokinesis is controlled by the activation state of Cdk1**. *Nat. Cell Biol.*, **9**(4):436–444, April 2007. 122

Table 7.1: Interactive Supplementary Material

Chapter	Subject	Interactive-Link[a]	Static-Link[b]
4	Notebook - Deterministic Model	`http://localhost:8888/notebooks/Chapter4/DeterministicModel.ipynb`	`https://github.com/el-uhu/thesis-notebooks/blob/master/Chapter4/DeterministicModel.ipynb`
	Notebook - Core Model	`http://localhost:8888/notebooks/Chapter4/CoreModel.ipynb`	`https://github.com/el-uhu/thesis-notebooks/blob/master/Chapter4/CoreModel.ipynb`
	Notebook - Single-Feedback Model	`http://localhost:8888/notebooks/Chapter4/SingleFeedbackModel.ipynb`	`https://github.com/el-uhu/thesis-notebooks/blob/master/Chapter4/SingleFeedbackModel.ipynb`
	Notebook - Dual-Feedback Model	`http://localhost:8888/notebooks/Chapter4/DualFeedbackModel.ipynb`	`https://github.com/el-uhu/thesis-notebooks/blob/master/Chapter4/DualFeedbackModel.ipynb`
	Notebook - Model-Prediction	`http://localhost:8888/notebooks/Chapter4/ModelPrediction.ipynb`	`https://github.com/el-uhu/thesis-notebooks/blob/master/Chapter4/ModelPrediction.ipynb`
5	Notebook - Data	`http://localhost:8888/notebooks/Chapter5/Data.ipynb`	`https://github.com/el-uhu/thesis-notebooks/blob/master/Chapter5/Data.ipynb`
	Notebook - Model	`http://localhost:8888/notebooks/Chapter5/Model.ipynb`	`https://github.com/el-uhu/thesis-notebooks/blob/master/Chapter5/Model.ipynb`
6	Notebook - Preprocessing	`http://localhost:8888/notebooks/Chapter6/01_Preprocessing.ipynb`	`https://github.com/el-uhu/thesis-notebooks/blob/master/Chapter6/01_Preprocessing.ipynb`
	Notebook - Extracting	`http://localhost:8888/notebooks/Chapter6/02_Extracting.ipynb`	`https://github.com/el-uhu/thesis-notebooks/blob/master/Chapter6/02_Extracting.ipynb`
	Notebook - Cleaning	`http://localhost:8888/notebooks/Chapter6/03_Cleaning.ipynb`	`https://github.com/el-uhu/thesis-notebooks/blob/master/Chapter6/03_Cleaning.ipynb`
	Notebook - Model	`http://localhost:8888/notebooks/Chapter6/04_Model.ipynb`	`https://github.com/el-uhu/thesis-notebooks/blob/master/Chapter6/04_Model.ipynb`
	Interactive Visualisation	`http://cellcycle.org.uk/static/PPSIM/timecourse.html`	`http://cellcycle.org.uk/static/PPSIM/timecourse.html`

[a] Requires a running docker-container. For instructions, see `https://github.com/el-uhu/thesis-notebooks`

[b] Requires a working internet-connection.